COPY 1

10:44:20 OCA PAD AMENDMENT - PROJECT HEADER INFORMATION 04/07/94

Active

Project #: E-21-635 Cost share #: Rev #: 7
Center # : 10/24-6-R6817-0A0 Center shr #: OCA file #:
Work type : RES
Contract#: MOA DATED 9/11/89 Mod #: ADM. REVISION Document : CONT
Prime #: Contract entity: GTRC

Subprojects ? : N CFDA: N/A
Main project #: PE #: N/A

Project unit: ECE Unit code: 02.010.118
Project director(s):
BRENNAN K ECE (404)894-6767

Sponsor/division names: MOTOROLA INC /
Sponsor/division codes: 212 / 049

Award period: 890911 to 950731 (performance) 951031 (reports)

Sponsor amount	New this change	Total to date
Contract value	0.00	73,050.00
Funded	0.00	73,050.00
Cost sharing amount		0.00

Does subcontracting plan apply ?: N

Title: MODELING OF THREE TERMINAL SEMICONDUCTOR DEVICES: HEMTS AND HBTS

PROJECT ADMINISTRATION DATA

OCA contact: Robert D. Simpkins 894-4820

Sponsor technical contact

DR. HERBERT GORONKIN
(602)897-5908

MOTOROLA INC.
7402 S.PRICE ROAD
TEMPE, ARIZONA 85283

Sponsor issuing office

TERRY HENG
(312)397-5000

MOTOROLA INC.
1303 ALGONQUIN RD.
SCHAUMBURG, IL. 60196

Security class (U,C,S,TS) : U ONR resident rep. is ACO (Y/N): N
Defense priority rating : N/A N/A supplemental sheet
Equipment title vests with: Sponsor X GIT
NONE PROPOSED.
Administrative comments -
ISSUED TO EXTEND TERM DATE OF THIS PROJECT TO COINCIDE WITH MAIN PROJECT
E-21-F14. THIS PROJECT WAS SET UP TO OBTAIN INDUSTRY MATCHING FOR NSF GRANT.

SR 6/10 NOFY

GEORGIA INSTITUTE OF TECHNOLOGY
OFFICE OF CONTRACT ADMINISTRATION

NOTICE OF PROJECT CLOSEOUT

c/o (W) 6 mos
Due 5/2/96

PUBLICATION DELAYED UNTIL

Closeout Notice Date 11/02/95
Original Closeout Started 08/23/90

Project No. E-21-635 Center No. 10/24-6-R6817-0A0

Project Director BRENNAN K School/Lab ECE

Sponsor MOTOROLA INC/

Contract/Grant No. MOA DATED 9/11/89 Contract Entity GTRC

Prime Contract No.

Title MODELING OF THREE TERMINAL SEMICONDUCTOR DEVICES: HEMTS AND HBTS

Effective Completion Date 950731 (Performance) 951031 (Reports)

Closeout Actions Required:	Y/N	Date Submitted
Final Invoice or Copy of Final Invoice	N	
Final Report of Inventions and/or Subcontracts	N	
Government Property Inventory & Related Certificate	N	
Classified Material Certificate	N	
Release and Assignment	N	
Other	N	

Comments

Subproject Under Main Project No.

Continues Project No.

Distribution Required:

Project Director	Y
Administrative Network Representative	Y
GTRI Accounting/Grants and Contracts	Y
Procurement/Supply Services	Y
Research Property Managment	Y
Research Security Services	N
Reports Coordinator (OCA)	Y
GTRC	Y
Project File	Y
Other	N
	N

Progress Report: Motorola Corp.

Project Title: Modeling of Three Terminal Semiconductor Devices: HBTs

Investigator: Dr. Kevin F. Brennan

Organization: School of Electrical Engineering and Microelectronics Research Center Georgia Institute of Technology

Address: School of Electrical Engineering Georgia Institute of Technology Atlanta, Georgia, 30332

Phone: (404) 894-6767

ABSTRACT

The purpose of this project is to develop a sophisticated ensemble Monte Carlo simulator to study the internal workings of heterostructure bipolar transistors, HBTs. The basic Monte Carlo simulation package has already been developed and utilized in the past to study high electron mobility transistors, HEMTs. It is necessary to adapt the existing HEMT simulator to study HBTs. Owing to the modular nature of the simulator, it can readily be altered without compromising the previously demonstrated accurate description of the transport physics present in submicron semiconductor devices. In this report, we outline the initial progress taken towards this end, and propose the next series of steps.

I. Outline of the Problem

We have recently developed an extensive numerical simulator for studying high electron mobility transistors, HEMTs, based on an ensemble Monte Carlo code coupled with a two-dimensional Poisson solver [1]. The program contains most of the essential physics necessary to fully characterize submicron HEMT operation, i.e., a description of the transport physics of the two-dimensional electron gas, nonstationary transport (ballistic transport and velocity overshoot), real space transfer, and the effects of the two-dimensional electric field profile. The basic kernal of the Monte Carlo code, the determination of the free flight time, the various scattering mechanisms, and the compilation of results, is universal. The program has been written in such a way, that the various physical aspects of each device, for example the two-dimensional electron gas physics present in a HEMT, etc., are isolated from other portions of the code. This modular aspect enables ready revision of the program for different devices.

In the case of heterostructure bipolar transistors, HBTs, different physical phenomena are present and missing as compared to a HEMT. In particular, there is no two-dimensional electron gas present in an HBT. Therefore, the two-dimensional electron gas physics must be removed from the HEMT simulator during conversion to the HBT simulator. In addition, real space transfer occurs via carrier heating in the lateral direction in a HEMT while the transport is in the direction perpendicular to the heterolayers in an HBT. This will carefully be treated in a manner similar to that developed in our heterostructure avalanche photodiode analysis [2].

HBT structures are of importance in both microwave and digital applications owing to their inherent high speed capabilities. One of the important figures of merit in microwave transistor design is the cutoff frequency, f_t, which is the frequency at which the current gain is reduced to unity. The cutoff frequency is related to the emitter-collector delay time, τ_{ec} as,

$$f_t = 1 / (2\pi \tau_{ec})$$

where τ_{ec} can be expressed as,

$$\tau_{ec} = \tau_E + \tau_B + \tau_C + \tau'_C$$

Each of the terms in the above expression for τ_{ec} contributes to the overall delay of the transistor. τ_E is the emitter depletion-layer charging time, τ_B is the base charging time, τ_C is the collector depletion layer transit time, and τ_C' is the collector charging time. Expressing the above quantities in a more fundamental manner, the cutoff frequency can be rewritten as [3],

$$f_t = (2\pi [kT(C_e+C_c+C_p)/qI_c + W^2/2D_B + (x_c-W)/2v_s])^{-1}$$

where W is the effective base width, C_e, C_c and C_p are the emitter, collector and parasitic capacitances respectively, x_c-W is the collector-base depletion layer width, D_B is the base diffusion constant, and I_c is the collector current. Inspection of the above equation shows that the cutoff frequency can be increased by reducing the base width, collector transit region, and the collector current or by greatly increasing the electron drift velocity within the collector and base regions.

The maximum frequency of oscillation, f_{max}, can be expressed in terms of f_t as [4],

$$f_{max} = 1/2\ (f_t f_c)^{1/2}$$

where f_c is the frequency equivalent of the RC time constant of the combined base resistance collector capacitance,

$$f_c = 1/(2\pi R_b C_c).$$

Hence, a reduction of the base resistance can greatly increase f_{max}.

In digital applications, the most important figure of merit is the switching time of the transistor, τ_s. The switching time can be estimated as [4],

$$\tau_s = 5/2\ R_b C_c + R_b/R_L\ \tau_b + (3C_c + C_L)R_L$$

Again, optimal performance is achieved at lowered base resistance and base transit time.

The gain of a BJT depends upon the ratio of the collector to emitter currents. The maximum value of this ratio, β_{max}, in a heterostructure bipolar transistor can be expressed as,

$$\beta_{max} = I_n/I_p = N_e/P_b\ v_{nb}/v_{pe}\ \exp(\Delta E_g/kT)$$

where ΔE_g is the band edge discontinuity between the emitter and base layers, N_e and P_b are the emitter and base doping concentrations respectively. Clearly, in order to achieve a high gain device, it is important to either dope the emitter considerably greater than the base or utilize a heterostructure in which ΔE_g is large. The primary advantage of heterostructure emitters is that the base doping concentration can be significantly increased thereby reducing the base resistance, while the presence of the emitter-base heterostructure enables high gain at reduced emitter to base doping ratio.

II. Work to Date

The high acceptor doping concentration present in the base

of an HBT leads to a large hole concentration in the base. As a consequence, injected electrons from the emitter experience a large interaction with the holes, leading to significant electron-hole scattering and screening of the electron-phonon interaction. It is necessary to include these two effects in any description of HBT performance since they can significantly increase the electron base transit time and thereby alter the cutoff frequency of the device. We have rederived the electron-hole interaction following the approach of Osman and Ferry [5]. The details of this calculation are included in an appendix affixed at the end of this report. The electron-hole scattering rate is,

$$1/\tau = p\ \mu\ e^4/(\pi\ \epsilon^2\ \hbar^3\ \beta^2\ [Q_{eh}/(Q_{eh}^2 + \beta^2)]$$

where,

$$\mu = m_e m_h/(m_e + m_h)$$

and,

$$Q_{eh} = 2\mu\ |k_1/m_e - k_2/m_h|$$

(e and h represent electron and hole respectively). The total rate is found by summing the above expression over all of the holes present in the base. Owing to the high hole concentration, the sum can be replaced by an integral and the total rate is found as,

$$\Gamma_{eh}(k_o) = p\mu e^4/(2\pi\epsilon^2\hbar^3) \int d^3k\ f_h(k)\ Q_{eh}/(Q_{eh}^2 + \beta^2)$$

where $f_h(k)$ is the hole distribution function in the base. Under most conditions, the hole distribution will be much cooler than the injected electron distribution. To a first order approximation, the hole distribution can be assumed to be given

by a drifted Maxwellian characterized by a hole temperature, T_h as,

$$f_h(k) = [\pi\hbar^2/(2m_h k_B T)]^{3/2} \exp[-\hbar^2 k^2/(2m_h k_B T)]$$

The above result is used in the Monte Carlo simulation in order to determine the probability of an electron-hole scattering event.

Preliminary calculations indicate that the electron-hole scattering rate is on the order of 10^{12} -10^{13} in GaAs, comparable to the electron-phonon scattering rate. Though the electron-hole scattering mechanism is elastic, i.e., the total kinetic energy of the particles is conserved, there can be energy loss from the electron gas into the hole gas leading to a net cooling of the hot injected electrons in the base. This in turn can lead to thermalization of the electrons with a resultant decrease in the device α, the ratio of collected to injected electron current.

The inclusion of electron-hole scattering in the Monte Carlo code requires knowledge of not only the overall rate but how the final state is determined as well, since the Monte Carlo analysis traces the trajectories of the carriers during their flights through the device. Hence, after a scattering event, it is necessary to specify the new electron state based on the physics of the interaction. In the case of electron-hole scattering, the final electron state depends upon both the initial electron and hole states. The initial electron state is known through the Monte Carlo simulation. The question is then, how do we specify the initial hole state? The most direct method is to use a bipolar Monte Carlo simulator in which both the electrons and holes are simulated concurrently. However, such a scheme is very

complicated and computationally intensive particularly if a two-dimensional Poisson solver is used. As a first attempt, we plan on using a unipolar simulator, electrons only, coupled with a two-dimensional Poisson solver, treating the holes using a drifted Maxwellian distribution. In this case, a random hole state can be found from the specified distribution to serve as the initial hole state for the scattering. The final state is then found in a manner analogous to that given in reference 6.

III. Future Directions

Screening of the electron-phonon interaction at high carrier concentrations can significantly reduce phonon scattering further enhancing the importance of electron-hole scattering in energy relaxation [5]. In addition, it is important to consider multiband electron-hole scatterings [7] since the relaxation rate varies with respect to the initial and final bands in which the electrons and holes lie. We plan to study these effects and to add them to our HBT simulator. Through the inclusion of electron-hole scattering, and screening effects, much of the important physics present in an HBT is included.

The simulator will further include a two-dimensional Poisson solver [1], transport across a heterostructure [2], and ballistic and velocity overshoot effects. We plan to study a novel means by which the collector transit time can be reduced by repeated velocity overshoot. Our approach is based on electron confinement within the high velocity gamma valley by accelerating the electrons up a potential "staircase" so as to avoid intervalley transfer [8]. The full details are disclosed in the accompanying

reprint of reference 8. The basic idea though can be summarized as follows: the electrons are confined to the gamma valley by losing excess kinetic energy gained from an applied field by "climbing" a series of potential steps formed from a heterostructure stack. In this way intervalley transfer is defeated leading to very high velocities, $\sim 5.0 \times 10^{7}$ cm/sec, over lengths on the order of 0.5 μm.

REFERENCES

[1] D.H. Park and K.F. Brennan, "Theoretical analysis of an $Al_{0.15}Ga_{0.85}As/In_{0.15}Ga_{0.85}As$ pseudomorphic HEMT using an ensemble Monte Carlo simulation," IEEE Trans. Electron Dev., vol. 36, pp. 1254-1263, 1989.

[2] K. Brennan, "Optimization and modeling of avalanche photodiode structures: Application to a new class of superlattice photodetectors, the p-i-n, p-n homojunction, and p-n heterojunction APDs," IEEE Trans. Electron Dev., vol. ED-34, pp. 1658-1669, 1987.

[3] S.M. Sze, Physics of Semiconductor Devices, 2nd Edition, J. Wiley and Sons, 1981, p. 159.

[4] H. Kroemer, "Heterostructure bipolar transistors and integrated circuits," Proc. of the IEEE, vol. 70, pp. 13-25, 1982.

[5] M.A. Osman and D.K. Ferry, "Monte Carlo investigation of the electron-hole interaction effects on the ultrafast relaxation of hot photoexcited carriers in GaAs," Phys. Rev. B, vol. 36, pp. 6018-6032, 1987.

[6] A. Matulionis, J Pozela and A. Reklaitis, "Monte Carlo treatment of electron-electron collisions," Solid State Comm., vol. 16, pp. 1133-1137, 1975.

[7] K. Sadra, C. M. Maziar, B. G. Streetman, and D. S. Tang, "Effects of multiband electron-hole scattering and hole wave-function symmetry on minority-electron transport in GaAs," J. Appl. Phys., vol. 66, pp. 4791- 4800, 1989.

[8] K. Brennan and K. Hess, "Transient electronic transport in staircase heterostructures," IEEE Electron Dev. Lett., vol. EDL-

4, pp. 419-421, 1983.

Appendix

Electron - Hole Scattering

$V(|\bar{r}-\bar{r}'|) = \frac{e^2}{4\pi\epsilon} \frac{e^{-\beta|\bar{r}-\bar{r}'|}}{|\bar{r}-\bar{r}'|}$ screened Coulomb interaction

$\beta \equiv$ inverse screening length.

Transition probability -

$$S_{k_0, \bar{x} \to \bar{x}_0', x'} = \frac{2\pi}{\hbar} |M|^2 f_{k_0} f_{\bar{x}} (1-f_{k_0'})(1-f_{\bar{x}'}) \delta(E_{k_0'} + E_{\bar{x}'} - E_{k_0} - E_{\bar{x}}$$

Need to evaluate M,

$$M = + \frac{e^2}{4\pi\epsilon} \iint d^3r' d^3r \frac{e^{-\beta|\bar{r}-\bar{r}'|}}{|\bar{r}-\bar{r}'|} \psi_{\bar{x}}^*(r) \psi_{\bar{x}}^*(r') \psi_{k_0'}(r) \psi_{\bar{x}'}(r')$$

Need to perform the integral in the above.

$$M = \frac{e^2}{4\pi\epsilon} \frac{1}{V^2} \iint d^3r' d^3r \frac{e^{-\beta|r-r'|}}{|r-r'|} e^{-i\bar{k}_0 r} e^{-i\bar{x} r'} e^{i\bar{x}_0' r} e^{i\bar{x}' r'}$$

$$M = \frac{e^2}{4\pi\epsilon} \frac{1}{V^2} \iint d^3r' d^3r \; e^{i(\bar{x}_0' - \bar{x}_0) r} \frac{e^{-\beta|r-r'|}}{|r-r'|} e^{i(\bar{x}' - \bar{x}) r'}$$

let $\bar{u} \equiv \bar{r} - \bar{r}'$

$\bar{r} = \bar{u} + \bar{r}'$

$$M = \frac{e^2}{4\pi\epsilon} \frac{1}{V^2} \iint du \; e^{i(\vec{x}_1' - \vec{x}_0) \cdot \bar{u}} \frac{e^{-\beta|u|}}{|u|}$$

$$* \int e^{i(\vec{x}_0' - \vec{x}_0 + \bar{x}' - \bar{x}) \cdot \bar{r}'} d^3r'$$

$$M = \frac{e^2}{4\pi\epsilon}\frac{1}{V^2}\int du\; e^{i(\bar{R}_0'-\bar{R}_0)\cdot\bar{u}}\frac{e^{-\beta|u|}}{|u|} * V\,\delta(\bar{R}_0'+\bar{R}', \bar{R}_0+\bar{R}) \quad (6.2)$$

Since,

$$\int e^{i(\bar{R}_0'-\bar{R}_0+\bar{R}'-\bar{R})\cdot\bar{r}'} d^3r' = V\,\delta(\bar{R}_0'+\bar{R}', \bar{R}_0+\bar{R})$$

$$M = \frac{e^2}{4\pi\epsilon}\frac{1}{V}\,\delta(\bar{R}_0'+\bar{R}', \bar{R}_0+\bar{R})\int du\; e^{i(\bar{R}_0'-\bar{R}_0)\cdot\bar{u}}\frac{e^{-\beta|u|}}{|u|}$$

Perform the 3rd integral in 3 dim.

$$M = \frac{e^2}{4\pi\epsilon}\frac{1}{V}\,\delta(\bar{R}_0'+\bar{R}', \bar{R}_0+\bar{R})\int_0^{2\pi}\int_0^{\pi}\int_0^{\infty} e^{i|\bar{R}_0'-\bar{R}_0|u\cos\theta}\frac{e^{-\beta u}}{u}\sin\theta\, u^2\, d\phi\, d\theta\, du$$

$$M = \frac{e^2}{4\pi\epsilon}\frac{2\pi}{V}\,\delta(\bar{R}_0'+\bar{R}', \bar{R}_0+\bar{R})\int_0^{\infty}\int_0^{\pi} e^{i|\bar{R}_0'-\bar{R}_0|u\cos\theta}\, e^{-\beta u}\, u\sin\theta\, d\theta\, du$$

Let $v = \cos\theta$

$dv = -\sin\theta\, d\theta$

$$-\int_{+1}^{-1} e^{i|\bar{R}_0'-\bar{R}_0|uv}\, dv = \frac{-1}{i|\bar{R}_0'-\bar{R}_0|u}\, e^{i|\bar{R}_0'-\bar{R}_0|uv}\Big|_{+1}^{-1}$$

$$= \frac{-1}{i|\bar{R}_0'-\bar{R}_0|u}\left(e^{-i|\bar{R}_0'-\bar{R}_0|u} - e^{i|\bar{R}_0'-\bar{R}_0|u}\right)$$

But

$$\frac{e^{i\theta}-e^{-i\theta}}{2i} = \sin\theta$$

$$\Pi = \frac{e^2}{4\pi\epsilon}\,\frac{2\pi}{V}\,\delta(\vec{k}_0'+\vec{k}',\vec{k}_0+\vec{k})\int_0^\infty \frac{e^{-\beta u}\,(+2)}{|\vec{x}_0'-\vec{x}_0|}\,\sin|\vec{x}_0'-\vec{x}_0|\,u$$ p.3

$$\Pi = +\frac{e^2}{\epsilon V}\,\delta(\vec{k}_0'+\vec{k}',\vec{k}_0+\vec{k})\int_0^\infty \frac{e^{-\beta u}\sin|\vec{x}_0'-\vec{x}_0|u}{|\vec{x}_0'-\vec{x}_0|}\,du.$$

$\Rightarrow$ Easier to ~~integrate~~ if we rewrite the sin again.

$$\Pi = \frac{+e^2}{\epsilon V}\,\delta(\vec{k}_0'+\vec{k}',\vec{k}_0+\vec{k})\int_0^\infty \frac{e^{-\beta u}}{|\vec{x}_0'-\vec{x}_0|}\left(\frac{e^{i(\vec{x}_0'-\vec{x}_0)u} - e^{-i(\vec{x}_0'-\vec{x}_0)u}}{2i}\right)du$$

~~integrate~~ out each term,

$$\int_c^\infty \frac{e^{(i(\vec{x}_0'-\vec{x}_0)-\beta)u}}{(2i)\,|\vec{x}_0'-\vec{x}_0|}\,du$$

$$-\frac{1}{2i}\,\frac{1}{|\vec{x}_0'-\vec{x}_0|}\left\{\frac{1}{i(\vec{x}_0'-\vec{x}_0)-\beta} - \frac{1}{-i(\vec{x}_0'-\vec{x}_0)-\beta}\right\}$$

∞ bound $\to 0$.
0 bound $\to 1$.

$$\frac{1}{2i}\,\frac{1}{|\vec{x}_0'-\vec{x}_0|}\left\{\frac{1}{\beta - i(\vec{x}_0'-\vec{x}_0)} + \frac{1}{\beta + i(\vec{x}_0'-\vec{x}_0)}\right\}$$

$$\frac{1}{2i}\,\frac{1}{|\vec{x}_0'-\vec{x}_0|}\left\{\frac{\beta + i(\vec{x}_0'-\vec{x}_0) - \beta + i(\vec{x}_0'-\vec{x}_0)}{\beta^2 + |\vec{x}_0'-\vec{x}_0|^2}\right\}$$

$$= \frac{1}{\beta^2+|\vec{x}_0'-\vec{x}_0|^2}$$ ✓

$$\eta = \frac{+e^2}{\epsilon V} \frac{\delta(\bar{k}_0' + \bar{k}', \bar{k}_0 + \bar{k})}{\beta^2 + |\bar{k}_0' - \bar{k}_0|^2} \quad \checkmark \quad (9.3).$$

assume that all the final states are unoccupied in the calculation of the scattering rate.

$\therefore f_{k_0'} = f_{k'} = 0.$

Let $f_{k_0} = 1.$

$$\therefore S_{k_0; k \to k_0', k'} = \frac{2\pi}{\hbar} \frac{e^4}{\epsilon^2 V^2} \frac{[\delta(k_0 + k, k_0' + k')]^2}{[|\bar{k}_0' - \bar{k}_0|^2 + \beta^2]^2} \frac{f_k \, \delta(E)}{}$$

The scattering rate is given thus as,

$$1/\tau = \frac{2V}{(2\pi)^3} \int_0^\infty dk'' \int_0^\pi d\theta \int_0^{2\pi} d\phi \; S_{k_0, k \to k_0', k'} \; k''^2 \sin\theta$$

where we simply integrate the transition probability over the final density of state expressed in terms of k''.

Change notation here to simplify.

$S(k_1 k_2 \to k_1' k_2')$

$k_1 : k_2$ are the initial states.

$k_1' : k_2'$ are the final states.

$|\bar{k}_0' - \bar{k}_0|^2 = |\bar{k}_1' - \bar{k}_1|^2$.

$$\therefore S(k_1 k_2 \to k_1' k_2') = \frac{2\pi}{\hbar} \frac{e^4}{\epsilon^2 V^2} \frac{\beta^2}{[|\bar{k}_1' - \bar{k}_1|^2 + \beta^2]^2} \delta(k_1 + k_2, k_1' + k_2')$$

Earlier

k_0, k_0' }

k, k' }

↑ init ↑ final

$$k_1' \to k_0' \qquad k_1 \to k_0$$
$$k_2' \to k' \qquad k_2 \to k$$

Let $V = 1$

P.C

$$1/\tau = \frac{2}{(2\pi)^3}\frac{2\pi}{\hbar}\frac{e^4}{\epsilon^2}\int d\vec{k}_1'\int d\vec{k}_2'\ \frac{\delta(\vec{k}_1+\vec{k}_2-\vec{k}_1'+\vec{k}_2')\ \delta(\epsilon_1+\epsilon_2-\epsilon_1'-\epsilon_2')}{[\beta^2+|\vec{k}_1'-\vec{k}_1|^2]^2}$$

$$= \frac{2}{(2\pi)^3}\frac{2\pi}{\hbar}\frac{e^4}{\epsilon^2}\int d\vec{k}_1'\ \frac{\delta[\frac{\hbar^2}{2m}(k_1^2+k_2^2-k_1'^2-|\vec{k}_1+\vec{k}_2-\vec{k}_1'|^2)]}{[\beta^2+|\vec{k}_1'-\vec{k}_1|^2]^2}$$

Let $\vec{k}_3 = \vec{k}_1'-\vec{k}_1$

$$= \frac{2}{(2\pi)^3}\frac{2\pi}{\hbar}\frac{e^4}{\epsilon^2}\frac{2m}{\hbar^2}\int d\vec{k}_3\ \frac{\delta[k_1^2+k_2^2-|\vec{k}_3+\vec{k}_1|^2-|\vec{k}_2-\vec{k}_3|^2]}{[\beta^2+k_3^2]^2}$$

$$= \frac{2}{(2\pi)^3}\frac{2\pi}{\hbar}\frac{e^4}{\epsilon^2}\frac{2m}{\hbar^2}\int d\vec{k}_3\ \frac{\delta[k_1^2+k_2^2-(k_3^2+k_1^2+2\vec{k}_3\cdot\vec{k}_1)-(k_2^2+k_3^2-2\vec{k}_2\cdot\vec{k}_3)]}{[\beta^2+k_3^2]^2}$$

$$= \frac{2}{(2\pi)^3}\frac{2\pi}{\hbar}\frac{e^4}{\epsilon^2}\frac{2m}{\hbar^2}\int_0^\infty k_3^2\,dk_3\int_0^{2\pi}d\phi\int_0^\pi \sin\theta\,d\theta\ \frac{\delta[-2k_3^2+2\vec{k}_3\cdot(\vec{k}_2-\vec{k}_1)]}{[\beta^2+k_3^2]^2}$$

$\Rightarrow$

$$= \frac{2}{(2\pi)^3}\frac{(2\pi)^2}{\hbar}\frac{e^4}{\epsilon^2}\frac{2m}{\hbar^2}\int_0^\infty k_3^2\,dk_3\int_0^\pi \sin\theta\,d\theta\ \frac{\delta[-2(\vec{k}_3\cdot(\vec{k}_1-\vec{k}_2)+k_3^2]}{[\beta^2+k_3^2]^2}$$

Note $\delta(ax) = \frac{1}{|a|}\delta(x)$

$$= \frac{2}{2\pi}\frac{2m}{\hbar^3}\frac{e^4}{\epsilon^2}\frac{1}{2}\int_0^\infty k_3^2\,dk_3\int_0^\pi \sin\theta\,d\theta\ \frac{\delta[k_3^2+\vec{k}_3\cdot(\vec{k}_1-\vec{k}_2)]}{[\beta^2+k_3^2]^2}$$

$$= \frac{2me^4}{2\pi\hbar^3\epsilon^2}\int_0^\infty k_3^2\,dk_3\int_0^\pi \frac{\delta(k_3^2+k_3 k\cos\theta)}{(\beta^2+k_3^2)^2}\sin\theta\,d\theta$$

where $\vec{k} \equiv \vec{k}_1-\vec{k}_2$

Let $x = \cos\theta$

$$= \frac{2me^4}{2\pi\hbar^3\epsilon^2}\int_0^\infty k_3^2\,dk_3\int_{-1}^{+1}\frac{\delta(x+k_3/k)}{k_3 k\,(\beta^2+k_3^2)^2}\,dx$$

$$= \frac{2me^4}{2\pi\hbar^3\epsilon^2}\int_0^\infty q_s^2\,dq_s\;\frac{1}{q_s q(\beta^2+q_s^2)^2}\left[\Theta\left(\frac{q_s}{q}+1\right)-\Theta\left(\frac{q_s}{q}-1\right)\right]$$

But $\Theta(x) = \begin{cases} 1 & x>0 \\ 0 & x<0 \end{cases}$

$$\Theta(q_s/q+1)-\Theta(q_s/q-1) = \begin{cases} 1 & q_s/q<1 \\ 0 & q_s/q>1 \end{cases}$$

The above gives the upper bound on the integral over k_s.

$$= \frac{2me^4}{2\pi\hbar^3\epsilon^2}\int_0^k \frac{k_s\,dk_s}{q(\beta^2+k_s^2)^2}$$

Let $u = k_s^2$

$du = 2k_s\,dk_s$

$$= \frac{me^4}{2\pi\hbar^3\epsilon^2}\int_0^{k^2}\frac{du}{q(\beta^2+u)^2}$$

$$= \frac{me^4}{2\pi\hbar^3\epsilon^2 q}\int_0^{k^2}\frac{du}{(\beta^2+u)^2}$$

Consider $\int\frac{dx}{(a+x)^2} = -\frac{1}{(a+x)}$

$$= \frac{me^4}{2\pi\hbar^3\epsilon^2 q}\left[-\frac{1}{(\beta^2+u)}\Big|_0^{k^2}\right]$$

$$= \frac{me^4}{2\pi\hbar^3\epsilon^2 k}\left[\frac{1}{\beta^2}-\frac{1}{\beta^2+k^2}\right]$$

$$= \frac{me^4}{2\pi\hbar^3\epsilon^2 k}\left[\frac{\beta^2+k^2-\beta^2}{\beta^2(\beta^2+k^2)}\right]$$

$$= \frac{me^4}{2\pi\hbar^3\epsilon^2\beta^2}\,\frac{k}{(\beta^2+k^2)}$$

$$\gamma_C = \frac{me^4}{2\pi\hbar^3\epsilon^2\beta^2}\,\frac{k}{(\beta^2+k^2)}$$

$$|\vec{R}| = |\vec{R}_1 - \vec{R}_2|$$

Factor of 2 greater than in the literature. Due to the Pauli Principle. If we don't consider the spin degeneracy, we get the same result as in the literature.

Electron-hole Scattering

$\vec{k}_1, \vec{k}_1' \equiv$ electrons ; $\vec{k}_2, \vec{k}_2' \equiv$ holes

$$1/\tau = \frac{2}{(2\pi)^3} \cdot \frac{2\pi}{\hbar} \int d\vec{k}_1' \int d\vec{k}_2' \frac{e^4}{\epsilon^2} \frac{\delta(\vec{k}_1+\vec{k}_2, \vec{k}_1'+\vec{k}_2') \, \delta(E_1+E_2-E_1'-E_2')}{(\beta^2 + |\vec{k}_1'-\vec{k}_1|^2)^2}$$

$$= \frac{2}{(2\pi)^2} \frac{e^4}{\epsilon^2} \frac{1}{\hbar} \int d\vec{k}_1' \frac{\delta\left(\frac{\hbar^2}{2m_e}\left(k_1^2 + m_e/m_h k_2^2 - k_1'^2 - m_e/m_h |\vec{k}_1+\vec{k}_2-\vec{k}_1'|^2\right)\right.}{(\beta^2 + |\vec{k}_1'-\vec{k}_1|^2)^2}$$

$$= \frac{2}{(2\pi)^2} \frac{e^4}{\epsilon^2} \frac{1}{\hbar} \frac{2m_e}{\hbar^2} \int d\vec{k}_s \frac{\delta(k_1^2 + m_e/m_h k_2^2 - |\vec{k}_s+\vec{k}_1|^2 - m_e/m_h |\vec{k}_2-\vec{k}_s|^2)}{(\beta^2+k_s^2)^2}$$

where $\vec{k}_s = \vec{k}_1' - \vec{k}_1$

$$= \frac{2}{(2\pi)^2} \frac{e^4}{\epsilon^2} \frac{2m_e}{\hbar^3} \int d\vec{k}_1 \frac{\delta(\cancel{k_1^2} + \cancel{m_e/m_h k_2^2} - k_s^2 - \cancel{k_1^2} - 2\vec{k}_s\cdot\vec{k}_1 - \cancel{m_e/m_h k_2^2} - \frac{m_e}{m_h}k_s^2 + \frac{2m_e}{m_h}\vec{k}_2\cdot\vec{k}_s)}{(\beta^2+k_s^2)^2}$$

$$= \frac{2}{(2\pi)^2} \frac{e^4}{\epsilon^2} \frac{2m_e}{\hbar^3} \int d\vec{k}_s \frac{\delta(-k_s^2 - m_e/m_h k_s^2 - 2\vec{k}_s\cdot\vec{k}_1 + 2m_e/m_h \vec{k}_2\cdot\vec{k}_s)}{(\beta^2+k_s^2)^2}$$

$$= \frac{2}{(2\pi)^2} \frac{e^4}{\epsilon^2} \frac{2m_e}{\hbar^3} \int d\vec{k}_s \frac{\delta[-k_s^2(1+m_e/m_h) - 2\vec{k}_s\cdot(\vec{k}_1 - m_e/m_h \vec{k}_2)]}{(\beta^2+k_s^2)^2}$$

Let $\vec{k} \equiv \vec{k}_1 - m_e/m_h \vec{k}_2$

$$\frac{2}{(2\pi)^2} \frac{e^4}{\epsilon^2} \frac{2m_e}{\hbar^3} \int d\vec{k}_s \frac{\delta[-k_s^2(1+m_e/m_h) - 2k_s k\cos\theta]}{(\beta^2+k_s^2)^2}$$

$$= \frac{2}{(2\pi)^2} \frac{e^4}{\epsilon^2} \frac{2m_e}{\hbar^3} \int d\vec{k}_s \frac{\delta[-2k_s k(k_s/2k(1+m_e/m_h) + \cos\theta)]}{(\beta^2+k_s^2)^2}$$

$$= \frac{2}{(2\pi)^2} \frac{e^4}{\epsilon^2} \frac{2m_e}{\hbar^3} \int d\vec{k}_s \frac{1}{2k_s k} \frac{\delta(k_s/2k(1+m_e/m_h) + \cos\theta)}{(\beta^2+k_s^2)^2}$$

$$\left(\frac{2}{2\pi}\right)^2 \frac{e^4}{\epsilon^2}\frac{2m_e}{\hbar^3}\frac{1}{2k}\int_0^\infty \frac{q_s^2\,dq_s}{q_s}\int_0^\pi d\theta\sin\theta\int_0^{2\pi} d\phi\;\frac{\delta\left(q_s/2k\,(1+m_e/m_n)+\cos\theta\right)}{\left(\beta^2+q_s^2\right)^2}$$ P.10

$$\frac{2m_e e^4}{(2\pi)\epsilon^2}\frac{1}{\hbar^3}\frac{1}{k}\int_0^\infty q_s\,dq_s\int_0^\pi \sin\theta\,d\theta\;\frac{\delta\left(\cos\theta+q_s/2k\,(1+m_e/m_n)\right)}{\left(\beta^2+q_s^2\right)^2}$$

Let $x=\cos\theta$

$dx=\sin\theta\,d\theta$

$$\frac{2m_e e^4}{(2\pi)\epsilon^2}\frac{1}{\hbar^3}\frac{1}{k}\int_0^\infty q_s\,dq_s\int_{-1}^{+1} dx\;\frac{\delta\left(x+q_s/2k\,(1+m_e/m_n)\right)}{\left(\beta^2+q_s^2\right)^2}$$

$$\frac{2m_e e^4}{2\pi\epsilon^2}\frac{1}{\hbar^3}\frac{1}{k}\int_0^\infty \frac{q_s\,dq_s}{\left(\beta^2+q_s^2\right)^2}\left[\theta\left(x+\frac{q_s}{2k}(1+m_e/m_n)\right)\right]_{-1}^{+1}$$

$$\frac{2m_e e^4}{2\pi\epsilon^2}\frac{1}{\hbar^3}\frac{1}{k}\int_0^\infty \frac{q_s\,dq_s}{\left(\beta^2+q_s^2\right)^2}\left[\theta\left(1+\frac{q_s}{2k}(1+m_e/m_n)\right)-\theta\left(-1+\frac{q_s}{2k}(1+m_e/m_n\right)\right.$$

$\frac{q_s}{2k}(1+m_e/m_n)<1$ nonzero value of 1.

$$q_s < \frac{2k}{(1+m_e/m_n)}$$

$$\frac{2m_e e^4}{2\pi\epsilon^2}\frac{1}{\hbar^3}\frac{1}{k}\int_0^{2k/(1+m_e/m_n)} \frac{q_s\,dq_s}{\left(\beta^2+q_s^2\right)^2}$$

Let $u=q_s^2$

$du=2q_s\,dq_s$

$$\int_0^\alpha \frac{du}{(\beta^2+u)^2} = \frac{-1}{\beta^2+u}\Bigg|_0^{\left[2k/(1+m_e/m_n)\right]^2}$$

$$=\left[\frac{1}{\beta^2}-\frac{1}{\beta^2+\frac{(2k)^2}{(1+m_e/m_n)^2}}\right]$$

Annual Report: Motorola Corp.

Project Title: Modeling of Three Terminal Semiconductor Devices: HBTs

Investigator: Dr. Kevin F. Brennan

Organization: School of Electrical Engineering and Microelectronics Research Center Georgia Institute of Technology

Address: School of Electrical Engineering Georgia Institute of Technology Atlanta, Georgia, 30332-0250

Phone: (404) 894-6767

ABSTRACT

During the first year of effort on this project we have developed the physics of electron-hole scattering. The details have been reported earlier but are reproduced here for completeness. Further work has been done concerning the fundamental advantages of HBTs, particularly for high frequency performance. We have worked through much of the basic physics of HBTs which we summarize here. Finally, we have enclosed copies of the material to be used during the annual review of this project in Phoenix in October, 1990.

I. Outline of the Problem

We have recently developed an extensive numerical simulator for studying high electron mobility transistors, HEMTs, based on an ensemble Monte Carlo code coupled with a two-dimensional Poisson solver [1]. The program contains most of the essential physics necessary to fully characterize submicron HEMT operation, i.e., a description of the transport physics of the two-dimensional electron gas, nonstationary transport (ballistic transport and velocity overshoot), real space transfer, and the effects of the two-dimensional electric field profile. The basic kernal of the Monte Carlo code, the determination of the free flight time, the various scattering mechanisms, and the compilation of results, is universal. The program has been written in such a way, that the various physical aspects of each device, for example the two-dimensional electron gas physics present in a HEMT, etc., are isolated from other portions of the code. This modular aspect enables ready revision of the program for different devices.

In the case of heterostructure bipolar transistors, HBTs, different physical phenomena are present and missing as compared to a HEMT. In particular, there is no two-dimensional electron gas present in an HBT. Therefore, the two-dimensional electron gas physics must be removed from the HEMT simulator during conversion to the HBT simulator. In addition, real space transfer occurs via carrier heating in the lateral direction in a HEMT while the transport is in the direction perpendicular to the heterolayers in an HBT. This will carefully be treated in a manner similar to that developed in our heterostructure avalanche photodiode analysis [2].

HBT structures are of importance in both microwave and digital applications owing to their inherent high speed capabilities. One of the important figures of merit in microwave transistor design is the cutoff frequency, f_t, which is the frequency at which the current gain is reduced to unity. The cutoff frequency is related to the emitter-collector delay time, τ_{ec} as,

$$f_t = 1 / (2\pi \tau_{ec})$$

where τ_{ec} can be expressed as,

$$\tau_{ec} = \tau_E + \tau_B + \tau_C + \tau'_C$$

Each of the terms in the above expression for τ_{ec} contributes to the overall delay of the transistor. τ_E is the emitter depletion-layer charging time, τ_B is the base charging time, τ_C is the collector depletion layer transit time, and τ_C' is the collector charging time. Expressing the above quantities in a more fundamental manner, the cutoff frequency can be rewritten as [3],

$$f_t = (2\pi [kT(C_e+C_c+C_p)/qI_c + W^2/2D_B + (x_c-W)/2v_s])^{-1}$$

where W is the effective base width, C_e, C_c and C_p are the emitter, collector and parasitic capacitances respectively, x_c-W is the collector-base depletion layer width, D_B is the base diffusion constant, and I_c is the collector current. Inspection of the above equation shows that the cutoff frequency can be increased by reducing the base width, collector transit region, and the collector current or by greatly increasing the electron drift velocity within the collector and base regions.

The maximum frequency of oscillation, f_{max}, can be expressed in terms of f_t as [4],

$$f_{max} = 1/2\ (f_t f_c)^{1/2}$$

where f_c is the frequency equivalent of the RC time constant of the combined base resistance collector capacitance,

$$f_c = 1/(2\pi R_b C_c).$$

Hence, a reduction of the base resistance can greatly increase f_{max}.

In digital applications, the most important figure of merit is the switching time of the transistor, τ_s. The switching time can be estimated as [4],

$$\tau_s = 5/2\ R_b C_c + R_b/R_L\ \tau_b + (3C_c + C_L)R_L$$

Again, optimal performance is achieved at lowered base resistance and base transit time.

The gain of a BJT depends upon the ratio of the collector to emitter currents. The maximum value of this ratio, β_{max}, in a heterostructure bipolar transistor can be expressed as,

$$\beta_{max} = I_n/I_p = N_e/P_b\ v_{nb}/v_{pe}\ \exp(\Delta E_g/kT)$$

where ΔE_g is the band edge discontinuity between the emitter and base layers, N_e and P_b are the emitter and base doping concentrations respectively. Clearly, in order to achieve a high gain device, it is important to either dope the emitter considerably greater than the base or utilize a heterostructure in which ΔE_g is large. The primary advantage of heterostructure emitters is that the base doping concentration can be significantly increased thereby reducing the base resistance, while the presence of the emitter-base heterostructure enables high gain at reduced emitter to base doping ratio.

II. Work to Date

The high acceptor doping concentration present in the base

of an HBT leads to a large hole concentration in the base. As a consequence, injected electrons from the emitter experience a large interaction with the holes, leading to significant electron-hole scattering and screening of the electron-phonon interaction. It is necessary to include these two effects in any description of HBT performance since they can significantly increase the electron base transit time and thereby alter the cutoff frequency of the device. We have rederived the electron-hole interaction following the approach of Osman and Ferry [5]. The details of this calculation are included in an appendix affixed at the end of this report. The electron-hole scattering rate is,

$$1/\tau = p\ \mu\ e^4/(\pi\ \epsilon^2\ \hbar^3\ \beta^2\ [Q_{eh}/(Q_{eh}^2 + \beta^2)]$$

where,

$$\mu = m_e m_h/(m_e + m_h)$$

and,

$$Q_{eh} = 2\mu\ |k_1/m_e - k_2/m_h|$$

(e and h represent electron and hole respectively). The total rate is found by summing the above expression over all of the holes present in the base. Owing to the high hole concentration, the sum can be replaced by an integral and the total rate is found as,

$$\Gamma_{eh}(k_o) = p\mu e^4/(2\pi\epsilon^2\hbar^3) \int d^3k\ f_h(k)\ Q_{eh}/(Q_{eh}^2 + \beta^2)$$

where $f_h(k)$ is the hole distribution function in the base. Under most conditions, the hole distribution will be much cooler than the injected electron distribution. To a first order approximation, the hole distribution can be assumed to be given

by a drifted Maxwellian characterized by a hole temperature, T_h as,

$$f_h(k) = [\pi\hbar^2/(2m_h k_B T)]^{3/2} \exp[-\hbar^2 k^2/(2m_h k_B T)]$$

The above result is used in the Monte Carlo simulation in order to determine the probability of an electron-hole scattering event.

Preliminary calculations indicate that the electron-hole scattering rate is on the order of 10^{12} -10^{13} in GaAs, comparable to the electron-phonon scattering rate. Though the electron-hole scattering mechanism is elastic, i.e., the total kinetic energy of the particles is conserved, there can be energy loss from the electron gas into the hole gas leading to a net cooling of the hot injected electrons in the base. This in turn can lead to thermalization of the electrons with a resultant decrease in the device α, the ratio of collected to injected electron current.

The inclusion of electron-hole scattering in the Monte Carlo code requires knowledge of not only the overall rate but how the final state is determined as well, since the Monte Carlo analysis traces the trajectories of the carriers during their flights through the device. Hence, after a scattering event, it is necessary to specify the new electron state based on the physics of the interaction. In the case of electron-hole scattering, the final electron state depends upon both the initial electron and hole states. The initial electron state is known through the Monte Carlo simulation. The question is then, how do we specify the initial hole state? The most direct method is to use a bipolar Monte Carlo simulator in which both the electrons and holes are simulated concurrently. However, such a scheme is very

complicated and computationally intensive particularly if a two-dimensional Poisson solver is used. As a first attempt, we plan on using a unipolar simulator, electrons only, coupled with a two-dimensional Poisson solver, treating the holes using a drifted Maxwellian distribution. In this case, a random hole state can be found from the specified distribution to serve as the initial hole state for the scattering. The final state is then found in a manner analogous to that given in reference 6.

Recent work [7] indicates that the electron-hole scattering rate plateaus and then surprising drops with increased hole carrier concentration beyond 10^{20} cm^{-3}. Interestingly, a nonstationary transport window appears at both low and very high base doping concentrations. Therefore, it is expected that at very high base dopings, both the transit time and base resistance are greatly reduced. However, there is a tradeoff due to the increase in back injected hole current into the emitter reducing the emitter injection efficiency. It is the purpose of this research to analyze the effect of increased base doping on the transit time using our Monte Carlo code and to calculate the ultimate theoretical limit of base doping for high frequency performance.

The focus of this research program is to develop a means of optimizing HBT structures and to predict the ultimate limits of performance of these devices. It is necessary to first define the principle engineering figures of merit by which HBTs can be judged. As discussed above, the cutoff frequency, f_t, and the maximum frequency of oscillation, f_{max}, are generally uwed in

order to characterize the microwave performance of an HBT. Neither of these measures, alone, however, serves as an adequate assessment of the highest frequency capable of a microwave transistor. A device designed to exhibit a very short transit time will necessarily have an f_t significantly larger than f_{max}. Since there is no power gain at frequencies beyond f_{max}, the device cannot be used at higher frequency in any practical application. Conversely, an HBT can be designed in which the base resistance is very small and as such would exhibit a very high f_{max}, but low f_t. Under these conditions, high frequency power gain can only be achieved through careful impedance matching requiring high Q components. Hence, it is important to assess both f_t and f_{max} in designing an HBT since a useful design requires the optimization of both quantities. Recent studies [8] indicate that as a practical guide to optimization, a device is considered optimized when the lesser of f_{max} and 2 f_t is as high as possible.

In an HBT made using an abrupt emitter-base junction a band-edge spike is formed which acts as an energy barrier reducing the emitter injection efficiency as well as increases the base-emitter turn-on voltage. Though the injection efficiency is lowered, the conduction band edge provides for high energy carrier injection into the base leading to nonstationary transport and a subsequent decrease in the emitter-collector transit time as discussed above. Hence an additional tradeoff exists in the design; the presence of a heterojunction can decrease the base transit time but at the expense of decreased emitter injection efficiency. In this project we will study the

effects of variation in the band edge discontinuity on the overall transit time and the emitter injection efficiency.

III. Future Directions

Screening of the electron-phonon interaction at high carrier concentrations can significantly reduce phonon scattering further enhancing the importance of electron-hole scattering in energy relaxation [5]. In addition, it is important to consider multiband electron-hole scatterings [7] since the relaxation rate varies with respect to the initial and final bands in which the electrons and holes lie. We plan to study these effects and to add them to our HBT simulator. Through the inclusion of electron-hole scattering, and screening effects, much of the important physics present in an HBT is included.

The simulator will further include a two-dimensional Poisson solver [1], transport across a heterostructure [2], and ballistic and velocity overshoot effects. We plan to study a novel means by which the collector transit time can be reduced by repeated velocity overshoot. Our approach is based on electron confinement within the high velocity gamma valley by accelerating the electrons up a potential "staircase" so as to avoid intervalley transfer [8]. The full details are disclosed in the accompanying reprint of reference 8. The basic idea though can be summarized as follows: the electrons are confined to the gamma valley by losing excess kinetic energy gained from an applied field by "climbing" a series of potential steps formed from a heterostructure stack. In this way intervalley transfer is defeated leading to very high velocities, $\sim 5.0 \times 10^7$ cm/sec,

over lengths on the order of 0.5 um.

REFERENCES

[1] D.H. Park and K.F. Brennan, "Theoretical analysis of an $Al_{0.15}Ga_{0.85}As/In_{0.15}Ga_{0.85}As$ pseudomorphic HEMT using an ensemble Monte Carlo simulation," IEEE Trans. Electron Dev., vol. 36, pp. 1254-1263, 1989.

[2] K. Brennan, "Optimization and modeling of avalanche photodiode structures: Application to a new class of superlattice photodetectors, the p-i-n, p-n homojunction, and p-n heterojunction APDs," IEEE Trans. Electron Dev., vol. ED-34, pp. 1658-1669, 1987.

[3] S.M. Sze, Physics of Semiconductor Devices, 2nd Edition, J. Wiley and Sons, 1981, p. 159.

[4] H. Kroemer, "Heterostructure bipolar transistors and integrated circuits," Proc. of the IEEE, vol. 70, pp. 13-25, 1982.

[5] M.A. Osman and D.K. Ferry, "Monte Carlo investigation of the electron-hole interaction effects on the ultrafast relaxation of hot photoexcited carriers in GaAs," Phys. Rev. B, vol. 36, pp. 6018-6032, 1987.

[6] A. Matulionis, J Pozela and A. Reklaitis, "Monte Carlo treatment of electron-electron collisions," Solid State Comm., vol. 16, pp. 1133-1137, 1975.

[7] D. A. Sunderland, and P. D. Dapkus, "The performance potential of p-n-p heterojunction bipolar transistors," IEEE Electron Dev. Lett., vol. EDL-6, pp. 648-651, 1985.

[8] A. F. J. Levi, R. N. Nottenburg, Y. K. Chen, P. H. Beton, and M. B. Panish, "Nonequilibrium electron dynamics in bipolar transistors," Solid-State Electron., vol. 32, pp. 1289-1295,

1989.

[9] K. Sadra, C. M. Maziar, B. G. Streetman, and D. S. Tang, "Effects of multiband electron-hole scattering and hole wave-function symmetry on minority-electron transport in GaAs," J. Appl. Phys., vol. 66, pp. 4791- 4800, 1989.

[10] K. Brennan and K. Hess, "Transient electronic transport in staircase heterostructures," IEEE Electron Dev. Lett., vol. EDL-4, pp. 419-421, 1983.

Appendix A

Electron - Hole Scattering

$$V(|\bar{r}-\bar{r}'|) = \frac{e^2}{4\pi\epsilon}\frac{e^{-\beta|\bar{r}-\bar{r}'|}}{|\bar{r}-\bar{r}'|}$$ screened Coulomb interaction

$\beta \equiv$ inverse screening length.

Transition probability -

$$S_{k_0,\lambda\to\lambda_0',\lambda'} = \frac{2\pi}{\hbar}|M|^2 f_{k_0} f_\lambda (1-f_{k_0'})(1-f_{\lambda'}) \delta(E_{k_0'}+E_{\lambda'}-E_{k_0}-E_\lambda$$

Need to evaluate M,

$$M = +\frac{e^2}{4\pi\epsilon}\iint d^3r' d^3r \frac{e^{-\beta|\bar{r}-\bar{r}'|}}{|\bar{r}-\bar{r}'|} \psi_{k_0}^*(r)\psi_\lambda^*(r')\psi_{k_0'}(r)\psi_{\lambda'}(r')$$

Need to perform the integral in the above.

$$M = \frac{e^2}{4\pi\epsilon}\frac{1}{V^2}\iint d^3r' d^3r \frac{e^{-\beta|r-r'|}}{|r-r'|} e^{-ik_0 r} e^{-i\lambda r'} e^{ik_0' r} e^{i\lambda' r'}$$

$$M = \frac{e^2}{4\pi\epsilon}\frac{1}{V^2}\iint d^3r' d^3r\ e^{i(k_0'-k_0)r} \frac{e^{-\beta|r-r'|}}{|r-r'|} e^{i(\lambda'-\lambda)r'}$$

Let $\bar{u} = \bar{r}-\bar{r}'$

$\bar{r} = \bar{u}+\bar{r}'$

$$M = \frac{e^2}{4\pi\epsilon}\frac{1}{V^2}\iint du\ e^{i(\vec{k}_0'-\vec{k}_0)\cdot\bar{u}} \frac{e^{-\beta|u|}}{|u|}$$

$$\cdot \int e^{i(\vec{k}_0'-\vec{k}_0+\vec{\lambda}'-\vec{\lambda})\cdot\bar{r}'} d^3r'$$

$$M = \frac{e^2}{4\pi\epsilon}\frac{1}{V^2}\int du\, e^{i(\bar{R}_0'-\bar{R}_0)\cdot\bar{u}}\frac{e^{-\beta|u|}}{|u|} * V\,\delta(\bar{R}_0'+\bar{R}', \bar{R}_0+\bar{R}) \quad \text{(8.2)}$$

since, $$\int e^{i(\bar{R}_0'-\bar{R}_0+\bar{R}'-\bar{R})\cdot\bar{r}'} d^3r' = V\,\delta(\bar{R}_0'+\bar{R}', \bar{R}_0+\bar{R})$$

$$M = \frac{e^2}{4\pi\epsilon}\frac{1}{V}\,\delta(\bar{R}_0'+\bar{R}', \bar{R}_0+\bar{R})\int du\, e^{i(\bar{R}_0'-\bar{R}_0)\cdot\bar{u}}\frac{e^{-\beta|u|}}{|u|}$$

Perform the d^3u integral in 3 dim.

$$M = \frac{e^2}{4\pi\epsilon}\frac{1}{V}\,\delta(\bar{R}_0'+\bar{R}', \bar{R}_0+\bar{R})\int_0^{2\pi}\int_0^{\pi}\int_0^{\infty} e^{i|\bar{R}_0'-\bar{R}_0|u\cos\theta}\frac{e^{-\beta u}}{u}\sin\theta\, u^2\, d\phi\, d\theta\, du$$

$$M = \frac{e^2}{4\pi\epsilon}\frac{2\pi}{V}\,\delta(\bar{R}_0'+\bar{R}', \bar{R}_0+\bar{R})\int_0^{\infty}\int_0^{\pi} e^{i|\bar{R}_0'-\bar{R}_0|u\cos\theta} e^{-\beta u}\, u\sin\theta\, d\theta\, du$$

Let $v \equiv \cos\theta$

$dv = -\sin\theta\, d\theta$

$$-\int_{+1}^{-1} e^{i|\bar{R}_0'-\bar{R}_0|uv}\, dv = \frac{-1}{i|\bar{R}_0'-\bar{R}_0|u} e^{i|\bar{R}_0'-\bar{R}_0|uv}\Big|_{+1}^{-1}$$

$$= \frac{-1}{i|\bar{R}_0'-\bar{R}_0|u}\left(e^{-i|\bar{R}_0'-\bar{R}_0|u} - e^{i|\bar{R}_0'-\bar{R}_0|u}\right)$$

But $$\frac{e^{i\theta}-e^{-i\theta}}{2i} = \sin\theta$$

$$\Pi = \frac{e^2}{4\pi\epsilon}\,\frac{2\pi}{V}\,\delta(\vec{k}_0'+\vec{k}',\vec{k}_0+\vec{k})\int_0^\infty \frac{e^{-\beta u}\,(+2)}{|\vec{r}_0'-\vec{r}_0|}\,\sin|\vec{r}_0'-\vec{r}_0|\,u \qquad \text{(P3)}$$

$$\Pi = \frac{+e^2}{\epsilon V}\,\delta(\vec{k}_0'+\vec{k}',\vec{k}_0+\vec{k})\int_0^\infty \frac{e^{-\beta u}\,\sin|\vec{r}_0'-\vec{r}_0|u}{|\vec{r}_0'-\vec{r}_0|}\,du .$$

Easier to ~~integrate~~ if we rewrite the sine again.

$$\Pi = \frac{+e^2}{\epsilon V}\,\delta(\vec{k}_0'+\vec{k}',\vec{k}_0+\vec{k})\int_0^\infty \frac{e^{-\beta u}}{|\vec{r}_0'-\vec{r}_0|}\left(\frac{e^{i(\vec{r}_0'-\vec{r}_0)u} - e^{-i(\vec{r}_0'-\vec{r}_0)u}}{2i}\right)du$$

integrate out each term,

$$\int_c^\infty \frac{e^{\left(i(\vec{r}_0'-\vec{r}_0)-\beta\right)u}}{(2i)\,|\vec{r}_0'-\vec{r}_0|}\,du$$

$$-\frac{1}{2i}\,\frac{1}{|\vec{r}_0'-\vec{r}_0|}\left\{\frac{1}{i(\vec{r}_0'-\vec{r}_0)-\beta} - \frac{1}{-i(\vec{r}_0'-\vec{r}_0)-\beta}\right\}$$

∞ bound $\to 0$.
0 bound $\to 1$.

$$\frac{1}{2i}\,\frac{1}{|\vec{r}_0'-\vec{r}_0|}\left\{\frac{1}{\beta - i(\vec{r}_0'-\vec{r}_0)} + \frac{1}{\beta + i(\vec{r}_0'-\vec{r}_0)}\right\}$$

$$\frac{1}{2i}\,\frac{1}{|\vec{r}_0'-\vec{r}_0|}\left\{\frac{\beta + i(\vec{r}_0'-\vec{r}_0) - \beta + i(\vec{r}_0'-\vec{r}_0)}{\beta^2 + |\vec{r}_0'-\vec{r}_0|^2}\right\}$$

$$\frac{1}{\beta^2+|\vec{r}_0'-\vec{r}_0|^2}$$ ✓

$$\eta = \frac{+e^2}{\epsilon V} \frac{\delta(\bar{k}_0' + \bar{k}', \bar{k}_0 + \bar{k})}{\beta^2 + |\bar{k}' - \bar{k}_0|^2} \quad \checkmark \quad (9.3).$$

assume that all the final states are unoccupied in the calculation of the scattering rate.

$\therefore f_{k_0'} = f_{k'} = 0.$

Let $f_{k_0} = 1.$

$$\therefore S_{k_0; k \to k_0', k'} = \frac{2\pi}{\hbar} \frac{e^4}{\epsilon^2 V^2} \frac{[\delta k_0 + k, k_0' + k']^2}{[|\bar{k}' - \bar{k}_0|^2 + \beta^2]^2} \frac{f_k \, \delta(E)}{}$$

The scattering rate is given thus as,

$$1/\tau = \frac{2V}{(2\pi)^3} \int_0^\infty dk'' \int_0^\pi d\theta \int_0^{2\pi} d\phi \; S_{k_0, k \to k_0', k'} \, k''^2 \sin\theta$$

where we simply integrate the transition probability over the final density of state expressed in terms of k''.

Change notation here to simplify.

$S(k_1 k_2 \to k_1' k_2')$

$k_1 : k_2$ are the initial states.

$k_1' : k_2'$ are the final states.

$|\bar{k}_0' - \bar{k}_0|^2 = |\bar{k}_1' - \bar{k}_1|^2$.

$$\therefore S(k_1 k_2 \to k_1' k_2') = \frac{2\pi}{\hbar} \frac{e^4}{\epsilon^2 V^2} \frac{f_x}{[|\bar{k}_1' - \bar{k}_1|^2 + \beta^2]^2} \delta(k_1 + k_2, k_1' + k_2')$$

Earlier

k_0, k_0' }

k, k' }

↑ initial ↑ final

$$\vec{q}_1' \to \vec{q}_0' \qquad \vec{q}_1 \to \vec{k}_0$$
$$\vec{q}_2' \to \vec{q}' \qquad \vec{q}_2 \to \vec{q}$$

Let $V=1$

P.C

$$1/\tau = \frac{2}{(2\pi)^3}\frac{2\pi}{\hbar}\frac{e^4}{\epsilon^2}\int d\vec{q}_1'\int d\vec{q}_2'\;\frac{\delta(\vec{q}_1+\vec{q}_2-\vec{q}_1'-\vec{q}_2')\;\delta(E_1+E_2-E_1'-E_2')}{[\beta^2+|\vec{q}_1'-\vec{q}_1|^2]^2}$$

$$= \frac{2}{(2\pi)^3}\frac{2\pi}{\hbar}\frac{e^4}{\epsilon^2}\int d\vec{q}_1'\;\frac{\delta\left[\frac{1}{2m}(q_1^2+q_2^2-q_1'^2-|\vec{q}_1+\vec{q}_2-\vec{q}_1'|^2)\right]}{[\beta^2+|\vec{q}_1'-\vec{q}_1|^2]^2}$$

Let $\vec{k}_0 = \vec{q}_1'-\vec{q}_1$

$$= \frac{2}{(2\pi)^3}\frac{2\pi}{\hbar}\frac{e^4}{\epsilon^2}\frac{2m}{\hbar^2}\int d\vec{k}_0\;\frac{\delta[q_1^2+q_2^2-|\vec{k}_0+\vec{q}_1|^2-|\vec{q}_2-\vec{k}_0|^2]}{[\beta^2+k_0^2]^2}$$

$$= \frac{2}{(2\pi)^3}\frac{2\pi}{\hbar}\frac{e^4}{\epsilon^2}\frac{2m}{\hbar^2}\int d\vec{k}_0\;\frac{\delta[q_1^2+q_2^2-(k_0^2+q_1^2+2\vec{k}_0\cdot\vec{q}_1)-(q_2^2+k_0^2-2\vec{k}_0\cdot\vec{q}_2)]}{[\beta^2+k_0^2]^2}$$

$$= \frac{2}{(2\pi)^3}\frac{2\pi}{\hbar}\frac{e^4}{\epsilon^2}\frac{2m}{\hbar^2}\int_0^\infty k_0^2\,dk_0\int_0^{2\pi}d\phi\int_0^\pi \sin\theta\,d\theta\;\frac{\delta[-2k_0^2+2\vec{k}_0\cdot(\vec{q}_2-\vec{q}_1)]}{[\beta^2+k_0^2]^2}$$

$\Rightarrow$

$$= \frac{2(2\pi)}{(2\pi)^3}\frac{2\pi}{\hbar}\frac{e^4}{\epsilon^2}\frac{2m}{\hbar^2}\int_0^\infty k_0^2\,dk_0\int_0^\pi \sin\theta\,d\theta\;\frac{\delta[-2(\vec{k}_0\cdot(\vec{q}_1-\vec{q}_2)+k_0^2]}{[\beta^2+k_0^2]^2}$$

Note $\delta(ax) = \frac{1}{|a|}\delta(x)$

$$= \frac{2}{2\pi}\frac{2m}{\hbar^3}\frac{e^4}{\epsilon^2}\frac{1}{2}\int_0^\infty k_0^2\,dk_0\int_0^\pi \sin\theta\,d\theta\;\frac{\delta[k_0^2+\vec{k}_0\cdot(\vec{q}_1-\vec{q}_2)]}{[\beta^2+k_0^2]^2}$$

$$\frac{2me^4}{2\pi\hbar^3\epsilon^2}\int_0^\infty k_0^2\,dk_0\int_0^\pi \frac{\delta(k_0^2+k_0 k\cos\theta)}{(\beta^2+k_0^2)^2}\sin\theta\,d\theta$$

where $\vec{k} = \vec{q}_1-\vec{q}_2$

Let $x = \cos\theta$

$$\frac{2me^4}{2\pi\hbar^3\epsilon^2}\int_0^\infty k_0^2\,dk_0\int_{-1}^{+1}\frac{\delta(x+k_0/k)}{k_0 k\,(\beta^2+k_0^2)^2}\,dx$$

$$\frac{2me^4}{2\pi\hbar^3\epsilon^2}\int_0^\infty q_s^2\,dq_s\,\frac{1}{q_s q(\beta^2+q_s^2)^2}\left[\Theta\left(\frac{q_s}{q}+1\right)-\Theta\left(\frac{q_s}{q}-1\right)\right]$$

But $\Theta(x)=\begin{cases}1 & x>0\\ 0 & x<0\end{cases}$

$$\Theta(q_s/q+1)-\Theta(q_s/q-1)=\begin{cases}1 & q_s/q<1\\ 0 & q_s/q>1\end{cases}$$

The above gives the upper bound on the integral over k_s.

$$\frac{2me^4}{2\pi\hbar^3\epsilon^2}\int_0^k\frac{k_s\,dq_s}{q(\beta^2+q_s^2)^2}$$

Let $u=q_s^2$

$du=2q_s\,dq_s$

$$\frac{me^4}{2\pi\hbar^3\epsilon^2}\int_0^{k^2}\frac{du}{q(\beta^2+u)^2}$$

$$\frac{me^4}{2\pi\hbar^3\epsilon^2 q}\int_0^{k^2}\frac{du}{(\beta^2+u)^2}$$

Consider $\int\frac{dx}{(a+x)^2}=-\frac{1}{(a+x)}$

$$\frac{me^4}{2\pi\hbar^3\epsilon^2 q}\left[-\frac{1}{(\beta^2+u)}\Big|_0^{k^2}\right]$$

$$\frac{me^4}{2\pi\hbar^3\epsilon^2 k}\left[\frac{1}{\beta^2}-\frac{1}{\beta^2+k^2}\right]$$

$$\frac{me^4}{2\pi\hbar^3\epsilon^2 k}\left[\frac{\beta^2+k^2-\beta^2}{\beta^2(\beta^2+k^2)}\right]$$

$$\frac{me^4}{2\pi\hbar^3\epsilon^2\beta^2}\,\frac{k}{(\beta^2+k^2)}$$

$$\gamma_C = \frac{me^4}{2\pi\hbar^3\epsilon^2(\beta^2} \frac{k}{(\beta^2+k^2)}$$

$$|\vec{r}_1| = |\vec{r}_1 - \vec{r}_2|$$

Factor of 2 greater than in the literature. Due to the Pauli Principle. If we don't consider the spin degeneracy, we get the same result as in the literature.

Electron-hole Scattering.

$\vec{k}_1, \vec{k}_1' \equiv$ electrons ; $\vec{k}_2, \vec{k}_2' \equiv$ holes

$$1/\tau = \frac{2}{(2\pi)^3}\cdot\frac{2\pi}{\hbar}\int d\vec{k}_1'\int d\vec{k}_2'\,\frac{e^4}{\epsilon^2}\,\frac{\delta(\vec{k}_1+\vec{k}_2,\vec{k}_1'+\vec{k}_2')\,\delta(E_1+E_2-E_1'-E_2')}{\left(\beta^2+|\vec{k}_1'-\vec{k}_1|^2\right)^2}$$

$$= \frac{2}{(2\pi)^2}\cdot\frac{e^4}{\epsilon^2}\,\frac{1}{\hbar}\int d\vec{k}_1'\,\frac{\delta\left(\frac{\hbar^2}{2m_e}\left(k_1^2+m_e/m_h\,k_2^2-k_1'^2-m_e/m_h\,|\vec{k}_1+\vec{k}_2-\vec{k}_1'|^2\right)\right.}{\left(\beta^2+|\vec{k}_1'-\vec{k}_1|^2\right)^2}$$

$$= \frac{2}{(2\pi)^2}\,\frac{e^4}{\epsilon^2}\,\frac{1}{\hbar}\,\frac{2m_e}{\hbar^2}\int d\vec{k}_s\,\frac{\delta(k_1^2+m_e/m_h\,k_2^2-|\vec{k}_s+\vec{k}_1|^2-m_e/m_h\,|\vec{k}_2-\vec{k}_s|^2)}{(\beta^2+k_s^2)^2}$$

where $\vec{k}_s = \vec{k}_1'-\vec{k}_1$

$$= \frac{2}{(2\pi)^2}\,\frac{e^4}{\epsilon^2}\,\frac{2m_e}{\hbar^3}\int d\vec{k}_1\,\frac{\delta(k_1^2+m_e/m_h\,k_2^2-k_s^2-k_1^2-2\vec{k}_s\cdot\vec{k}_1-m_e/m_h\,k_2^2-\frac{m_e}{m_h}k_s^2+\frac{2m_e}{m_h}\vec{k}_2\cdot\vec{k}_s)}{(\beta^2+k_s^2)^2}$$

$$= \frac{2}{(2\pi)^2}\,\frac{e^4}{\epsilon^2}\,\frac{2m_e}{\hbar^3}\int d\vec{k}_s\,\frac{\delta(-k_s^2-m_e/m_h\,k_s^2-2\vec{k}_s\cdot\vec{k}_1+2m_e/m_h\,\vec{k}_2\cdot\vec{k}_s)}{(\beta^2+k_s^2)^2}$$

$$= \frac{2}{(2\pi)^2}\,\frac{e^4}{\epsilon^2}\,\frac{2m_e}{\hbar^3}\int d\vec{k}_s\,\frac{\delta[-k_s^2(1+m_e/m_h)-2\vec{k}_s\cdot(\vec{k}_s-m_e/m_h\,\vec{k}_2)]}{(\beta^2+k_s^2)^2}$$

Let $\vec{k} \equiv \vec{k}_1 - m_e/m_h\,\vec{k}_2$

$$\frac{2}{(2\pi)^2}\,\frac{e^4}{\epsilon^2}\,\frac{2m_e}{\hbar^3}\int d\vec{k}_s\,\frac{\delta[-k_s^2(1+m_e/m_h)-2k_s k\cos\theta]}{(\beta^2+k_s^2)^2}$$

$$\frac{2}{(2\pi)^2}\,\frac{e^4}{\epsilon^2}\,\frac{2m_e}{\hbar^3}\int d\vec{k}_s\,\frac{\delta[-2k_s k(k_s/2k(1+m_e/m_h)+\cos\theta)]}{(\beta^2+k_s^2)^2}$$

$$= \frac{2}{(2\pi)^2}\,\frac{e^4}{\epsilon^2}\,\frac{2m_e}{\hbar^3}\int d\vec{k}_s\,\frac{1}{2k_s k}\,\frac{\delta(k_s/2k(1+m_e/m_h)+\cos\theta)}{(\beta^2+k_s^2)^2}$$

$$\left(\frac{2}{2\pi}\right)^2 \frac{e^4}{\epsilon^2} \frac{2m_e}{\hbar^3} \frac{1}{2k} \int_0^\infty \frac{q_s^2 dq_s}{q_s} \int_0^\pi d\theta \sin\theta \int_0^{2\pi} d\phi \; \frac{\delta\left(q_s/2k\,(1+m_e/m_n) + \cos\theta\right)}{\left(\beta^2 + q_s^2\right)^2}$$ (p.10)

$$\frac{2m_e e^4}{(2\pi)\epsilon^2} \frac{1}{\hbar^3} \frac{1}{k} \int_0^\infty q_s\, dq_s \int_0^\pi \sin\theta\, d\theta \; \frac{\delta\left(\cos\theta + q_s/2k\,(1+m_e/m_n)\right)}{\left(\beta^2 + q_s^2\right)^2}$$

Let $x = \cos\theta$

$dx = \sin\theta\, d\theta$

$$\frac{2m_e e^4}{(2\pi)\epsilon^2} \frac{1}{\hbar^3} \frac{1}{k} \int_0^\infty q_s\, dq_s \int_{-1}^{+1} dx \; \frac{\delta\left(x + q_s/2k\,(1+m_e/m_n)\right)}{\left(\beta^2 + q_s^2\right)^2}$$

$$\frac{2m_e e^4}{2\pi\epsilon^2} \frac{1}{\hbar^3} \frac{1}{k} \int_0^\infty \frac{q_s\, dq_s}{\left(\beta^2 + q_s^2\right)^2} \left[\theta\left(x + \frac{q_s}{2k}\,(1+m_e/m_n)\right)\right]_{-1}^{+1}$$

$$\frac{2m_e e^4}{2\pi\epsilon^2} \frac{1}{\hbar^3} \frac{1}{k} \int_0^\infty \frac{q_s\, dq_s}{\left(\beta^2 + q_s^2\right)^2} \left[\theta\left(1 + \frac{q_s}{2k}\,(1+m_e/m_n)\right) - \theta\left(-1 + \frac{q_s}{2k}\,(1+m_e/m_n\right)\right.$$

$\frac{q_s}{2k}(1+m_e/m_n) < 1$ nonzero value of 1.

$$q_s < \frac{2k}{(1+m_e/m_n)}$$

$$\frac{2m_e e^4}{2\pi\epsilon^2} \frac{1}{\hbar^3} \frac{1}{k} \int_0^{2k/(1+m_e/m_n)} \frac{q_s\, dq_s}{\left(\beta^2 + q_s^2\right)^2}$$

Let $u = q_s^2$

$du = 2q_s\, dq_s$

$$\int_0^\alpha \frac{du}{(\beta^2+u)^2} = \frac{-1}{\beta^2+u} \Bigg|_0^{\left[2k/(1+m_e/m_n)\right]^2}$$

$$= \left[\frac{1}{\beta^2} - \frac{1}{\beta^2 + (2k)^2}\right]$$

Appendix B

Modeling of Three Terminal Semiconductor Devices: Heterojunction Bipolar Transistors (HBTs)

Steven Janzou
and
Kevin Brennan

School of Electrical Engineering
and
Microelectronics Research Center
Georgia Institute of Technology
Atlanta, Georgia 30332

ABSTRACT

The most promising high frequency, low power consumption semiconductor device is the heterojunction bipolar transistor (HBT). Though the HBT is not a new device concept, the advent of epitaxial semiconductor growth techniques, which enable monolayer growth control, has lead to the development of HBTs with nanometer feature sizes. These devices are among the fastest transistor structures ever produced. The ultimate limits of performance of these devices are presently unknown since their operation is beyond the capabilities of most present day simulators. It is the purpose of this work to analyze the operation of HBTs using a first principles ensemble Monte Carlo model coupled with a two-dimensional Poisson solver. The utility of this approach is that the transport physics which govern HBT operation, velocity overshoot and ballistic transport, are incorporated naturally, enabling an accurate determination of the device performance. It is expected that from this work the long term prospectus of HBTs will become known.

HBT Description

The emitter-base junction is formed between two dissimilar materials. The most common HBT utilizes npn doping in an AlGaAs/GaAs/GaAs material system as shown below.

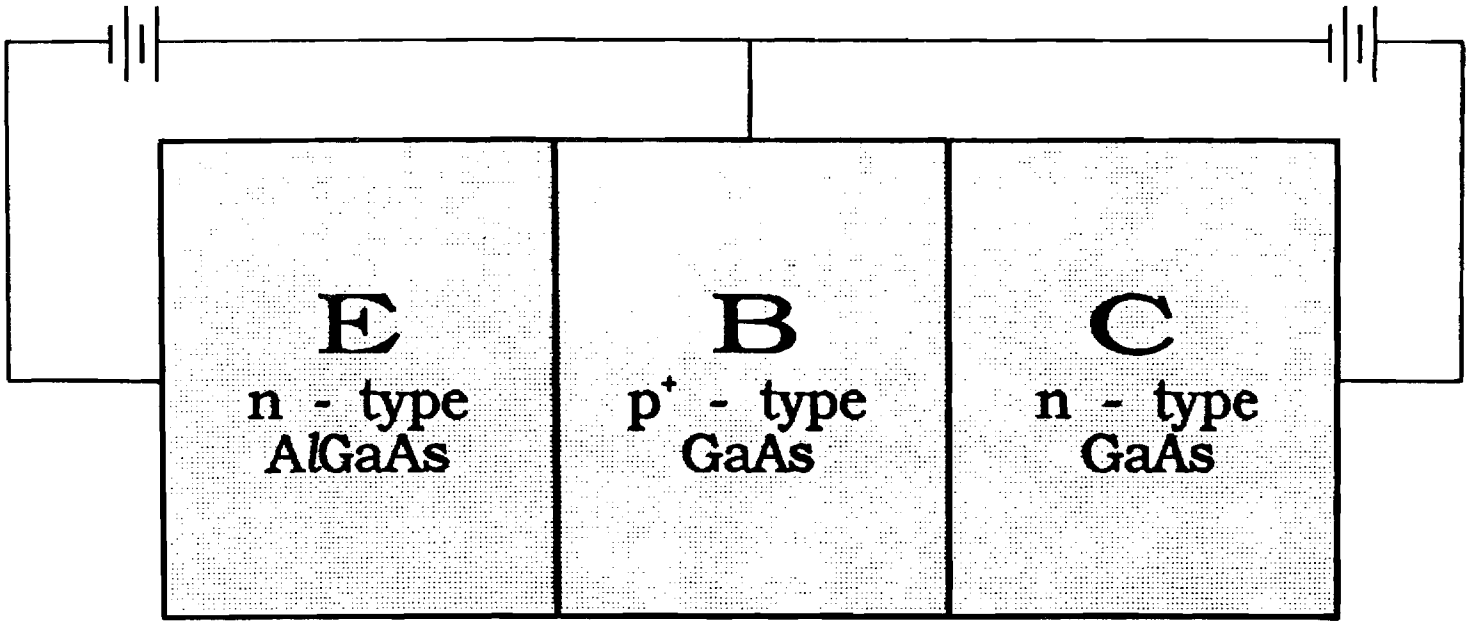

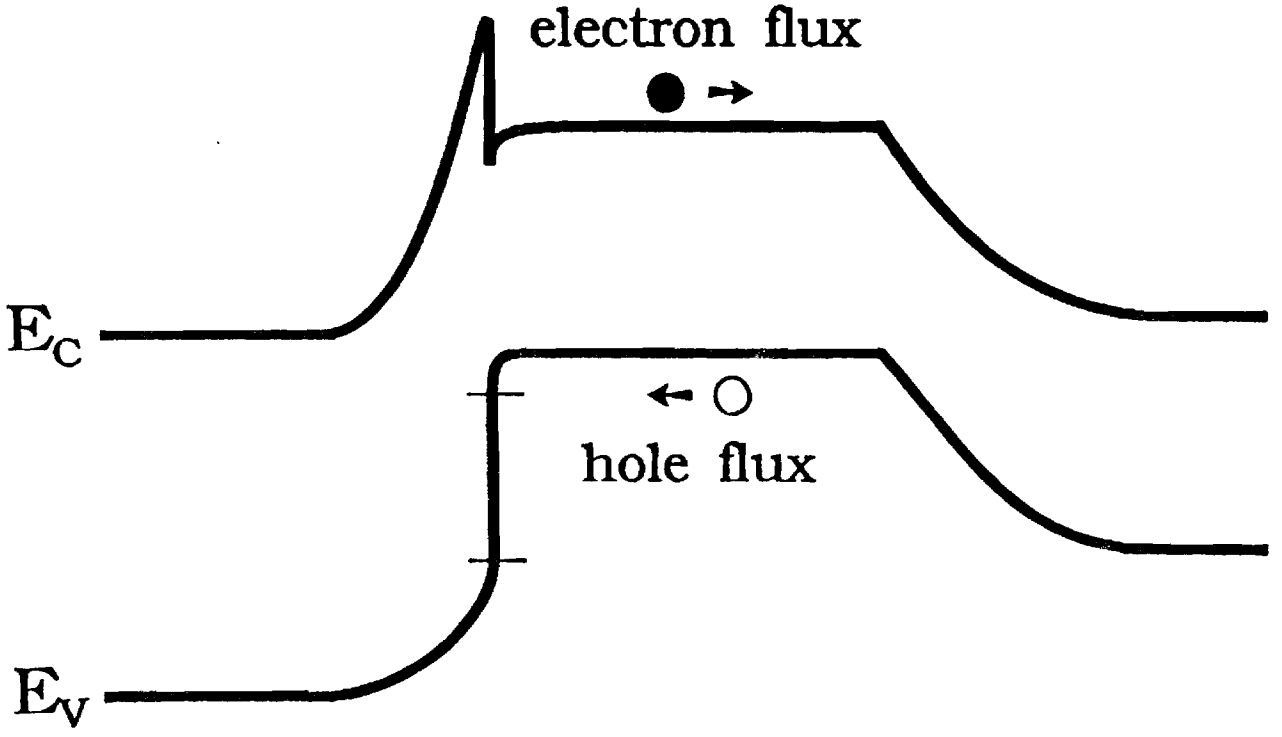

HBT Geometry

A typical HBT device geometry from *Mark Lundstrom at the Short Course on Computational Electronics, Univ. of Illinois, May 23-25, 1990.*

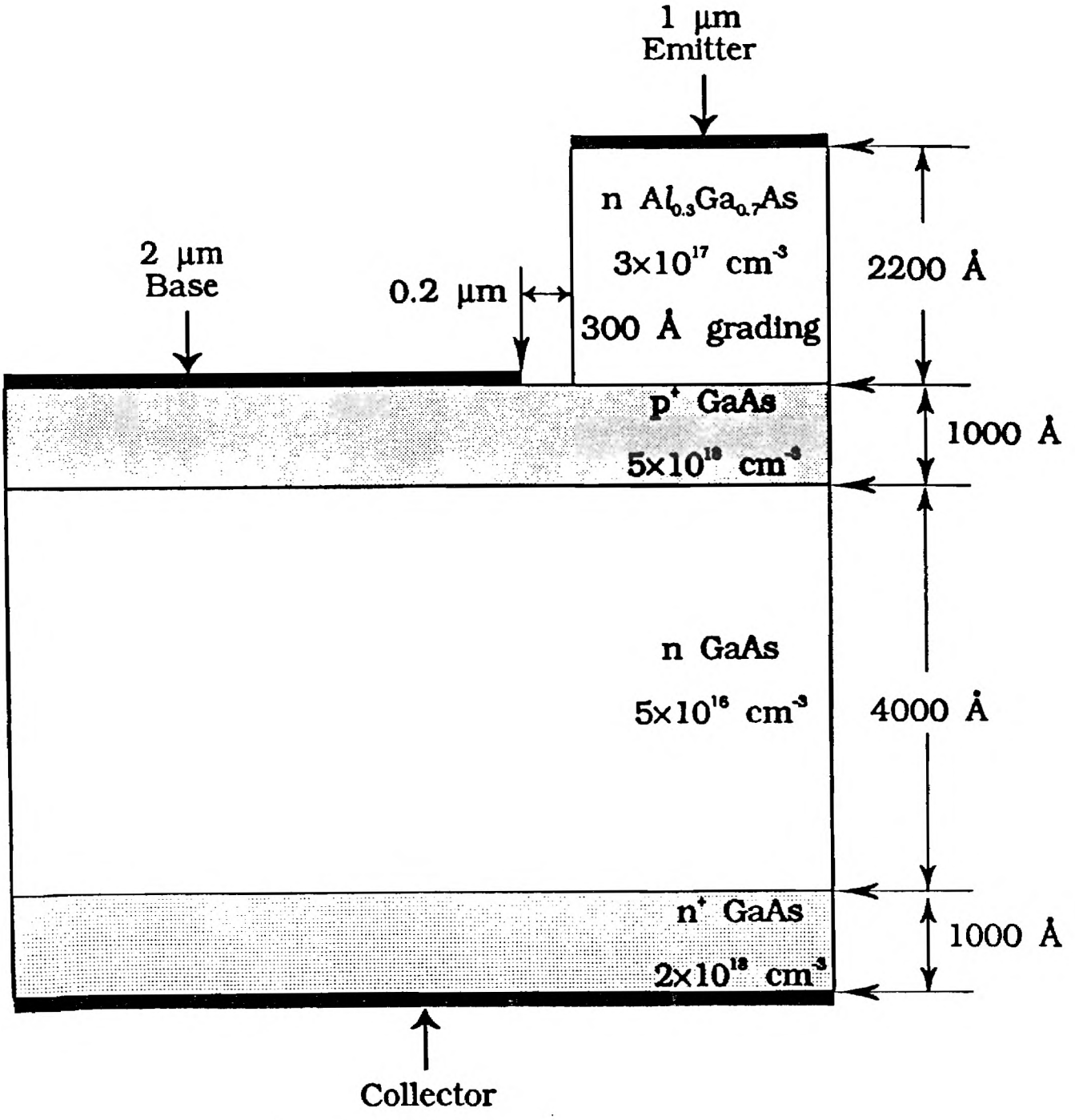

HBT Advantages

(1) DC gain for a HBT is proportional to: $e^{\Delta E_g/kT}$, where ΔE_g is the heterojunction band gap difference. Therefore, the gain is dominated by ΔE_g.

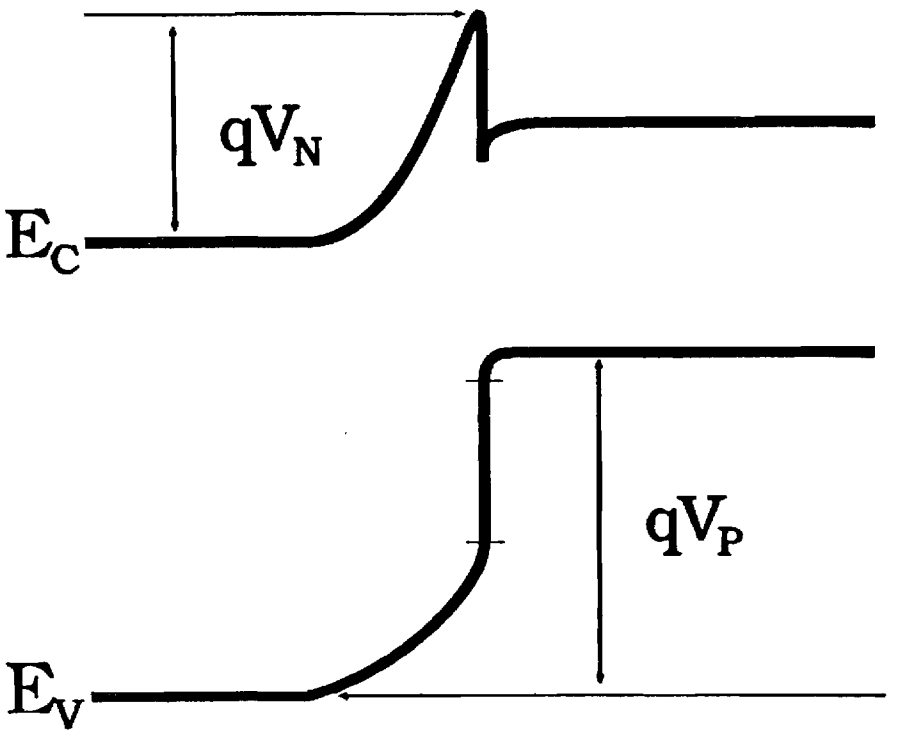

$$\Delta E_g = qV_P - qV_N$$

HBT Advantages

(2) Speed/power performance comparison for several different semiconductor devices from *Robert P. Mandel, Solid State Technology, Jan. 1982, pp. 94-103.*

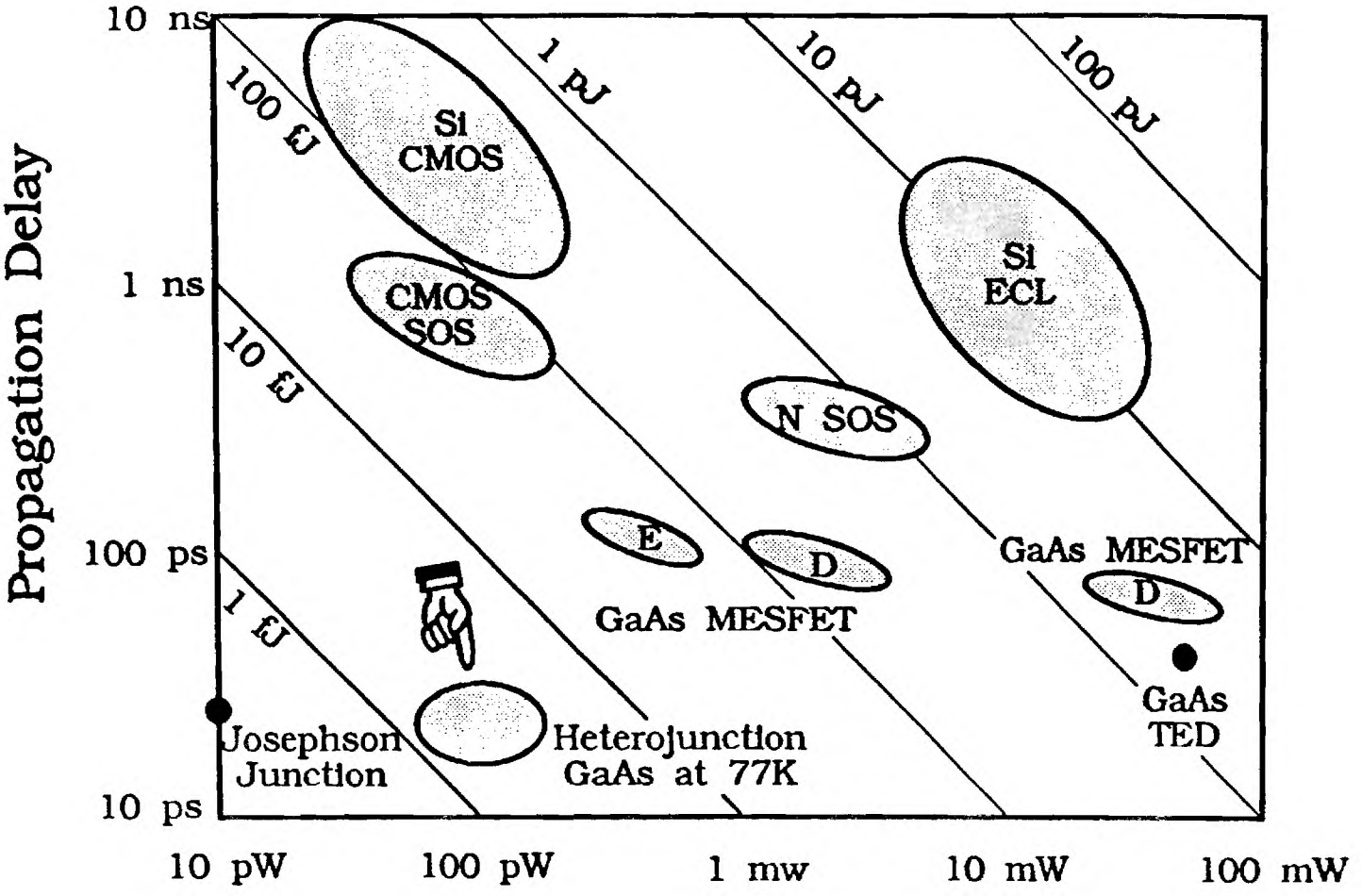

HBT The Problem

Analyze and design new heterostructure bipolar transistor (HBT) structures to determine the ultimate limits of HBT performance as measured in terms of the maximum frequency of operation, f_{max}.

From the following expression for f_{max}, it is clear that f_{max} depends upon numerous parameters. The most readily engineered quantities are the base resistance, R_B, the base transit time, τ_B, and the collector depletion layer transit time, τ_C.

HBT Optimization

The maximum frequency of operation, f_{max}, can be increased without sacrificing gain. The maximum frequency of operation for a HBT is given by:

$$f_{max} = \left[\frac{f_t}{8 \pi R_B C_{BC}} \right]^{1/2}$$

where:

$R_B \equiv$ base resistance, proportional to $1/P_B$.

$P_B \equiv$ base doping.

$C_{BC} \equiv$ base-collector capacitance.

$$1/f_t = 2\pi \left[\tau_E + \tau_B + \tau_C + \tau_{CC} \right]$$

$\tau_E \equiv$ emitter depletion layer charging time.

$\tau_B \equiv$ base transit time.

$\tau_C \equiv$ collector depletion layer transit time.

$\tau_{CC} \equiv$ collector charging time.

We seek a HBT design in which ΔE_g is sufficiently large to preserve the gain; yet, R_B, τ_B, and τ_C are very small to increase f_{max}.

HBT Models

A comparison of some of the existing HBT models.

Analytic Models

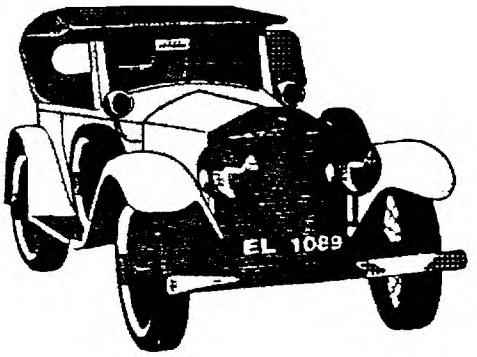

+) Computational ease.
+) Device features and physics are explicitly stated.
-) Difficult to incorporate nonlinear and two dimensional effects accurately.
-) Fails generally for submicron devices.

Drift-Diffusion Models

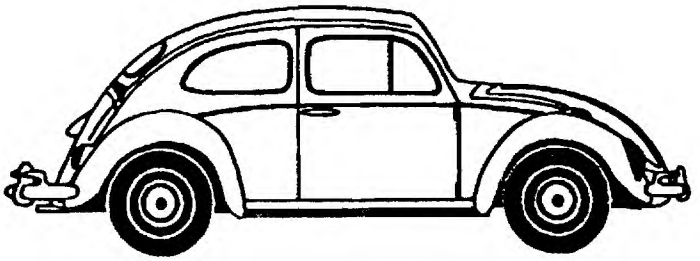

+) Incorporates two dimensional effects.
+) Can treat complicated geometries.
-) Fails generally in device structures which exhibit nonstationary transport effects, i.e. submicron geometries.

Ensemble Monte Carlo Models

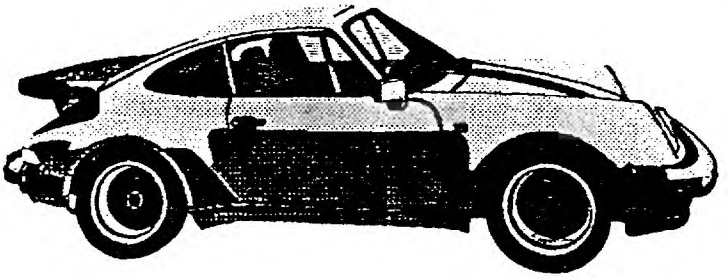

+) Can treat virtually all semiclassical devices accurately.
-) Requires large computational overhead.

HBT:
Our Modeling Approach

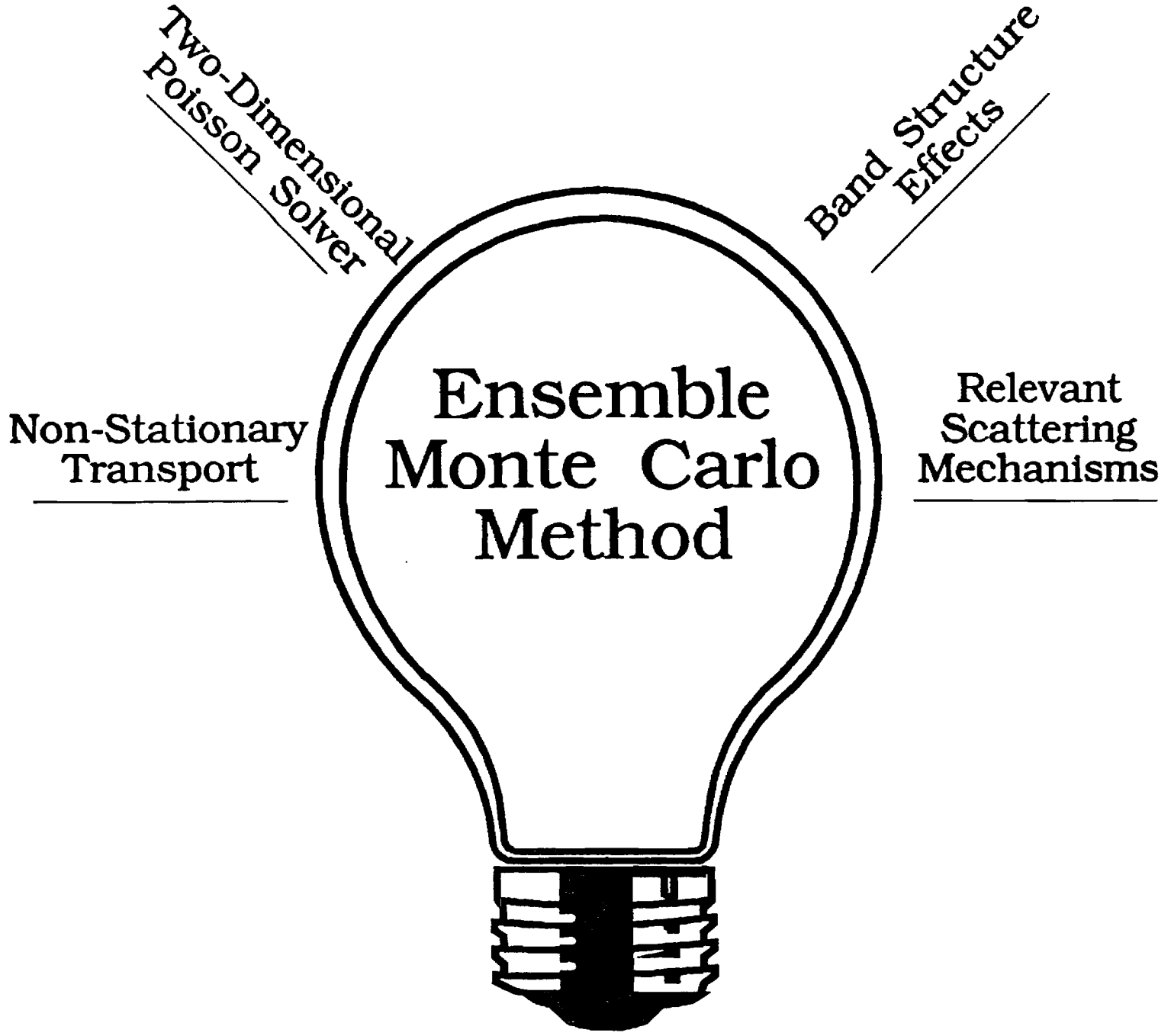

HBT
Transistor Simulation

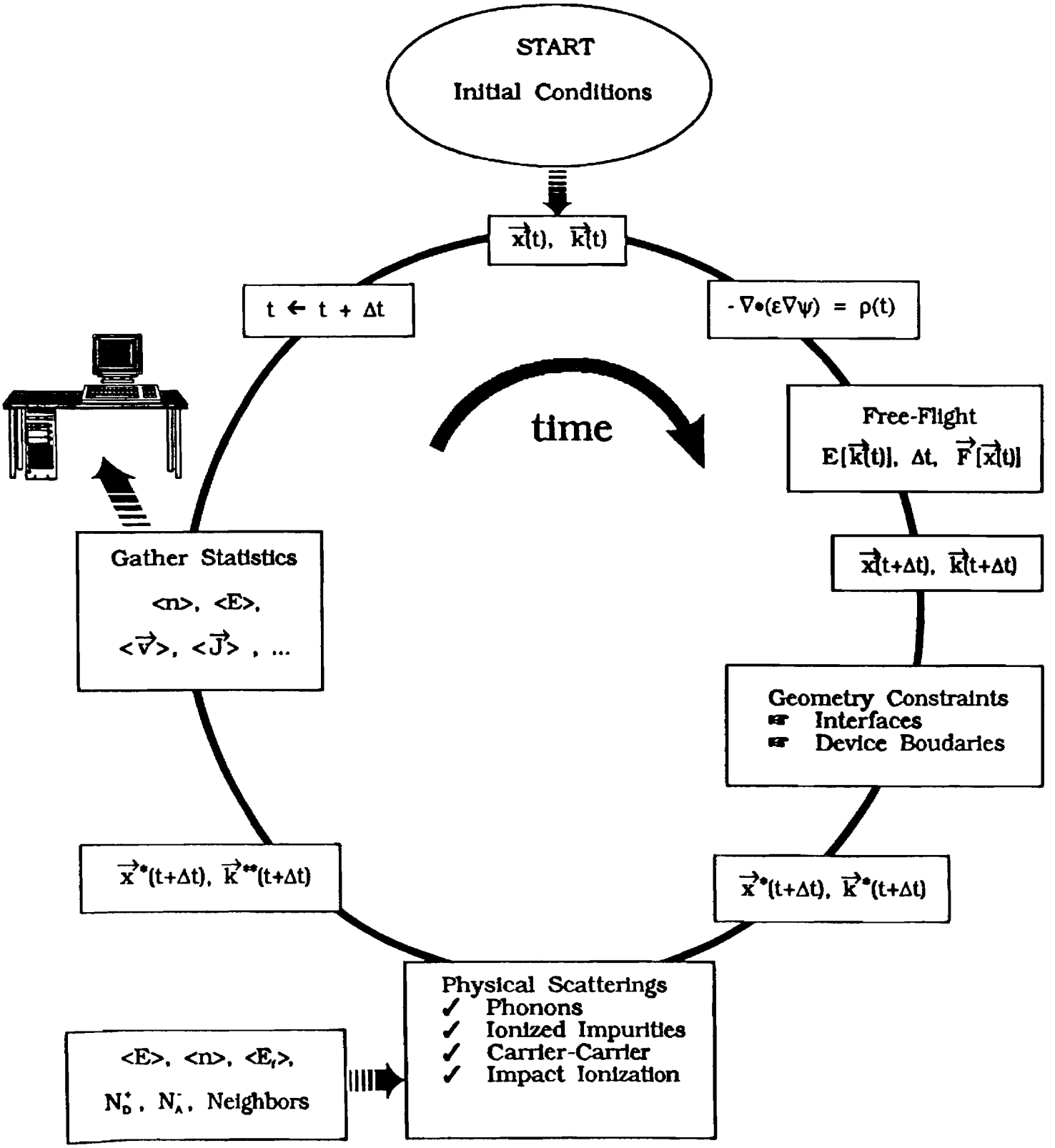

HBT:
Our Results

HBT
Future Directions

A problem with existing HBTs is velocity saturation in the collector region. We propose a step structure for the collector region as shown below.

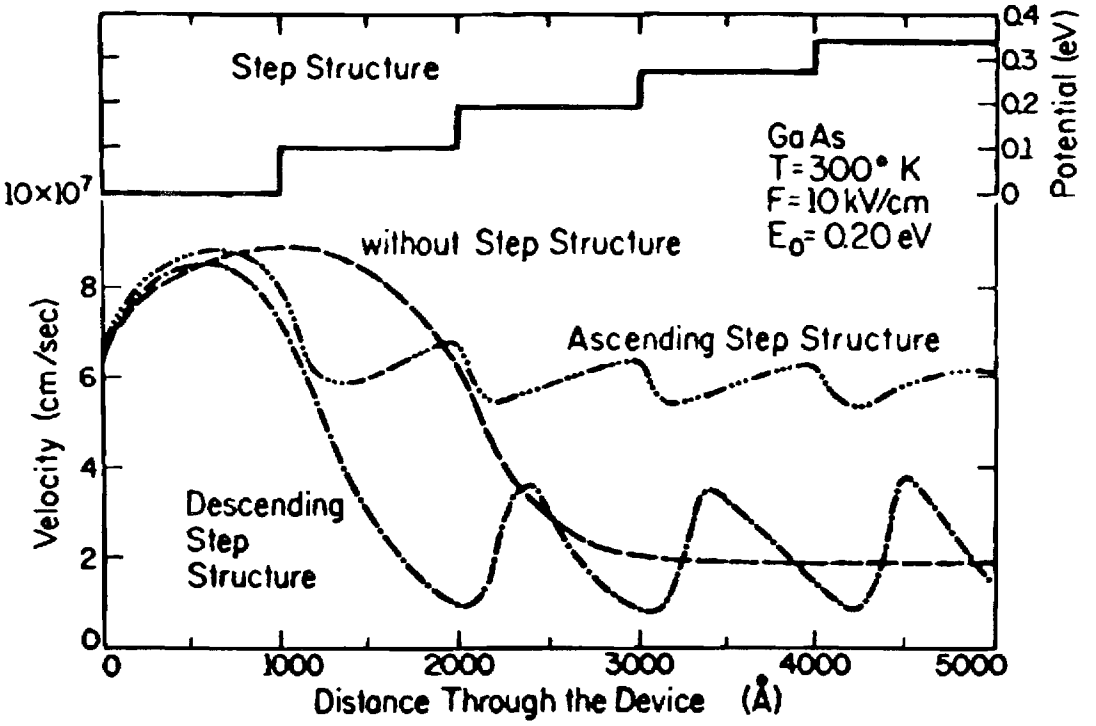

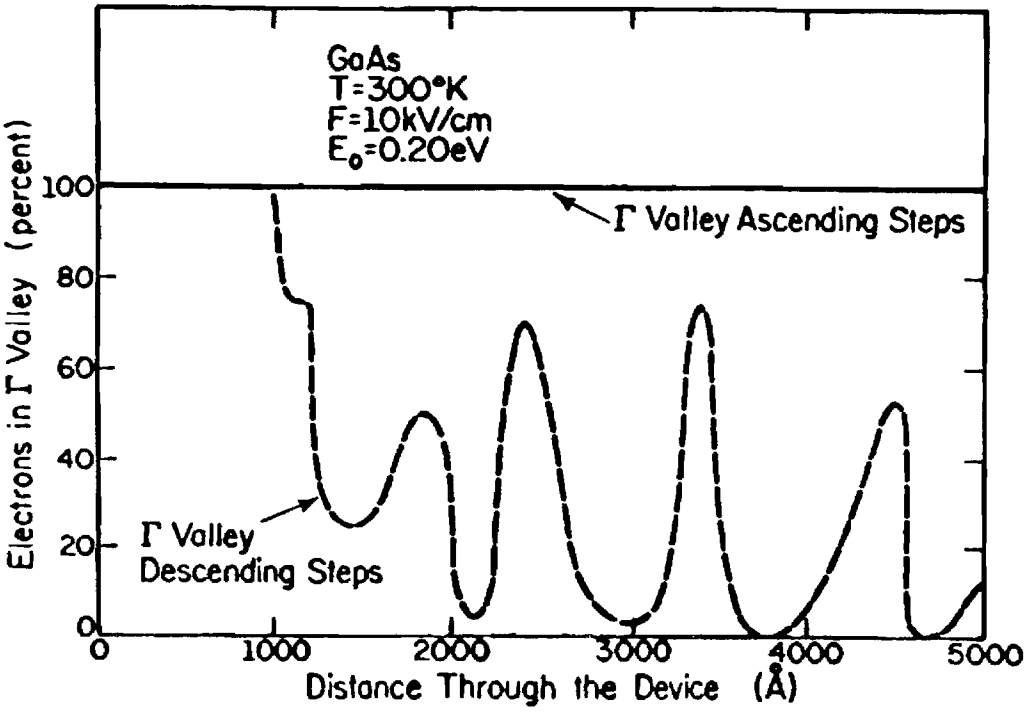

K. Brennan and K. Hess, IEEE Electron Device Letters, vol. EDL-4, pp. 419-421, 1983.

Annual Project Report: Motorola Corp.

Project Title: Modeling of Three Terminal Semiconductor Devices: HBTs

Investigator: Dr. Kevin F. Brennan

Organization: School of Electrical Engineering and Microelectronics Research Center Georgia Institute of Technology

Address: School of Electrical Engineering Georgia Institute of Technology Atlanta, Georgia 30332-0250

Phone: (404) 894-6767

ABSTRACT

During the second year of effort on this project we have completed the development of a general two-dimensional Poisson solver which can be applied to a multi-heterojunction device. In this report, the details of the Poisson solver are disclosed and the issues encountered and resolved are presented. Much work has been done in parallel towards the development of a reliable ensemble Monte Carlo simulator which is to be coupled with the new Poisson solver. The details of the Monte Carlo simulator have been published in the Proceedings of the Minnesota Supercomputer Institute and are also included here. In the very near future, we will be ready to begin simulation of the electron flights in a realistic heterostructure transistor.

I. Introduction

The ultimate goal of this research is the successful simulation of a heterostructure bipolar transistor, HBT, in order to determine the fundamental limits of its operation. An HBT is an extraordinarily complicated semiconductor device since it involves the transport of two carrier species and operates over both long and short timescales. Any complete model of an HBT must be able to correctly include the physics which governs transient carrier transport in very small structures (subpicosecond regime) as well as include carrier generation/recombination processes (nanoseconds and longer). The necessity of modeling transport processes on such very different timescales, in this case three to six orders of magnitude, creates extreme computational demands. In fact, on present machines it is prohibitive to simulate both timescales concurrently; starting with the subpicosecond (femtosecond) timescale and progressing continuously towards the nanosecond and longer timescales. It is clear that separate simulations of the long and short timescales must be made. Our approach is to use the ensemble Monte Carlo method coupled with a two-dimensional Poisson solver to determine the short timescale behavior of an HBT, leaving the long timescales to a steady-state drift-diffusion analysis. The ensemble Monte Carlo method has been chosen since all of the important physics which governs the short timescale behaviors can be readily included in a precise manner. The major limitation of the Monte Carlo method is its excessive computational appetite which restricts its application to only short timescale studies.

The first stage of this research is the development of an electron simulator based on a Poisson solver coupled to the ensemble Monte Carlo technique. It is important to recognize that only the electrons undergo dramatic field heating within an HBT since they are the only carriers injected at high energy out of the emitter. Therefore, it is important to take into account hot electron dynamics, i.e. velocity overshoot and ballistic transport. As mentioned above, the Monte Carlo model naturally includes all of the details of velocity overshoot and ballistic transport from first principles. Coupled with the two-dimensional Poisson solver, the model will provide an accurate picture of the electron dynamics in an HBT geometry which will in turn enable a realistic determination of the device cutoff frequency and current-voltage characteristics. Initially, the holes will be included only as a source of scatterings within the base region. In general, the holes in an HBT are in quasi-equilibrium owing to the very small electric field within the base region. As a result, the hole current can be reliably approximated by analytical expressions to a great extent.

In this report, we will review our progress to date in fashioning an ensemble Monte Carlo electron simulator coupled with a two-dimensional Poisson solver for determining the transient behavior of an HBT. The details of the Poisson solver as well as the difficulties and solutions encountered in its development will be reviewed. A review article outlining many of the features of our ensemble Monte Carlo simulator is included in the Appendix. In addition, we will discuss a parallel effort that we have begun to develop a drift-diffusion and ultimately a

hydrodynamic simulator which can be employed in HBT simulation.

II. Poisson Solver Development

Four general methods were considered for use in the Poisson solver. These were: finite element, control volume, boundary element, and the finite difference methods. After reviewing the advantages and disadvantages of each of these methods the finite difference method was selected. The finite difference method was chosen since it provides the most straight-forward implementation and is the most appropriate for coupling to the Monte Carlo simulation.

Following the selection of the finite difference method, various solution techniques were investigated. The first such method uses an initial coarse uniform mesh with finer, uniform meshes superimposed within the areas containing the highest field gradients [1]. The particular advantage of this approach is that it enables an accurate solution within regions in which the field changes rapidly with the fewest number of points necessary. As a result, it provides fairly good accuracy without sacrificing speed of computation. The primary limitation of this procedure is that the finer uniform mesh spacings are one half the spacing of the surrounding coarser uniform mesh. In a device such as an HBT, highly nonuniform mesh spacings are required within the junction areas in order to attain useful accuracy. The Bigelow approach [1] cannot handle these nonuniformities. Another problem encountered using the Bigelow approach in an HBT geometry is the difficulty of maintaining charge neutrality owing to the sharp changes in carrier concentrations near the junctions. Due to

these limitations, a solution method which incorporates a non-uniform mesh was chosen.

In order to ensure the accuracy of the Poisson solver, we first calculated the potential profile using analytical methods, primarily using the depletion approximation. Calculation of the potential profile in a typical HBT geometry revealed the existence of both high potential gradients and high carrier concentration gradients throughout the device. To ensure an accurate numerical calculation, a large number of grid points is required to give reasonable accuracy. However, as the number of grid points grows, the computational time increases greatly. Recognizing this inherent speed vs. accuracy tradeoff, initially a 128 x 128 two-dimensional mesh was chosen as the "best" compromise. Owing to the large number of points, an iterative solution method was then selected over a direct method. The iterative method also allows for future grid adaptation. Of the possible iterative methods, we considered SOR, successive over relaxation, ADI, alternating direction implicit, and SLOR, successive line over relaxation. Based on speed, accuracy and ease of use, the SLOR method was chosen.

The emitter-base and base-collector junctions present additional constraints on the problem. The continuity of the D field must be preserved across the junctions in accordance with Maxwell's Equations. Two different approaches were considered for treating the junction boundary conditions. These were:

1. solve the point form of Gauss' Law over the entire region to account for the heterojunctions.

2. solve Poisson's Eq. in each region (emitter, base, and collector) where the dielectric is constant and use the boundary conditions of the continuity of the electric flux at the interfaces.

The second approach was chosen since it provides a straight-forward calculation of the electric field and the discrete approximation is numerically consistent with the Neumann conditions imposed on the non-contact boundaries. The second approach has the further advantage in that it most easily handles geometries composed of rectangular regions.

Next several methods of grid point assignment were considered. These are:

1. assignment based on the atomic monolayer thichness in each material system. In other words, the smallest mesh spacing is one monolayer width and all mesh points are spaced at integer multiples of the lattice constant from one another.

2. piecewise linear assignment differing in region according to the following,

a. bulk regions - little potential variation, contains the fewest points.

b. bulk-depletion regions - (defined as the transition regions between the bulk and the depletion regions) these regions contain large carrier concentrations gradients.

c. depletion regions - potential has a quadratic behavior.

d. junction regions - large changes in both potential and carrier concentrations. These regions contain the largest number of points.

From computer experimentation, it was found that better

convergence and numerical stability are obtained using the piecewise linear grid assignments.

The SLOR method was thoroughly tested before applying it to an HBT structure. These tests included:

1. comparison to a textbook problem solved using analytical techniques.
2. application to pn homojunctions with the same doping concentration on either side of the junction.
3. application to pn homojunctions with different doping concentrations on either side of the junction.
4. application to pn heterojunctions with the same doping concentration on either side of the junction.
5. application to pn heterojunctions with different doping concentrations on either side of the junction.
6. application to a rectangular HBT geometry with the same doping concentration throughout.
7. application to a rectangular HBT geometry with different doping concentrations throughout.

At this point, it is necessary to extend the model to treat "L" shaped HBT geometries as shown in Figure 1. "L" shaped geometries are the most common device structures typically used in practice. The particular difficulty in the numerical solution of the Poisson Eq. for these geometries is the corner point. Here the normal derivative is assumed to be zero. The calculated conduction band profile for the device geometry of Figure 1 is shown in Figure 2. In calculating the conduction band profile (equivalently the potential profile), some assumption about the

charge assignment must be made since at this point the charge transport dynamics are not yet included (the Monte Carlo code needs to be coupled to the Poisson solver for this). The charge assignment throughout the device is based on the depletion approximation. Ultimately, the initial assigment of the charge distribution will not matter once the Monte Carlo code is coupled to the Poisson solver.

Finally, the last issue which must be addressed is the convergence criterion. Initially, convergence of the SLOR method was defined based upon the change in the potential after each iteration. Although the change in potential is very small when the solution is reached, this criterion does not guarantee that the residual, $\nabla^2\phi + \rho/\epsilon$, of the discrete approximation is small. It is necessary then to not only check the change in the potential but also ensure that the residual is below some specified value. For example, the calculated conduction band profile shown in Figure 2 had a change in potential of less than 2×10^{-5}. However, the residual was on the order of 10^{10} due to the large value of the ratio of the charge density to the dielectric constant of $\sim 10^{14}$. The residual remains large because of the imposition of the depletion approximation at the bulk depletion region (region defined as the transition region between the bulk and depletion region of the junction). The depletion region approximation introduces an unrealistic step function in the charge density according to:

$$-\rho/\epsilon = 0 \quad \text{(bulk)}$$

$$|-\rho/\epsilon| = 10^{14} \quad \text{(depletion region)}$$

This large discontinuity introduces numerical instabilities into

the solution. Therefore, a free carrier concentration is introduced to give a more realistic value to $-\rho/\epsilon$ in the bulk depletion region.

The free carrier concentrations are introduced according to the following assumptions:

1. Only majority carriers are considered.

2. Free carriers are included only in the bulk and a transitional part of the depletion region adjacent to the bulk. The transitional part (bulk depletion region described above) is assumed to be of two Debeye length in width in the lightly doped region.

3. The free carrier distributions are assumed to have the following forms:

$$F_{1/2}(\eta) \sim \exp(\eta) \qquad \text{(nondegenerate)}$$

$$\eta \equiv (E - E_f)/kT$$

$$F_{1/2}(\eta) \sim \frac{4}{3\sqrt{\pi}}\,\eta^{3/2} \qquad \text{(degenerate)}$$

Further, in order to accurately assess the value of the residual, a scaled version of the Poisson Equation is solved. The scaling is applied in a similar manner to that discussed in reference 2. Large variations in the potential are handled using a damping term in the manner discussed in Viallet and Mottet [3].

In summary, the final Poisson solver consists of:

1. solution by the SLOR method.
2. a three point boundary condition method applied at both Neumann and junction boundaries.
3. scaled and unscaled Poisson Eq. solutions.

4. potential updating with damping factors.

5. free majority carriers in bulk and Debeye transition regions.

The Poisson solver has been tested on symmetric and asymmetric pn heterojunctions and extended to rectangular HBT geometries currently. Sample calculations are presented in Figures 3-5. The calculated potential profile for a symmetrically doped HBT device, 10^{16} n-type AlGaAs/ 10^{16} p-type GaAs/ and 10^{16} n-type GaAs HBT structure is shown in Figure 3. As can be seen from inspection of Figure 3, the solution method is tested assuming a poor initial guess for the potential, V=1. For reference, the potential is calculated using the depletion approximation.

The potential profile for an asymmetrically doped HBT device is shown in Figure 4. Again a poor initial guess for the potential of 1 V is chosen. As can be seen, the method agrees closely with the calculated potential predicted using the depletion approximation.

Finally, the doping concentrations of the device structure shown in Figure 1 are used in a rectangular HBT geometry. The calculated potential profile is presented in Figure 5. In this case the residuals are less than 10^{-3} (scaled). Excellent agreement is found between the numerical solution and the depletion approximation.

Currently, the Poisson solver discussed in this section will handle rectangular HBT structures of arbitrary doping concentrations and geometrical lengths. However, to accomodate arbitrary lengths, many grid points must be chosen to maintain accuracy. The assignment of grid points follows the piecewise

linear assignment scheme discussed above. We are currently developing an efficient means of adding points to the grid; maximum accuracy at minimum number of grid points to preserve calculation speed. This efficient adaptive grid will be constructed assuming:

1. a linear variation of the potential to neighboring grid points.
2. analytical expressions for the potential at various locations within the structure.
3. location of grid points where the residual is largest.

The grid will first be optimized separately in each dimension and then ultimately to the L-shaped HBT device geometry of Figure 1.

III. Hydrodynamic/Drift-Diffusion Model

As discussed in the Introduction, a complete model of an HBT requires separate simulations of the device operation during two very different timescales of operation, very short (subpicosecond) and relatively long (nanosecond-microsecond). The short timescale operation is best understood using the ensemble Monte Carlo technique. The long timescale operation cannot be treated using the Monte Carlo approach since no computer could presently simulate the flight of many particles for microsecond or even nanosecond durations using femtosecond time steps. What is typically done is a hybrid model is adopted. The short timescales are simulated using a model like the Monte Carlo that is specifically designed to accurately treat subpicosecond transport phenomena while the long timescales, those involving generation/recombination processes, are investigated using models

adapted specifically to study long term steady-state operation such as the drift-diffusion model.

The drift-diffusion model simply solves the steady-state drift-diffusion current density equations for electrons and holes including generation/recombination processes coupled to a two-dimensional Poisson solver. Standard drift-diffusion methods cannot be applied to short timescales due to their failure to track the energy of the carriers. These models assume either a constant or field-dependent mobility and diffusivity. This is adequate for large devices in which the fields are relatively small and the carriers can be treated as in a quasi-equilibrium. In small geometry devices and for heterostructure injection, the use of a field-dependent mobility is no longer valid. Such an assumption in this case would hide important transient effects, i.e., velocity overshoot and ballistic transport common in HBT devices.

An alternative macroscopic model to the drift-diffusion method is the hydrodynamic model. The hydrodynamic model includes energy balance as well as the current continuity equations in its solution. In this manner, the mobility and diffusivity can be made energy dependent which leads to a reasonably accurate means of estimating transient effects.

We are presently working towards the development of a hydrodynamic model coupled with the two-dimensional Poisson solver. This work is being pursued by another Ph.D. student, Mr. Ali Salem under my direction. We expect to complete the model within the next two years after which it will be applied to HBT analysis as well as the Monte Carlo model discussed in

Sections II and III. It should be noted that support for this part of the program is independent of Motorola and is provided by the National Science Foundation. Nevertheless, Motorola benefits directly from this part of the research.

IV. Future Directions

The first task we are planning is the optimization of the Poisson solver mesh for the L-shaped HBT geometry as discussed in Section II. After this optimization is made, the Poisson solver will be coupled to the ensemble Monte Carlo code and we will be ready to begin calculations of the electron transit time through the device as well as the current-voltage characteristics. In order to compare these calculations to experimental measurements several issues need further to be addressed. These are:

1. determination of the effective emitter and collector junction biases including contact effects.
2. inclusion of a realistic treatment of the base contact.
3. charge scaling for the Monte Carlo particles.
4. possible (if necessary) statistical enhancement of certain regions of the structure for an accurate determination of the charge density.

REFERENCES

[1] J. Bigelow, "A multilevel two-dimensional Poisson equation solver," M.S. Thesis, University of Illinois, Urbana, Ill. 1988.

[2] P. A. Markowich, C. A. Ringhofer, S. Selberherr, and M. Lentini, "A singular perturbation approach for the analysis of the fundamental semiconductor equations," IEEE Trans. Elect. Dev., vol. ED-30, pp. 1165-1180, Sept. 1983.

[3] J. E. Viallet and S. Mottet, "Heterojunction under Fermi-Dirac statistics: General state of equations and steady state numerical methods," NASECODE IV Conf., pp. 530-535, Dublin, 1985.

HBT Geometry

The section of a typical HBT device geometry on which the electric field is solved.

Due to the symmetry of self-aligned HBTs, this is the section of interest.

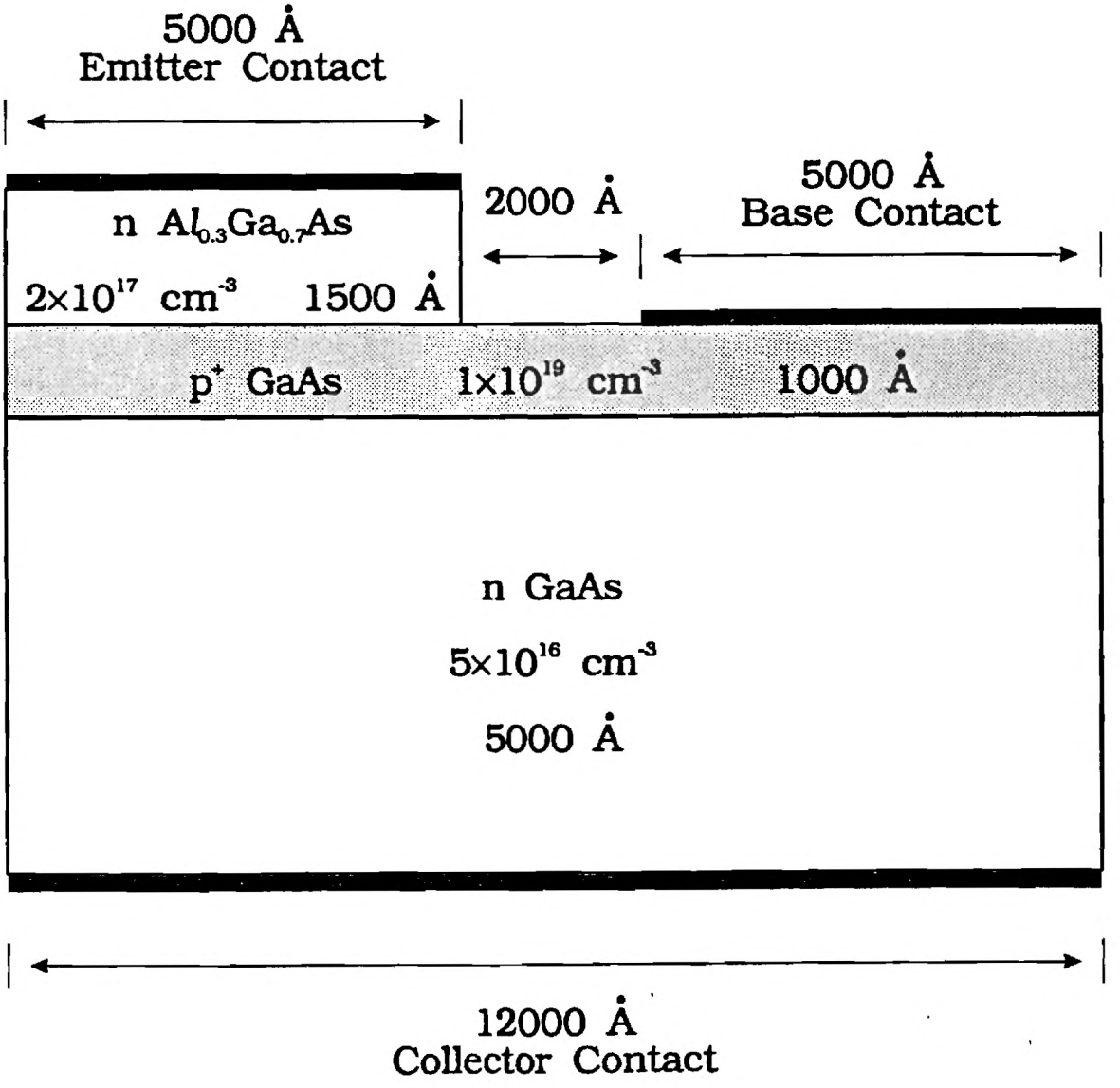

Figure 1: Schematic drawing of a typical HBT geometry. This structure was obtained from review of the literature.

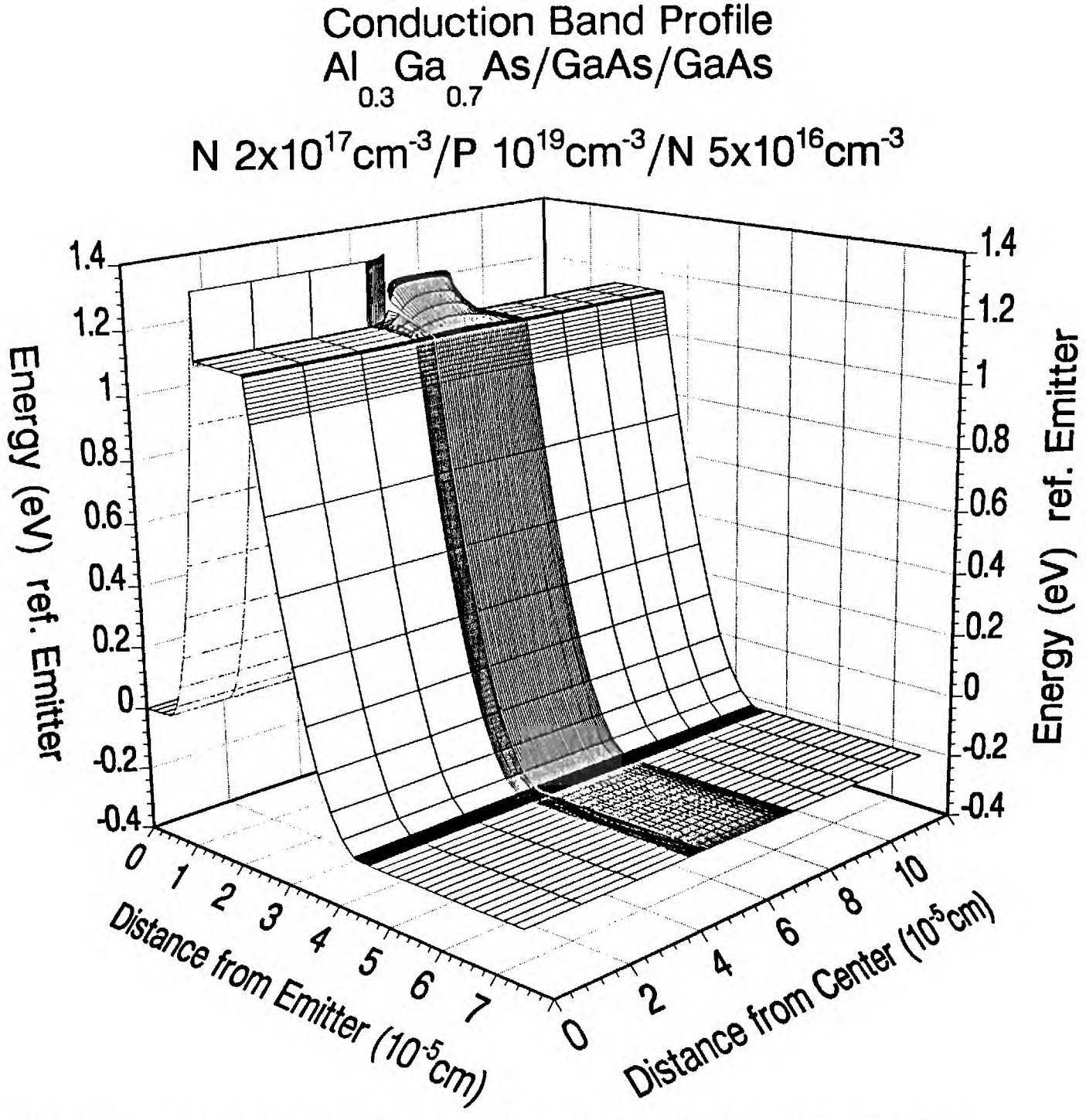

Figure 2: Calculated three dimensional potential profile for the device shown in Figure 1.

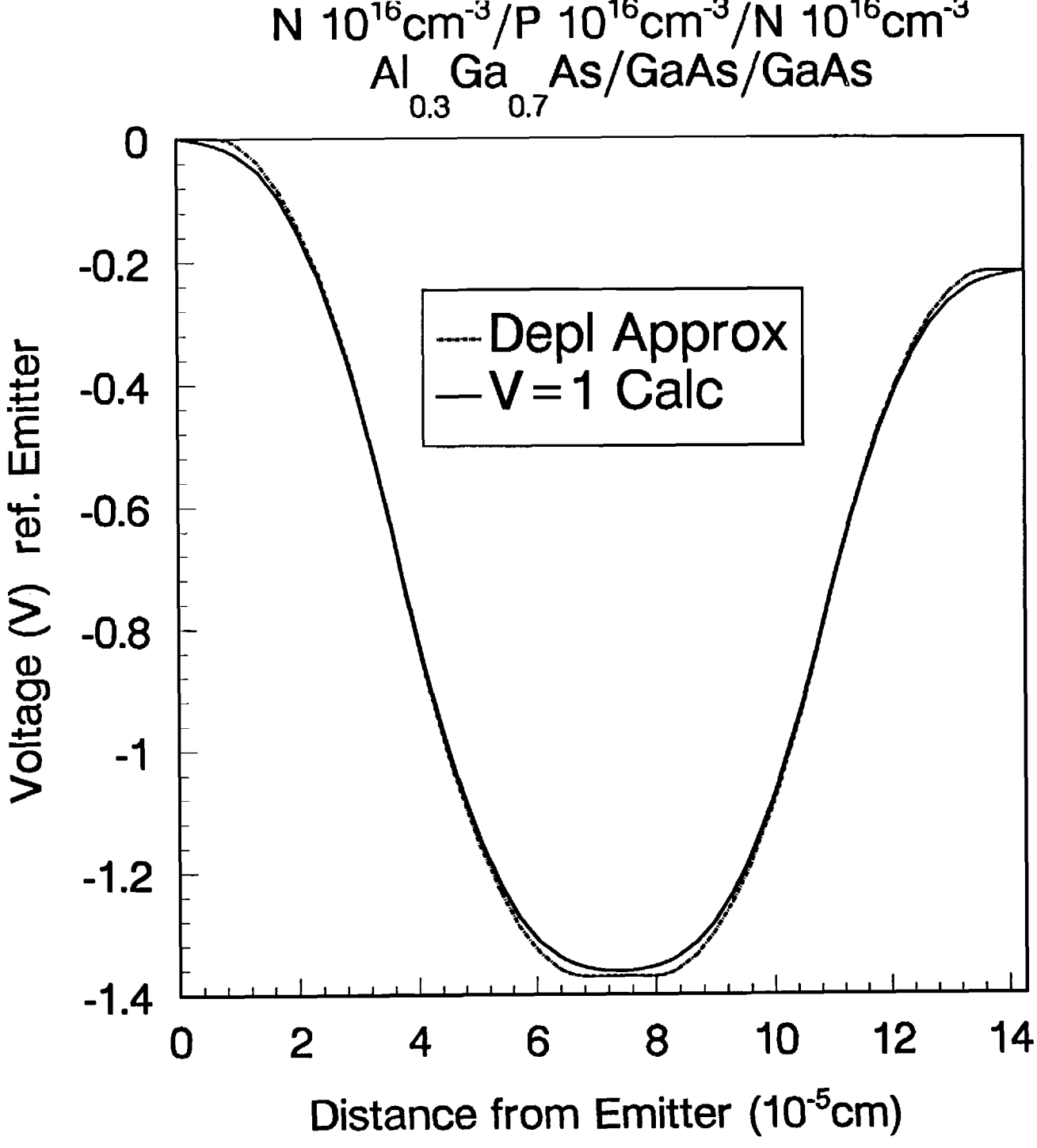

Figure 3: Calculated potential vs. distance in a symmetrically doped HBT structure. An initial guess of 1 V everywhere was made for the calculated potential.

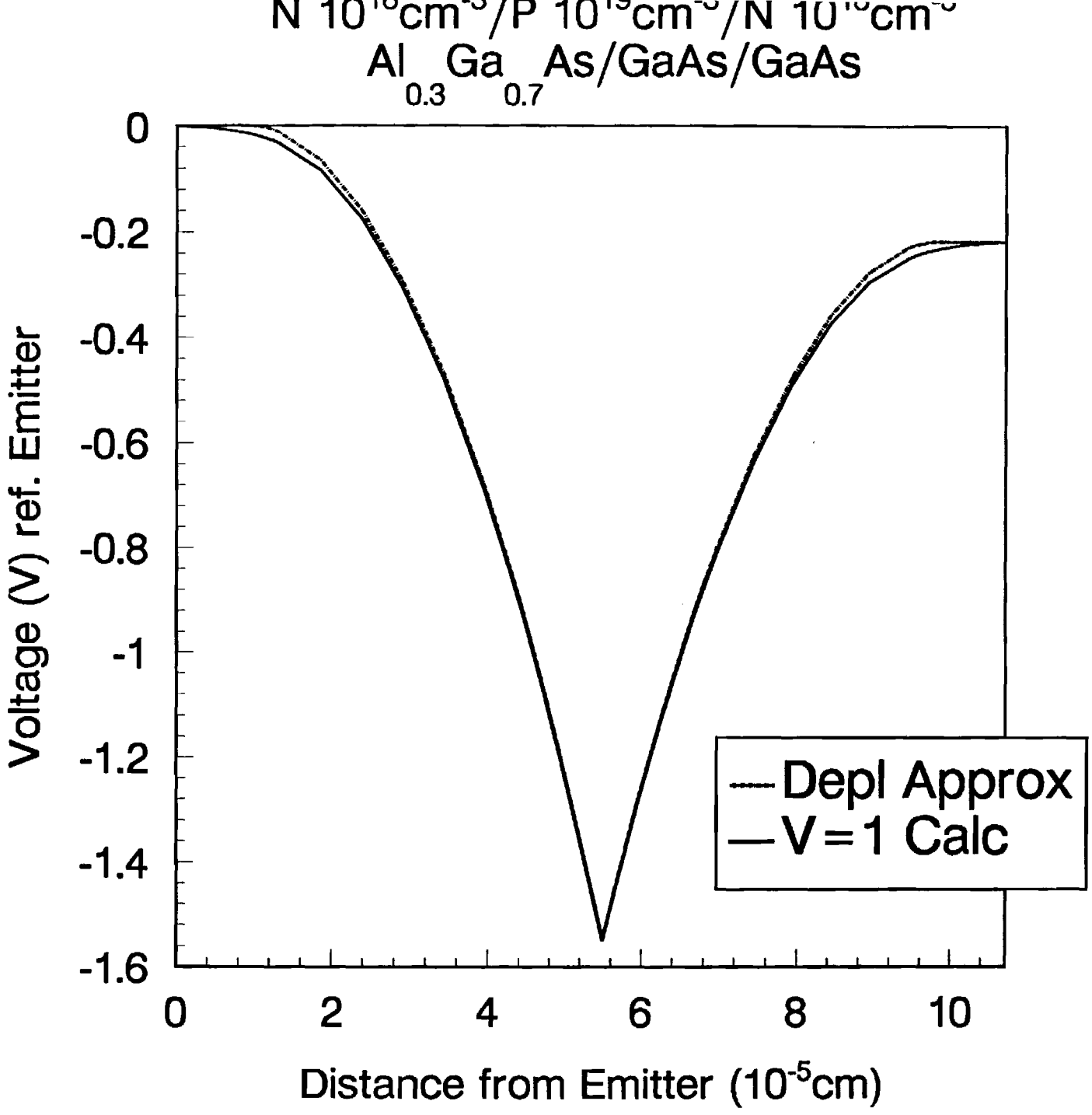

Figure 4: Calculated potential vs. distance in an asymmetrically doped HBT structure. Again an initial guess of 1 V is made.

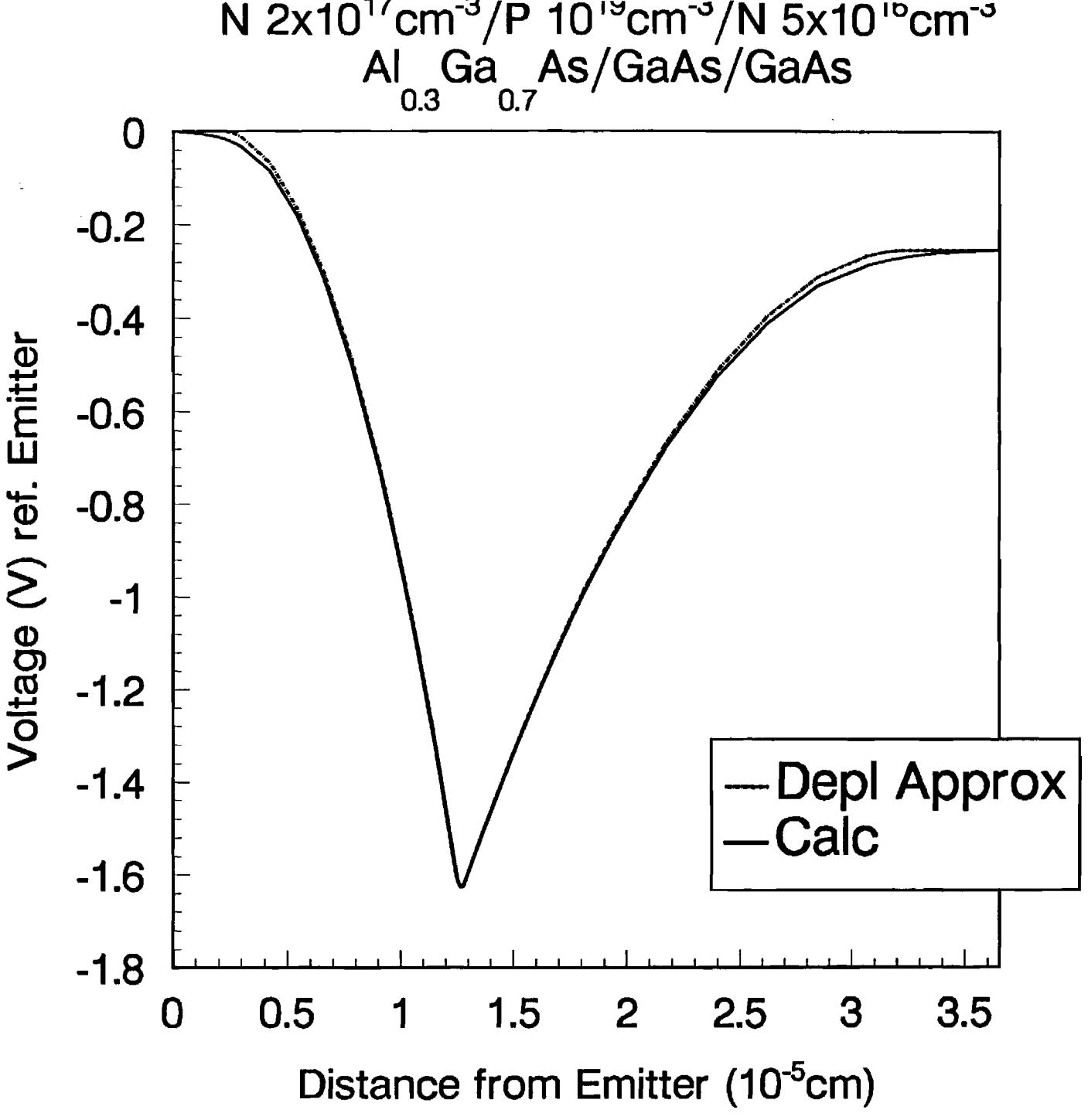

Figure 5: Calculated potential vs. distance for the device sketched in Figure 1.

SIMULATION OF ADVANCED SEMICONDUCTOR DEVICES USING SUPERCOMPUTERS

Kevin F. Brennan

Nabil Mansour

and

Yang Wang

School of Electrical Engineering
and
Microelectronics Research Center
Georgia Institute of Technology
Atlanta, Georgia 30332-0250

ABSTRACT

The current generation of advanced semiconductor devices often exhibit nonlinear effects which require numerical approaches to their simulation. In addition to nonlinearities, the accurate description of the behavior of ever increasingly small devices, as well as those which contain heterostructures or superlattices, demands extraordinarily complex techniques which typically overwhelm most computational environments. Under these conditions, the supercomputer provides the only reasonable means by which the behavior of advanced semiconductor devices can be examined in detail. In this paper, we present a discussion of computational techniques and their application to modeling avalanching semiconductor devices within a supercomputer environment. Specifically, issues such as velocity and current estimators, bipolar simulation, temporal response, and subensemble simulation will be addressed. Calculated results are presented for representative systems to illustrate the use of these estimators.

I. Introduction

Accurate simulation of any semiconductor device requires the development of numerical estimators which properly report the macroscopic variables of interest. Various estimators for the same macroscopic observables can give very different values depending upon how these estimators are defined. In developing an estimator caution must be exercised in order to ensure that the estimator reports what is actually desired. If one is interested in comparing results to experimental data then the estimators employed must report physically observable quantities in a manner consistent with measurement. Alternatively, one may be interested in studying the internal workings of a device which cannot be experimentally probed requiring the development of an alternative estimator which reports different information than before. It is of further interest to have estimators which serve as a control on the accuracy of the simulation. In this paper we outline various estimators for the drift velocity, current and temporal response of semiconductor devices.

Though it is important that one fashion estimators which can reliably determine macroscopic observables from Monte Carlo simulation, it is also imperative that a reliable materials parameter set be determined. We have studied the effect of variations in the material parameters on the steady-state transport in bulk GaAs and AlGaAs. Here we review that study pointing out how uncertainties in various parameters influence the macroscopic observables calculated in the steady-state.

Finally, we present a review of our previous studies of avalanching photodetectors which incorporate many of these issues. Though we have applied many of the techniques outlined below to the study of HEMTs, a review of our HEMT work is omitted here to avoid needless repetition with the many other fine presentations, which exhaustively cover HEMT modeling, in the series of talks of which this lecture is part.

II. Estimators for steady-state simulation

The carrier velocity is of great interest in semiconductor device simulation since it lies as the basis to the understanding of many different important observables such as the current and frequency response. There are numerous ways in order to estimate the carrier velocities as well as how to calculate their average. Here we restrict ourselves to discussing four different estimators for steady-state simulation which have various degrees of validity. Alternative velocity estimators of use in transient simulations have been discussed before [1]. The four velocity estimators of interest are as follows: velocity based on energy gain, velocity based on energy loss, instantaneous velocity calculated from the gradient of the band structure, and the velocity calculated from the average distance traveled. The first two estimators, velocity based on energy gain and loss, apply only to constant electric field simulations. These two estimators approach one another in value at steady state, since the energy gain from the electric field must be balanced, on average, by the energy loss to the phonons. The two estimators do not necessarily agree perfectly, even in steady state, since the energy gain from the field occurs in a continuous manner while the energy loss follows from discrete events. The mean velocity is determined by averaging over the distribution in either case.

The mean velocity can also be calculated by averaging over the instantaneous carrier velocities derived from the gradient of E(k). This estimator has the important advantage of retaining its validity under all conditions. Another estimator which can be used under all conditions is the velocity calculated from the average distance traveled. The velocity based on distance traveled is related to that based on the instantaneous velocity since the distance is calculated from the product of the instantaneous velocity and the simulation time.

Nevertheless, the averaging is slightly different between the two and as such leads to some variance in their values.

It is useful to first calibrate the estimators based on the gradient of E(k) and the average distance traveled to the energy gain and loss estimators since the latter two are useful in defining steady-state conditions. We can then determine the simulation time needed in order for the system to reach steady-state and obtain some measure of the convergence of the gradient of E(k) estimator. The values of each velocity estimator are plotted in order to show their relative convergence in Figure 1 as a function of simulation time in bulk material. Steady-state conditions, as defined as the time elapsed until the energy gain and loss are comparable, are attained after 40 psec as is shown in Figure 1. It should be noted that the final convergence point is obtained by asymptotically extending the energy gain and loss curves until they intersect. Inspection of Figure 1 also indicates that the other estimators, those based on the instantaneous velocity and distance traveled, fluctuate within the limits defined by the energy gain and loss estimators. Hence, by taking the average value in the asymptotic limit of the instantaneous velocity estimator, an accurate value of the steady state carrier drift velocity can be attained. Plots of the velocity as a function of time at other electric field strengths exhibit qualitatively the same behavior as that shown in Figure 1. It is important to note that the asymptotic limit of the average value of the instantaneous velocity estimator can be used under all conditions for device simulation, whereas the energy balance approach is only useful in the absence of transient effects.

It is interesting to compare the Monte Carlo calculations to experimental measurements in order to ascertain the accuracy of the code and the estimators employed. In Figure 2, the calculated electron steady-state drift velocity as a function of applied

electric field in bulk GaAs is plotted along with previous Monte Carlo calculations [2] and experimental data [3]. The calculated points represent the converged average determined from the four estimators discussed above found in a manner similar to that shown in Figure 1. As can be seen from Figure 2, the present calculations agree favorably with the previous results over the full range of applied electric field values considered.

The excellent agreement between the experimental data and the calculated values depends upon the choice of material parameters as well as the accuracy of the estimators. If the selected material parameter set is unreliable, then the resulting calculations will of course be as well. Numerous material parameters are needed in an ensemble Monte Carlo simulation. Among these are the:

density

dielectric constants (low and high frequency)

lattice constant

direct energy gap

effective masses (gamma and satellite valleys, valence bands)

valley separation energies

optical phonon energy

sound velocity

nonparabolicities (gamma and satellite valleys)

impact ionization threshold energy

impact ionization rate factor

intervalley coupling constants and phonon energies.

Though some of these parameters are reasonably well known and widely accepted, such as the density and lattice constants, others are notoriously difficult to extract from experiment

and as such are highly uncertain. Among these parameters are the intervalley coupling constants, valley separation energies, impact ionization threshold and rate factor and nonparabolicities. In an attempt to ascertain how variations in some of these parameters effect the steady-state macroscopic observables we have performed a series of "computer experiments" in which different parameters are varied at will and their effects on these observables are assessed [4]. Specifically, we have examined how variations in the polar optical phonon energy, dielectric constants, effective masses and intervalley separation energies and coupling constants alter the velocity-field relationship in bulk AlGaAs. Through computer experiments such as these, one can determine a reliable set of material parameters which can reproduce the steady-state macroscopic observables.

Our ensemble Monte Carlo model has been used to determine the steady-state drift velocity based on the previously discussed estimators in bulk GaAs as shown in Figure 2. The corresponding parameters used in the simulation are collected in Table 1. The fit, though not exact, is well within the inherent uncertainty in the earlier Monte Carlo calculation [2], as well as the uncertainty in the experiments [3]. The parameters listed in Table 1 were selected from both the literature [5-9] and by repeatedly varying the parameters in order to match the experimental measurements.

We have also examined the electron drift velocity in bulk AlGaAs, however, to date no experimental measurements for this material system are available. As a consequence, a definitive set of parameters is difficult to establish. Nevertheless, we have endeavored to prepare a set of parameters based again on the literature [6-9]. These parameters are collected in Table 2. In order to ascertain the effect of uncertainties in these parameters we have performed a series of "computer experiments" in which variations in each parameter are analyzed.

As an example of the degree of sensitivity of the steady-state drift velocity to variations in the material parameters, we present calculations of the velocity field relation in bulk AlGaAs (32% Al). As can be seen from inspection of Figures 3-6, the peak drift velocity is most sensitive to the choice of the intervalley separation energies and optical phonon energy. Variations in the gamma valley effective mass as well as the dielectric constants also effect the drift velocity but mostly through the value of the threshold field. Comparison of the various curves in Figures 3-6 shows that fluctuations can have a drastic effect on the macroscopic observables of the system.

In selecting a set of material parameters for numerical simulation, it is perhaps best to first search the literature. Of course, there is never universal agreement on the values of these parameters so the choice is often not well defined. Nevertheless, one makes a best "guess" as to the values of these parameters. After a selection has been made, it is instructive to perform "computer experiments" to check for agreement with experimental measurements, if any are available, to further improve the accuracy of the simulation.

It should be noted that a definitive set of parameters for even a well studied material such as GaAs has not been standardized. Presently, there is much variation in the Monte Carlo simulation community on material parameters. We do not pretend to offer a definitive set here, but only point out that the steady state velocity-field relation is most sensitive to variations in the intervalley separation energies and optical phonon energy as compared to other parameters such as the intervalley coupling constants. It should be further noted that steady-state simulation is not sufficient by itself to fully determine all of the transport parameters since some parameters, such as the intervalley coupling constants, have greater influence on transient phenomena and are best determined from relaxation experiments. It has been suggested [10] that some standardization of parameters within the

Monte Carlo community be attempted. It is hoped that the work reported here and in reference [4] is a modest step towards that goal.

One of the most important macroscopic observables in semiconductor device simulation is the current density. We have chosen to calculate the current density based on the instantaneous velocity using the gradient of E(k). The total current density is calculated at each simulation step by constructing the sum of the instantaneous velocities over the entire distribution.

The steady-state current density is then determined from the asymptote of the current versus time. The current density is plotted as a function of time in Figure 7 under two different gate voltages for a C structure. As can be clearly seen from this curve, the current fluctuates initially and reaches a steady-state value within 4-5 psec. The faster convergence of this estimator is due to the many more particles simulated (~9000) in the HEMT device than in the bulk simulation reported above (~2000). The particular advantage of calculating the current in this manner as opposed to that using a Gaussian surface is that steady-state is reasonably well defined and fluctuations due to the relatively small number of simulated carriers are averaged out. In the Gaussian surface approach, the current density fluctuates wildly throughout the entire course of the simulation even after steady-state is reached since at some instances many carriers cross a boundary while few do at other times. Experimental measurements would however record a constant flux in steady-state. Therefore, the Gaussian surface approach does not truly represent the experiments.

The particular limitation of the instantaneous velocity model is that the current density through different contacts is not immediately obtained. The above mentioned approach gives the current density carried by the entire distribution but does not distinguish

between those carriers collected within different contacts; i.e., substrate, gate or drain in a FET for example. In order to separate out these contributions, it is useful to plot the number of carriers collected as a function of time to obtain the asymptotic percentage of carriers collected at each contact. From the ratio of the carriers collected at a particular contact to the total number of carriers present, the current through that contact can be determined.

Another important estimator is the temporal response of a device. In a unipolar device, the time response can be readily calculated as the average transit time of the particles. However, the definition of the time response of a device in which the carrier concentration increases or decreases through generation or recombination events is nontrivial. Here we discuss the temporal response of an avalanching device in which secondary carriers are created during the time course of the simulation. The full details of the technique have been discussed elsewhere [11].

In order to properly quantify the time dependence of a device in the presence of multiplication it is necessary to employ a bipolar simulator. Such a scheme is diagrammatically presented in Figure 8. In this particular scheme an iterative approach between separate electron and hole simulators is chosen. One of course can couple the two simulators into only one program. However, we have found that even on a supercomputer the complete simulation takes many cpu hours. The most efficient simulation overall is achieved using the iterative approach since there is less risk of machine failure before meaningful results are reported. The simulation is briefly explained as follows. First, a deterministic number of photogenerated electrons are launched and their motion through the device is tracked. Upon the occurence of an impact ionization event, the time and spatial location of the secondary carriers, both electron and hole, is noted. The secondary

electron is subsequently added to the simulation while the secondary hole information is stored for later use. This continues until all of the electrons, both parent and secondary, are collected at the n+ contact. The hole transit histories are next simulated using as input the spatial locations of the secondary holes born in the initial electron transit. The time of hole flight is equal to the sum of the individual hole transit times and their time delay prior to their production. Based on this information, the total current in the first iteration can be calculated. Successive iterations are performed until convergence is achieved.

III. Application of the simulation techniques to APDs

The study of wide band gap interband impact ionization devices such as avalanche photodiodes, APDs, requires treatment of high energy, high electric field effects. Specifically, it is important to accurately portray the energy band structure, the full details of the carrier-phonon scatterings, as well as bipolar transport. All of these effects are incorporated in our ensemble Monte Carlo simulator for interband impact ionization. Two additional parameters, from those used in bulk steady-state simulation, are typically used in Monte Carlo studies of impact ionization. These are the impact ionization threshold energy and the Keldysh p factor which represents the impact ionization probability. These two parameters are usually determined by comparing the Monte Carlo calculations of the bulk impact ionization rates to experimental data. It should be recognized that, though the Monte Carlo method affords a fairly complete theory of carrier transport, it nevertheless includes a fair amount of parametrization at present. In principle, all of the details of semi-classical transport could be included in a Monte Carlo model but in practice owing to computer capacity limitations, some physical ingredients are included through parametrization. In the case of interband impact ionization, the ionization rate is assumed

to be $\vec{k}$ independent and the probability is parametrized by a scalar constant ρ. Improvements on this approach are difficult yet will certainly be made.

The microscopic physics of the impact ionization mechanism can be analyzed by tracing the carrier trajectories in k space using the Monte Carlo method. A typical history of an electron flight in bulk GaAs is plotted in Figure 9. After an impact ionization event, the electron is restarted from the zone minimum. As can clearly be seen from this figure, the electron history is extremely complicated. The electron undergoes occasional local fluctuations from the average during which its energy can be vastly different from the average steady-state value. It is during these departures from the average behavior that an impact ionization event occurs. The usefulness of the Monte Carlo method is that it makes no a priori assumptions about the nature of the electron's trajectory in the study of impact ionization. This enables predictive investigations of the behavior of APDs. In other words, once the Monte Carlo method is "calibrated" to predict a similar rate to the experimental bulk ionization measurements, it can be applied with a fair degree of confidence to new structures in which the ionization rate has not yet been measured. In this way, one can design and optimize novel semiconductor APDs.

The critical issue in the design of an interband APD is the determination of the electron and hole ionization coefficients in these structures. As is well known, optimal performance of an APD as measured in terms of lowest excess noise, and highest bandwidth, is achieved under unipolar ionization conditions. In other words, if only one carrier species, notably the injected carrier, contributes to the ionization process then the excess noise factor always lies between 1 and 2 and the bandwidth is greatest. Unfortunately, in most bulk compound semiconductor materials, the electron and hole impact ionization rates are

roughly comparable. Therefore, APDs made from these materials will exhibit poor noise and bandwidth performance.

The introduction of a superlattice/multi-quantum well structure provides a means by which the electron distribution can be selectively heated so as to artificially enhance the electron to hole ionization rates ratio [11-14]. Such a structure is diagrammatically presented in Figure 10. The multi-quantum well system is made using alternating layers of GaAs and AlGaAs and is used to form the intrinsic region of a p-i-n diode.

The action of the multi-quantum well structure on the electron ionization process can be ascertained by comparing the ionization rate profile in its presence or absence [15]. Figure 11 plots the number of electron ionizations as a function of position at various applied electric field strengths in bulk GaAs. As can be clearly seen from this figure, the impact ionizations occur randomly throughout the material. The introduction of a multi-quantum well structure imparts a spatially deterministic aspect to the impact ionization rate as can be seen from inspection of Figure 12. The spatial localization of the electron ionization events in this structure is striking. Notice that the vast majority of events occur near the heterojunction interface, ~10 - 100 A away from the discontinuity. It is interesting to further compare the electron ionization profiles to the corresponding hole ionization profiles. Figures 13 and 14 illustrate the hole ionization profiles in bulk GaAs and a multi-quantum well geometry respectively. Again, within the bulk material the ionization rate is strictly random. Interestingly, within the multi-quantum well geometry, the hole ionization profile is again basically random in strong contrast to the electron ionization profile. This is apparently due to the difference in the band edge discontinuities as well as the different electron and hole relaxation rates.

From the above discussion, it is clear that the Monte Carlo method provides a very clear demonstration of the effect of a multi-quantum well geometry, or more generally a periodic potential, on the ionization rate. The Monte Carlo analysis can also provide estimates of the relevant macroscopic observables of interest. For APDs, the electron and hole ionization rates ratio is of great importance. The electron and hole ionization rates ratio within a 500/500 A wide GaAs/AlGaAs multi-quantum well structure are plotted as a function of electric field in Figure 15. For comparison, recent experimental data in a comparable structure are plotted as well. Notice the good agreement between the theory and experiment. It should be noted that the theoretical result was made several years in advance of the experimental measurement [16].

Another important macroscopic observable in APD analysis is the temporal response. Generally, the temporal response of an APD is difficult to determine numerically and requires the simulation of both carrier species. As an example, we consider the temporal response of the simple five stage, GaAs/AlGaAs multiquantum well APD similar to that sketched in Figure 10. Following the approach discussed above, the instantaneous current within a multiquantum well APD is plotted as a function of time in Figure 16 at an applied electric field of 400 kV/cm. The result shown in Figure 16 is for electron ionization only but includes the first generation of holes produced.

In order to check the validity of this result, we and other colleagues have developed an analytical theory [17] based on a marked filtered Bernoulli branching process. Each event of this process contributes electron and hole component currents appropriate to the times and positions of the particle births. The corresponding analytical result is presented in Figure 17 for the electron impulse response function in the same device considered above. The general similarity of the impulse response function calculated from either model

is apparent from comparison of Figures 16 and 17. Both curves peak at about the same place and both curves decay with a rather flat tail. The analytical impulse response function is generally less smooth than the simulated function and it exhibits a shorter tail. Both of these characteristics can be attributed to the assumption of constant transit time (velocity) for each carrier in each material within the analytical model. The simulation, on the other hand, includes transit-time dispersion naturally and as such leads to a longer tail in the response.

The simulation can be readily applied to devices which exhibit double carrier multiplication. As mentioned above, the numerical simulation tracks all of the carriers, electrons and holes born during the passage of the initial electron pulse through the device. The overall impulse response function, which is comprised of the electron and hole currents, is presented in Figure 18. Three iterations of the coupled electron and hole simulators are reported. As can be seen from Figure 18, the close agreement between curves 2 and 3 indicates good convergence of the simulation. There is a significant difference between the first and third iterations; the duration of the time response is increased by more than 8 psec. The presence of only a small amount of secondary hole ionization acts to greatly extend the duration of the pulse.

As a further example of the use of the simulation methods useful in APD modeling, we consider the calculation of the standard deviation of the time response of an APD. In this case, we simulate a series of subensembles in order to obtain the mean time response and the first standard deviation of the time response. In spite of using supercomputers, the computational time required in order to generate the standard deviation is excessive since numerous, ~50, trials are run for each ensemble. These restrictions limit the simulations to only the electron-current contribution of the impulse response function and its standard

deviation. The simulated results are shown in Figure 19. As can be seen from Figure 19, there exists both temporal and gain randomness giving rise to fluctuations in the carrier number (as reflected by the magnitude of the current) and the transit time.

It is interesting to compare the simulated results for the electron current time response and its standard deviation to analytical results derived from the impulse response of the device. The details of this theory have been presented in reference [17]. As can be seen from comparison of Figures 19 and 20, the analytical model shows similar gain fluctuations to that predicted by the simulations. However, since no temporal uncertainties are included in the analytical model, the temporal dispersion predicted by the simulations is not obtained in the analytical calculations.

IV. Unipolar avalanching devices

Ideally, a solid-state photodetector which utilizes only one ionizing carrier species would, by design, provide extremely low noise, high speed performance. Such a structure cannot provide multiplicative gain via interband impact ionization since this process naturally involves both electrons and holes. An alternative avalanche mechanism, impact ionization of electrons out of confined quantum states [18,19] provides a means by which a unipolar avalanching device can be made. In this process, incident electrons impact excite quantum confined electrons to energies greater than the well barrier height as shown diagrammatically in Figure 21.

The physics of confined quantum state impact ionization has been exhaustively presented in references 19 and 20. The process can be described by a screened Coulomb interaction between an incident free electron and a confined state electron. From inspection of Figure 21, it is clear that the ionization rate must exhibit a threshold energy in a symmetric well structure since not all of the incident electrons have sufficient kinetic energy

in order to impact excite confined carriers out of the well. If the well is made asymmetric such that the trailing barrier height is half the leading barrier height, then all of the incident electrons have sufficient kinetic energy to cause impact ionization of the confined electrons. Nevertheless, due to momentum conservation requirements, a threshold state can still exist in the asymmetric structure. It is interesting to compare the operation of a symmetric well structure, as shown in Figure 22, to that of an asymmetric well device, as sketched in Figure 23 in order to observe the effect of the device geometry on the ionization rate.

The electron transition rate as a function of incident kinetic energy can be calculated for both the symmetric and asymmetric designs using the approach outlined in references 19 and 20. The ionization probability is plotted as a function of incident electron energy for both a symmetric and an asymmetric GaAs/AlGaAs multiquantum well structure in Figures 24 and 25. Inspection of these figures shows that the transition rate is an order of magnitude greater within the asymmetric structure than within the symmetric device for comparable geometries, as expected due to the lower threshold energy in the asymmetric design.

Though the asymmetric design generally exhibits a greater transition rate under comparable conditions, this does not by itself ensure a superior design. It is also important that the detector exhibit very low dark current. The most important sources of dark current within the confined quantum state detectors are thermionic emission and tunneling currents. The thermionic emission current is most sensitive to temperature, while the tunneling current is primarily effected by the applied electric field across the barrier, at fixed free carrier concentration and trailing barrier height. The magnitude of the dark currents in representative GaAs/AlGaAs designs are presented in Figures 26 and 27. Notice that for the particular design considered here, that the thermionic emission current is negligible only

at very low absolute temperatures, below 10 K. Likewise, the tunneling current is significant above 10 kV/cm. Hence, the choice of an asymmetric well design offers a tradeoff in higher ionization rate versus higher dark current. Further work is in progress concerning the design issues of confined quantum state photomultipliers. Above we present only a brief introduction to the subject.

IV. Conclusions

In this paper, we have discussed various estimators of macroscopic observables, material paramter selection, and their application to semiconductor device simulation. Specifically, we have outlined approaches for determining the carrier drift velocity, under constant electric field, steady-state conditions as well as in the most general case, the current density, and the time response of a device. We have outlined simulation strategies for analyzing avalanche photodiodes, APDs, incorporating many of these estimators and techniques. The determination of the key engineering figures of merit useful in the characterization of multi-quantum well APDs using the numerical simulation models has been presented. The computational strategies outlined here can be used to study both unipolar and bipolar semiconductor devices including carrier generation or recombination processes. Due to the extensive computational requirements implicit in these simulation techniques, supercomputers provide the most useful platform for their application.

Acknowledgements

The authors gratefully acknowledge the use of the Pittsburgh Supercomputer Center and the National Center for Supercomputing Applications in Urbana, Illinois. Computer time at the Urbana Center was provided by a grant through the National Center for

Computational Electronics. This work was sponsored in part by Bell Communications Research through contract E21-633 and by the National Science Foundation through a Presidential Young Investigator Award made to K. Brennan.

REFERENCES

[1] K. F. Brennan, Ph.D. Thesis, Univ. of Ill., Urbana, Illinois (1984).

[2] J. G. Ruch and G. S. Kino, Phys. Rev., 174, (1968) 921.

[3] T. H. Windhorn, T. J. Roth, L. M. Zinkiewicz, O. L. Gaddy, and G. E. Stillman, Appl. Phys. Lett., 40, (1982) 513.

[4] K. F. Brennan, D. H. Park, K. Hess, and M. A. Littlejohn, J. Appl. Phys., 63, (1988) 5004.

[5] S. Adachi, J. Appl. Phys., 58, (1985) R1.

[6] M. A. Littlejohn, J. R. Hauser, and T. H. Glisson, J. Appl. Phys., 48, (1977) 4587.

[7] R. Raizbehzadeh, Ph.D. Thesis, University of Wisconsin-Madison (1986).

[8] R. J. Schuelke, Ph.D. Thesis, Purdue University (1984).

[9] T. Wang, Ph.D. Thesis, University of Illinois, Urbana-Champaign, (1986).

[10] D. K. Ferry, NCCE Workshop on Computational Electronics, Urbana, Illinois (May 1990).

[11] R. Chin, N. Holonyak, Jr., G. E. Stillman, J. Y. Tang, and K. Hess, Electron Lett., 16 (1980) 467.

[12] F. Capasso, W. T. Tsang, A. L. Hutchinson, and G. F. Williams, Appl. Phys. Lett., 40 (1982) 38.

[13] K. Brennan, T. Wang, and K. Hess, IEEE Electron. Dev. Lett., EDL-6, (1985) 199.

[14] K. Brennan, K. Hess, and F. Capasso, Appl. Phys. Lett., 50 (1987) 1897.

[15] K. Brennan, IEEE J. Quantum Electron., 24 (1988) 2001.

[16] T. Kagawa, H. Iwamura, and O. Mikami, Appl. Phys. Lett., 54, (1989) 33.

[17] K. F. Brennan, Y. Wang, M. C. Teich, B. E. A. Saleh, and T. Khoorsandi, IEEE Trans. Electron Dev., ED-35, (1988) 1456.

[18] J. S. Smith, L. C. Chiu, S. Margalit, A. Yariv, and A. Y. Cho, J. Vac. Sci. Technol. B, 1 (1983) 376.

[19] S. L. Chuang and K. Hess, J. Appl. Phys., 59 (1986) 2885.

[20] Y. Wang, D. H. Park, and K. F. Brennan, IEEE J. Quantum Electron., 26, (1990) 285.

Figure Captions

Figure 1: Calculated electron drift velocity as a function of simulation time for four different estimators. The calculations are performed under constant electric field conditions. Notice that good agreement between the four estimators is achieved within the asymptotic limit.

Figure 2: Calculated and experimental data of the steady-state velocity plotted as a function of applied electric field in bulk GaAs.

Figure 3: Calculated electron steady state velocity in bulk AlGaAs (32% Al composition) as a function of applied electric field with the intervalley separation energies as a parameter. The peak velocity is greatest the larger the intervalley separation energies are. This arises due to the greater confinement of the electrons within the low effective mass, high mobility gamma valley.

Figure 4: Calculated electron steady state velocity in bulk AlGaAs (32% Al composition) as a function of applied electric field with the optical phonon energy as a parameter. Notice that the peak drift velocity is greatly effected by the choice of phonon energy. The peak velocity is largest at greatest phonon energy due to the increased gamma valley confinement owing to the more effective carrier cooling.

Figure 5: Calculated electron steady state velocity in bulk AlGaAs (32% Al composition) as a function of applied electric field with the effective mass as a parameter.

Figure 6: Calculated electron steady state velocity in bulk AlGaAs (32% composition) as a function of applied electric field with the dielectric constants as a parameter. The dielectric constants act to alter the electron-optical phonon scattering rate. Notice that the choice of dielectric constants effects the threshold field more than the peak velocity.

Figure 7: Plot of the instantaneous current density as a function of simulation time in a HEMT structure at different gate biases. The steady-state current density is determined from the asymptote of each curve.

Figure 8: Schematic representation of the bipolar simulation technique for studying the temporal response of an avalanching device. This technique can be used generally to study all avalanching devices. It is possible to combine the two simulators into one master code which would then have the advantage that self-consistent effects could be included.

Figure 9: Calculated electron energy history within bulk GaAs at an applied electric field of 500 kV/cm. The zeros represent impact ionization events. Notice the very complicated trajectory the electron experiences during its flight. This indicates the complexity involved in fully describing the impact ionization process.

Figure 10: Sketch of the conduction and valence bands in a GaAs/AlGaAs multi-quantum well structure under bias.

Figure 11: Number of electron ionization events plotted as a function of distance traveled measured in angstroms in bulk GaAs at various applied electric field strengths of 350, 400

and 500 kV/cm. Both initial and secondary electrons (those born from impact ionization events) are simulated. Notice the great degree of randomness in the ionization rate.

Figure 12: Number of electron ionization events in a simple multi-quantum well APD similar to that sketched in Figure 10, plotted as a function of position. Notice the great degree of localization in the ionization process produced by the introduction of the periodic potential.

Figure 13: Number of hole ionization events in bulk GaAs plotted as a function of position at various electric field strengths of 350, 400 and 500 kV/cm. The randomness of the ionization profile is readily apparent.

Figure 14: Number of hole ionization events in a GaAs/AlGaAs multi-quantum well APD plotted as a function of position. In this case, the hole ionization events occur at random within the GaAs layers and no spatial localization is apparent.

Figure 15: Calculated electron to hole ionization rates ratio in bulk GaAs and a 500/500 A GaAs/AlGaAs well/barrier wide multi-quantum well structure as a function of applied electric field. The solid triangle represents the experimental data reported in reference 16 for a similar, but not exactly the same, device geometry. Notice the significant increase in the ionization rates ratio at 250 kV/cm.

Figure 16: Impulse response function obtained from the simulation of a five-stage MQW superlattice APD operated at an applied field of 400 kV/cm. Hole impact ionization is

assumed to be absent, yet the secondary holes produced in the electron impact ionization events are still simulated to account for the transit time.

Figure 17: Impulse response function obtained from the analytical model for a five-stage MQW superlattice APD operated at 400kV/cm. Again, hole impact ionization is assumed to be absent.

Figure 18: Overall impulse response function for a simple multi-quantum well APD consisting of five stages and formed from GaAs/AlGaAs. The presence of only a small amount of secondary hole ionization acts to greatly extend the duration of the pulse.

Figure 19: Simulated electron-current contribution to the impulse response function plotted with their one-standard deviation limits.

Figure 20: Analytical calculation of the electron-current contribution to the impulse response function plotted along with the one-standard deviation limits.

Figure 21: Initial and final states for the electron-electron interaction in a confined quantum well structure.

Figure 22: Schematic drawing of the symmetric well confined quantum state photomultiplier under bias.

Figure 23: Schematic drawing of the asymmetric well confined quantum state photomultiplier under bias.

Figure 24: Calculated transition rate for an incident electron as a function of incident energy in a 200/1000 A well/barrier width symmetric well confined quantum state device.

Figure 25: Calculated transition rate for an incident electron as a function of incident energy in a 200/1000 A well/barrier width asymmetric well confined quantum state device.

Figure 26: Calculated two-dimensional thermionic emission current out of a GaAs/AlGaAs quantum well plotted as a function of ambient temperature.

Figure 27: Calculated two-dimensional tunneling current out of a GaAs/AlGaAs asymmetric quantum well plotted as a function of applied electric field strength.

Table I

GaAs

Bulk Material Parameters

Parameter	Value
Lattice Constant (cm)	5.6533×10^{-8}
Longitudinal Phonon Energy (eV)	0.033
Sound Velocity (cm/sec)	5.24×10^{5}
Low-Frequency Dielectric Constant	12.90
High-Frequency Dielectric Constant	10.92

Valley Dependent Parameters

Parameter	Γ	L	X
Effective Mass (m^*/m_o)	0.063	0.23	0.43
Nonparabolicity (eV^{-1})	0.69 (β=0.85)	0.65	0.36
Energy Band Gap (eV) (relative to valence band)	1.4255	1.706	1.89848
Valley Separation (eV)	---	0.2845	0.476
Optical Phonon Energy (eV)	---	0.0343	0.0343
Number of Equivalent Valley	1	4	3
Intervalley Deformation Potential (eV/cm)			
from Γ	0	1×10^{9}	1×10^{9}
from X	1×10^{9}	9×10^{8}	9×10^{8}
from L	1×10^{9}	1×10^{9}	9×10^{8}
Intervalley Phonon Energy			
from Γ	0.0	0.03	0.0299
from X	0.0299	0.0293	0.0299
from L	0.03	0.029	0.0293

Table II

AlGaAs

Bulk Material Parameters

Parameter	Value
Lattice Constant (cm)	5.653×10^{-8}
Longitudinal Phonon Energy (eV)	0.038
Sound Velocity (cm/sec)	5.426×10^{5}
Low Frequency Dielectric Constant	11.90
High Frequency Dielectric Constant	10.05

Valley Dependent Parameters

Paramter	Γ	L	X
Effective Mass (m^*/m_o)	0.086	0.233	0.411
Nonparabolicity (eV^{-1})	0.550	0.624	0.325
Energy Band Gap (eV)	1.822	1.9385	1.961
(relative to valence band)			
Valley Separation (eV)	0.0	0.117	0.139
Optical Phonon Energy (eV)	---	0.0385	0.0385
Number of Equivalent Valley	1	4	3
Intervalley Deformation			
Potential (eV/cm)			
from Γ	0.0	8.4×10^{8}	1×10^{9}
from X	1×10^{9}	9×10^{8}	9.32×10^{8}
from L	8.4×10^{8}	8.4×10^{8}	9×10^{8}
Intervalley Phonon Energy			
from Γ	0.0	0.0343	0.0355
from X	0.0355	0.0351	0.0355
from L	0.0343	0.0338	0.0351

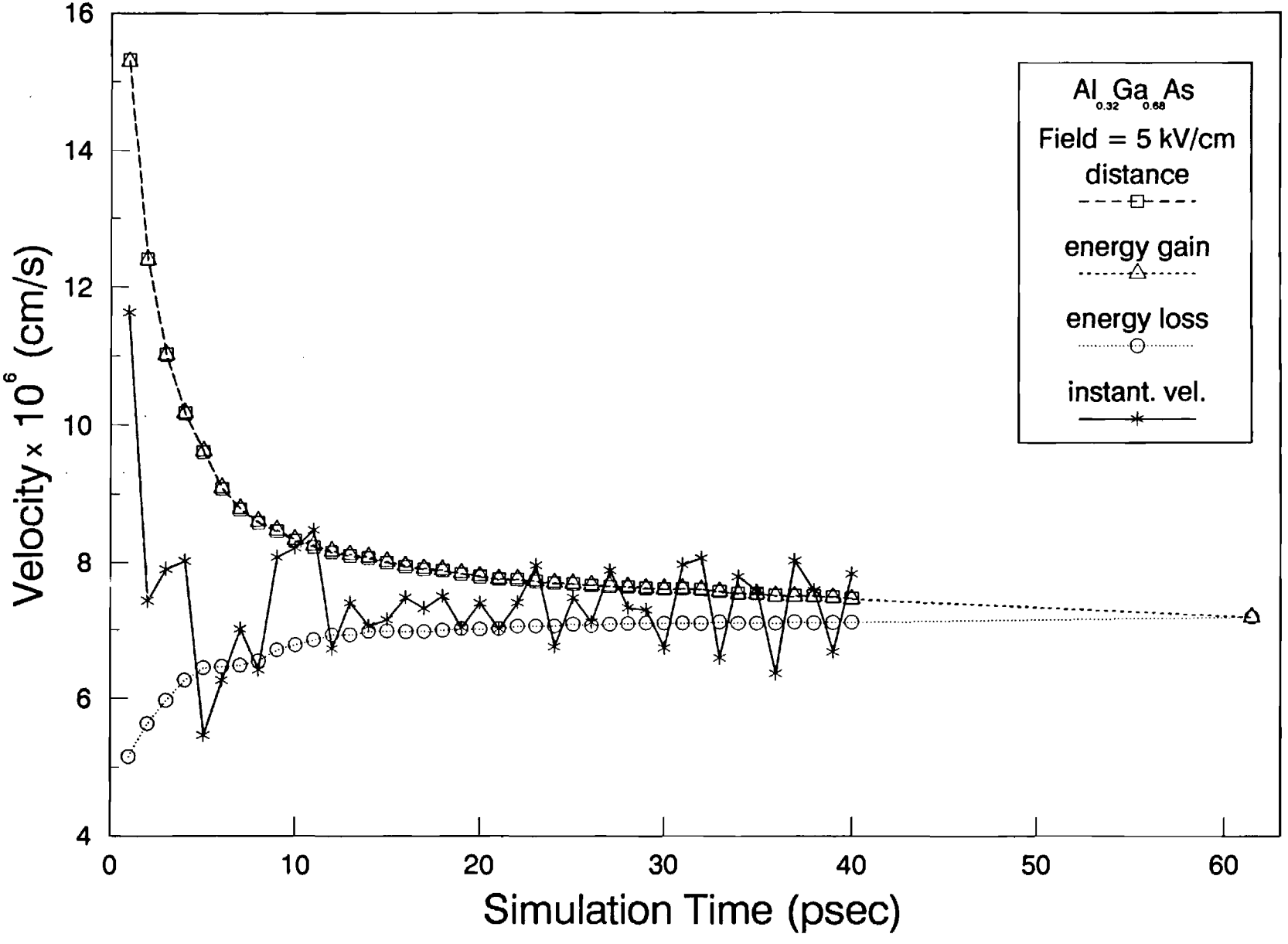
Al 0.32 Ga 0.68 As
Field = 5 kV/cm
distance
energy gain
energy loss
instant. vel.
Velocity x 10^6 (cm/s)
Simulation Time (psec)
16
14
12
10
8
6
4
0
10
20
30
40
50
60

Fig. 1

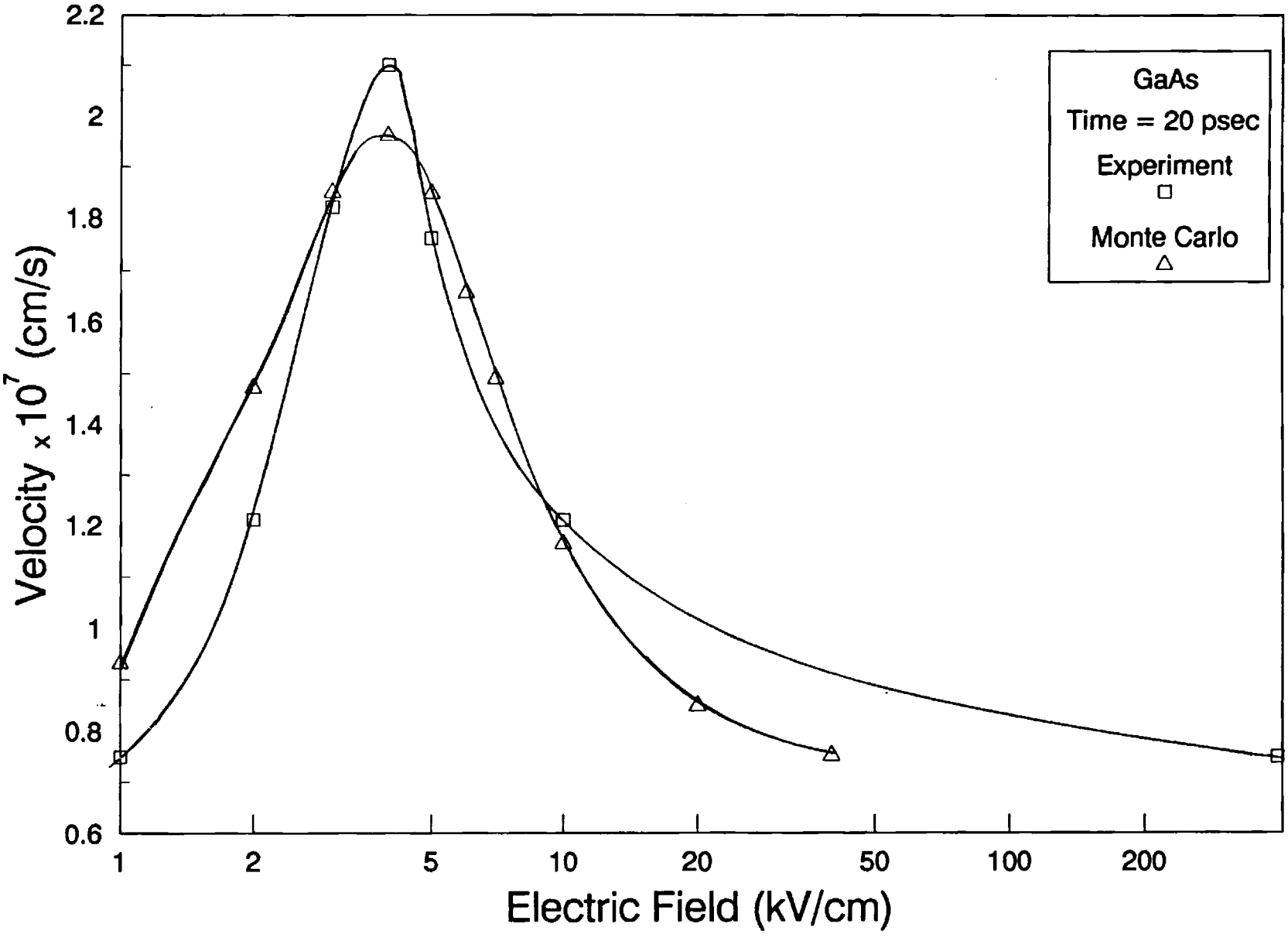
GaAs
Time = 20 psec
Experiment
Monte Carlo
Velocity x10^7 (cm/s)
2.2
2
1.8
1.6
1.4
1.2
1
0.8
0.6
1
2
5
10
20
50
100
200
Electric Field (kV/cm)

Fig. 2

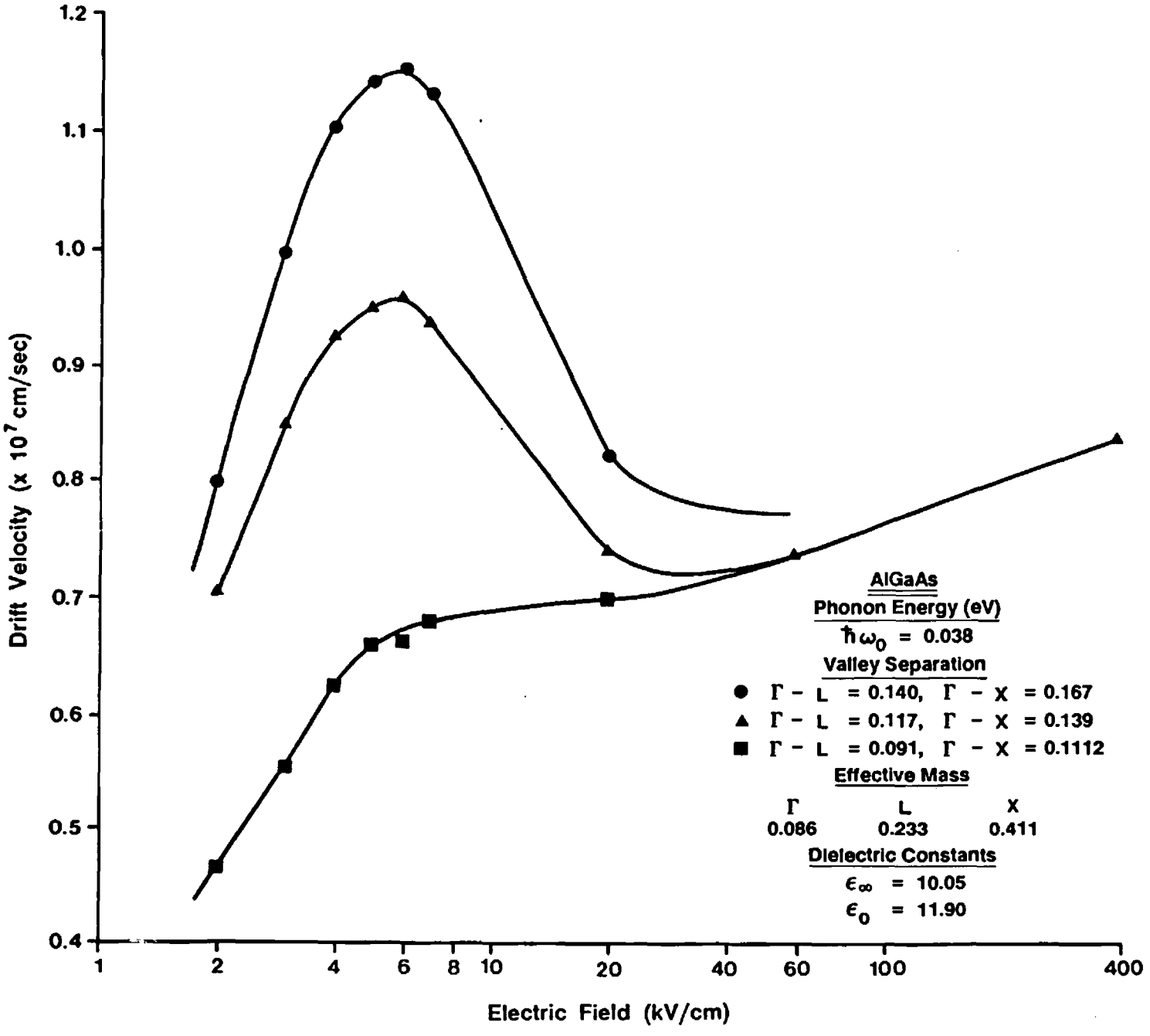
Drift Velocity (x 10^7 cm/sec)
1.2
1.1
1.0
0.9
0.8
0.7
0.6
0.5
0.4
1
2
4
6
8
10
20
40
60
100
400
Electric Field (kV/cm)
AlGaAs
Phonon Energy (eV)
ħω0 = 0.038
Valley Separation
● Γ - L = 0.140, Γ - X = 0.167
▲ Γ - L = 0.117, Γ - X = 0.139
■ Γ - L = 0.091, Γ - X = 0.1112
Effective Mass
Γ L X
0.086 0.233 0.411
Dielectric Constants
ε∞ = 10.05
ε0 = 11.90

Fig 3

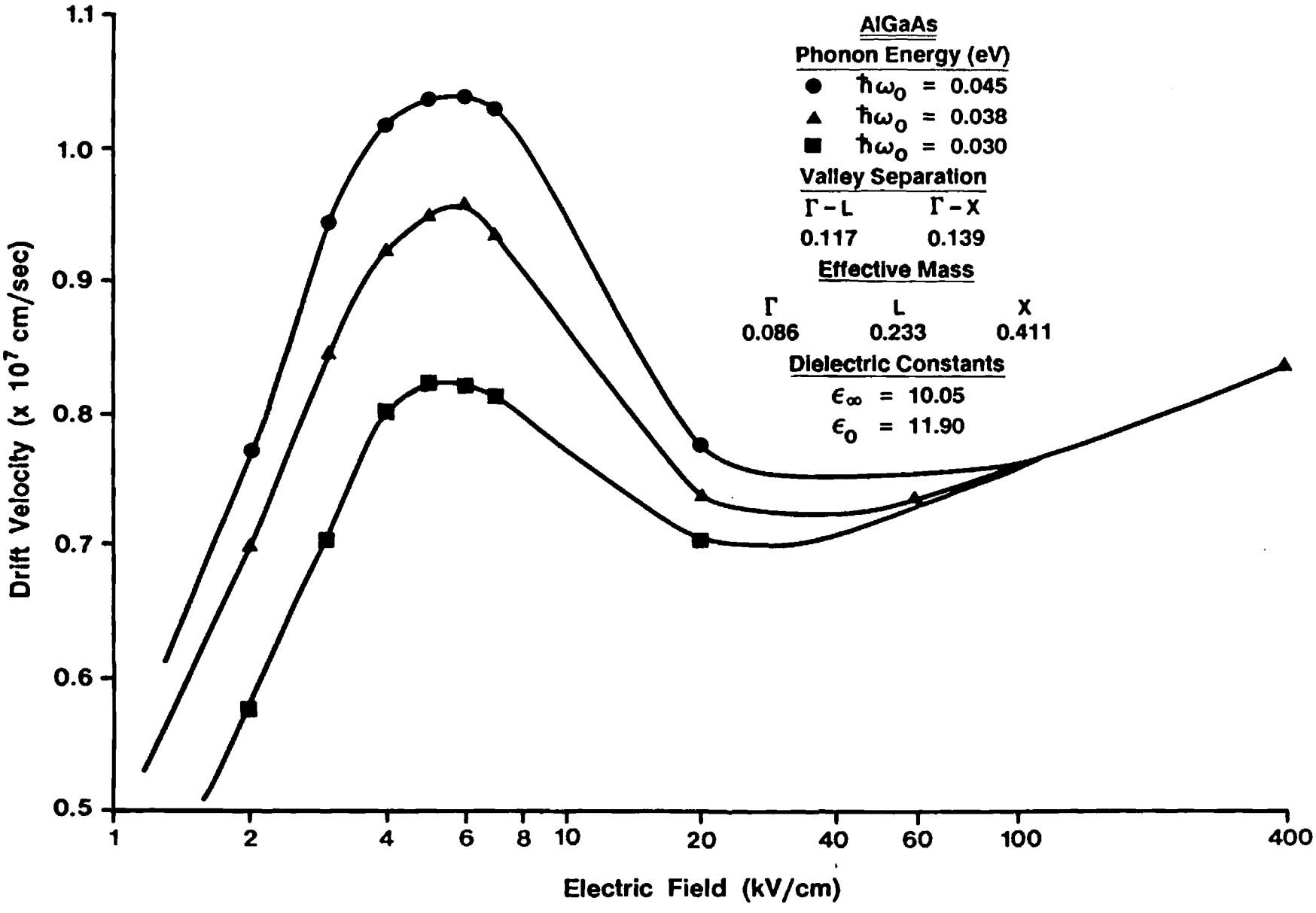
AlGaAs
Phonon Energy (eV)
● $\hbar\omega_0$ = 0.045
▲ $\hbar\omega_0$ = 0.038
■ $\hbar\omega_0$ = 0.030
Valley Separation
Γ - L Γ - X
0.117 0.139
Effective Mass
Γ L X
0.086 0.233 0.411
Dielectric Constants
ϵ_∞ = 10.05
ϵ_0 = 11.90
Drift Velocity (x 10^7 cm/sec)
1.1
1.0
0.9
0.8
0.7
0.6
0.5
1
2
4
6
8
10
20
40
60
100
400
Electric Field (kV/cm)

Fig. 4

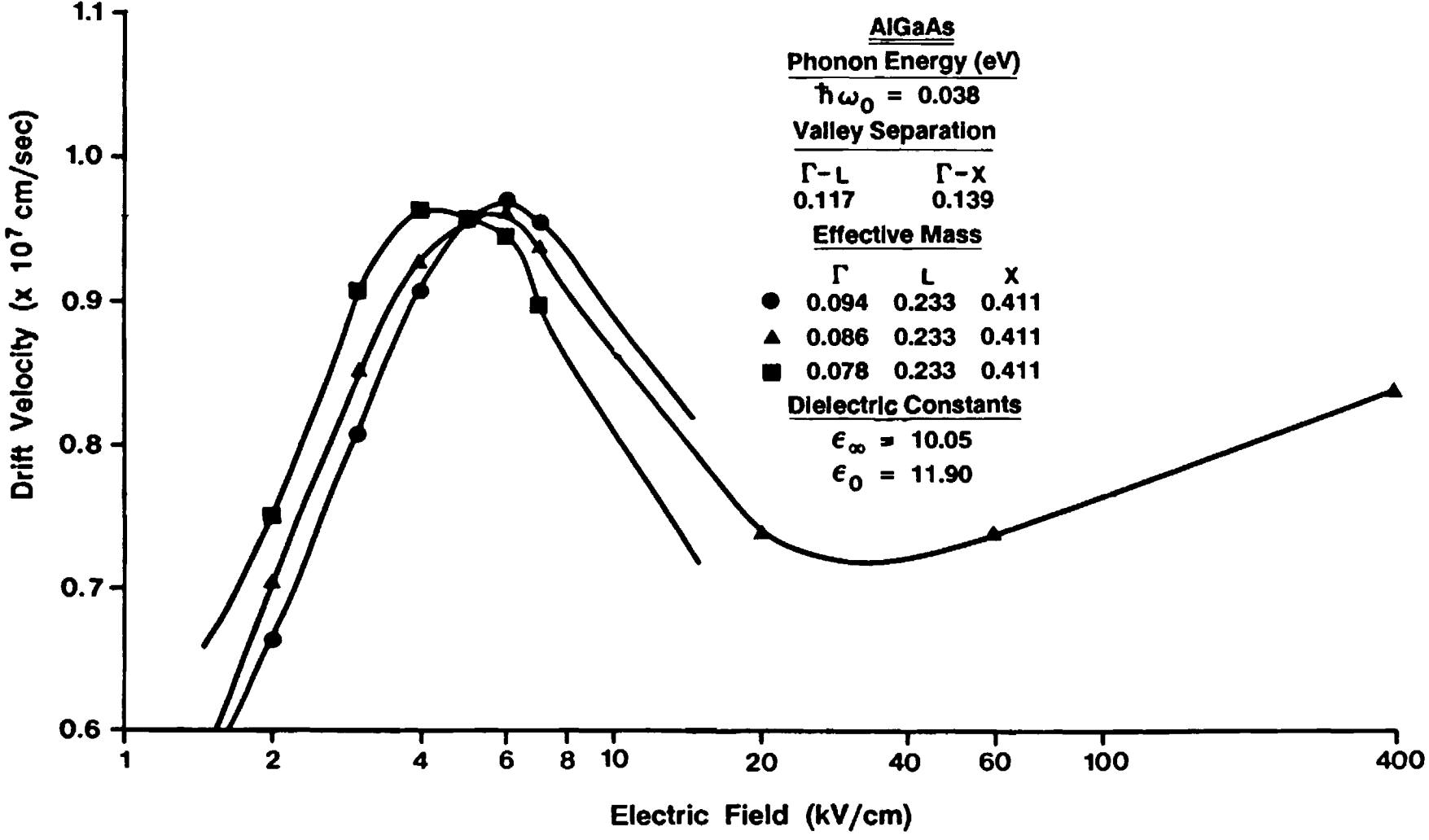
AlGaAs
Phonon Energy (eV)
$\hbar\omega_0$ = 0.038
Valley Separation
Γ-L 0.117
Γ-X 0.139
Effective Mass
Γ L X
● 0.094 0.233 0.411
▲ 0.086 0.233 0.411
■ 0.078 0.233 0.411
Dielectric Constants
ϵ_∞ = 10.05
ϵ_0 = 11.90
Drift Velocity (x 10^7 cm/sec)
1.1
1.0
0.9
0.8
0.7
0.6
1
2
4
6
8
10
20
40
60
100
400
Electric Field (kV/cm)

Fig. 5

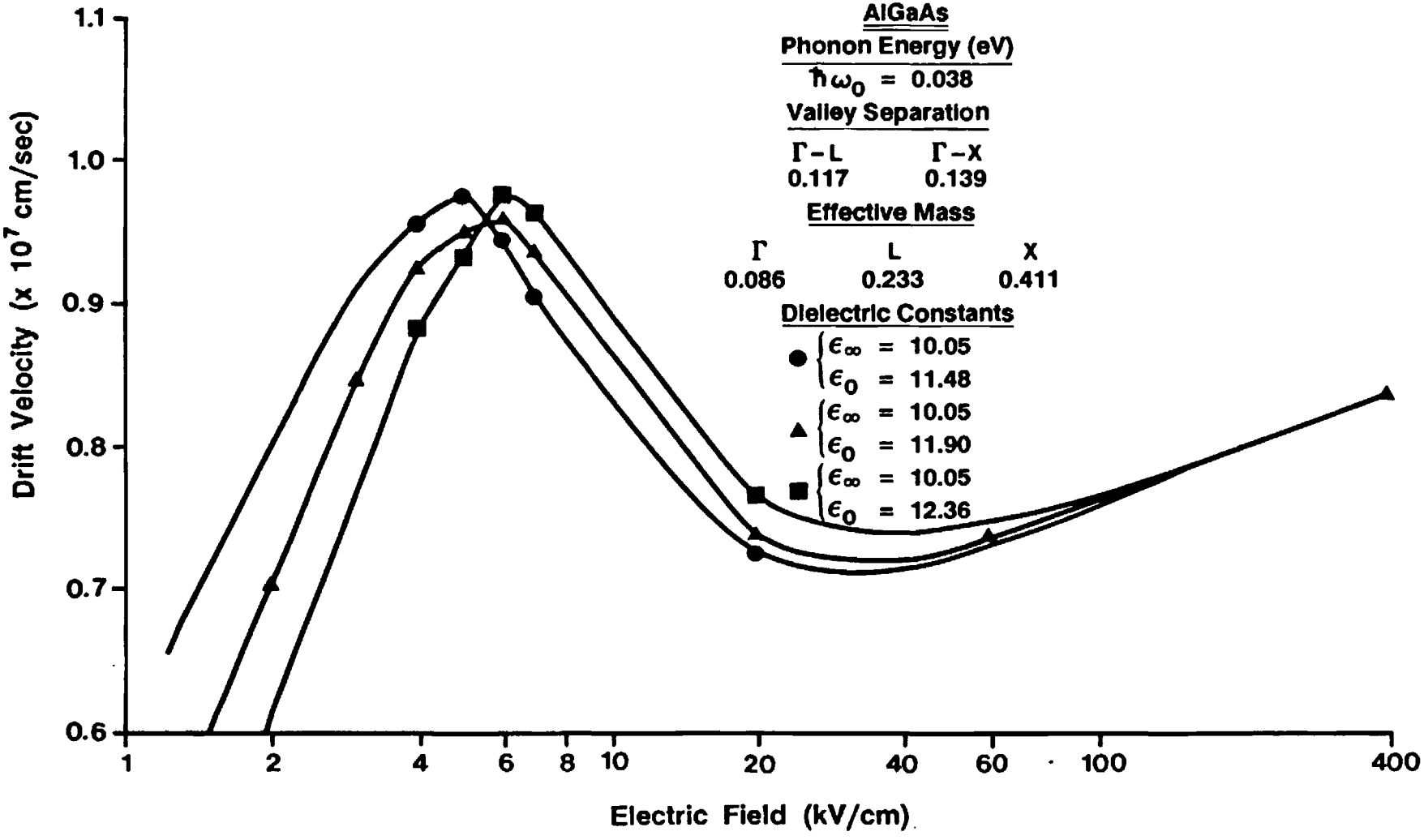
AlGaAs
Phonon Energy (eV)
$\hbar\omega_0$ = 0.038
Valley Separation
Γ-L 0.117
Γ-X 0.139
Effective Mass
Γ 0.086
L 0.233
X 0.411
Dielectric Constants
● ϵ_∞ = 10.05, ϵ_0 = 11.48
▲ ϵ_∞ = 10.05, ϵ_0 = 11.90
■ ϵ_∞ = 10.05, ϵ_0 = 12.36
Drift Velocity (x 10^7 cm/sec)
1.1
1.0
0.9
0.8
0.7
0.6
1
2
4
6
8
10
20
40
60
100
400
Electric Field (kV/cm)

Fig. 6

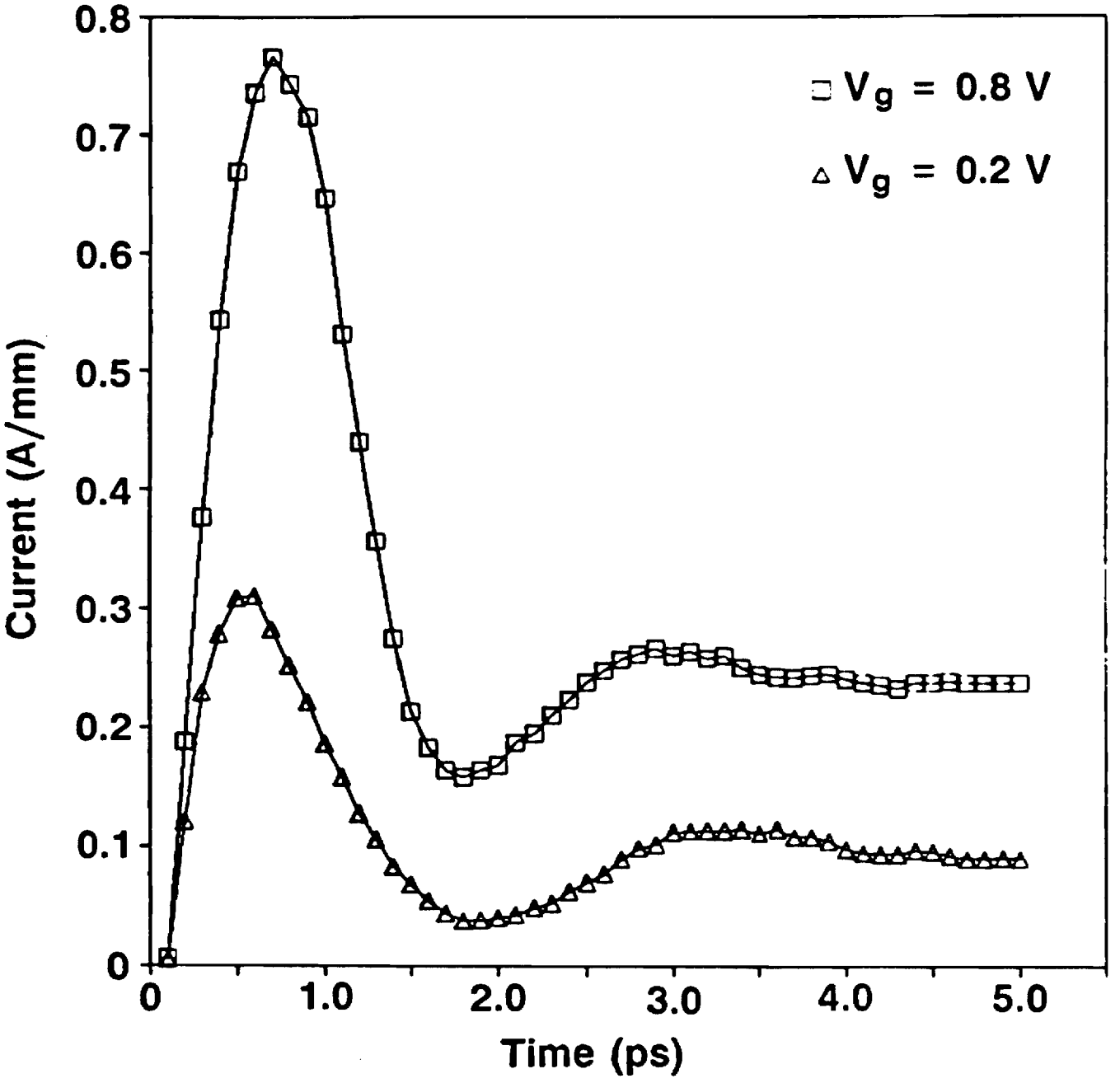
0.8
0.7
0.6
0.5
0.4
0.3
0.2
0.1
0
Current (A/mm)
□ V_g = 0.8 V
△ V_g = 0.2 V
0
1.0
2.0
3.0
4.0
5.0
Time (ps)

Fig. 7

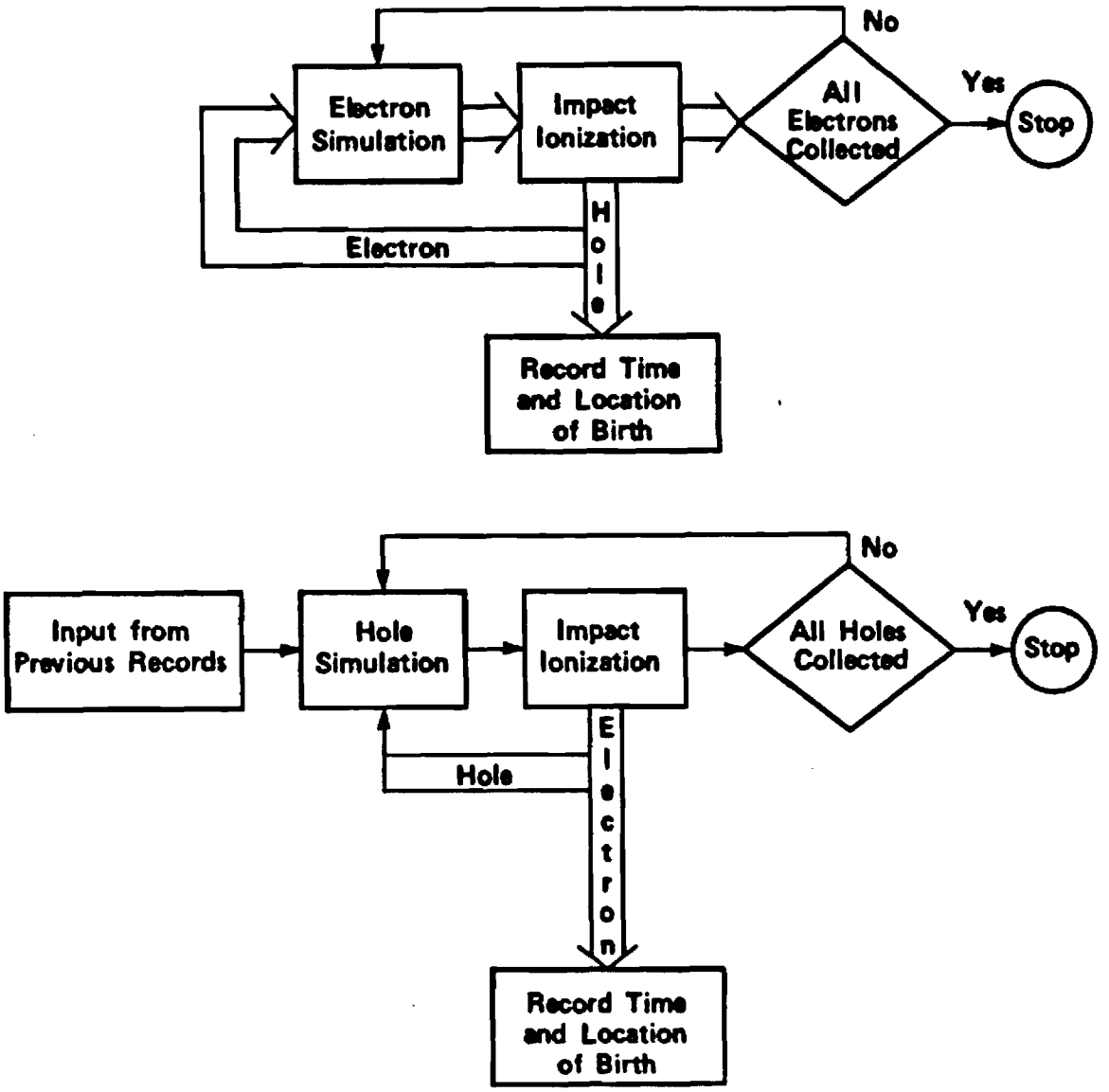
No
Electron Simulation
Impact Ionization
All Electrons Collected
Yes
Stop
Hole
Electron
Record Time and Location of Birth
No
Input from Previous Records
Hole Simulation
Impact Ionization
All Holes Collected
Yes
Stop
Hole
Electron
Record Time and Location of Birth

Fig. 8

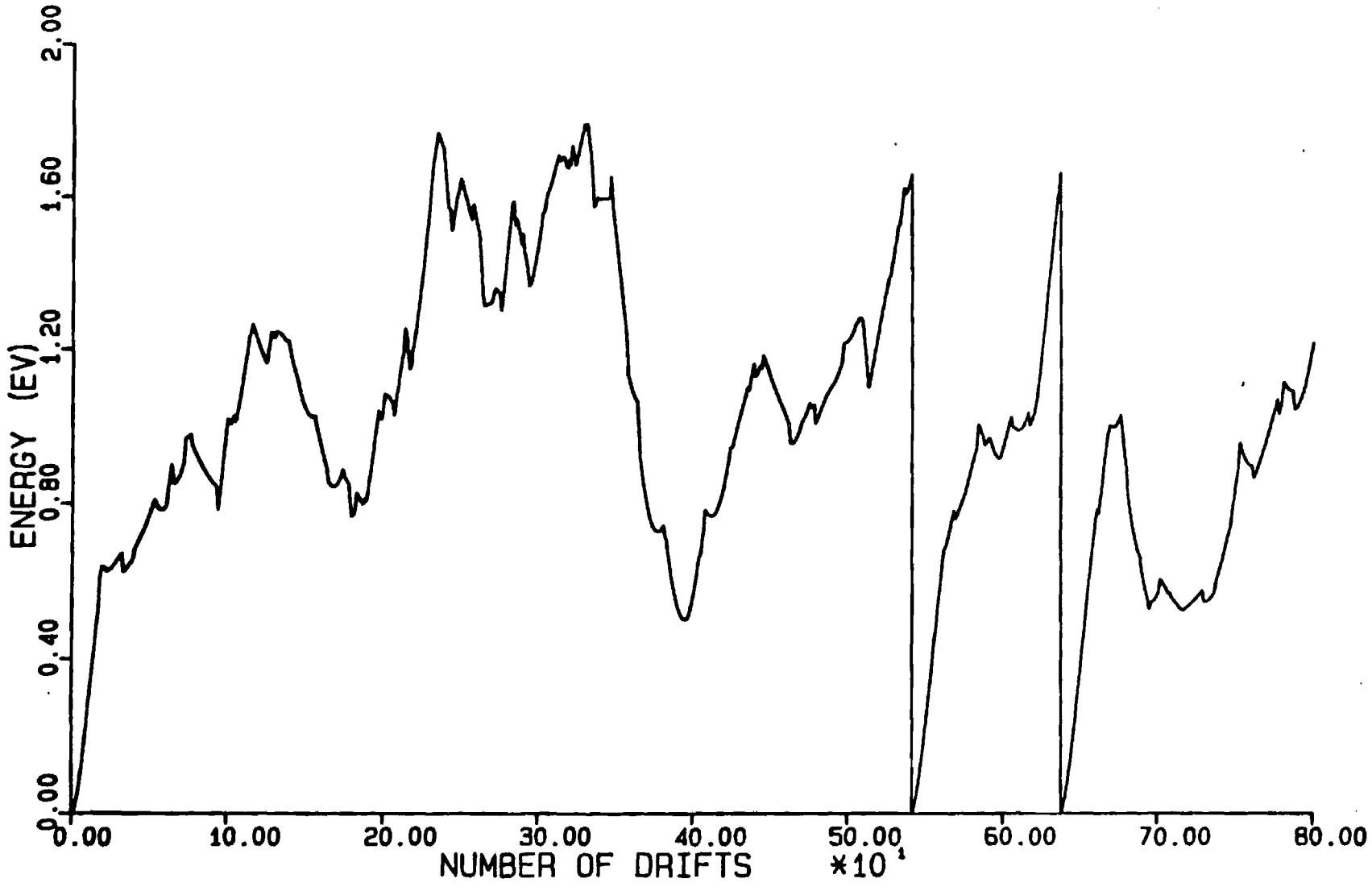
ENERGY (EV)
0.00
0.40
0.80
1.20
1.60
2.00
0.00
10.00
20.00
30.00
40.00
50.00
60.00
70.00
80.00
NUMBER OF DRIFTS
*10 1

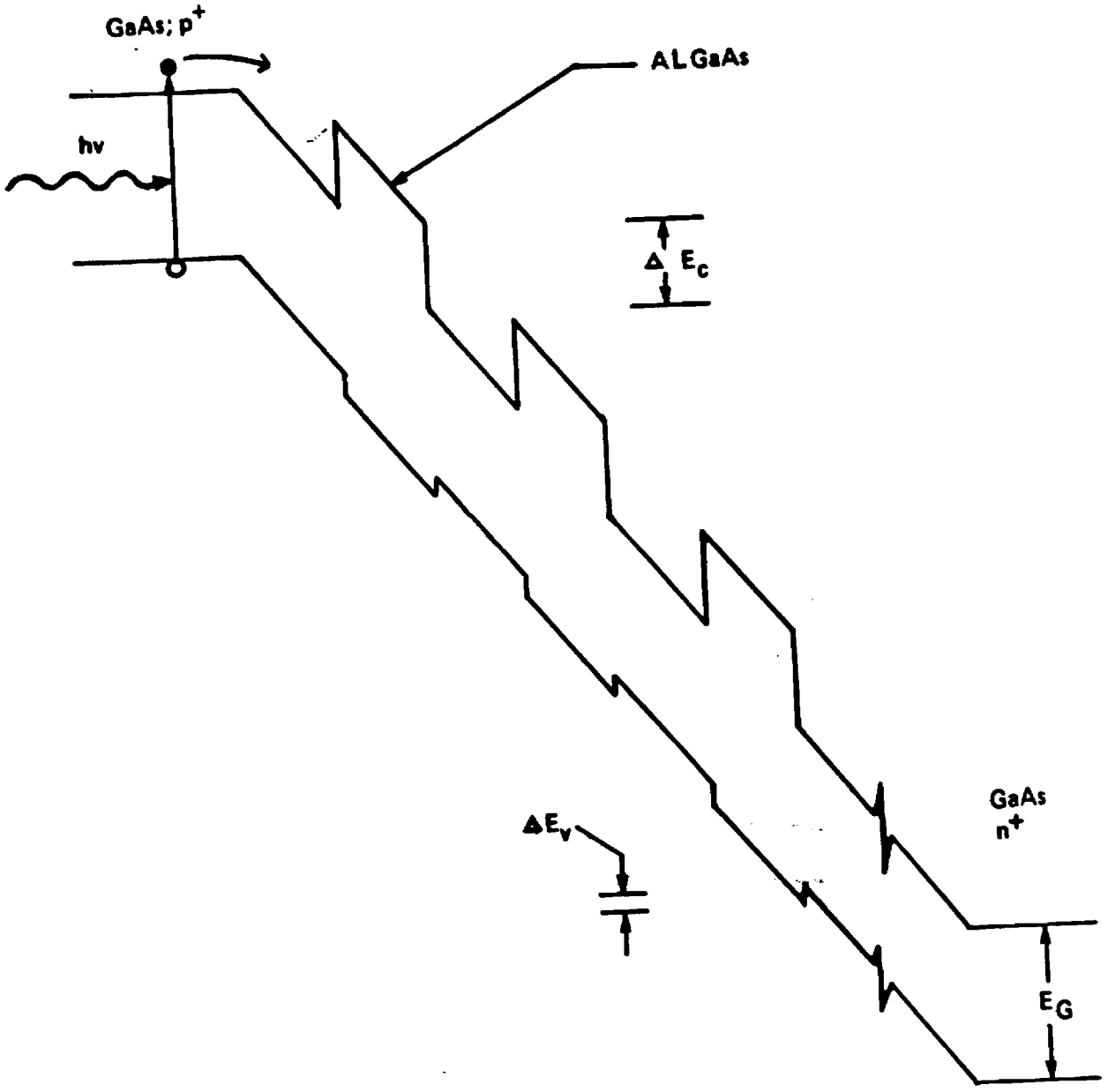

Fig 10

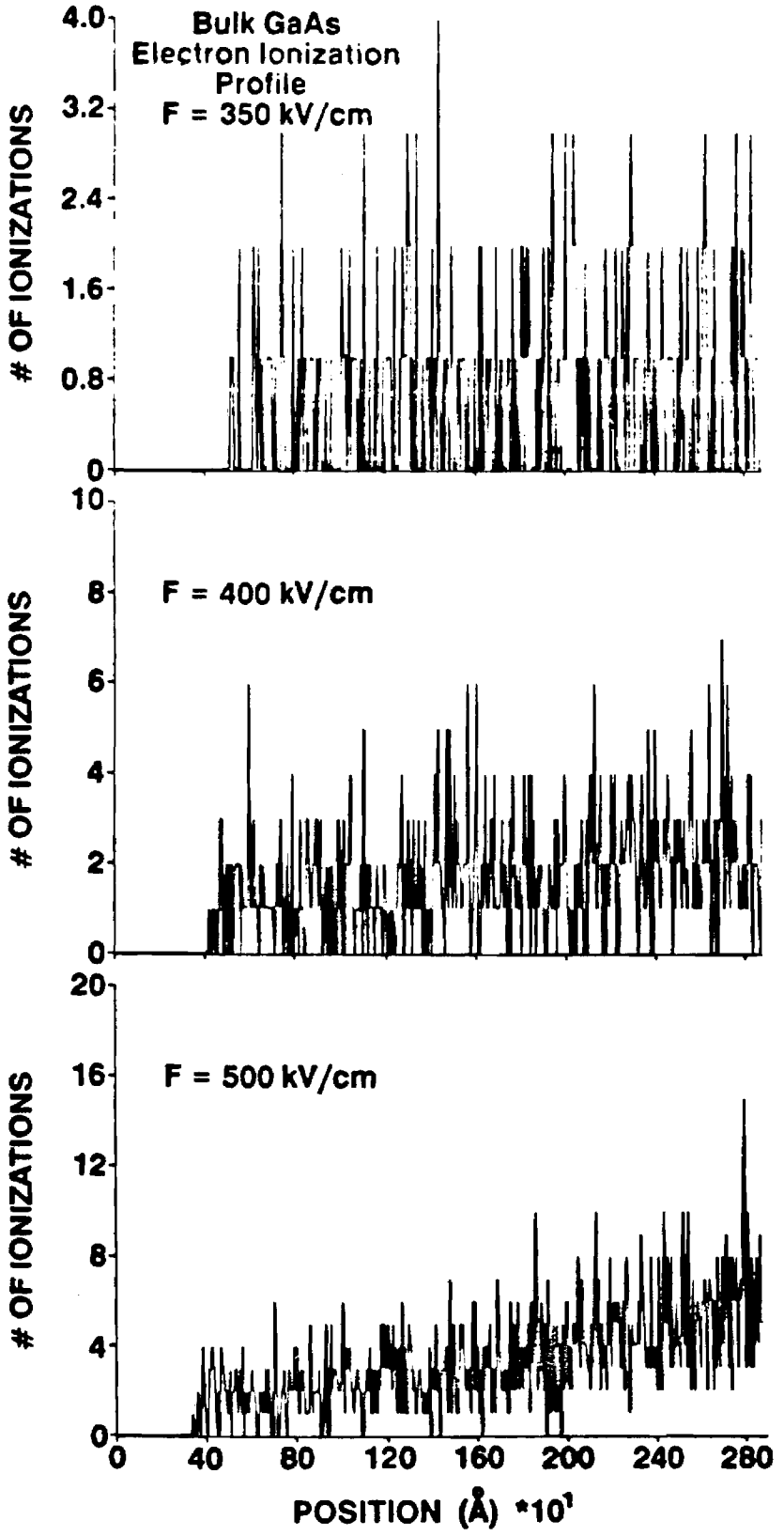
Bulk GaAs
Electron Ionization
Profile
F = 350 kV/cm
F = 400 kV/cm
F = 500 kV/cm
# OF IONIZATIONS
# OF IONIZATIONS
# OF IONIZATIONS
4.0
3.2
2.4
1.6
0.8
0
10
8
6
4
2
0
20
16
12
8
4
0
0
40
80
120
160
200
240
280
POSITION (Å) *10¹

Fig. 11

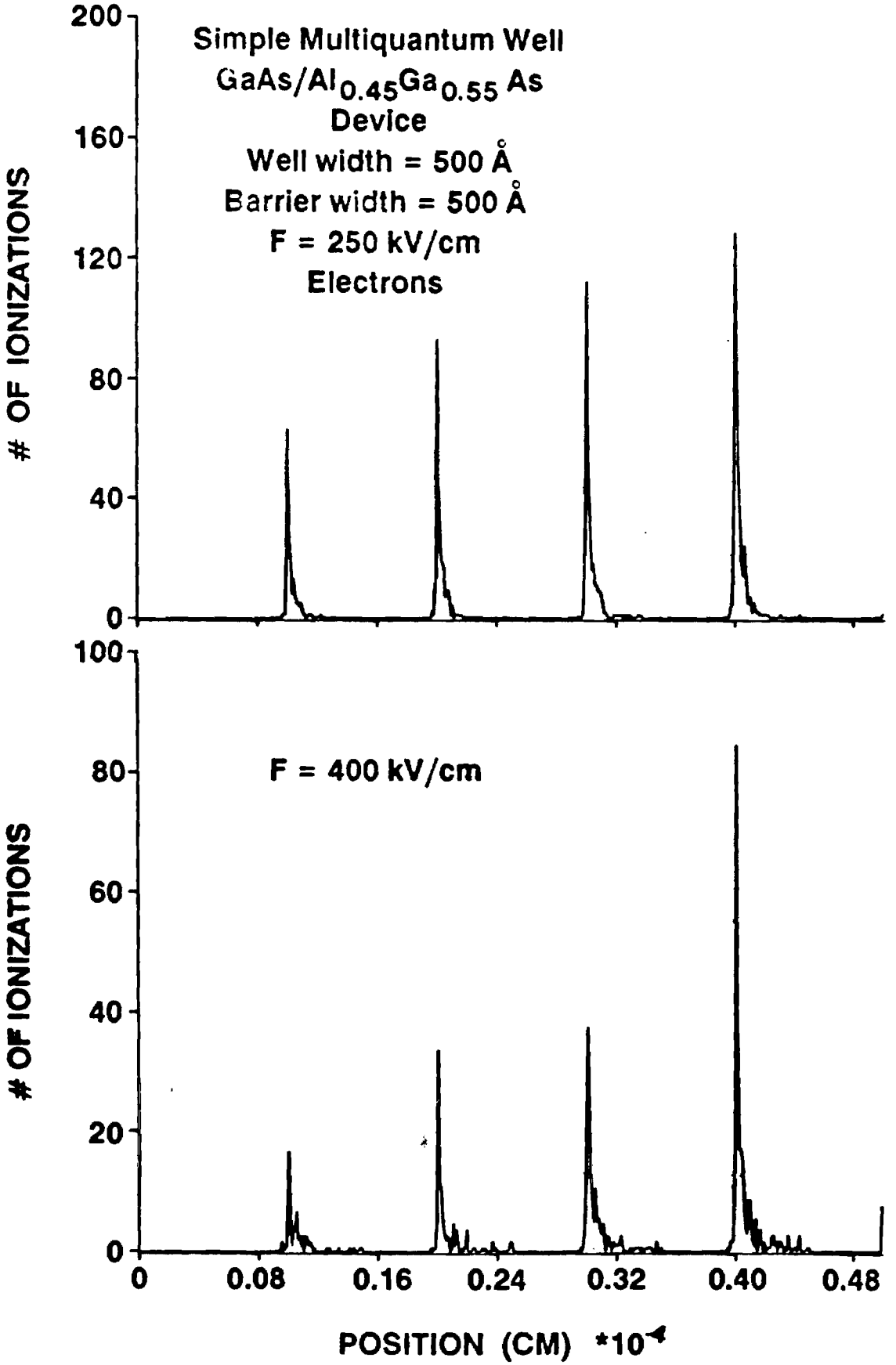
Simple Multiquantum Well
GaAs/Al0.45Ga0.55 As
Device
Well width = 500 Å
Barrier width = 500 Å
F = 250 kV/cm
Electrons
OF IONIZATIONS
200
160
120
80
40
0
F = 400 kV/cm
# OF IONIZATIONS
100
80
60
40
20
0
0
0.08
0.16
0.24
0.32
0.40
0.48
POSITION (CM) *10-4

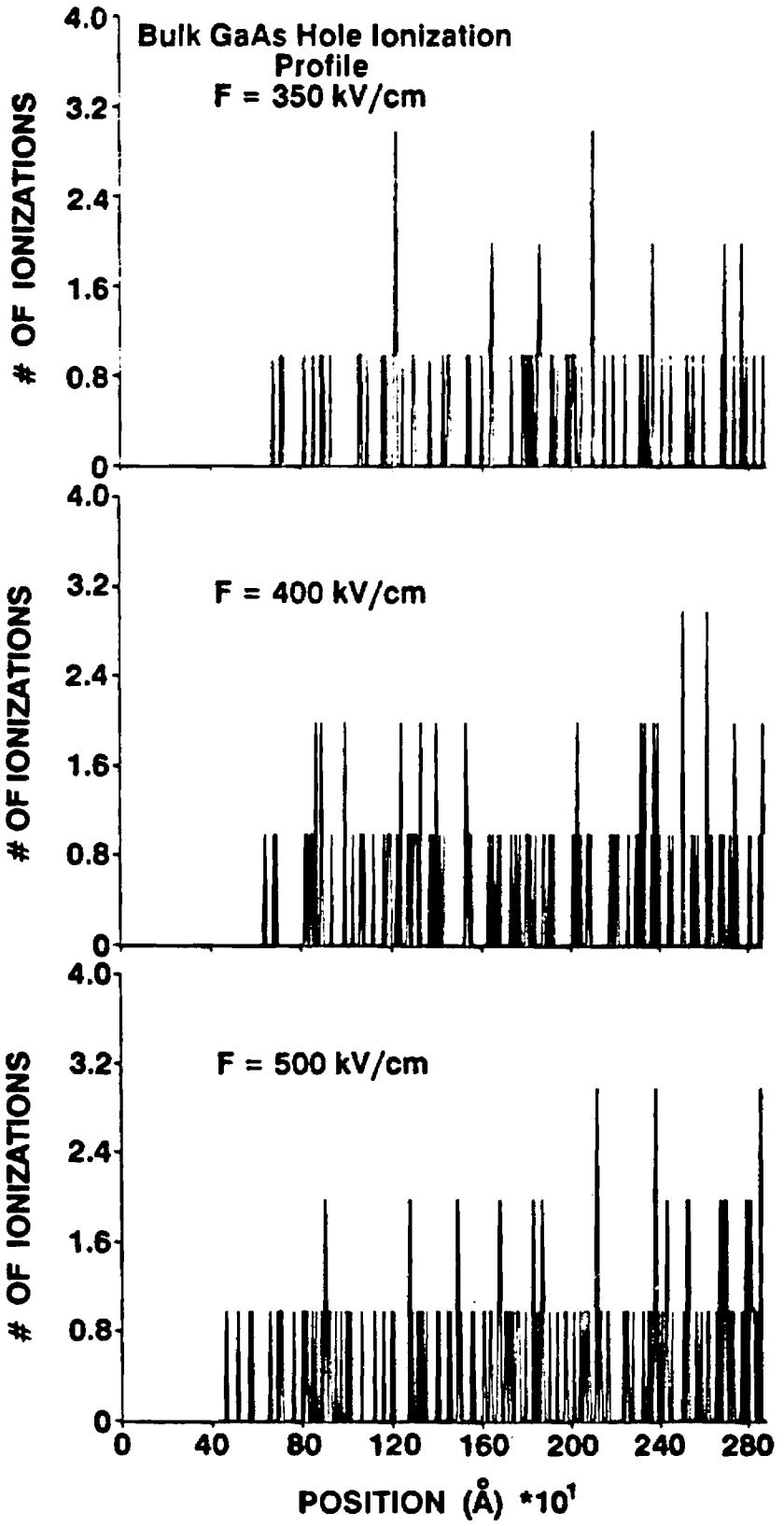
Bulk GaAs Hole Ionization Profile
F = 350 kV/cm
F = 400 kV/cm
F = 500 kV/cm
# OF IONIZATIONS
# OF IONIZATIONS
# OF IONIZATIONS
4.0
3.2
2.4
1.6
0.8
0
0
40
80
120
160
200
240
280
POSITION (Å) *10¹

Fig. 13

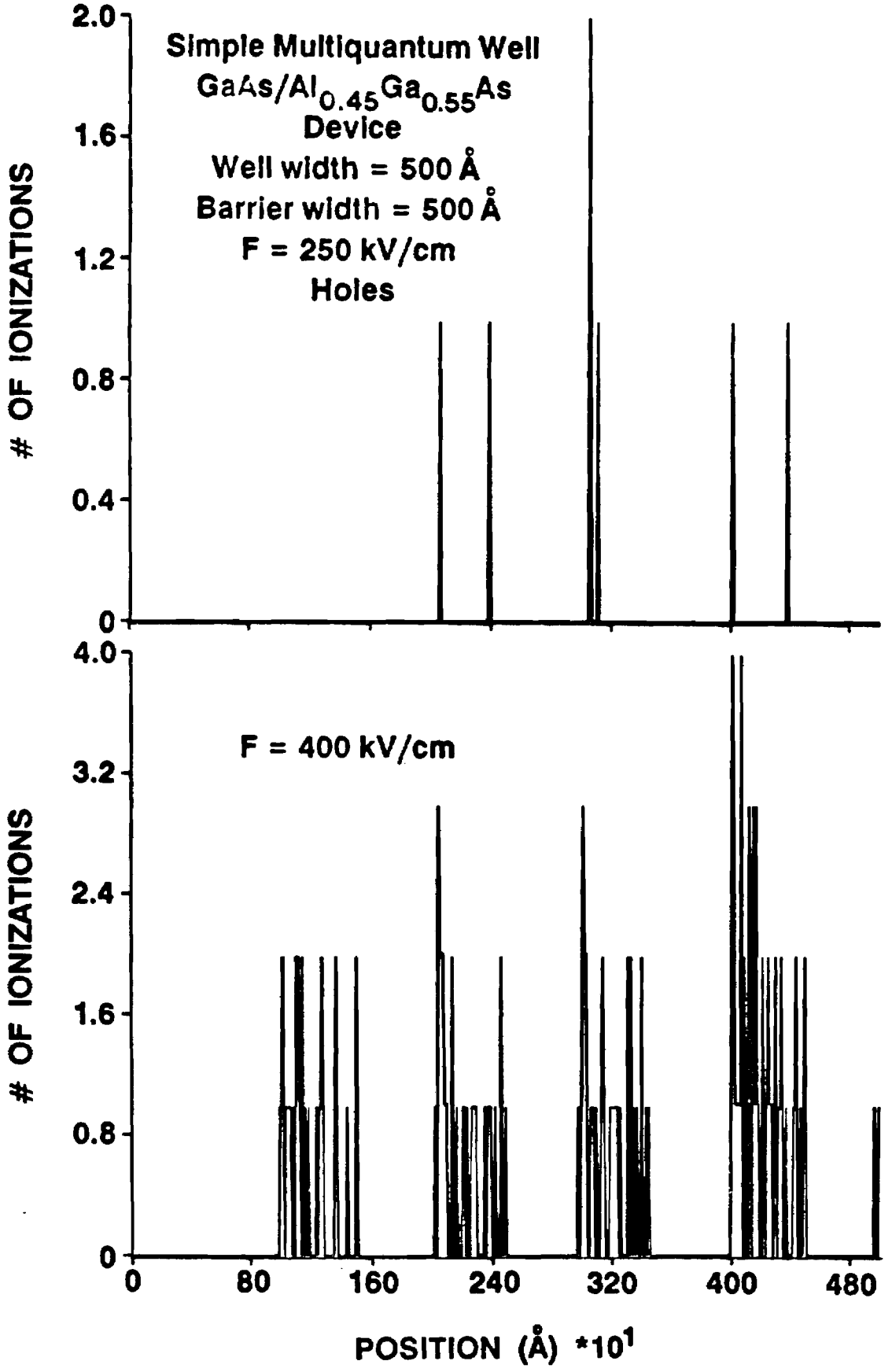
Simple Multiquantum Well
GaAs/Al0.45Ga0.55As
Device
Well width = 500 Å
Barrier width = 500 Å
F = 250 kV/cm
Holes
F = 400 kV/cm
# OF IONIZATIONS
# OF IONIZATIONS
2.0
1.6
1.2
0.8
0.4
0
4.0
3.2
2.4
1.6
0.8
0
0
80
160
240
320
400
480
POSITION (Å) *10¹

Fig. 14

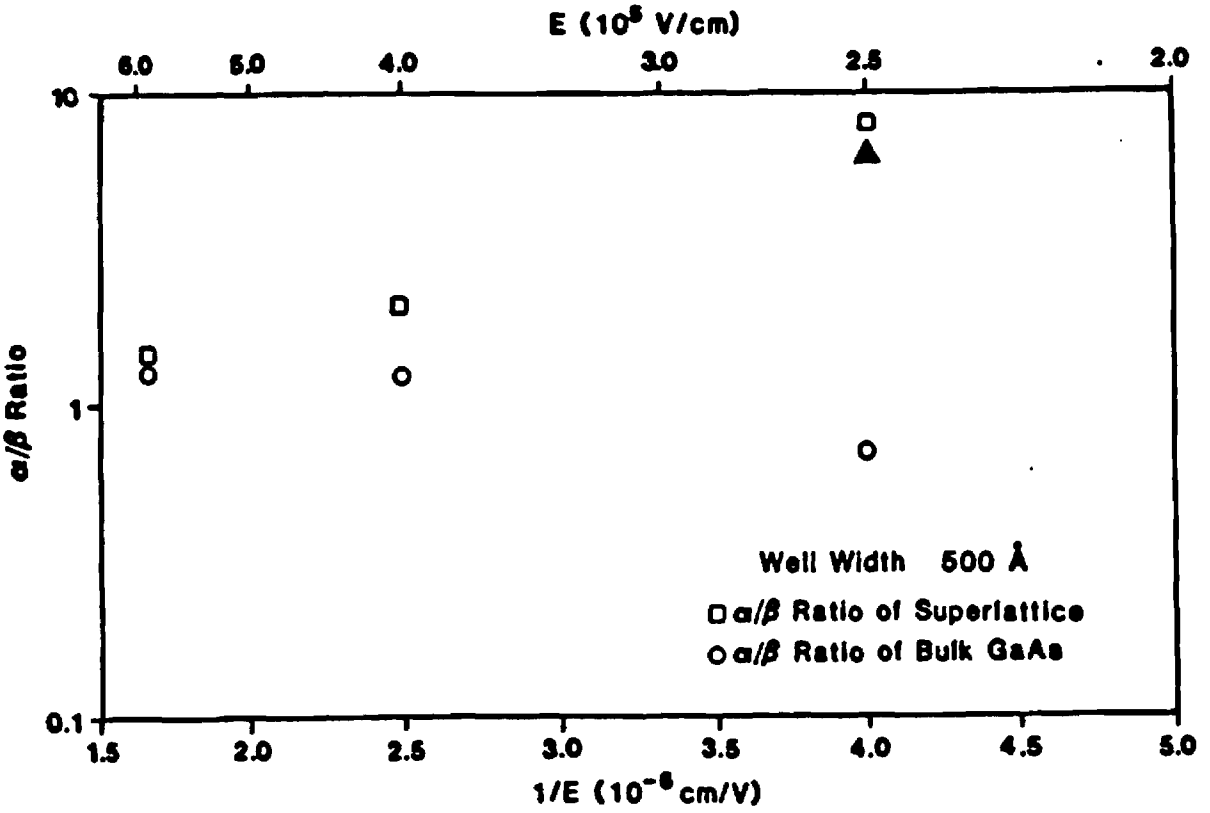
E (10^5 V/cm)
6.0
5.0
4.0
3.0
2.5
2.0
10
1
0.1
α/β Ratio
Well Width 500 Å
□ α/β Ratio of Superlattice
○ α/β Ratio of Bulk GaAs
1.5
2.0
2.5
3.0
3.5
4.0
4.5
5.0
1/E (10^{-6} cm/V)

Fig. 15

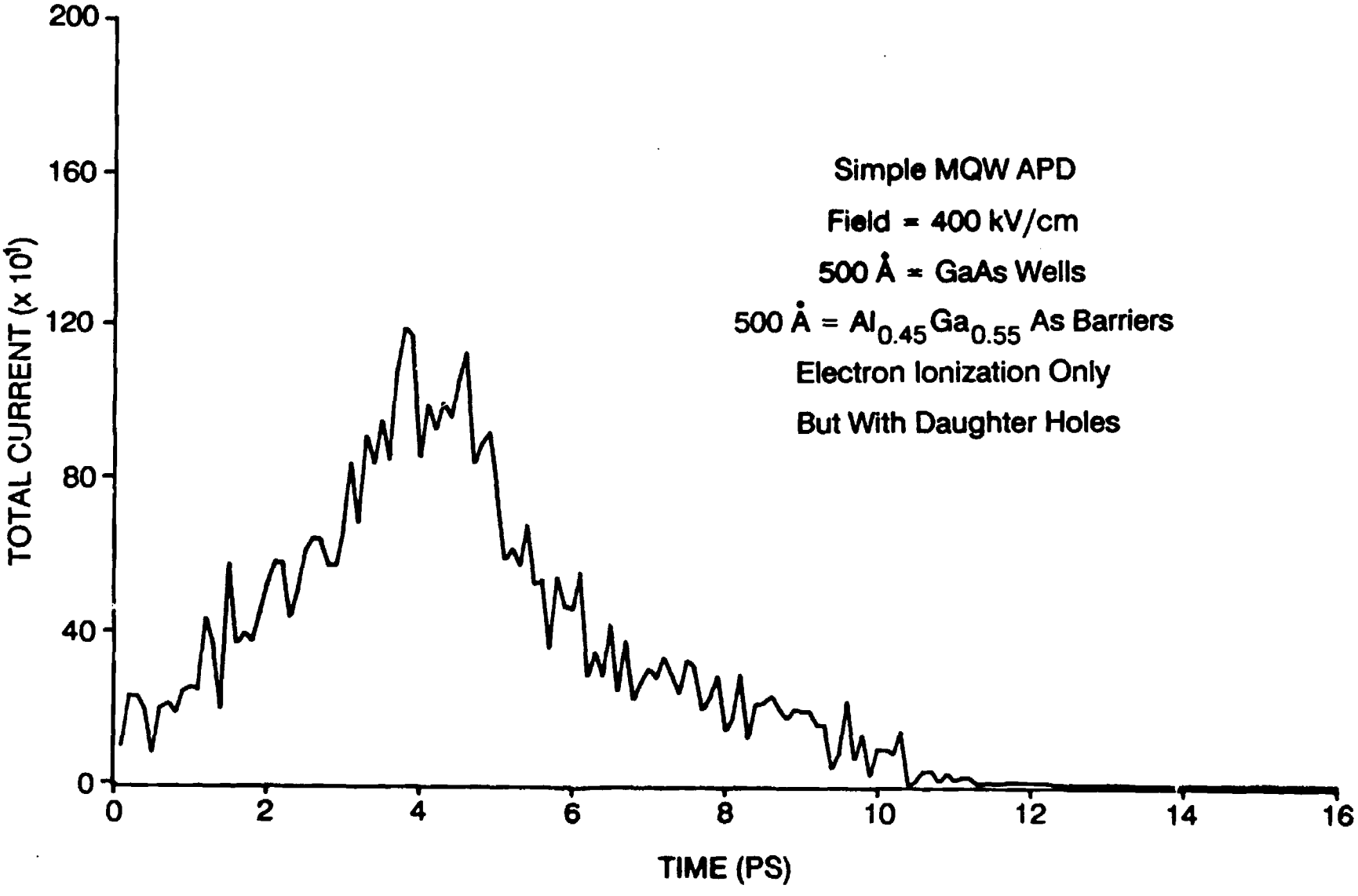
200
160
120
80
40
0
TOTAL CURRENT (x 10⁴)
0
2
4
6
8
10
12
14
16
TIME (PS)
Simple MQW APD
Field = 400 kV/cm
500 Å = GaAs Wells
500 Å = Al0.45Ga0.55 As Barriers
Electron Ionization Only
But With Daughter Holes

Fig. 16

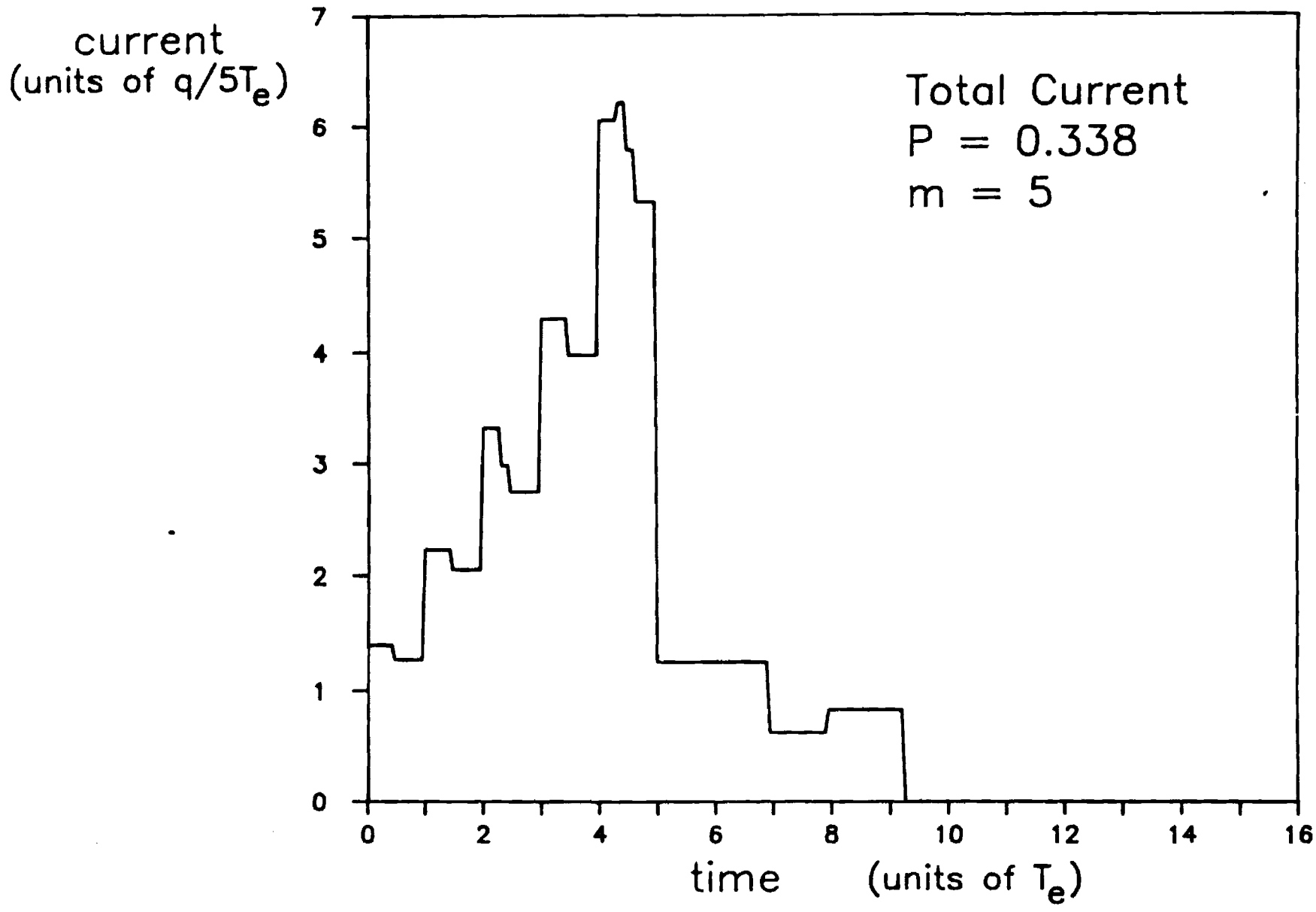
current
(units of q/5T_e)
Total Current
P = 0.338
m = 5
0
1
2
3
4
5
6
7
0
2
4
6
8
10
12
14
16
time (units of T_e)

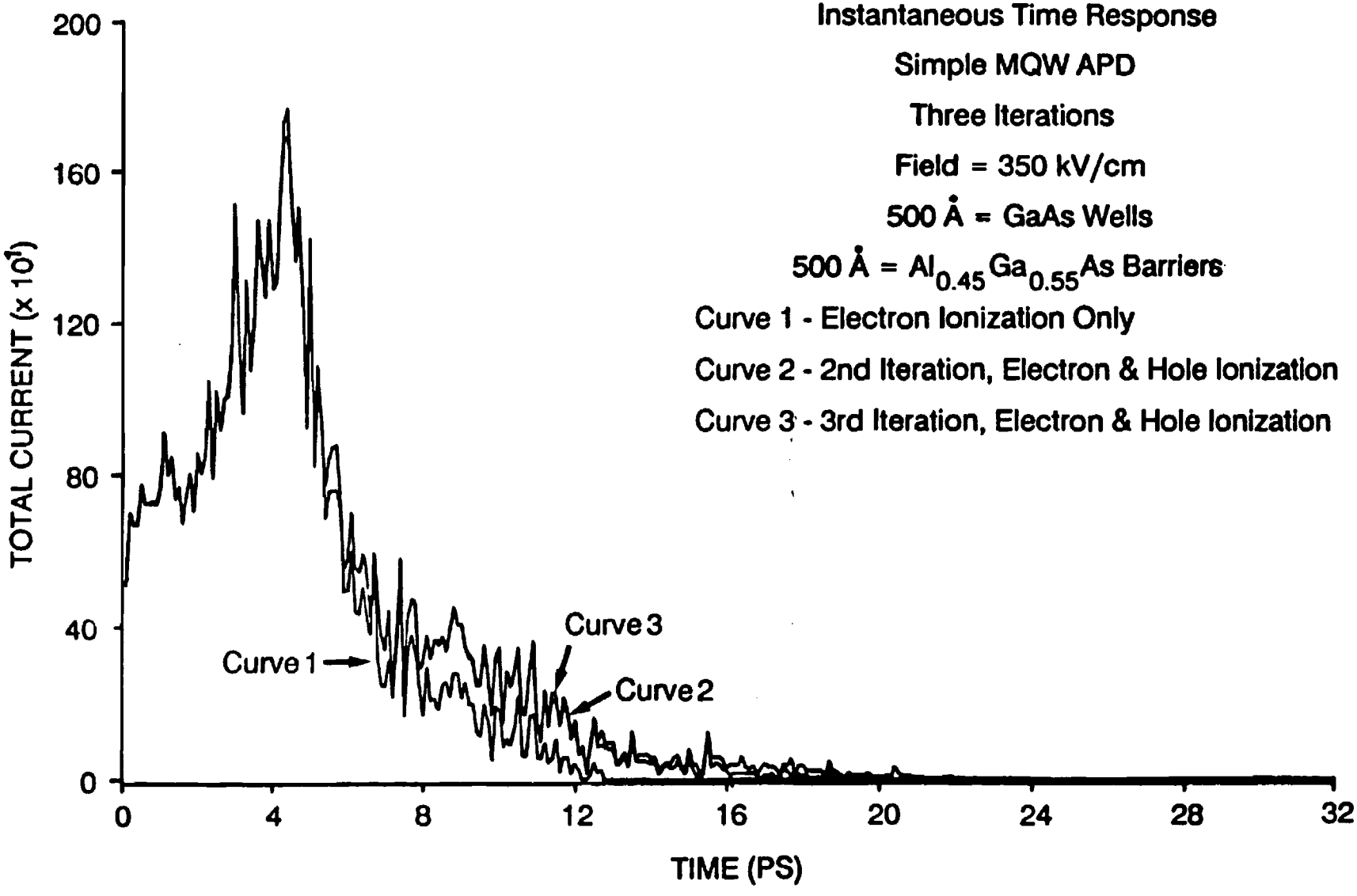
Instantaneous Time Response
Simple MQW APD
Three Iterations
Field = 350 kV/cm
500 Å = GaAs Wells
500 Å = $Al_{0.45}Ga_{0.55}As$ Barriers
Curve 1 - Electron Ionization Only
Curve 2 - 2nd Iteration, Electron & Hole Ionization
Curve 3 - 3rd Iteration, Electron & Hole Ionization
TOTAL CURRENT (x 10^1)
200
160
120
80
40
0
0
4
8
12
16
20
24
28
32
TIME (PS)
Curve 1
Curve 2
Curve 3

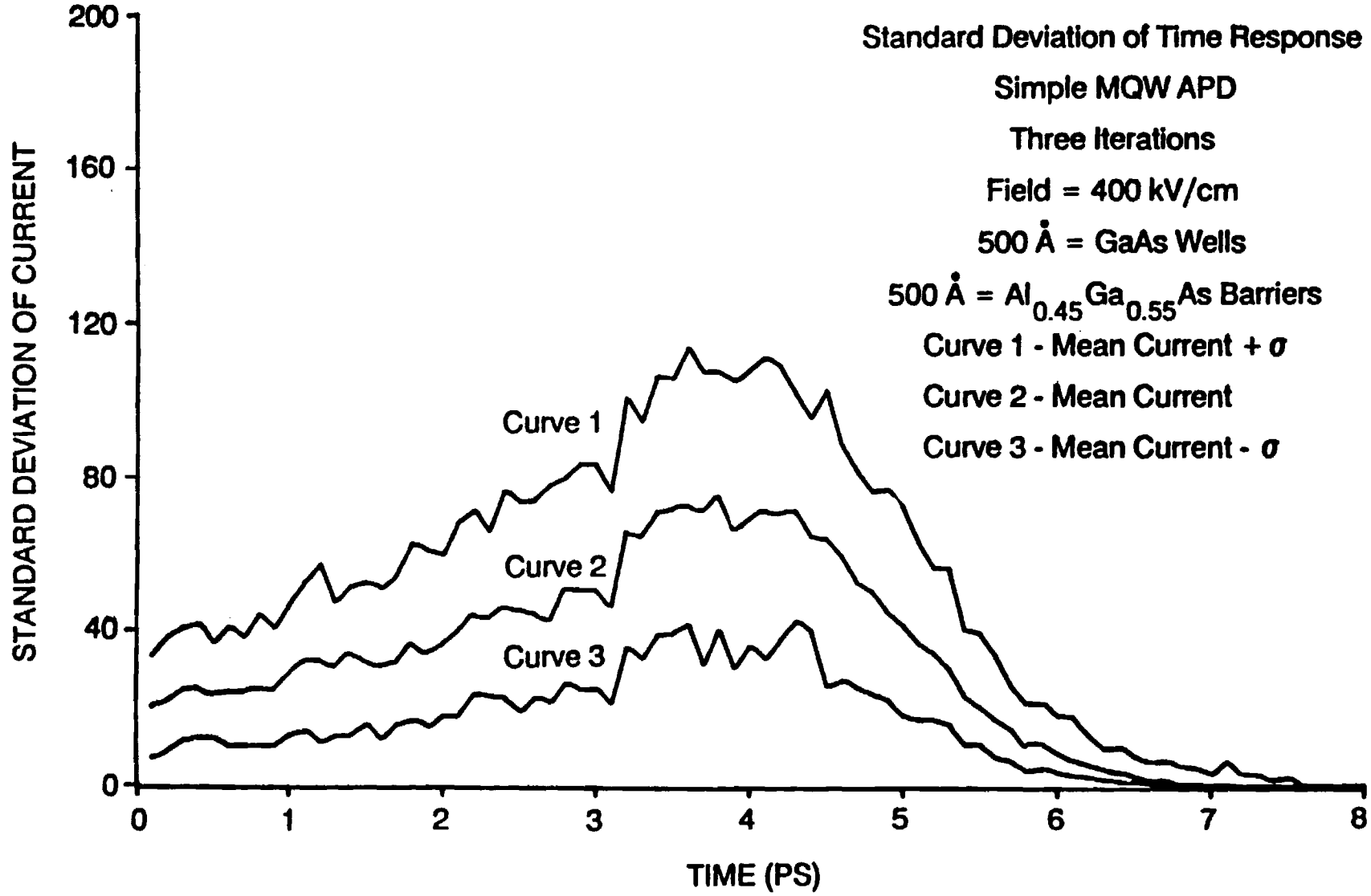
Standard Deviation of Time Response
Simple MQW APD
Three Iterations
Field = 400 kV/cm
500 Å = GaAs Wells
500 Å = $Al_{0.45}Ga_{0.55}As$ Barriers
Curve 1 - Mean Current + σ
Curve 2 - Mean Current
Curve 3 - Mean Current - σ
STANDARD DEVIATION OF CURRENT
200
160
120
80
40
0
Curve 1
Curve 2
Curve 3
0
1
2
3
4
5
6
7
8
TIME (PS)

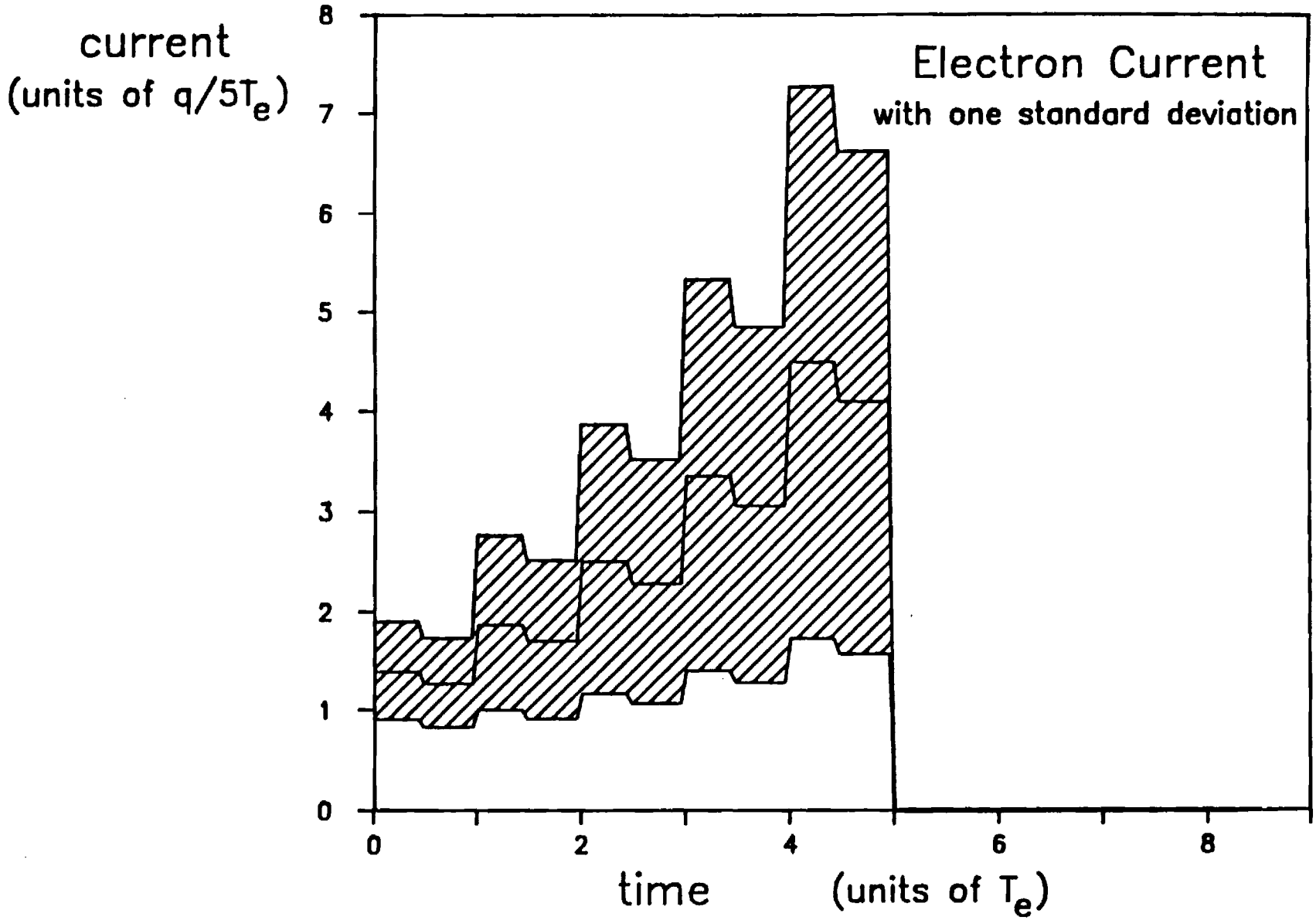
current
(units of q/5T_e)
Electron Current
with one standard deviation
8
7
6
5
4
3
2
1
0
0
2
4
6
8
time
(units of T_e)

Fig 20

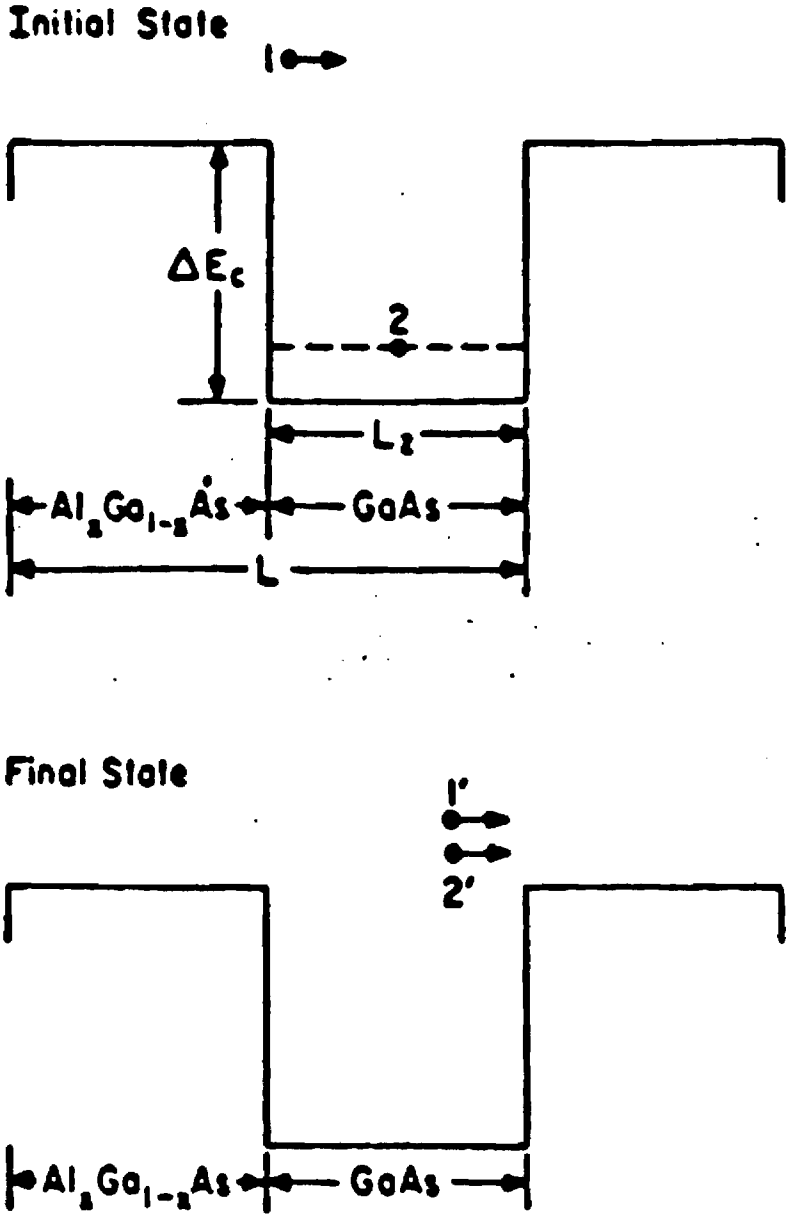
Initial State
1
ΔEc
2
Lz
Al$_z$Ga$_{1-z}$As
GaAs
L
Final State
1'
2'
Al$_z$Ga$_{1-z}$As
GaAs

Fig. 21

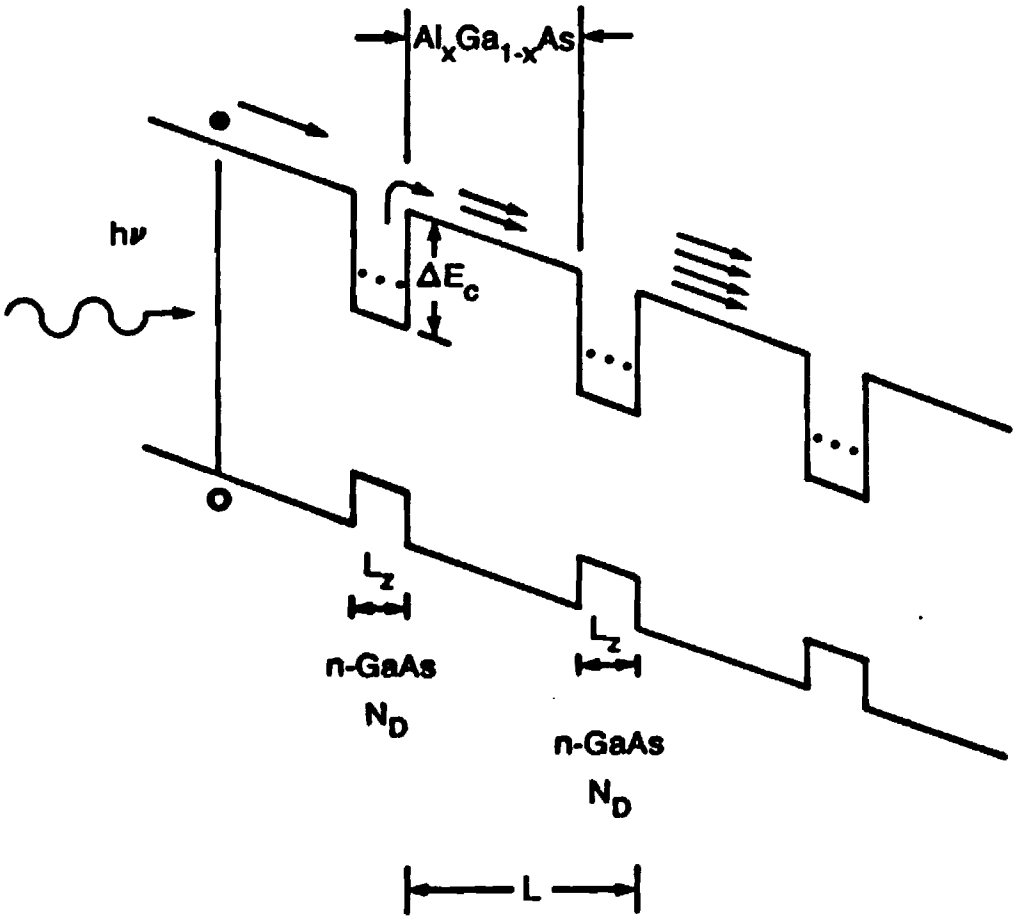

Fig 22

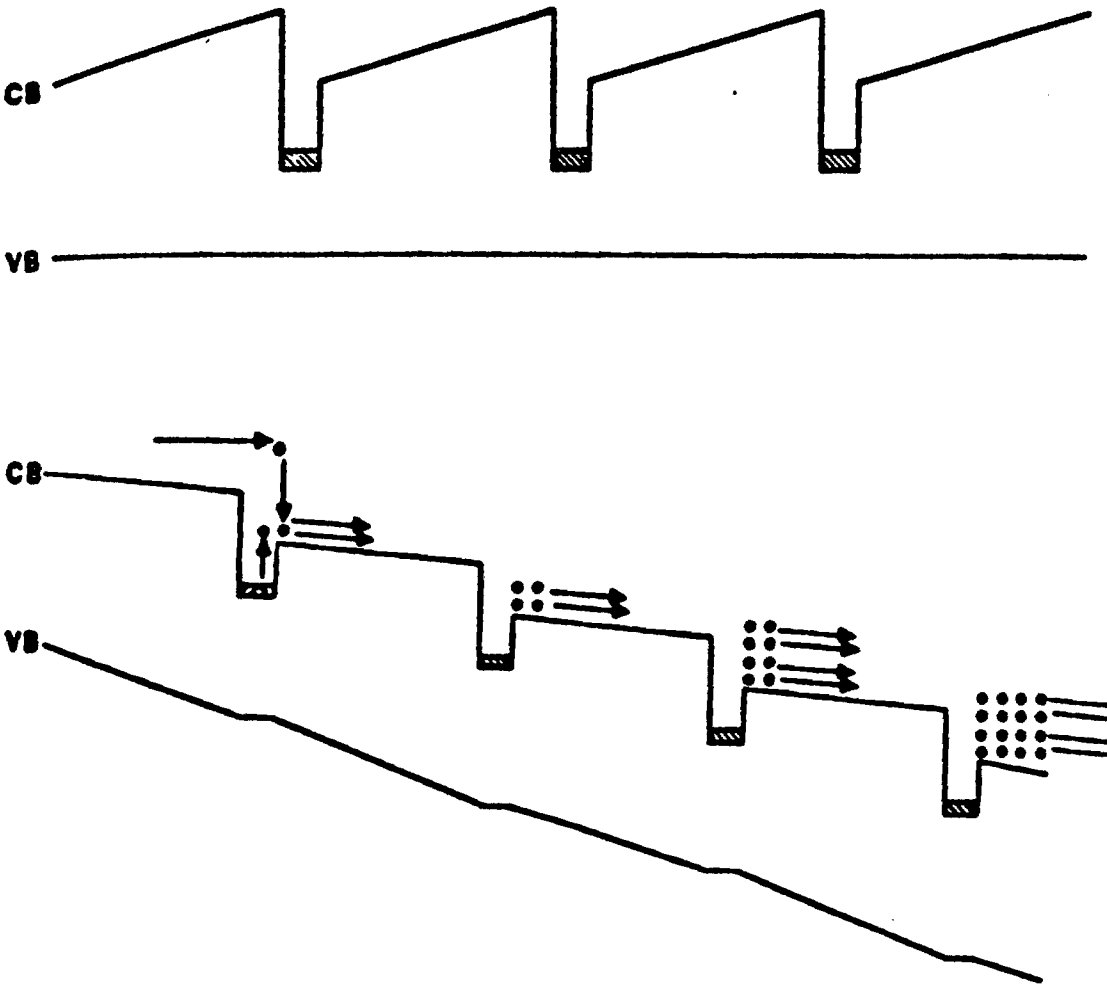

Fig 23

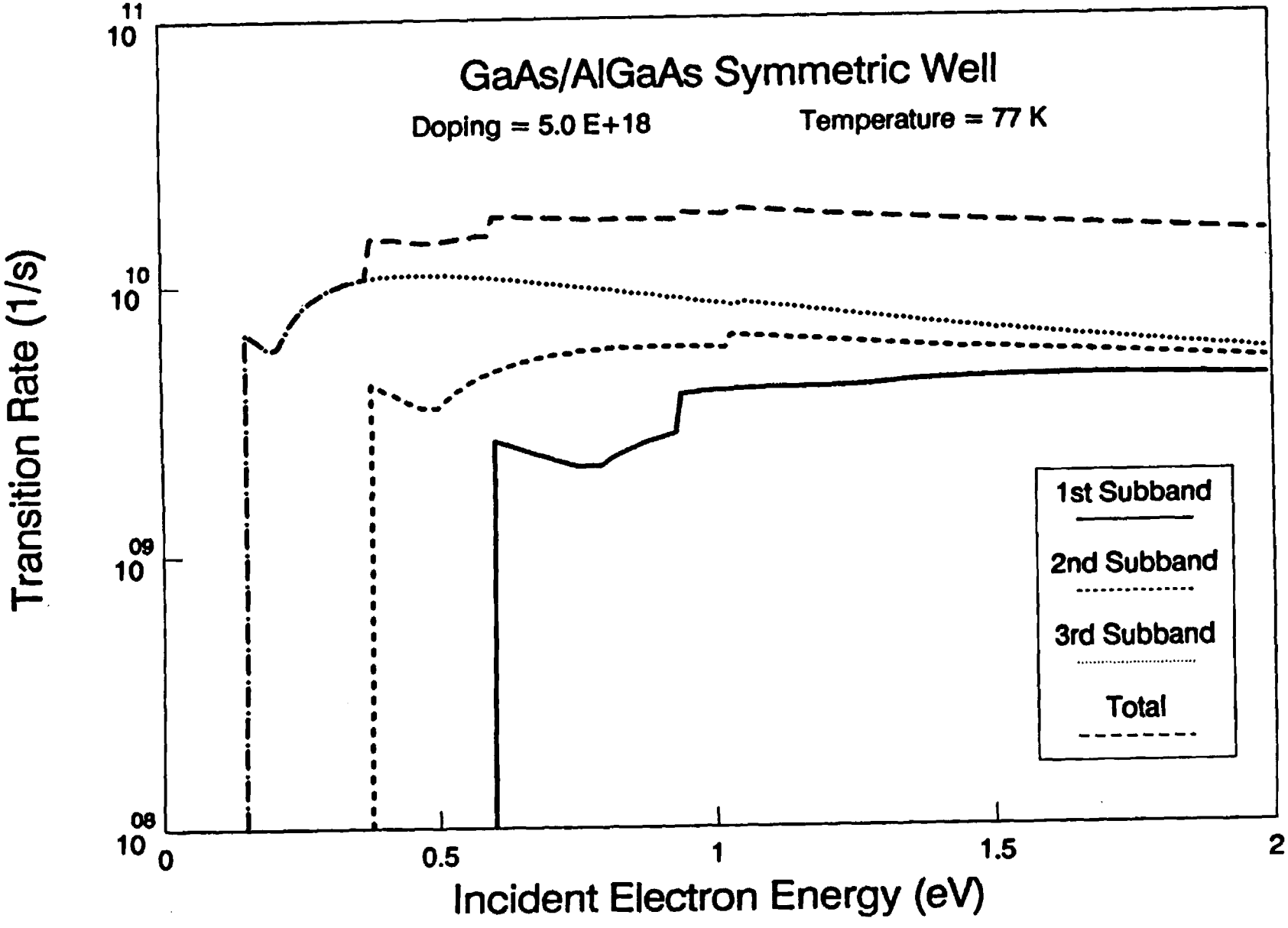
GaAs/AlGaAs Symmetric Well
Doping = 5.0 E+18
Temperature = 77 K
Transition Rate (1/s)
10^11
10^10
10^09
10^08
0
0.5
1
1.5
2
Incident Electron Energy (eV)
1st Subband
2nd Subband
3rd Subband
Total

Fig. 24

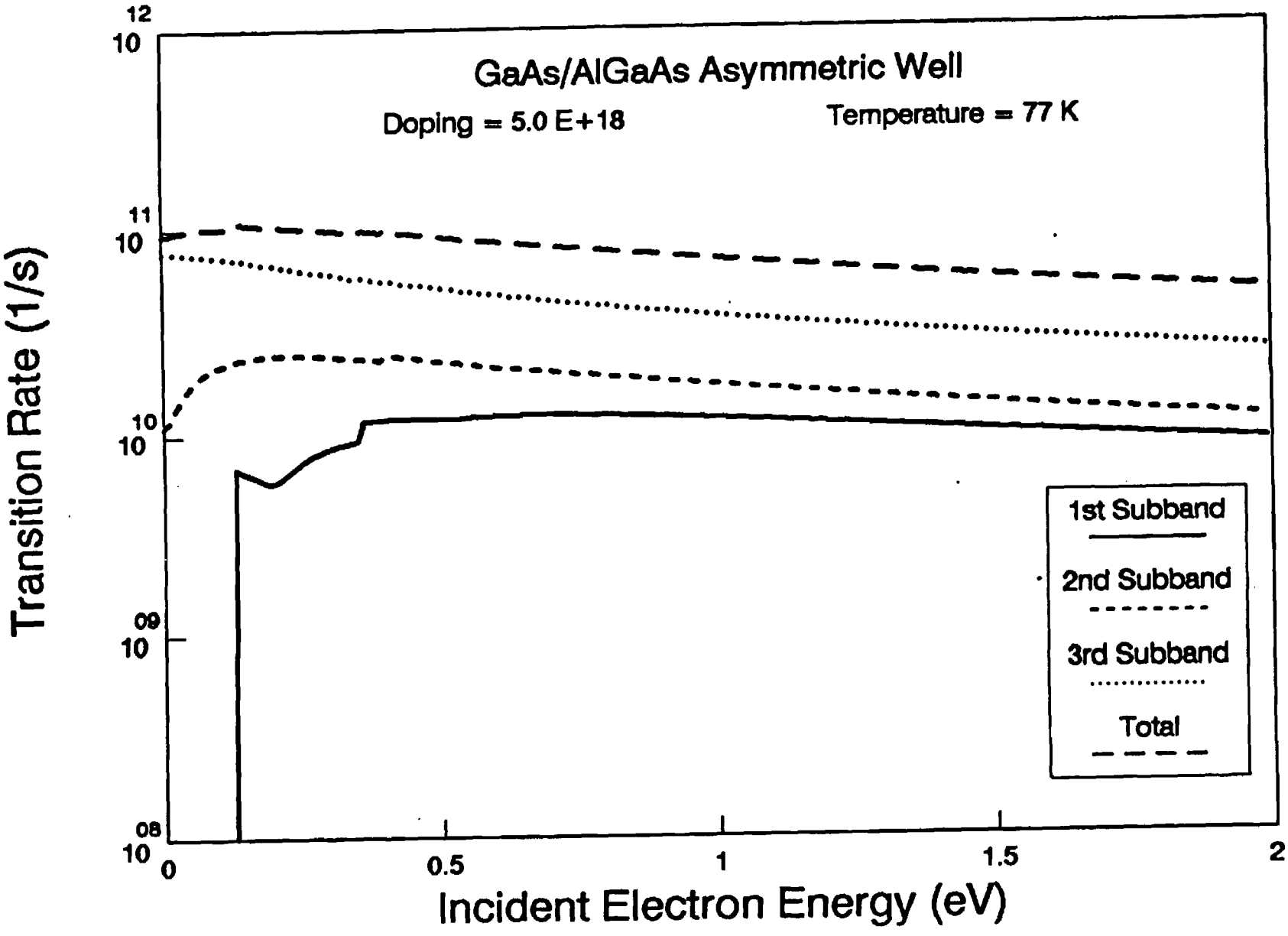
GaAs/AlGaAs Asymmetric Well
Doping = 5.0 E+18
Temperature = 77 K
Transition Rate (1/s)
12
10
11
10
10
10
09
10
08
10
0
0.5
1
1.5
2
Incident Electron Energy (eV)
1st Subband
2nd Subband
3rd Subband
Total

Fig. 25

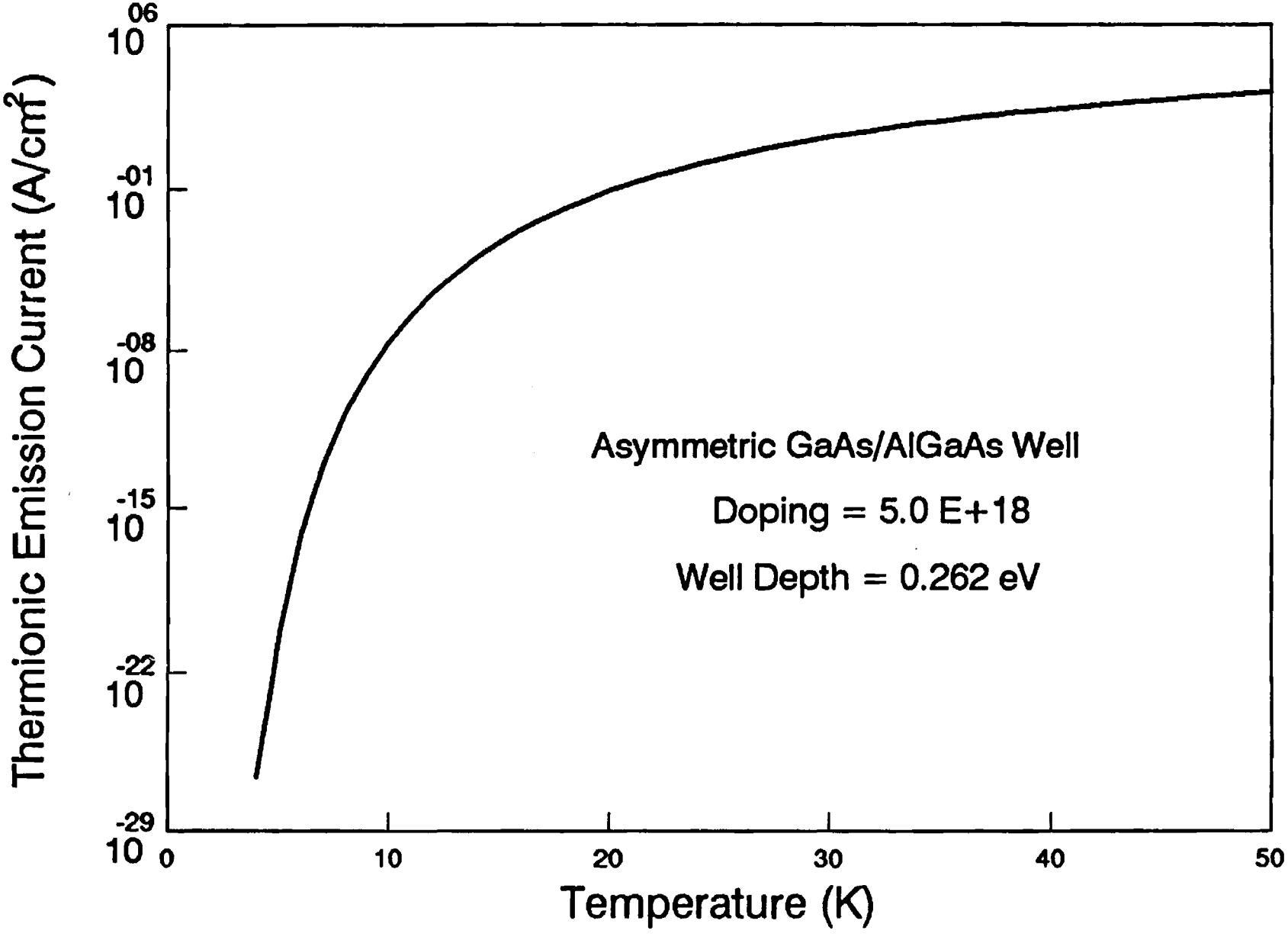
Thermionic Emission Current (A/cm²)
10^06
10^-01
10^-08
10^-15
10^-22
10^-29
0
10
20
30
40
50
Temperature (K)
Asymmetric GaAs/AlGaAs Well
Doping = 5.0 E+18
Well Depth = 0.262 eV

Fig. 26

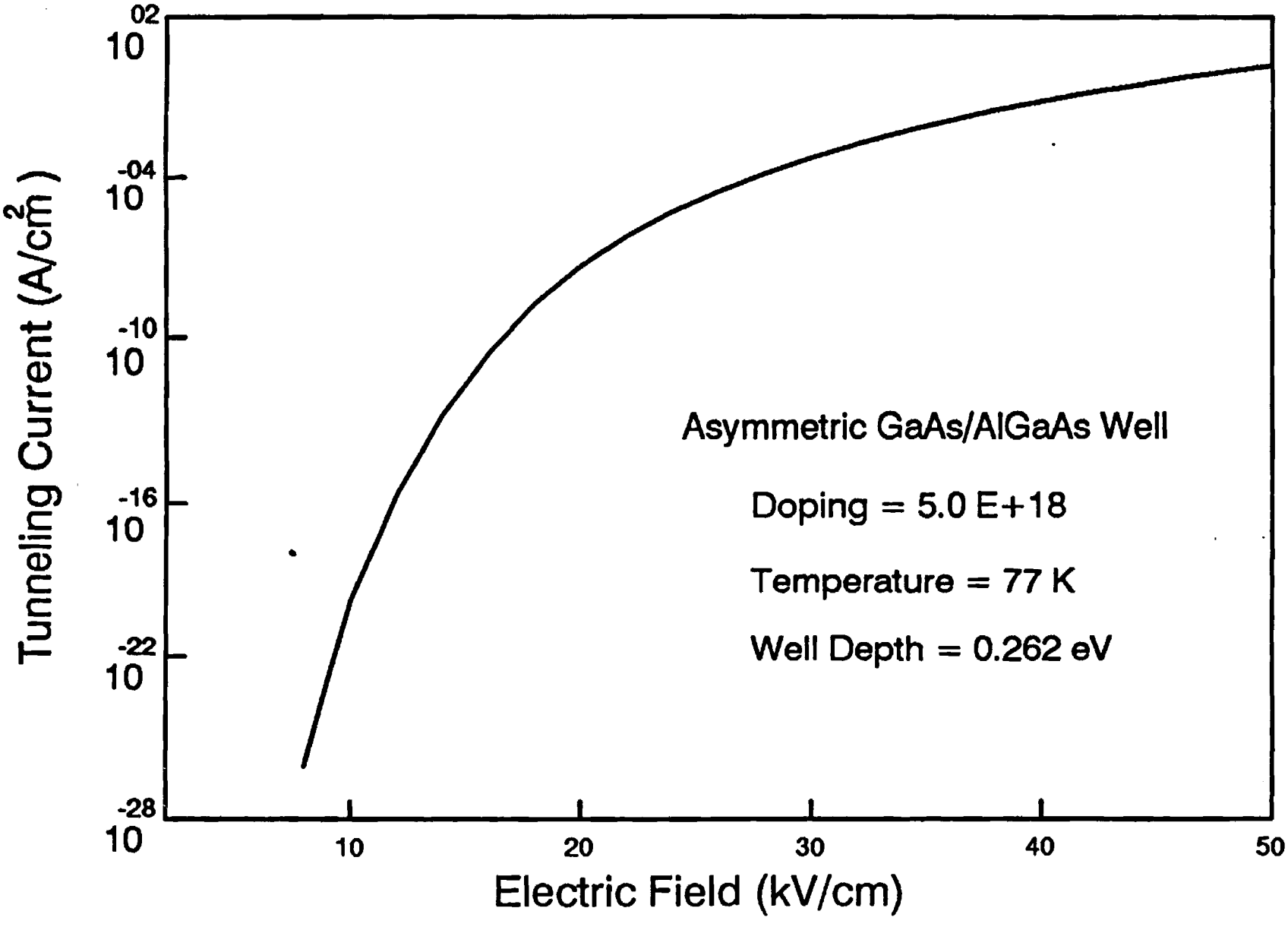
Tunneling Current (A/cm²)
10^02
10^-04
10^-10
10^-16
10^-22
10^-28
10
20
30
40
50
Electric Field (kV/cm)
Asymmetric GaAs/AlGaAs Well
Doping = 5.0 E+18
Temperature = 77 K
Well Depth = 0.262 eV

Fig. 27

E21-G35
#14

Annual Project Report: Motorola Corp.

Project Title: Modeling of Three Terminal Semiconductor Devices: HBTs

Investigator: Dr. Kevin F. Brennan

Organization: School of Electrical Engineering and Microelectronics Research Center Georgia Institute of Technology

Address: School of Electrical Engineering
Georgia Institute of Technology
Atlanta, Georgia 30332-0250

Telephone: (404) 894-6767

Telefax: (404) 894-4700

ABSTRACT

During the fourth year of this project we have succeeded in modeling a GaAs/AlGaAs bipolar transistor structure. Specifically, the effect of fermi level pinning and the base transit time on the device performance were examined. A manuscript has been submitted to IEEE Transactions on Electron Devices for publication based on this work. This report discusses the results presented in that paper and followup studies.

In this report we discuss the salient features of our two-dimensional simulator used in the study of heterostructure bipolar transistors and calculated results of the effect of the Fermi level pinning on the common emitter current gain. The model consists of an ensemble Monte Carlo calculation coupled with a two-dimensional drift-diffusion solver. The full details of our investigation are reported in the enclosed paper entitled, "Ensemble Monte Carlo study of Fermi level pinning and transit times in AlGaAs/GaAs heterojunction bipolar transistors" which has been submitted to IEEE Transactions on Electron Devices. Here, we simply outline the approach and results.

The features of our model can be understood as follows. The model consists of two separate parts. First a drift-diffusion solver is used to solve the Poisson equation and the electron and hole current continuity equations. From this solution, the two-dimensional steady-state electric field profile throughout the device structure is determined. Once a realistic steady-state electric field profile is known, the steady-state dynamics of the electrons can be analyzed using an ensemble Monte Carlo simulation. The electric field is input into the Monte Carlo simulator and an ensemble of electrons is launched from the emitter. The electrons' flight through the device is traced in both k and real space subject to the device boundary conditions and the electric field profile until steady-state is achieved. It is important to note that self-consistency is neglected; the electric field profile, calculated from the drift-diffusion solver, is used throughout the entire course of the simulation.

From the Monte Carlo simulation, the average electron velocity, transit time, energy, etc. can be ascertained. The common emitter current gain, β, defined as the ratio of the collector current to the base current is determined from the Monte Carlo simulation by counting the number of electrons that are collected at the subcollector and the number of electrons collected at the base contact. The ratio of these two numbers gives β.

In order to validate the model, calculated results are first compared to accepted calculations in the literature. Owing to the symmetry of the device, only half of the actual structure is simulated as shown in Figure 1. The device consists of an AlGaAs emitter grown on top of a p-type GaAs base layer and n-type GaAs collector. The dimensions and doping concentrations are illustrated in Figure 2. The initial and boundary conditions used in the ensemble Monte Carlo simulation are schematically shown in Figure 3. As can be seen from Figure 3, the carriers are injected from the emitter into the base region. The contacts are assumed to be perfectly absorbing; all carriers which enter the contact are collected. At all of the other boundaries, specular reflection is assumed to occur. Two different initial launching conditions for the electrons at the emitter are considered. These are low and high energy injection corresponding to a graded and abrupt junction respectively. As can be seen from Figure 4, only the electrons within the high energy tail of the emitter distribution function are injected into the base. Finally, two different conditions are considered for Fermi level pinning at the base contact as shown in Figure 5. The first case is an ideal

FIGURE 1 The simulation region is determined by the symmetry of HBT structures.

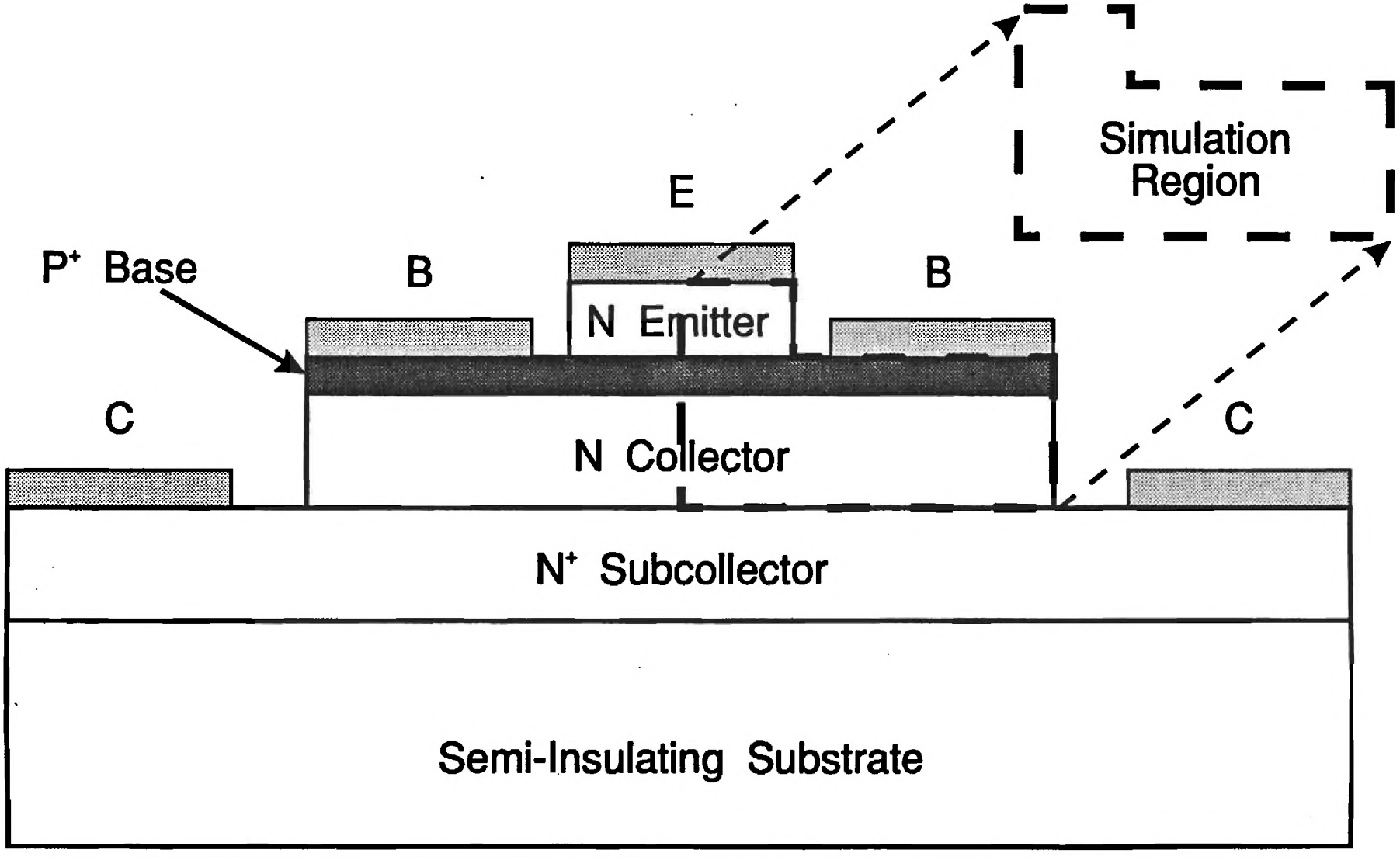

Hayama, et. al., IEEE Trans. Elec. Dev., vol. 8, no. 5, pp. 246-248, May 1987.

FIGURE 2

We examined the HBT structure previously studied by a one-dimensional EMC model.

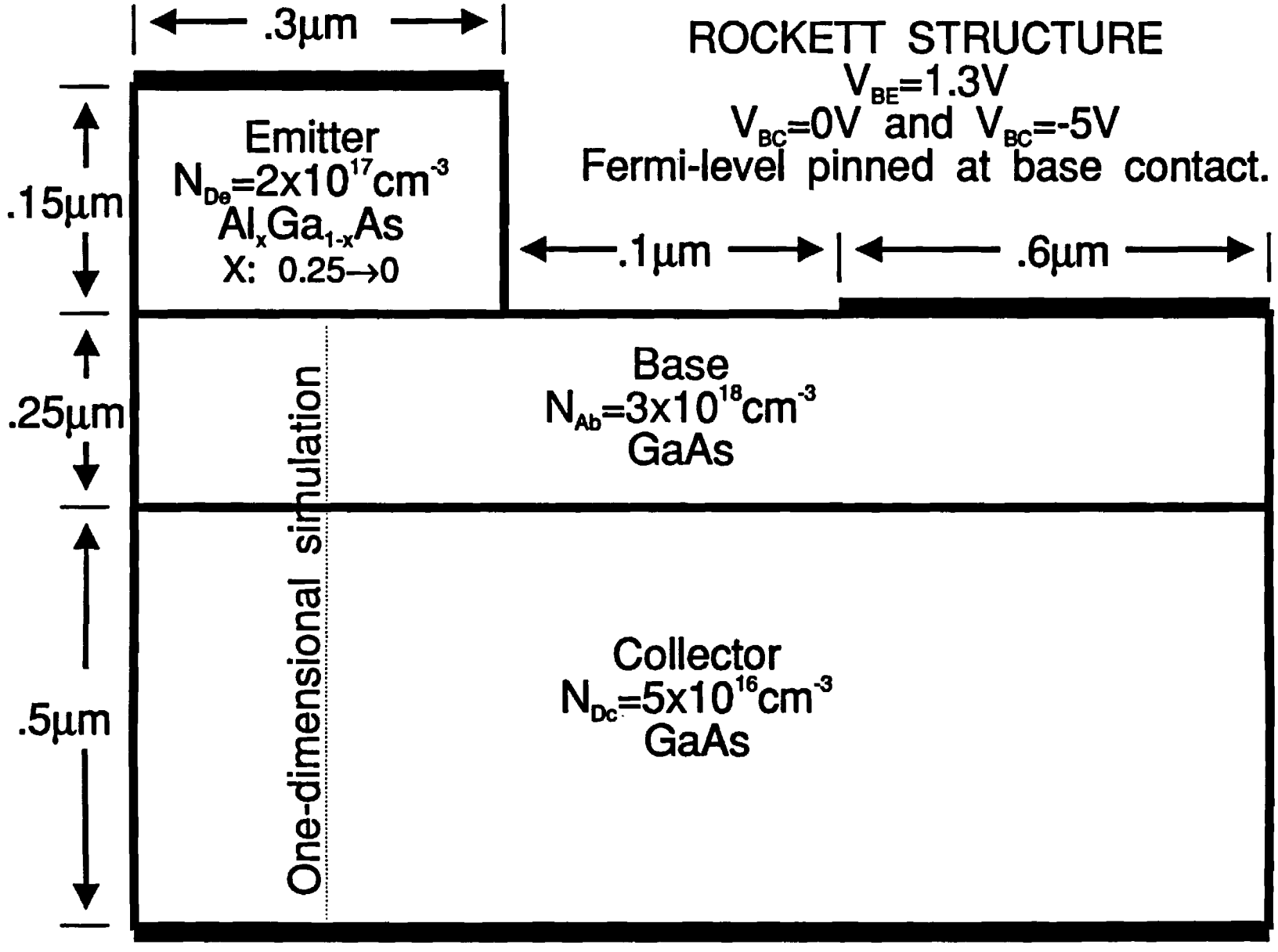

Rockett, IEEE Trans. Elec. Dev., vol. 35, no. 10, pp. 1573-1579, Oct. 1988.

FIGURE 3

Initial and boundary conditions used in the model are based on the simulation region.

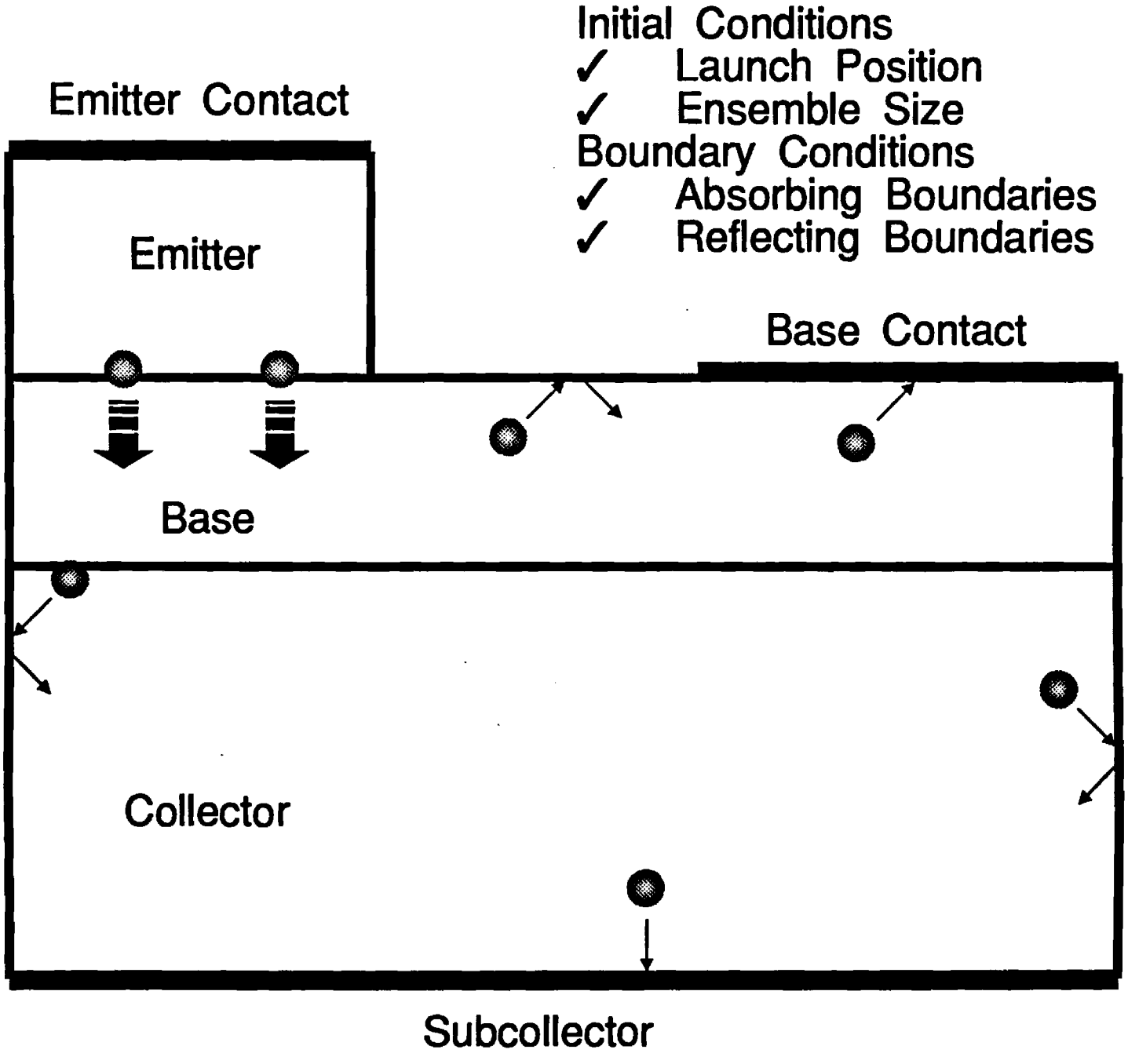

Two conditions for the launch energy of the electrons are considered at the emitter base junction.

FIGURE 4

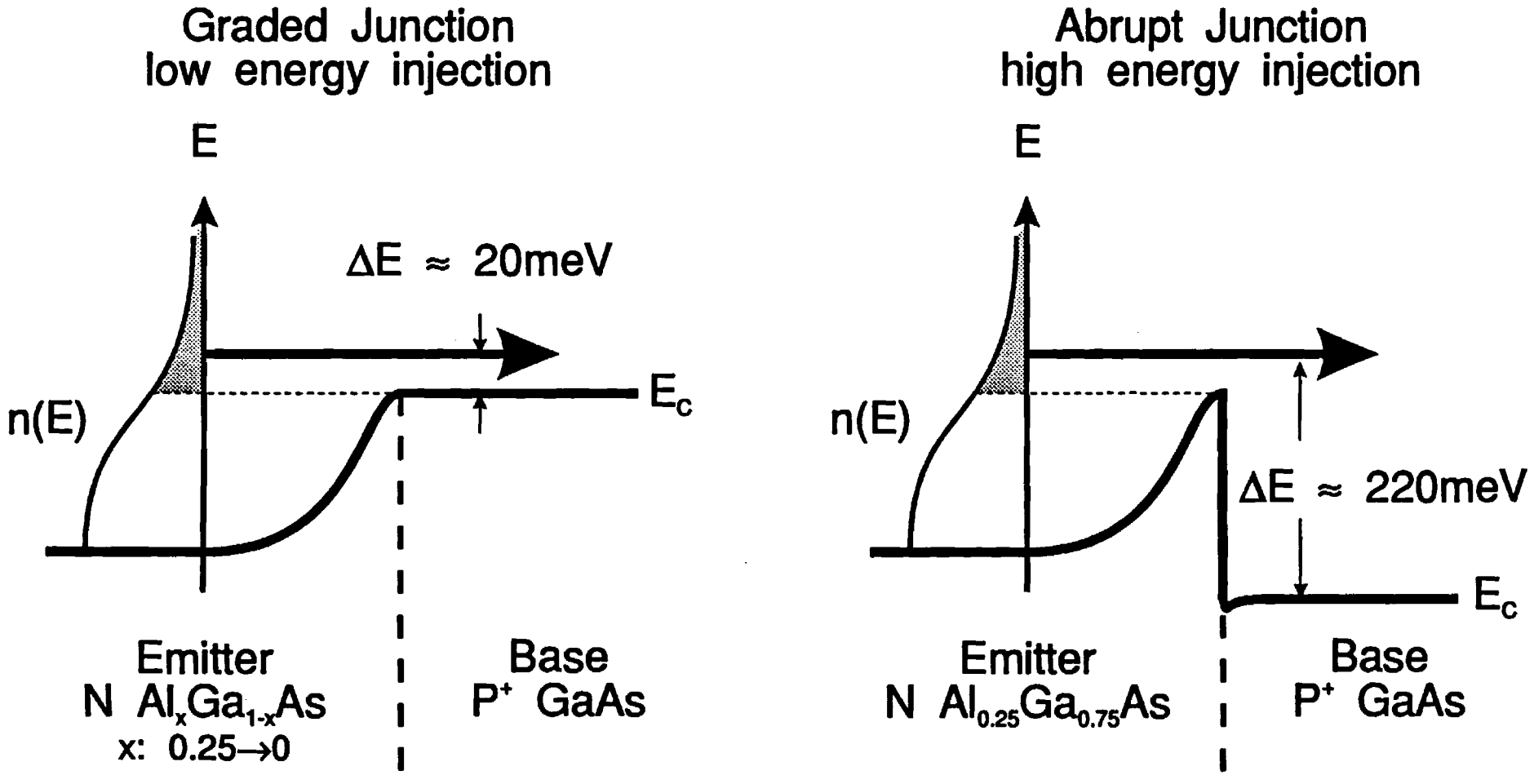

FIGURE 5

Two conditions are considered for Fermi level pinning at the base contact.

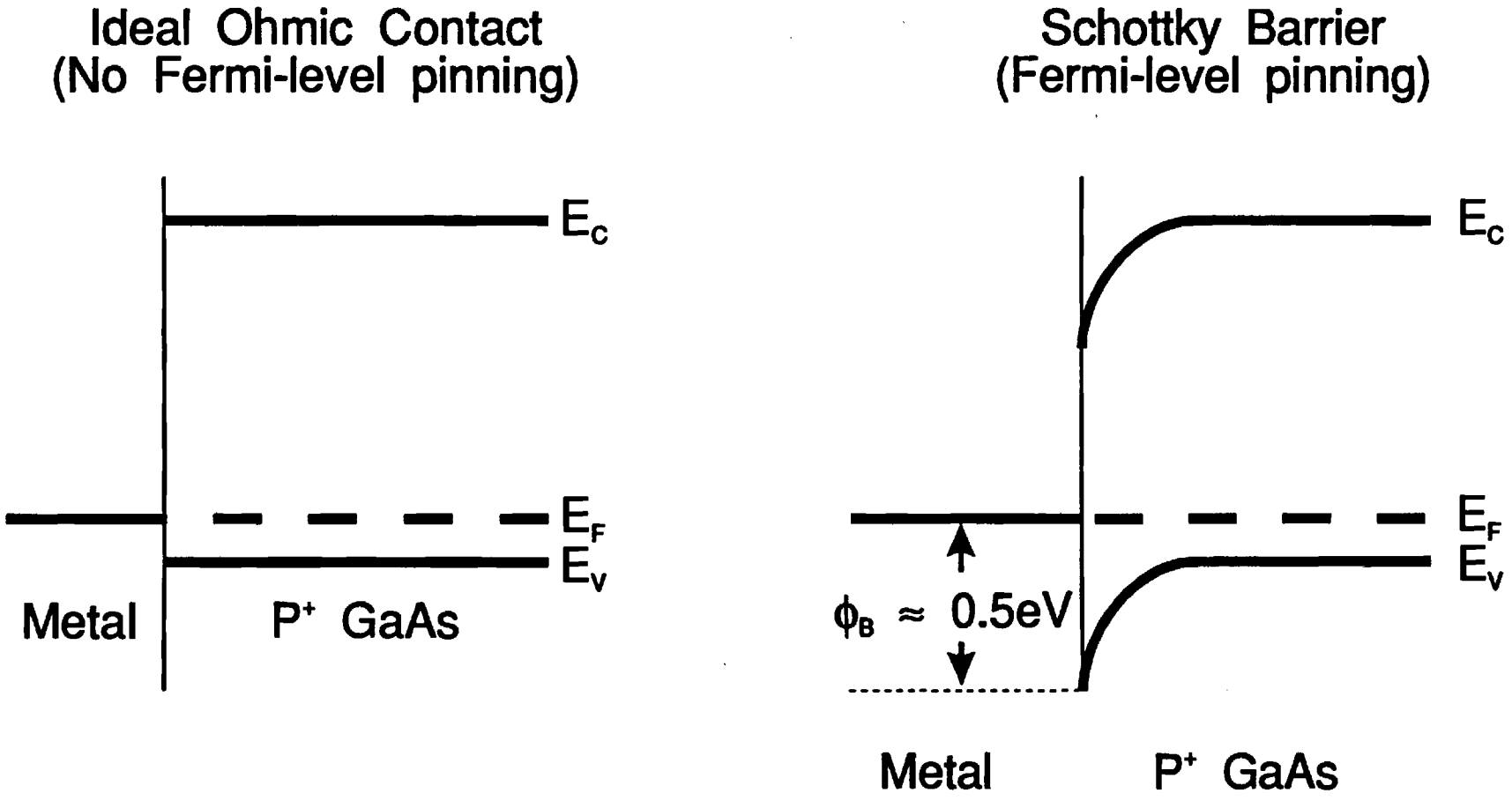

Rhoderick and Williams, Metal-Semiconductor Contacts 2nd ed., Oxford 1988.

ohmic contact wherein there is no Fermi-level pinning while in the second case, a Schottky barrier, there is Fermi-level pinning. In the study presented here, the choice of either model for the base contact is contrasted to see its effect on the common emitter gain of the device.

Before the simulator is applied to the study of the Fermi-level pinning at the base contact, it is important to compare the model to other accepted models of heterostructure bipolar transistors, HBTs. We compared our calculations to those of Rockett [1] for the device structure shown in Figure 2. Rockett's calculations are made using a one dimensional Monte Carlo simulation while ours are made in two dimensions. Nevertheless, excellent agreement is obtained for the calculated drift velocity between the two models, thus validating our results.

An experimentally studied HBT structure was examined next using our model [2]. The device analyzed along with the layer dimensions and doping concentrations is shown in Figure 6. Several different device configurations were studied. Specifically, different conditions, either graded or abrupt junctions, for the emitter were considered. In addition, the device performance was evaluated with and without Fermi level pinning at the base contact. The calculated results for the dc gain under these different conditions are reported in Figure 7. As can be seen from Figure 7, Fermi level pinning leads to a significant decrease in β.

The choice of the injection condition at the emitter, either an abrupt or graded junction, also effects the common emitter

FIGURE 6

We also examined an experimentally studied HBT structure.

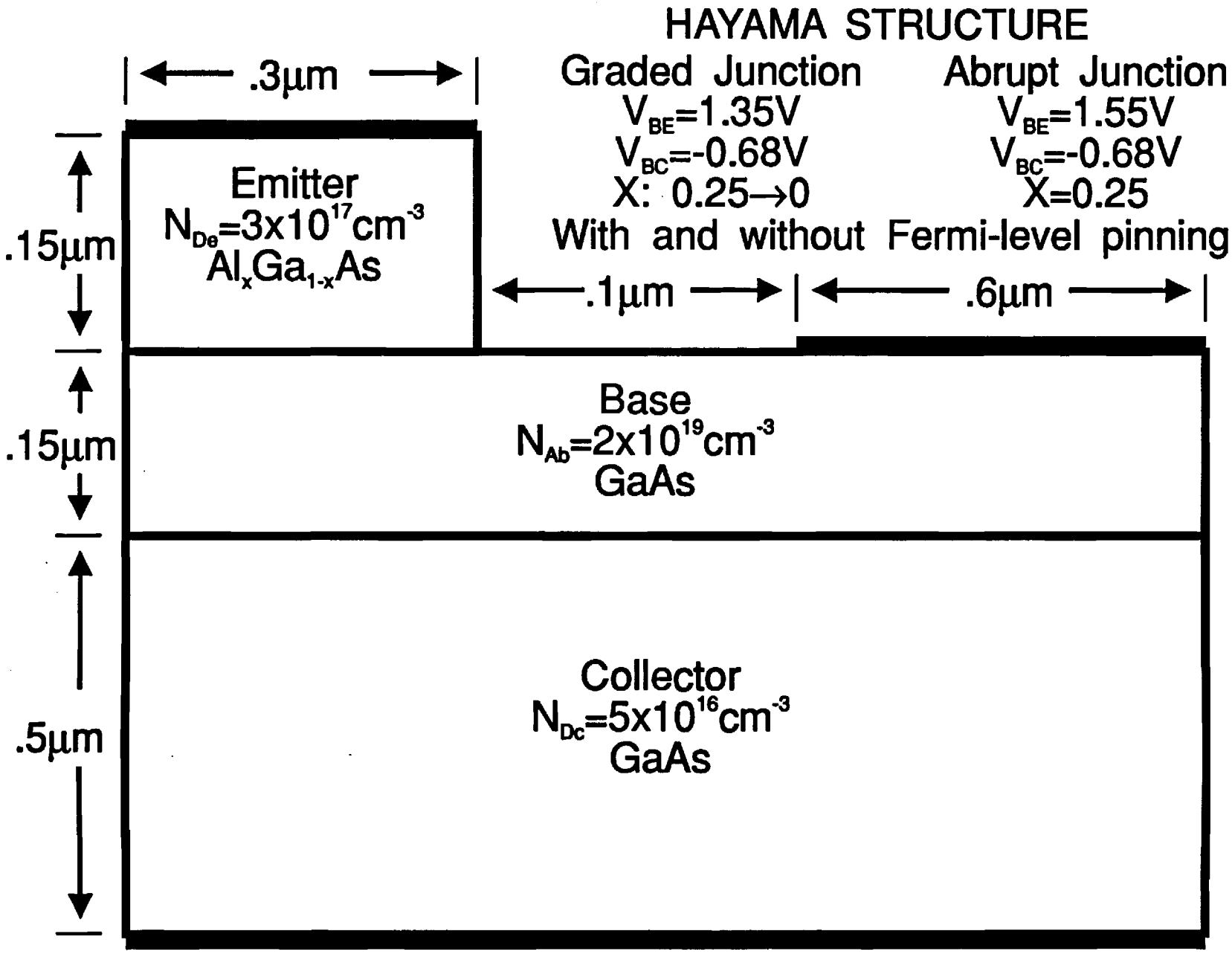

Hayama et. al., IEEE Elec. Dev. Lett., vol. 8, no. 5, pp. 246-248, May 1987.

FIGURE 7

The common emitter current gain, β, was found to have a greater dependence on emitter-base junction type than on Fermi-level pinning at the base contact.

$$\beta \equiv \frac{\text{Collector Current}}{\text{Base Current}} = \frac{\text{Number Collected at Subcollector}}{\text{Number Collected at Base Contact}}$$

	Abrupt Jnc.	Graded Jnc.
Fermi-Level Pinned	17.2	11.1
Fermi-Level Unpinned	20.1	12.9

Consistent with experimental observations

Lee et. al., IEEE Elec. Dev. Lett., vol. 10, no. 5, pp. 200-202, May 1989.

gain. Inspection of Figure 7 shows that the injection condition has a more drastic effect on the common emitter current gain. In fact, β is about 35% lower with a graded emitter than an abrupt emitter in an otherwise identical device. The lower β is due to the fact that the electrons traverse through the base much slower following low energy injection (graded emitter) than from high energy injection (abrupt emitter). This is due predominantly to the occurence of velocity overshoot within the first 0.1 μm of the base region. In comparison, following low energy injection from the graded junction, the transit time is more than four times longer within the first 0.1μm of the base.

Finally, the model was used to observe intervalley transfer as well as longitudinal diffusion. Figures 8 and 9 illustrate the electron valley occupancy as a function of position. The shading of the circles represents the valley. White, unshaded, corresponds to the gamma valley, gray corresponds to the L valley and black corresponds to the X valley. The figures show the instantaneous positions of the simulated electrons after 20 ps of Monte Carlo simulation time. This choice is consistent with steady-state conditions within the device. Each circle represents one simulated electron. For clarity, only 1000 randomly selected electrons are displayed in the diagram out of the entire ensemble of 5000 electrons. Figure 8 shows the electron valley and positions for a graded emitter injection scheme while Figure 9 shows the electron valley and positions for an abrupt emitter junction. Close inspection of the two curves shows that the electrons are more closely bunched near the emitter in the graded

FIGURE 8

The electron valley position plot for the graded junction Hayama structure after 20ps.

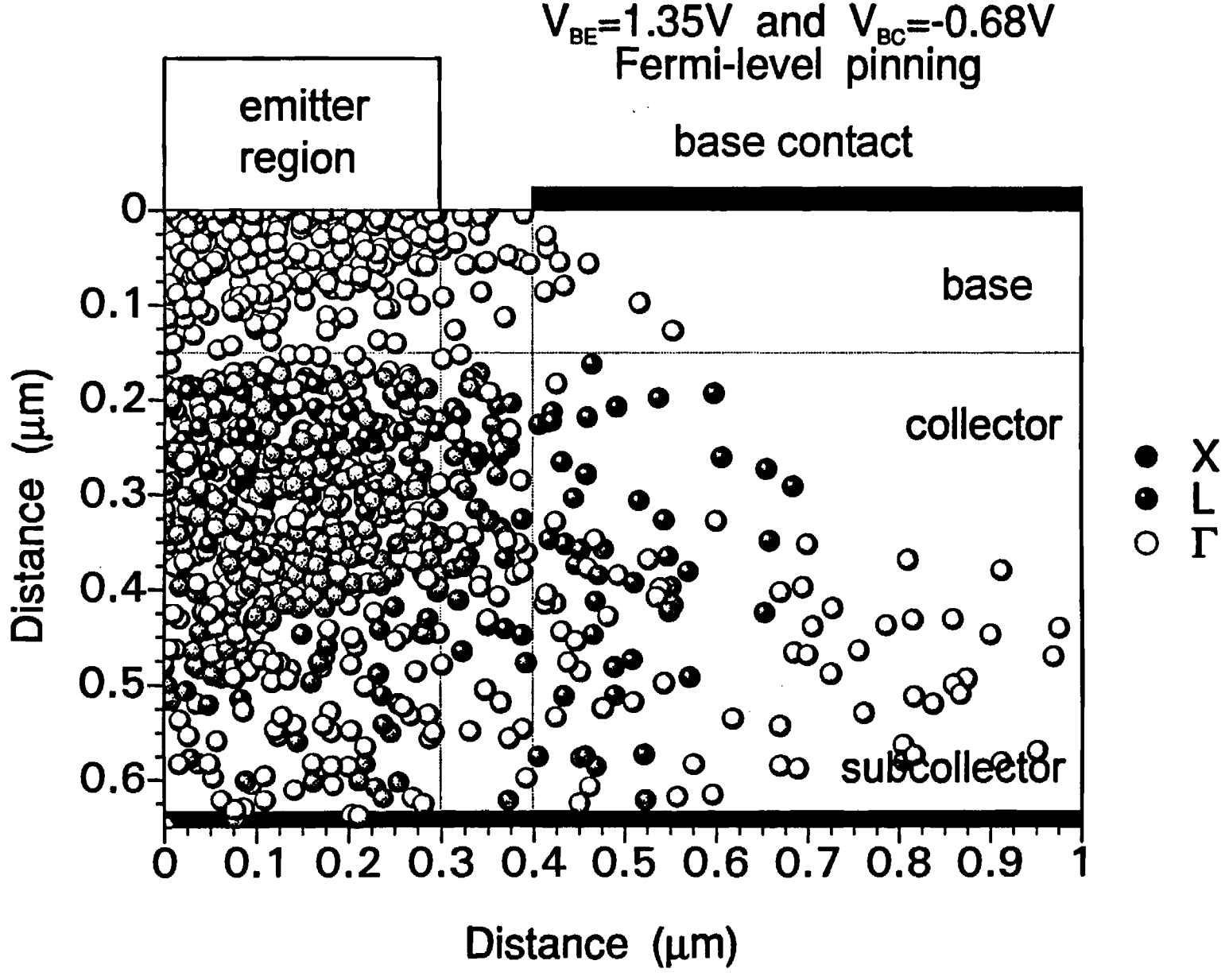

FIGURE 9

The electron valley position plot for the abrupt junction Hayama structure after 20ps.

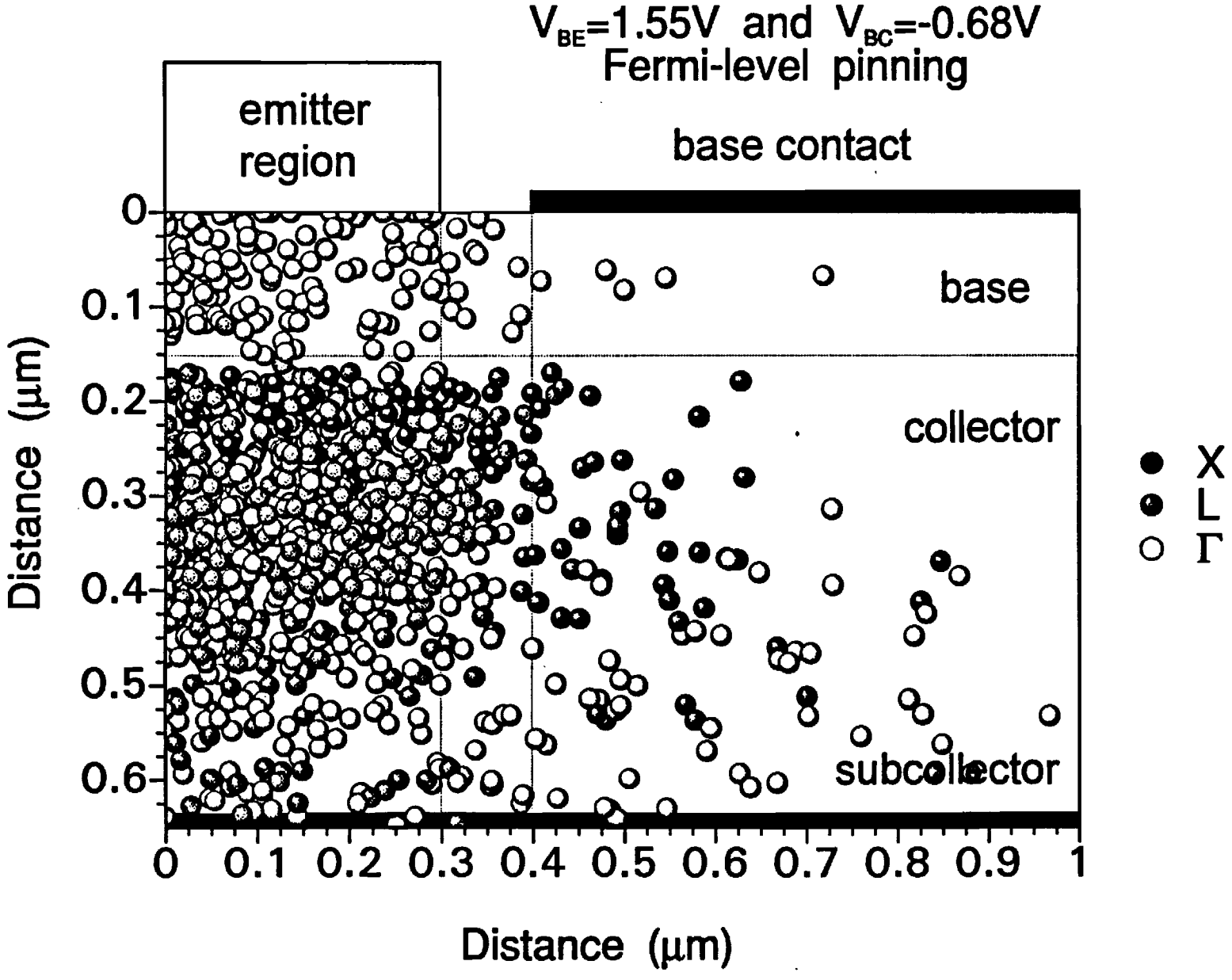

junction device than in the abrupt junction device. This is due to the presence of significant velocity overshoot at the emitter in the abrupt junction device. As a result, the electrons move more rapidly from the emitter-base junction following high energy injection as opposed to low energy injection. Further inspection of these figures shows that there is a slightly greater amount of diffusion into the extrinsic base region following low energy injection than high energy injection.

During the next year of this program we will extend the analysis described above to study the effect of different base contact emitter spacings and the presence and absence of Fermi level pinning at that interface. In addition, we plan to develop a self-consistent model and apply it to the study of an HBT device including potential steps within the collector depletion region. A previous investigation [3] shows that there is a strong possibility of achieving high speed performance with this structure.

References

[1] P. I. Rockett, "Monte Carlo study of the influence of collector region velocity overshoot on the high-frequency performance of AlGaAs/GaAs heterojunction bipolar transistors," IEEE Trans. Electron Dev., vol. 35, no. 10, pp. 1573-1579, Oct. 1988.

[2] N. Hayama, A. Okamoto, M. Madihian, and K. Honjo, "Submicrometer fully self-aligned AlGaAs/GaAs heterojunction bipolar transistor," IEEE Electron Device Letters, Vol. EDL-8, pp. 246-248, May, 1987.

[3] K. Brennan and K. Hess, "Transient electronic transport in staircase heterostructures", IEEE Electron Device Letters, Vol. EDL-4, pp. 419-421, November, 1983.

Ensemble Monte Carlo Study of Fermi Level Pinning and Transit Times in AlGaAs/GaAs Heterojunction Bipolar Transistors

Steven H. Janzou

Nabil S. Mansour

Arlynn W. Smith

and

Kevin F. Brennan

School of Electrical Engineering

and

Microelectronics Research Center

Georgia Institute of Technology

Atlanta, Georgia 30332-0250

and

Herb Goronkin, Fellow IEEE

Phoenix Corp. Research Labs.

Motorola, Inc.

Tempe, AZ 85284

Abstract

We present calculations of the electron transit time and common emitter current gain in the presence and absence of Fermi level pinning using a two-dimensional ensemble Monte Carlo calculation coupled with a two-dimensional drift-diffusion solver. The drift-diffusion solver is used to calculate the steady-state electric field profile from the device dimensions,

doping concentrations, and applied biases. A realistic field profile is thereby obtained which is then used in the context of the ensemble Monte Carlo simulation to calculate the steady-state electron transport properties of the device. The device model is first "benchmarked" to a previously accepted calculation and a representative heterostructure bipolar transistor is examined. The average electron drift velocity, transit time and common emitter current gain, β, are calculated in the presence and absence of Fermi level pinning at the base contact, and in devices with either an abrupt or a graded emitter-base junction. It is found that β is only weakly effected by the Fermi level pinning in the device structure considered since the separation between the emitter and base contacts is relatively small. The common emitter current gain is found to depend more upon the energy injection condition. Finally, the two-dimensional aspects of the device are illustrated and their effects on device performance are addressed.

I. Introduction

As is well known, the use of heterojunctions in bipolar transistors has several important advantages over more common homojunction transistors [1,2]. Principally, the current injection ratio can be vastly increased without lowering the base doping concentration. The presence of a high doping concentration within the base lowers the base resistance thereby drastically improving both the high current and the high frequency performance of the device. Additionally, the emitter doping can be lowered leading to reduced emitter-base capacitance and enhanced switching speed. A variety of heterojunction bipolar transistors (HBTs) varying in terms of their doping concentrations and material systems have been experimentally and theoretically examined to determine the device operating characteristics [1-3]. Owing to the cost, time and complexity involved in the growth and fabrication of experimental HBT structures, a reliable and realistic model is of enormous value in the study and optimization of HBT devices.

The transport dynamics within an HBT device are extremely complex. Most structures are made with narrow base regions and different collector designs in order to improve the speed performance of the device. Most designs typically rely on the use of non-stationary transport effects, velocity overshoot and ballistic transport, in order to achieve high speed performance [4]. Modeling of these effects in realistic structures requires advanced models based on the direct solution of the Boltzmann equation, such as the ensemble Monte Carlo (EMC) model. Several Monte Carlo models have been developed and applied to the study of HBT structures [5-9]. These models contain many advanced features including a

hydrodynamic solution for the hole transport [5] as well as hole-plasmon scattering [6]. However, none of the previous models, to the authors' knowledge, have examined the effect of including the extrinsic base region and the subsequent pinning of the Fermi level at the base contact in investigations of HBT performance.

In this paper, an ensemble Monte Carlo technique coupled with a drift-diffusion solver is used to study the two-dimensional nature of HBT devices. The details of the simulation are reviewed in Section II. The model is then compared to other accepted models from the literature as discussed in Section III. The effect of the inclusion of the extrinsic base region and the subsequent pinning of the Fermi level on the calculated common emitter current gain as well as carrier transit time is investigated in Section IV. Electron valley identity plots as well as transit time curves are presented which introduce new insights into HBT transport behavior. The transit time curves show distinct regions of the device in which non-stationary transport effects are prominent. The electron valley population plots clearly show the two-dimensional aspects of the device behavior.

II. Model Description

The calculations presented herein are based on two different simulators which are used in sequence to evaluate the electron transport dynamics in the device. A given simulation consists of two main steps. First, a complete drift-diffusion solver, semiconductor total energy balance simulator in two dimensions, STEBS2D [10], is used to obtain the electric-field profile based on the device dimensions, dopings and biasing conditions. STEBS2D enables the calculation of the steady-state two-dimensional electric field profile within the device which is then input into the Monte Carlo simulation. Using the calculated two-dimensional

electric field profile from STEBS2D, the EMC simulator traces the electron trajectories throughout the device. From the Monte Carlo calculation, the average carrier transit times, drift velocities and valley populations can be assessed under steady-state operating conditions. The effect of Fermi-level pinning at the base contact is included into STEBS2D by adding a surface charge concentration at the base contact in order to raise the electron concentration at the base-metal contact to match the experimentally determined barrier height [11]. Raising the electron concentration within the base region pins the Fermi level at the base-metal interface in essentially the same manner as lowering the hole concentration through the introduction of surface state recombination processes (see Tiwari et al. [12,13]) in equilibrium. The Fermi level pinning is similar between the two approaches outside of equilibrium provided that the current level flowing through the contact is low. For the work considered here, the base current levels are typically small enough that this choice of boundary condition is acceptable. We have chosen this form of the boundary condition, the introduction of surface charge rather than the introduction of surface recombination processes, for simplicity.

The EMC model is based on a three valley (Γ-L-X) non-parabolic band structure which includes all of the relevant scattering mechanisms, i.e., ionized impurity, alloy, acoustic, polar optical, and intervalley phonon scatterings [14]. The Monte Carlo simulation is three dimensional in k-space and two-dimensional in real space. For simplicity it is assumed that the emitter current is dominated completely by thermionic emission events. Therefore, only those carriers within the high energy tail of the electron distribution within the emitter are injected into the base. The initial energy and momentum of each launched electron is chosen stochastically from within this high energy tail. Both abrupt and linearly graded (0.25

to 0.0 Al content) emitter-base junctions are considered. In either case, the electrons are injected just at the emitter-base junction, the difference being that in the abrupt case the barrier for injection is very much larger than that for the graded case. The ensemble Monte Carlo simulation progresses until the macroscopic quantities of interest, particularly velocity, energy, valley populations, etc., have reached their steady-state values. Steady-state is typically achieved after 20 to 100 ps of simulation time. In the calculations presented here, the total simulation time is 50ps unless otherwise noted.

At present the EMC model is not self-consistent; the field is not updated after the initial solution from STEBS2D. Under active biasing conditions of the device, the electric fields within the regions of interest considered here (emitter-base depletion region, base, and base-collector depletion region) are dominated by the applied biases. The injected electron distribution only slightly perturbs the electric field profile. This is particularly true for low injection conditions which are assumed throughout.

The number of simulated electrons chosen influences both the computational time and the statistical accuracy of the calculation. As the number of simulated electrons increases, statistical fluctuations decrease but at the expense of added computational time. It is our experience that an ensemble of 5000 electrons provides a reasonable compromise between statistical accuracy and computational time in these simulations.

The electrical and transport boundary conditions employed in the model are as follows. The emitter-base junction, base contact and collector contact regions are treated as perfectly absorbing boundaries. When an electron crosses one of these boundaries, it is considered collected and is removed from the simulation. Another electron is then relaunched in order to

maintain space-charge neutrality. All other boundaries of the device are treated as perfectly reflecting where specular reflection is assumed. Dirichlet boundary conditions are applied at all of the contact regions, while Neumann boundary conditions are assumed along all other surfaces.

Estimators of the important macroscopic observables are based on both time and position. The device is partitioned into a series of horizontal lines spaced a distance 125 Å apart in order to accumulate values of interest as a distance along the axis of the device (defined as the distance from the emitter-base junction to the collector contact). The value of a given macroscopic variable, x_p, at a given plane, p, is computed from

$$x_p = \sum_{k=1}^{n_p} \frac{x_{p,k}}{n_p} \qquad (1)$$

where n_p is the number of electrons which have traversed plane p, and $x_{p,k}$ is the quantity of interest for electron k. The macroscopic variables computed include the electron transit time, the instantaneous velocity along the axis of the device, the electron energy, and electron valley. The carrier transit times are determined directly from the simulation, by summing up the electron transit times as they cross into each region.

III. Comparison to Other Models

In order to "benchmark" our model we have compared it to Monte Carlo calculations of electron transport in HBT structures made by Rockett [8]. The structure examined is similar to that presented in Figure 1 with the specific layer widths, doping concentrations, and material compositions shown in the diagram. Calculations are made with the transistor biased into the active mode assuming a graded emitter-base junction. Grading of the emitter-base

junction results in low energy injection of the electrons. The Fermi level at the base contact is taken to be pinned in the calculations made within this section. Two different base-collector biases are considered, V_{BC}= 0 and -5 V holding the emitter-base bias at 1.3 V. At no base-collector bias, the collector depletion region width is found to be 0.2 μm while it increases to 0.43 μm at -5 V reverse bias. The calculated electron drift velocity as a function of distance along the axis of the device is shown in Figure 2 at both collector biasing conditions. As can be seen from Figure 2, the velocity increases dramatically near the base-collector junction due to velocity overshoot effects as discussed by Rockett [8]. The increase in velocity near the collector contact is due to the absorbing boundary condition. Since the carriers are assumed to be swept out of the device, no backscatterings out of the contact region are allowed. The net forward momentum and subsequently the velocity of the electrons is then somewhat overestimated. As discussed by Rockett [8] this computational artifact has no sizeable effect on the transit time results. Comparison of these calculations to those of Rockett [8] show excellent agreement, the only appreciable difference being that our peak overshoot velocity is smaller than that predicted by the one-dimensional solution of Rockett [8] due to the spreading of the carriers into the extrinsic base region of the device.

It is instructive to plot the electron transit time as a function of distance along the axis of the device in order to fully observe the effects of velocity overshoot within the device. The electron transit time as a function of distance is plotted in Figure 3 at both V_{BC} = 0 and -5 V. Inspection of Figure 3 shows that four distinct regions of electron transport are discernible. The first region corresponds to electron transport within the base bulk layer. In the base bulk region of the device, the average electron drift velocity is relatively low due to the low

energy injection condition at the graded emitter-base junction and the relatively low electric field present in the highly doped base. The calculated average electron drift velocity within the base is comparable to the steady-state low field drift velocity in bulk GaAs [14]. The second region, corresponding to the nearly horizontal line in Figure 3, arises from velocity overshoot near the base-collector junction. This portion extends from 0.225 μm to 0.29 μm at V_{BC}=0V and from 0.225 to 0.27 μm at V_{BC}=-5V indicating that the velocity overshoot persists over greater distances at 0V base-collector bias. This is as expected since at higher electric fields intervalley transfer occurs more rapidly in GaAs leading to quenching of the overshoot [15]. The third region of the transit time curves corresponds to transport within the collector depletion region. This portion extends from 0.3 to 0.5 μm at V_{BC}= 0V and from 0.28 to 0.7 μm at V_{BC}= -5V. The depletion region width increases, of course, under reverse bias. The average electron drift velocity within the collector depletion region is comparable to the saturated high field drift velocity in GaAs at 300K as expected. The fourth region of the transit time curves corresponds to transport within the collector bulk region. In this region the electric field is much lower and the electrons begin to re-transfer into the Γ valley from the L and X valleys. As a result the electron drift velocity increases initially and the transit time decreases. Near the collector contact in the 0V bias case, the transit time increases slightly owing to the fact that the carriers are beginning to thermalize at this point.

Finally, we calculate the average base, τ_B, and collector, τ_C, transit times within the device again assuming a graded emitter-base junction. At V_{BC}= 0V, τ_B= 4.38 ps and τ_C= 6.65 ps while at V_{BC}= -5V, τ_B= 4.22 ps and τ_C= 7.98 ps. The difference between the collector transit times is due to the presence of the much higher electric field within the collector

depletion region at high base-collector reverse bias. Though under either base-collector bias, 0 or -5 V, there is a high field present at the base-collector junction which causes the velocity overshoot. At 0V bias the depletion region is much smaller, thus the electrons experience a weaker field throughout most of the collector. As a result, many of the electrons can re-transfer from the high mass, L and X valleys, back into the low mass Γ valley wherein their drift velocity is much greater. This results in a substantially lower average transit time for the electrons.

The transit time results as well as the drift velocity calculations are completely consistent with Rockett's results [8]. The detailed physics of these calculations have been explained at length by Rockett [8] and will not be repeated here. It is our goal in this section to establish the consistency of our approach with other accepted models of HBTs as well as to demonstrate the utility of the transit time curves in evaluating the transport dynamics within the device.

IV. Effect of Fermi Level Pinning

The effect of Fermi level pinning on the common emitter current gain, β, in an HBT structure is investigated in this section. Again we use the device structure sketched in Figure 1 with the corresponding material parameters listed in the figure. To the authors' knowledge, this is the first time that the effect of Fermi level pinning at the base contact has been investigated in the context of a Monte Carlo simulation of an HBT. Figure 4 shows the conduction band bending in the presence of Fermi level pinning at the base contact. Notice that the pinning leads to the formation of a potential well in the proximity of the base contact. Physically, the presence of Fermi level pinning and the subsequent formation of the potential

well is expected to act to capture electrons which diffuse into the extrinsic base region. The number of carriers which can successfully transit the base region is reduced. As a result, the β of the device would be smaller. If pinning is neglected, no potential well is formed at the base contact. Fermi level pinning is incorporated into our model by adjusting the boundary condition at the base contact in the STEBS2D model as discussed in Section II.

Two different initial conditions for the electron launching energy are considered in order to simulate devices with abrupt and graded emitter-base junctions. The abrupt junction is simulated by assuming a barrier of 0.188 eV above which the carriers are injected thermionically in accordance with the scheme discussed in Section II. For the graded junction no barrier is assumed at the emitter-base junction. Therefore, in the abrupt case, only high energy electrons are injected, while in the graded case, low energy electrons are injected into the base. The average energy of the injected electrons in the abrupt case is 0.208 eV while in the graded case it is 0.0205 eV. In order to insure that the high energy tails of the injected electron distributions are comparable, the emitter-base is forward biased at 1.5 V for the abrupt junction and at 1.3V for the graded junction. In either situation, the base-collector voltage remains fixed at -5.0 V. The combination of high or low initial launching energy and whether the Fermi level is pinned or unpinned at the base contact leads to four different situations. Each condition is designated by high pinned, high unpinned, low pinned or low unpinned, where high or low represents either high or low energy injection respectively and pinned or unpinned represents either the presence or absence of Fermi level pinning at the base contact.

β is calculated from the ratio of the number of electrons collected at the collector

contact to the number of electrons collected at the base contact. The calculated values of β are presented in Table I. The first set of results illustrates the effect of the injection energy on β assuming that the Fermi level remains pinned at the base contact. The second set of results illustrates the effect of the presence or absence of pinning on β assuming high energy injection conditions. As can be seen from Table I, β is greater at high energy injection than at low energy injection. Comparison of Cases 1 and 2 shows that the common emitter current gain has a greater dependence on the initial energy condition than on the nature of the base contact pinning. These results are qualitatively consistent with the experimental work of Lee et al. [16] which demonstrated that Fermi level pinning alone has little effect on β at emitter base spacings, S_{EB}, less than 0.2 μm. The stronger dependence of β on the initial launching energy condition can be understood as follows. At the high energy injection condition chosen here, all other factors being equal, the electrons have a much greater probability of traversing the base. They enter the base at a much higher velocity and therefore transit the base, on average, in less time. Since the electrons under these conditions spend less time in the base, they are less prone to scatterings which will redirect their motion towards the base contact and subsequent collection. Hence, more electrons successfully transit the base and are ultimately collected at the collector contact.

The injection energy condition also strongly effects the carrier transit times through the device. The average electron transit time as a function of distance along the axis of the device is plotted in Figure 5. As is clearly seen from Figure 5, the average electron transit time is substantially less in the abrupt junction device than in the graded junction device. The most dramatic difference occurs for the base transit time. Notice that the electrons traverse

through the base much faster following high energy injection than low energy injection. This is due predominately to the occurrence of velocity overshoot within the first 0.1μm of the base region. The time the electrons take to travel 0.1μm following high energy injection in the structure is calculated to be 0.37 ps. Linearly extrapolating, this translates into a total base transit time of 0.92ps which is much less than the calculated base transit time of 1.8 ps, clearly signifying the presence of a substantial increase in the velocity within the first 0.1μm over the last portion of the base. In comparison, following low energy injection, the transit time is more than four times longer for the first 0.1μm of the base. This is as expected for low energy injection since the current then proceeds by diffusive transport within the base.

To further understand the workings of this device structure and to clearly illustrate its two-dimensional effects, we show a series of plots which depict the real space position of the electrons in Figures 6-9. Each circle in the diagrams represents one simulated electron. For clarity, only 1000 randomly selected electrons out of the entire ensemble of 5000 electrons are displayed. The shading of the circles is representative of the instanteously occupied valley, Γ, L or X, after the simulation time considered. In each case presented, the total simulation time elapsed is 50 ps, well after the device has attained steady-state conditions. Electrons within the Γ valley are unshaded (white), electrons within any one of the L valleys are gray, while those electrons within any one of the X valleys are shaded black. Figures 6 and 7 show the electron population assuming the Fermi level is pinned, a graded emitter-base junction biased at 1.3 V and low energy injection conditions at 0V and -5V base-collector biasing respectively. The valley occupancy within the intrinsic and extrinsic base and collector regions at both base-collector biases is tabulated in Table II. Comparison of these results

shows that the two-dimensional spreading of the electrons is much greater under 0V bias than -5V bias. The electrons diffuse less at high base-collector bias as compared to low base-collector bias due to the much greater electric field present in the collector depletion region. Therefore, inclusion of two-dimensional effects is most important at low base-collector bias. Further inspection of Figure 6 clearly shows the electrons re-transfering back into the Γ valley after transiting the collector depletion region. As discussed above, at 0V bias, the collector depletion region is much smaller and as a result the electrons experience a much smaller electric field after traversing 0.5 μm along the device axis. In contrast, inspection of Figure 7 shows the electrons remain predominately within the L and X valleys throughout their entire flight through the collector at -5V bias.

It is interesting to further compare the electron population plots at high and low energy injection conditions. In Figures 8 and 9, we compare the device behavior at low and high energy injection conditions respectively under otherwise identical operating conditions; the Fermi level is pinned and the collector is biased at -5V. Only the first 500 Å of the base region along the device axis is plotted in each diagram, showing the concentration of electrons present under these conditions. Comparison of these two figures clearly shows that the electron concentration is far greater within the first 500 Å of the base region, on average, following low energy injection than high energy injection. This is consistent with the results shown in Figure 5 in which it is seen that the transit time is much greater for electrons within the base following low energy injection than for those following high energy injection due to velocity overshoot in the base. As a result, the carriers tend to move more rapidly from the emitter-base junction following high energy injection as opposed to low energy injection.

Further inspection of Figures 8 and 9 shows that there is a slightly greater amount of diffusion into the extrinsic base region following low energy injection than high energy injection.

V. Conclusions

We have presented calculations of the effects of the Fermi level pinning at the base contact and the nature of the emitter-base junction (abrupt or graded) on the average electron transit time and the common emitter current gain. The calculations are made using a two-dimensional ensemble Monte Carlo simulation coupled with a two-dimensional drift-diffusion solver. The model is first compared to another existing simulation and excellent agreement between the two approaches is obtained. It is found that the common emitter current gain has a greater dependence on the emitter-base junction type than on the nature of the base contact pinning for the particular device geometry considered. This agrees qualitatively with previous experimental measurements [16]. The energy injection condition also strongly effects the average electron transit time through the device. Transit time curves clearly illustrate that the average electron transit time is substantially less in the abrupt junction device than in the graded junction device. The most dramatic difference occurs for the base transit time. The electrons are observed to traverse through the base much faster following high energy injection than low energy injection. This is due predominately to the occurrence of velocity overshoot within the first 0.1μm of the base region. In comparison, following low energy injection, the transit time is more than four times longer for the first 0.1μm of the base.

Though our model is not presently complete, it nevertheless provides a new means of examing HBT device performance and of assessing the importance of two-dimensional

effects. Future work will address the inclusion of electron-hole scattering both through plasmon interactions [17] and through short range scatterings. In addition, the model will be made self-consistent to enable calculation of the device performance during transients.

Acknowledgements

The portion of this work performed at Georgia Tech was sponsored by the Motorola Corp. through contract E21-635 and by the National Science Foundation through a Presidential Young Investigator Award made to K. Brennan.

The authors would like to thank Dr. Rimantis Vaitkus for many helpful discussions.

References

[1] H. Kroemer, "Heterostructure bipolar transistors and integrated circuits," *Proc. IEEE,* vol. 70, no. 1, pp. 13-25, Jan. 1982.

[2] P. M. Asbeck, M-C. F. Chung, J. A. Higgins, N. H. Sheng, G. J. Sullivan, and K-C. Wang, "GaAlAs/GaAs heterojunction bipolar transistors: Issues and prospects for applications," *IEEE Trans. Electron. Dev.*, vol. 36, no. 10, pp. 2032-2041, Oct. 1989.

[3] P. M. Asbeck, "Bipolar transistors", in High-Speed Semiconductor Devices, edited by S. M. Sze, J. Wiley and Sons, 1990, pp. 335-398.

[4] T. Ishibashi and Y. Yamauchi, "A possible near-ballistic collection in an AlGaAs/GaAs HBT with a modified collector structure," *IEEE Trans. Electron. Devices.*, vol. 35, no. 4, pp. 401-404, April, 1988.

[5] K. Tomizawa, Y. Awano, and N. Hashizume, "Monte Carlo simulation of AlGaAs/GaAs heterojunction bipolar transistors," *IEEE Elec. Dev. Lett.*, vol. 5, no. 9, pp. 362-364, Sept. 1984.

[6] R. Katoh, M. Kurata, and J. Yoshida, "Self-consistent particle simulation for (AlGa)As/GaAs HBT's with improved base-collector structures," *IEEE Trans. Elec. Devices*, vol. 36, no. 5, pp. 846-853, May 1989.

[7] C.M. Maziar, M.E. Klausmeier-Brown, S. Bandyopadhyay, M.S. Lundstrom, and S. Datta, "Monte Carlo evaluation of electron transport in heterojunction bipolar base structures," *IEEE Trans. Elec. Devices*, vol. 33, no. 7, pp. 881-887, July 1986.

[8] P.I. Rockett, "Monte carlo study of the influence of collector region velocity overshoot on the high-frequency performance of AlGaAs/GaAs heterojunction bipolar

transistors," *IEEE Trans. Elec. Devices*, vol. 35, no. 10, pp. 1573-1579, Oct. 1988.

[9] J. Hu, D. Pavlidis, and K. Tomizawa, "Monte Carlo studies of the effect of emitter junction grading on the electron transport in InAlAs/InGaAs," *IEEE Trans. Elec. Devices*, vol. 39, no. 6, pp. 1273-1281, June 1992.

[10] A. W. Smith, "Light confinement and hydrodynamic modelling of semiconductor structures by volumetric methods," Ph.D. Thesis, Georgia Institute of Technology, Atlanta, Ga. May, 1992.

[11] E. H. Rhoderick and R. H. Williams, Metal-Semiconductor Contacts 2nd ed.. Oxford: Clarendon Press, 1988.

[12] S. Tiwari, S. L. Wright, and A. W. Kleinsasser, "Transport and related properties of (Ga,Al)As/GaAs double heterostructure bipolar junction transistors," *IEEE Trans. Elec. Devices*, vol. 34, no. 2, pp. 185-187, Feb. 1987.

[13] S. Tiwari, D. J. Frank, and S. L. Wright, "Surface recombination in GaAlAs/GaAs heterostructure bipolar transistors," *J. Appl. Phys.*, vol. 64, pp. 5009-5012, Nov. 15, 1988.

[14] K. F. Brennan, D. H. Park, K. Hess, and M. A. Littlejohn, "Theory of the velocity-field relation in AlGaAs," *J. Appl. Phys.*, vol. 63, pp. 5004-5008, May 15, 1988.

[15] J. Y. Tang and K. Hess, "Investigation of transient electronic transport in GaAs following high energy injection, *IEEE Trans. Electron Dev.*, vol. ED-29, no. 12, Dec. 1982.

[16] W-S. Lee, D. Ueda, T. Ma, Y-C. Pao, J. S. Harris, Jr., "Effect of emitter-base spacing on the current gain of AlGaAs/GaAs heterojunction bipolar transistors," *IEEE Elec.*

Device Lett., vol. 10, no. 5, pp. 200-202, May 1989.

[17] N.S. Mansour, K. Diff, and K.F. Brennan, "Comparison of different formulations of the electron-plasmon scattering rate and the dispersion relation on bulk semiconductor transport," *J. Appl. Phys.*, vol. 69, no. 9, pp. 6506-6509, May 1, 1991.

Figure Captions

Fig. 1 Schematic drawing including definitions of the device parameters of the HBT structures studied in this work.

Fig. 2 Instantaneous velocity along the axis of the device from the emitter-base junction at zero and -5V base-collector bias. The apparent increase in the calculated drift velocity near the collector contact is an artifact of the model due to the perfectly absorbing boundary condition assumed at the collector. Since no backscatterings are allowed at the collector contact, the net momentum and velocity of the carriers is somewhat overestimated.

Fig. 3 Transit time along the axis of the device from the emitter-base junction at zero and -5V base collector bias.

Fig. 4 Sketch of the conduction band energy showing Fermi level pinning at the base contact. Only the first 1000 Å of the base region, including both the intrinsic and extrinsic regions, is shown. Notice the -0.5 eV potential energy well formed at the base contact.

Fig. 5 Transit time along the axis of the device from the emitter base junction for both abrupt and graded emitter base junctions. The Fermi-level is pinned at the base contact.

Fig. 6 Electron valley population occupancy (Γ-white, L-gray, X-black) as a function of position after 50ps of simulation time for the structure sketched in Figure 1. The Fermi level is pinned and low energy injection conditions apply. The base-collector bias is 0V. Notice the significant diffusion of the carriers within the collector region.

Fig. 7 Electron valley population occupancy (Γ-white, L-gray, X-black) as a function of position after 50ps of simulation time at low energy injection and Fermi-level pinning.

The base-collector is biased at -5V. Less carrier diffusion is present in this case.

Fig. 8 Electron valley population occupancy (Γ-white, L-gray, X-black) as a function of position after 50ps of simulation time at low energy injection and Fermi-level pinning showing only the first 500Å of the base region. The base-collector is biased at -5V.

Fig. 9 Electron valley population occupancy (Γ-white, L-gray, X-black) as a function of position after 50ps of simulation time at high energy injection and Fermi level pinning showing only the first 500Å of the base region. The base-collector is biased at -5V. Comparison to Fig. 8 shows that there are roughly 1/2 the number of electrons present within this range of the device.

Table I

Effect of the emitter-base junction type and Fermi level pinning on the calculated value of the emitter current gain, β.

Case 1: Fermi level remains pinned at the base contact

	Abrupt Junction	Graded Junction
β	6.0	3.6

Case 2: High energy injection maintained.

	Abrupt Junction	Graded Junction
β	6.0	7.15

Table II

Valley population percentages in the base and collector regions of the device.

Case 1: V_{BC}=0.0V, low energy injection, with Fermi-level pinning at the base contact.

	Base	Extrinsic Base	Collector	Extrinsic Collector
Γ	100.0	100.0	46.1	68.9
L	0.0	0.0	48.8	26.4
X	0.0	0.0	5.1	4.7

Percentage of total concentration.

Base	Extrinsic Base	Collector	Extrinsic Collector
38.4	7.4	33.0	21.2

Case 2: V_{BC}=-5.0V, low energy injection, with Fermi-level pinning at the base contact.

	Base	Extrinsic Base	Collector	Extrinsic Collector
Γ	100.0	100.0	9.6	8.9
L	0.0	0.0	64.2	66.7
X	0.0	0.0	26.2	24.4

Percentage of total concentration.

Base	Extrinsic Base	Collector	Extrinsic Collector
32.1	7.2	43.9	16.8

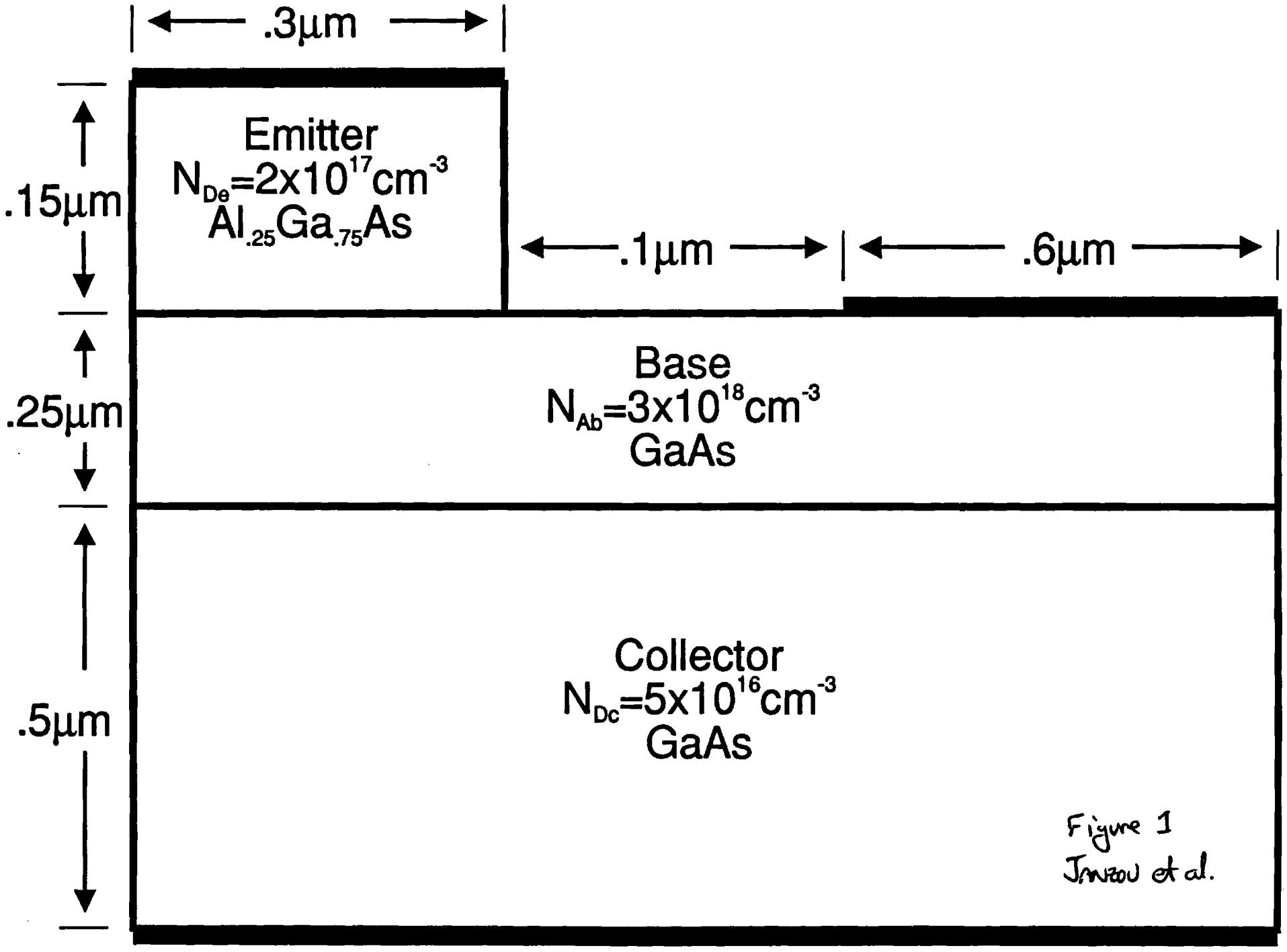

Figure 1
Inuzou et al.

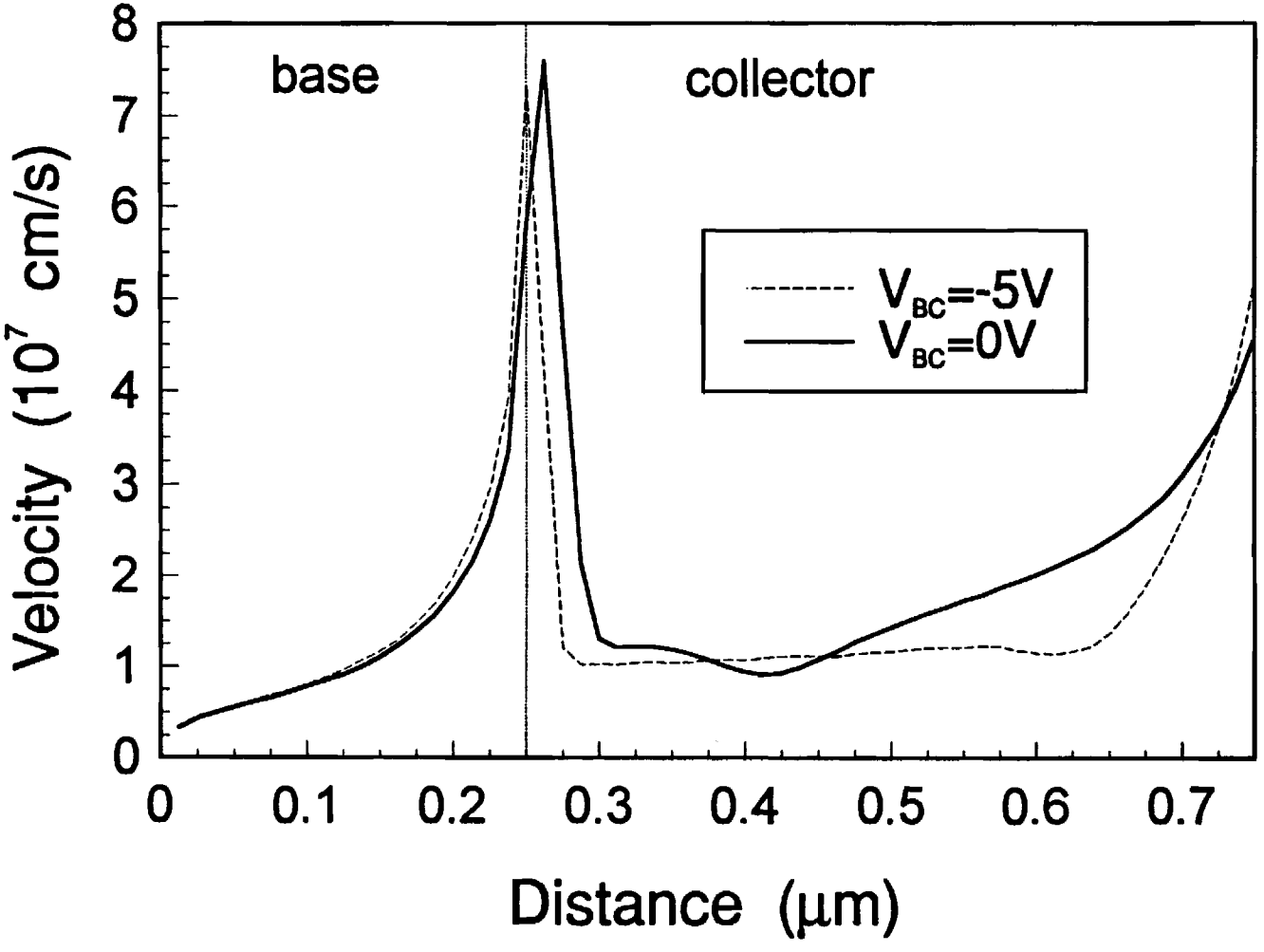

Figure 2
Jaouen et al.

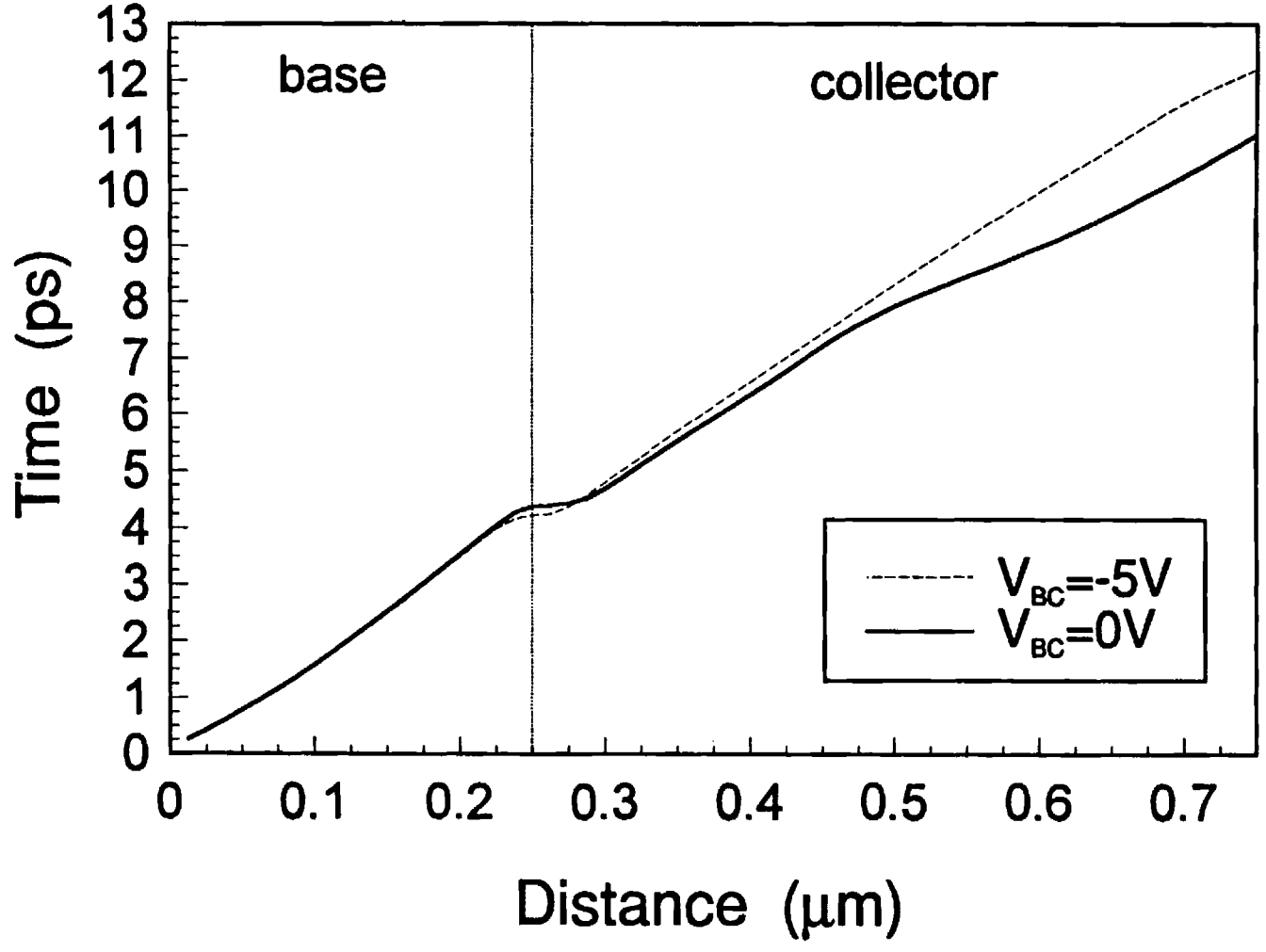

Figure 3
Janzou et al.

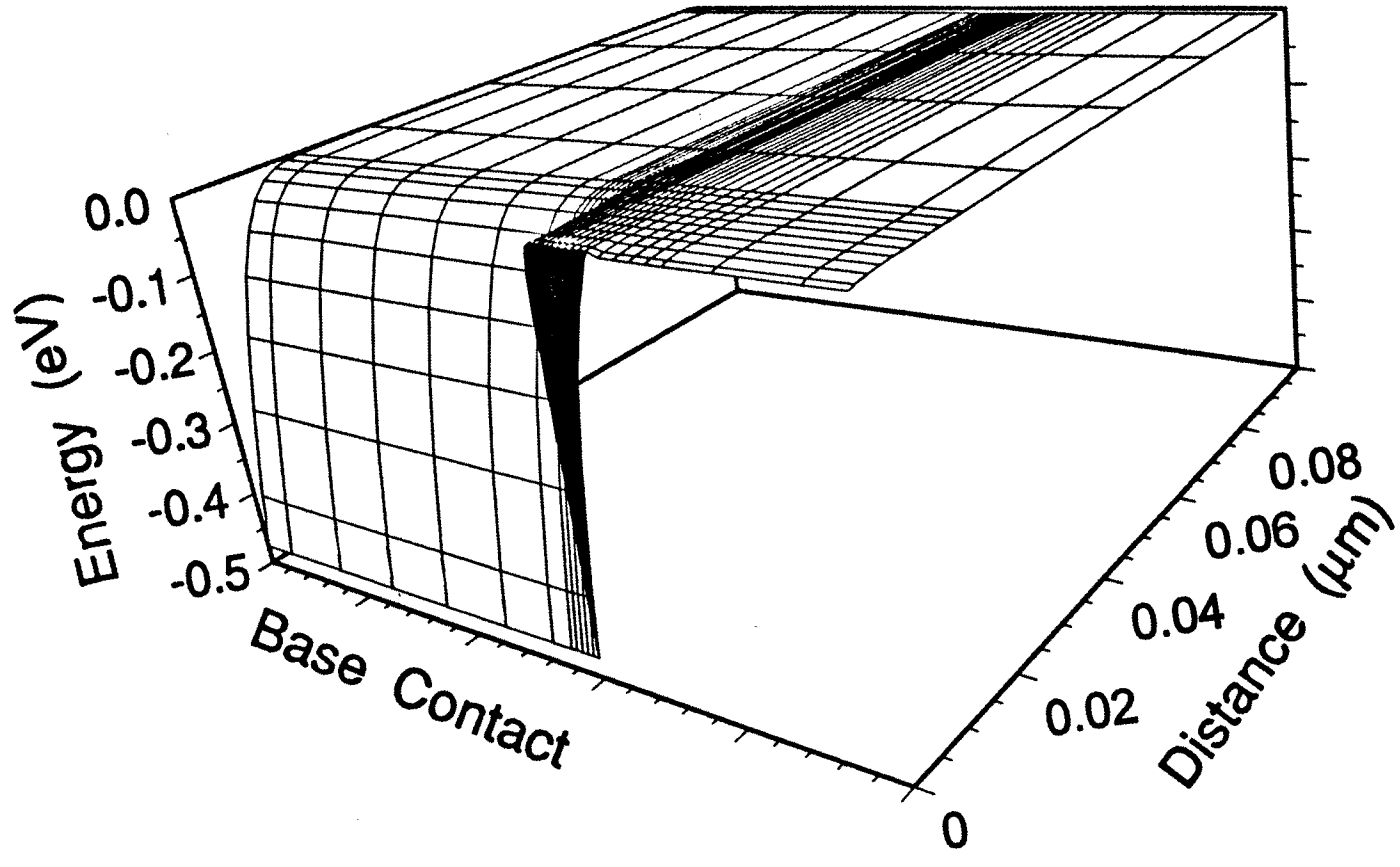

Figure 4
Inazu et al.

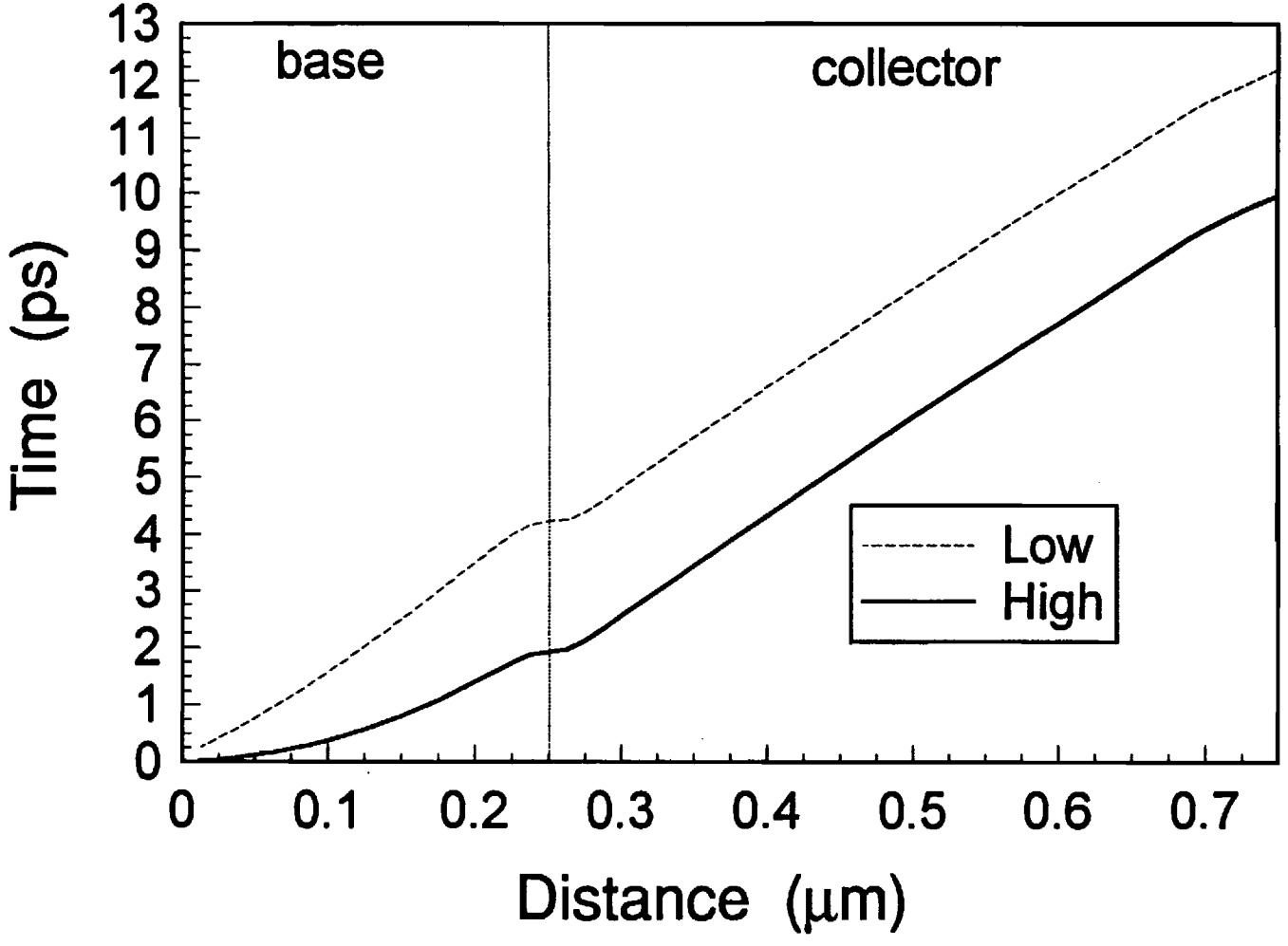

Figure 5
Inzlow et al.

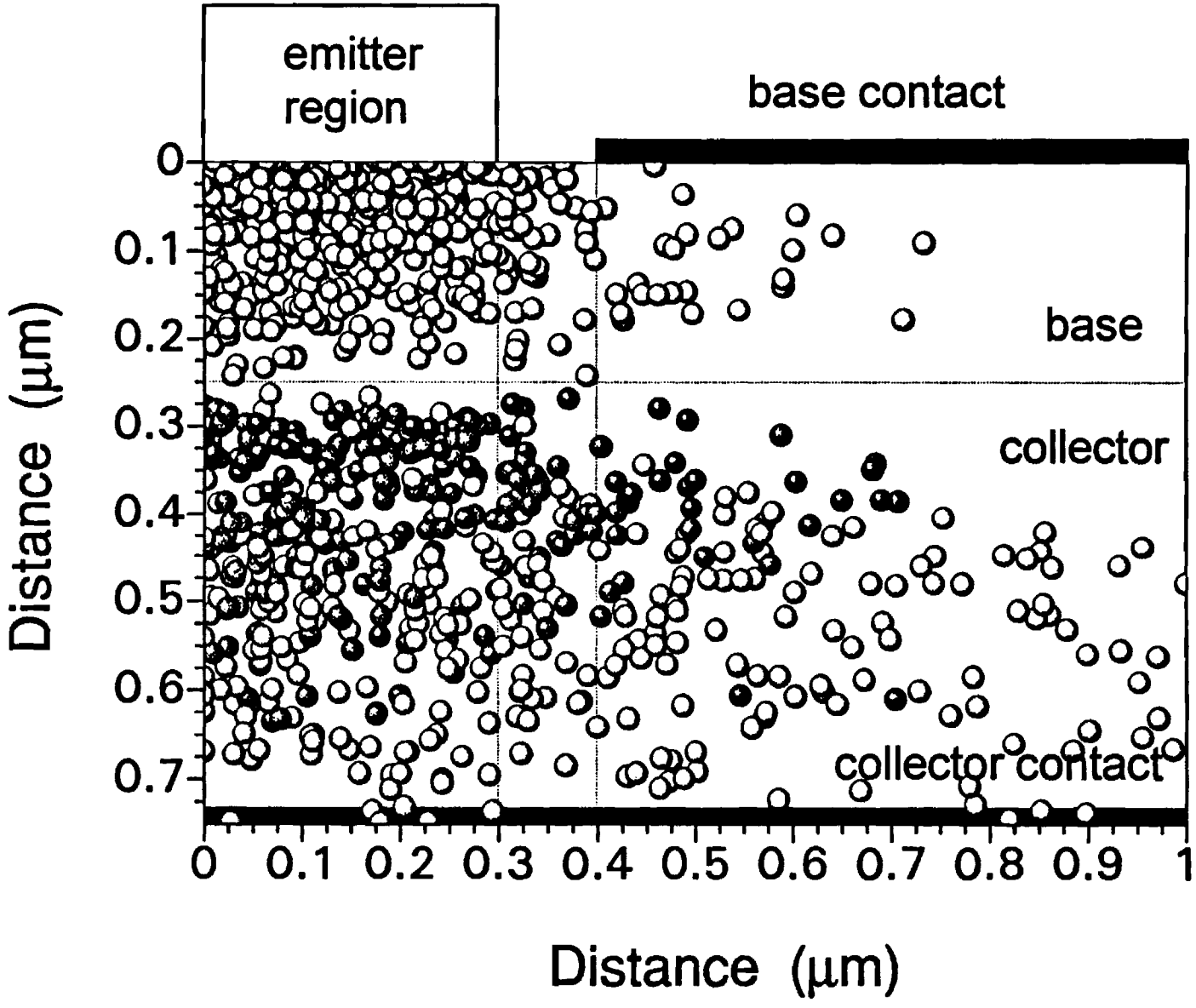

Figure 6
Inoue et al.

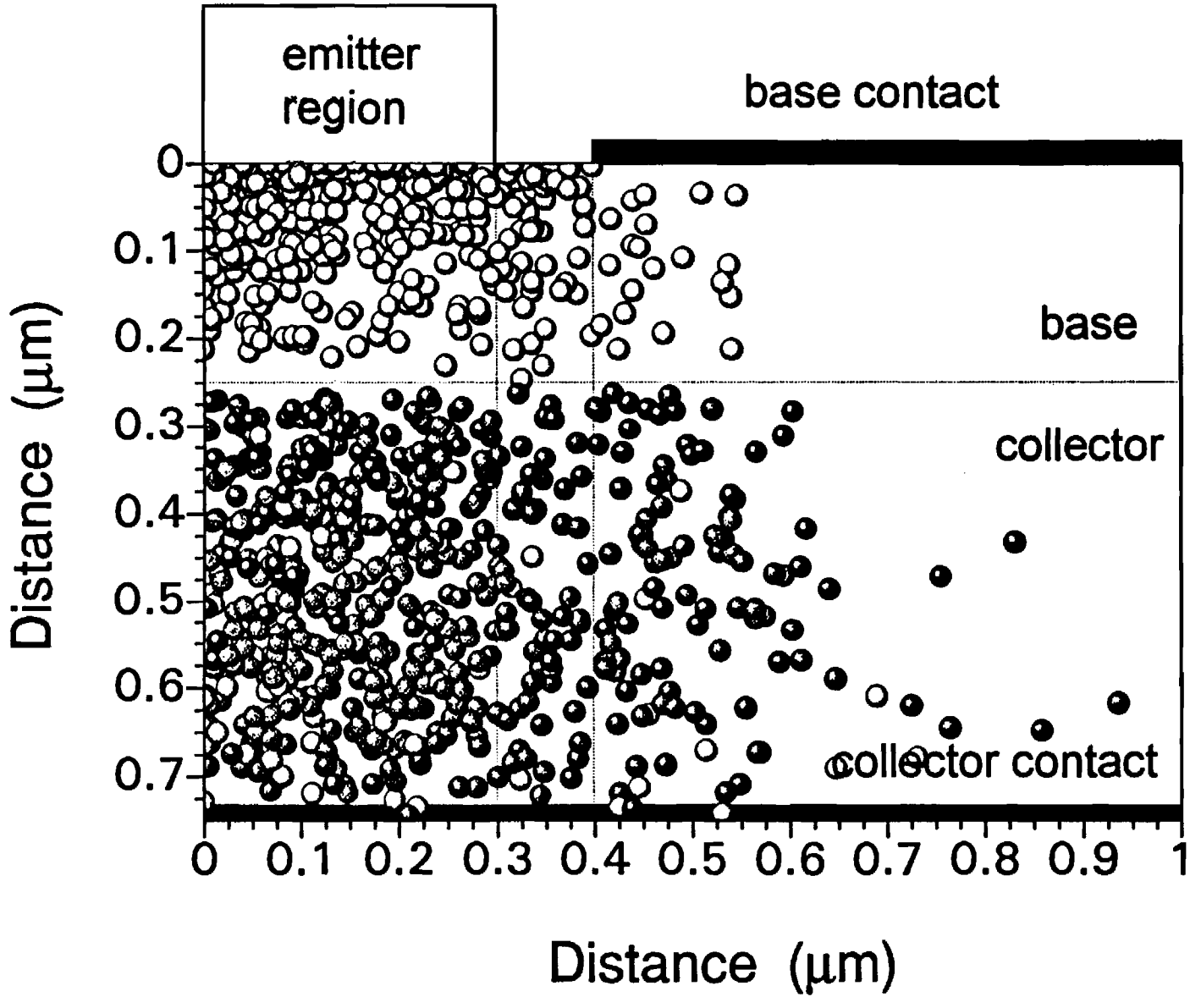

Figure 7
Jansen et a

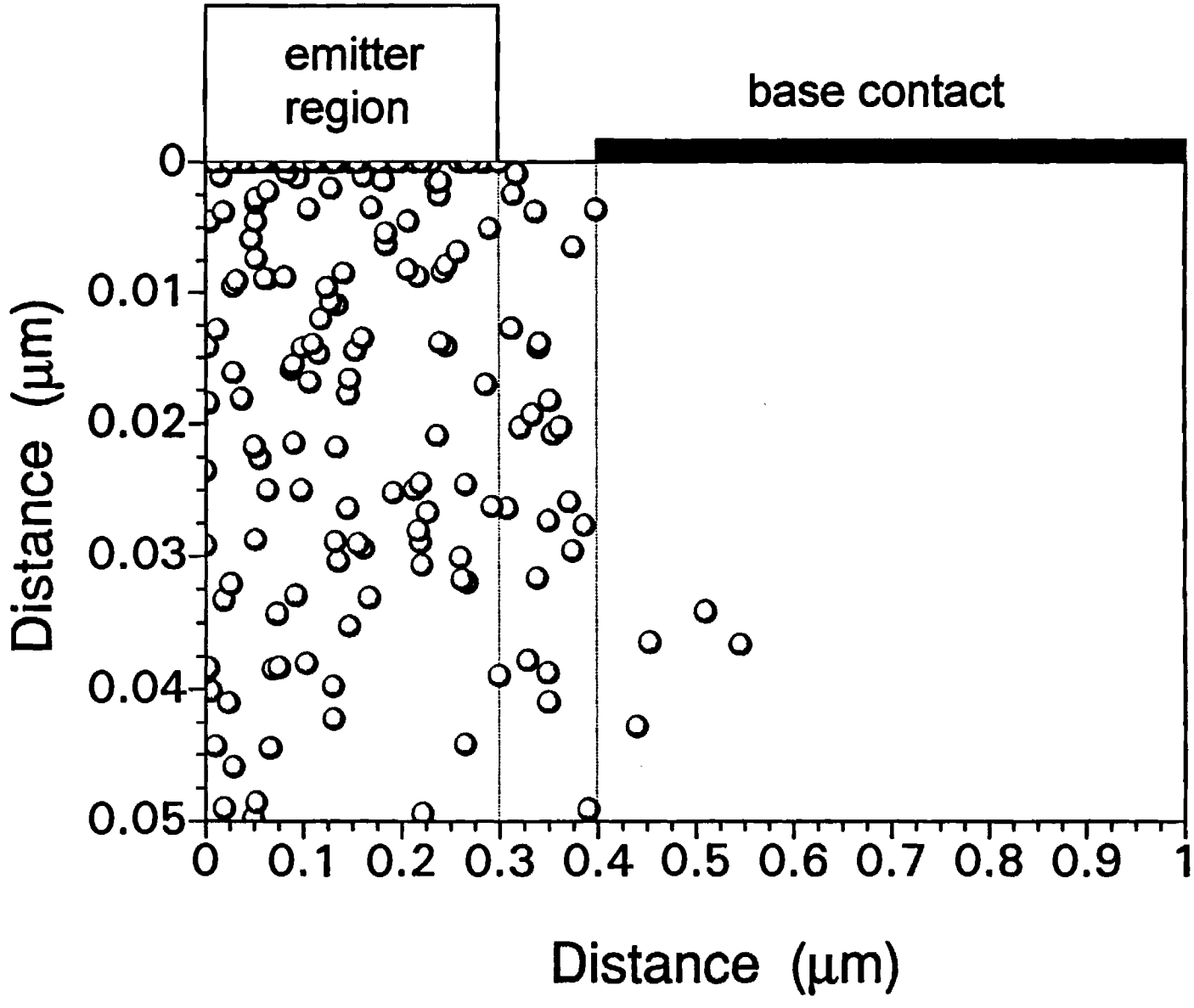

Figure 8
Janzen et al.

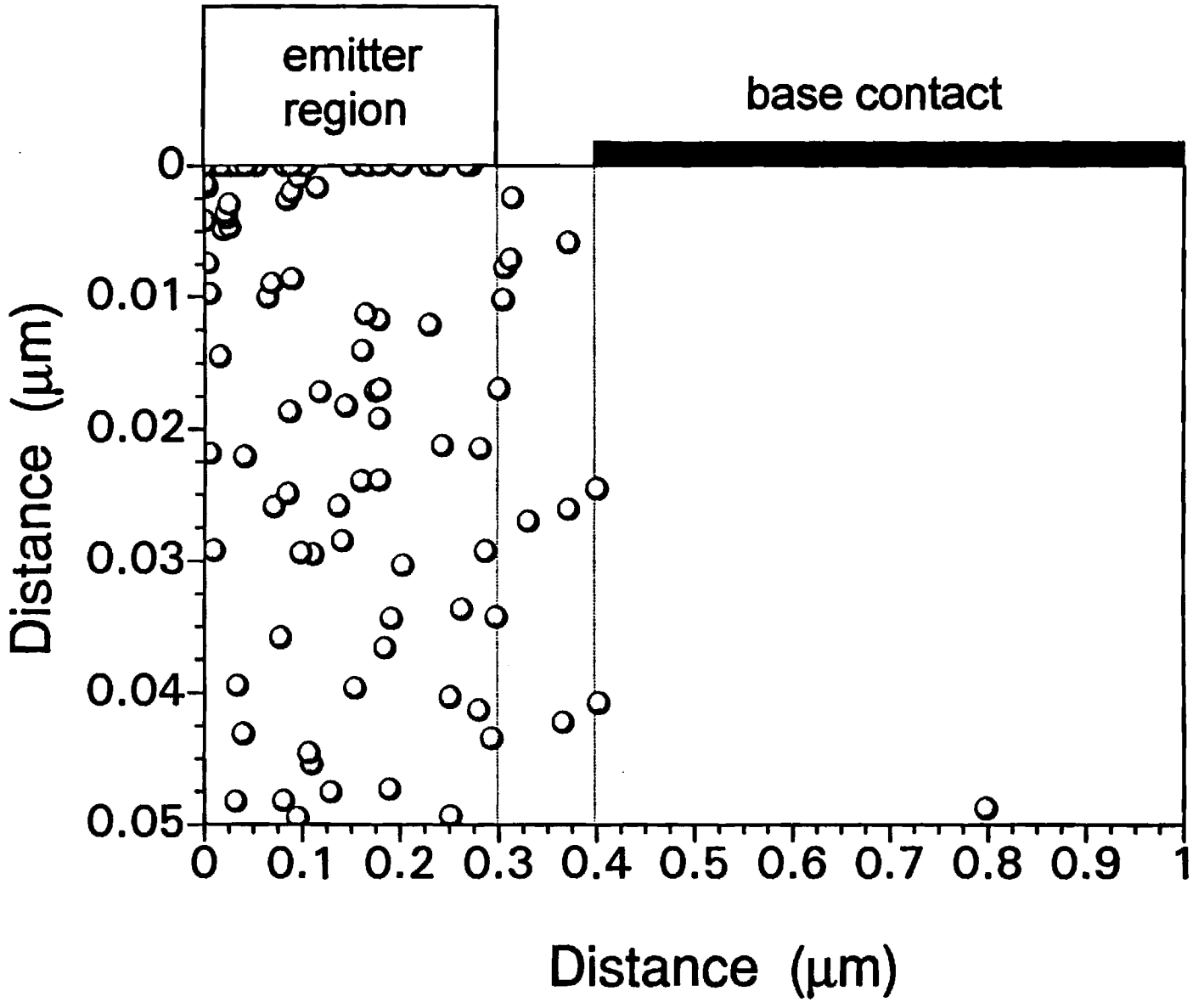

Figure 9
Janzov et al.

1992-1993 Annual Project Report: Motorola, Inc.

Project Title: Modelling of Three Terminal Semiconductor Devices: Heterojunction Bipolar Transistors (HBTs)

Investigators: Steven H. Janzou and Dr. Kevin F. Brennan

Organization: School of Electrical Engineering and
Microelectronics Research Center
Georgia Institute of Technology
791 Atlantic Drive, NW
Atlanta, GA 30332-0269
(404) 894-6767

Abstract

During the last year of the project many issues have been addressed. The three primary areas of focus have been: 1) Fermi-level pinning along the free surface between the emitter and base contacts, 2) conduction band step structures added in the high field collector regions, and 3) development of the self-consistent Hybrid model, in which the potential and the hole transport dynamics are described by a Drift-Diffusion model, and the electron transport dynamics are described by an Ensemble Monte-Carlo model. The investigation of Fermi-level pining showed that the high speed performance of AlGaAs/GaAs HBTs is relatively insensitive to the pinning condition. The addition of step structures to the collector region showed that faster transit times are possible but difficult to realize in the AlGaAs/GaAs material system. The ongoing development of the self-consistent Hybrid model will allow a more detailed study of HBTs through accurate inclusions of two-dimensional effects (pinning, charge spreading, current crowding, etc.) . From this Hybrid model the ultimate goal of this project, the long term prospectus of HBTs, will be achieved.

Work Completed

1. Fermi-level Pinning

The study of Fermi-level pinning along the free surface between the emitter and base contacts [1] demonstrated that the major high-speed effect of the pinning was on the base transit time. The collector transit time was found to be almost independent of the presence or absence of pinning. As is well known, the base transit time in AlGaAs/GaAs HBTs can be made a negligible component of the overall base collector transit time by using thin base regions. The base transit time is a primary concern in Si-Ge HBTs [2]. Therefore, the study of the Fermi-level pinning on high-speed performance is more appropriate for Si-Ge HBTs. This is a subject of future work which will involve the reformulation of an existing Si Monte Carlo model [3] to HBT structures.

The dc effect of the pinning has been shown experimentally to reduce the common emitter current gain, β [4]. To compute β, accurate calculations of the current densities are required. The hole current density is calculated using a drift-diffusion formulation. In order to include non-stationary transport effects, the electron current density is computed through the Monte Carlo model. Since the potential is a function of both the hole and electron distributions, realistic computations necessitate the updating of the potential and hole distributions after the electron distribution has changed. This is the primary goal of the Hybrid model which will be described later.

2. Collector Step Structures

The incorporation of conduction band step structures in the collector region of HBT devices to reduce the base collector transit time was examined. Both ascending steps [5] and descending steps [6] were included into HBT collector structures. The ascending steps were considered because they showed good Γ-valley confinement as described by Brennan [5]. Several ascending step structures were studied. However, when ascending step structures were used in the collector regions in HBTs, the additional electric field from the ascending steps increased [7] the already high collector depletion fields leading to rapid intervalley transfer which reduced the overall average velocity in the devices. The conduction band profile and the average velocity as a function of distance from the emitter-base junction for a typical ascending step structure HBT are shown in Fig. 1 and Fig. 2, respectively. The HBT structure examined in these figures consisted of a 1500Å n-$2\times10^{17}cm^{-3}$ $Al_{0.3}Ga_{0.7}As$ emitter region, a 500Å P-$10^{19}cm^{-3}$ GaAs base region, and a collector which consisted of a 1500Å i-GaAs region and a 2500Å n-$5\times10^{16}cm^{-3}$ GaAs region. The HBT was simulated with a forward base-emitter bias of 1.5V and no base-collector bias. In Fig. 1 and Fig. 2, three ascending steps were added to the collector region starting 200Å from the base-collector junction (junction at 500Å in Fig. 1 and Fig. 2). Each step had a conduction band discontinuity of 170meV ($X_{Al} = 0.22$) and a step length of 500Å. In Fig. 1 and Fig. 2, the dotted line corresponds to the HBT structure with no steps and the solid line corresponds to the HBT with the ascending steps added. In the velocity curve of Fig. 2, the velocity is initially reduced when the steps are added due to low energy electrons which are scattered back

toward the emitter base junction from the first ascending step shown at 700Å in Fig. 1. The velocity drops faster and lower with the steps added due to the higher fields which lead to earlier intervalley transfer. The velocity increases after the steps are crossed (700Å, 1200Å, and 1700Å) due to energy loss and subsequent reentry into the high speed Γ-valley. The conduction band discontinuities using $Al_xGa_{1-x}As$ could not be made large enough to compensate for the high field resulting from the collector depletion field and the ascending step field. Therefore, different material systems need to be considered when using ascending steps. Another possible problem with the ascending step structure is charge trapping at the step edge (see Fig. 1).

Descending step collector structures were then considered for high speed HBT performance. Descending steps showed promise by allowing for repeated velocity overshoot [6] and by reducing [7] the high field in the collector regions of HBTs. When the descending steps are used in the collector region in an HBT structure, the high collector field can be reduced to a reasonable value ($\lesssim$ 10kV/cm). An optimal range of field values (5kV/cm to 10kV/cm) was determined by running Monte Carlo simulations for intrinsic GaAs with different energy injection values for electrons and different background fields guided by the work of Tang and Hess [8]. After testing many configurations, we found that a descending step structure consisting of four steps: (1) ΔE_C=350meV, SL=1390Å, (2) ΔE_C=350meV, SL=1040Å, (3) ΔE_C=93meV, SL=300Å, (4) ΔE_C=93meV, SL=800Å; added to the collector region 30Å from the base-collector junction reduced the base collector transit time by 15%. The underlying HBT structure consisted of a 1500Å n-$2x10^{17}cm^{-3}$ $Al_{0.3}Ga_{0.7}As$ emitter region, a 500Å P-$10^{19}cm^{-3}$ GaAs base region, and a collector which consisted of a 2500Å i-GaAs region and a 5000Å n-$10^{16}cm^{-3}$ GaAs region. The HBT was simulated with a forward base-emitter bias of 1.5V and no base collector bias. The conduction band profile and the average velocity as a function of distance from the emitter-base junction are shown in Fig. 3 and Fig. 4, respectively. In Fig. 3 and Fig. 4, the dotted line corresponds to the HBT structure with no step structure and the solid line corresponds to the HBT with the above descending step structure added. In Fig. 4, the velocity is shown to be greatly enhanced over the first descending step (530Å to 1920Å), toward the end of the second step (1920Å to 2960Å), toward the end of the third step (2960Å to 3260Å), and toward the end of the fourth step (3260Å to 4060Å). At the end of each step the velocity drops sharply and then rises to values above that without the step structure. The drops in velocity at each step edge are due to the large gain in energy from the step as shown in Fig. 3. One problem with the descending step structures is that with the limit of X_{Al}=0.45 (ΔE_C=0.35eV), and the high collector fields (~35kV/cm in i-GaAs region), the step length is limited to $\leq$1400Å in order to achieve a optimal overall field value $\leq$10kV/cm. Since very few scatterings occur over this step length [8], there is very little energy loss in the step. However, the field provides an energy gain mechanism which increases the energy of the electron. The overall effect on the electron energy is a net increase for all fields above ~2kV/cm. Therefore, at the end of each step the large conduction band discontinuity leads to intervalley transfer and the reduction in velocity as shown in Fig. 4. Since these calculations were done in a non self-consistent manner (i.e. with a fixed steady-state field) and showed only a 15% improvement, no manuscript was submitted for publication. This work will be completed as soon as the self-consistent Hybrid model is operational.

Doping variations to decrease the overall collector field have also been examined. From the p^+-base region, short variously doped regions are added until the bulk n-collector region doping is reached. For example, we considered p^+-i-p-i-n^--i-n doping with regional lengths of 200Å to 500Å added to the collector. This progressive doping acts to reduce the field over most of the collector. A problem with this approach is that for dopings less than $\sim 5x10^{16}cm^{-3}$ the field becomes very large and a short high field transition from the p^+-base region to n-collector region becomes difficult. The best doping configuration appears to be similar to that proposed by Katoh *et. al.* [9].

Using steps and doping in the collector region provides additional engineering parameters for designing high speed HBTs. The parameters of step length and step discontinuity are available when using step collector structures. The parameters of doping region length and doping concentration are available when considering doping collector structures. A combination of these four parameters will lead to enhanced transport through the collector region. We have examined different combinations of steps and dopings in order to optimize device speed - increases in average electron velocities and reductions in transit times. We have not studied the effects of these collector structures in a self-consistent manner (i.e. field updating throughout simulation). When these devices are studied using the Hybrid model, we will be able to accurately describe performance at various current densities and accurately assess dc behavior through the common emitter current gain.

Work in Progress

Our current focus is on the development of the self-consistent Hybrid model. As mentioned in all our studies to date, the calculations of engineering figures of merit require the accurate assessment of current densities. In order to remove any arbitrariness and to minimize approximations in the current density calculations an accurate self consistent model is desired. In a self-consistent Hybrid model, the potential and hole dynamics will be described by a Drift-Diffusion model (DDM) [10] and the high speed non-stationary transport dynamics of the electrons will be described by an ensemble Monte-Carlo model (EMC) [11]. Each of the DDM and the EMC is currently working independently for various HBT structures. All the calculations presented in this report have been done using the two models in a non self-consistent manner. That is, a given HBT structure is first simulated using the DDM to obtain the steady-state potential, electron, and hole distributions. The steady-state potential is used to determine the fixed steady-state field to be used throughout the EMC model simulation. The EMC model then simulates the electron dynamics using this steady-state field. In the self-consistent Hybrid model, the potential and hole distributions will be updated at a given time interval (~50fs) by the DDM while the electron dynamics will be continually updated by the EMC model.

To accomplish the Hybrid model, a robust fast DDM is necessary. For frequent updating of the potential and hole distribution the underlying matrix solver must be fast and stable. We have evaluated several packages to accomplish this task. We are currently using the NSPCG [12] library. However, we have found this package unsuitable for some HBT structures. To that end we have been developing a more robust matrix solver to handle these

cases. It is based on a Bi-Conjugate Gradient method [13] of solving finite differences. We are currently finishing this matrix solver. Also, our new post-doctoral assistant Dr. Arlynn Smith has been developing an adaptive gridding algorithm to enhance both the speed and accuracy of the DDM which he developed and will be used in the Hybrid model.

Future Work

A projected time line is shown in Fig. 5. When the self-consistent Hybrid model is complete, we plan to first reexamine the Fermi-level pinning at the base contact in the context of a self-consistent two-dimensional model. In this manner, we will be able to accurately calculate current densities and, hence, β. Next, we will reexamine the step and doping modifications to the collector region to calculate their effect on HBT performance. Then, we will determine the range of performance increases in the BCT devices [14]. We will examine various lengths and dopings of the collector structures and calculate their effect on device characteristics (average velocity, transit times, average energy, etc.). We plan on initially examining HBT structures in the AlGaAs/GaAs material system and then looking at other binary and ternary systems (e.g. AlInAs/InP). Also, as previously mentioned, we can extend a different Monte Carlo simulation model to examine the Fermi-level pinning effect in the Si material system.

Projected Time Line for 1993-1994

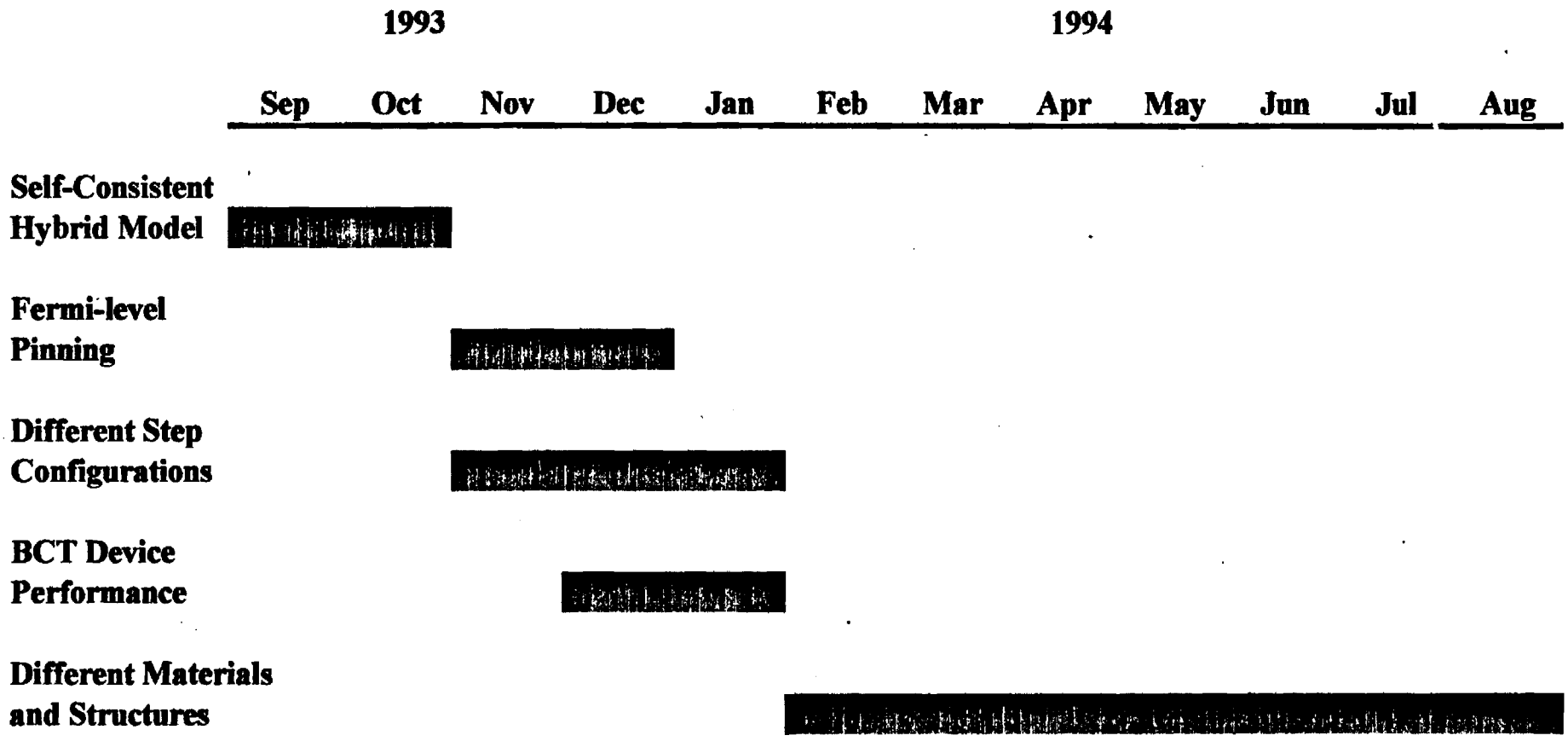

References

[1] S.H. Janzou, N.S. Mansour, A.W. Smith, K.F. Brennan, and H.Goronkin, "Ensemble Monte Carlo Study of Fermi-level Pinning and Emitter-Base Junction Type in AlGaAs/GaAs Heterojunction Bipolar Transistors," Manuscript being reworked for resubmission to *IEEE Trans. Elec. Dev.*

[2] S.S. Iyer, G.L. Patton, J.M.C. Stork, B.S. Meyerson, and D.L. Harame, "Heterojunction bipolar transistors using Si-Ge alloys," *IEEE Trans. Elec. Dev.*, vol. 36, no. 10, pp. 2043-2064, Oct. 1989.

[3] J.Y. Tang and K. Hess, "Impact ionization of electrons on silicon (steady state)," *J. Appl. Phys.*, vol. 54, pp. 5139-5144, 1983.

[4] W-S. Lee, D. Ueda, T. Ma, Y-C. Pao, and J.S. Harris, Jr., "Effect of emitter-base spacing on the current gain of AlGaAs/GaAs heterojunction bipolar transistors," *IEEE Elec. Dev. Lett.*, vol. 10, no. 5, pp. 200-202, May 1989.

[5] K. Brennan and K. Hess, "Transient electronic transport in staircase structures," *IEEE Elec. Dev. Lett.*, vol. EDL-4, no. 11, pp. 419-421, Nov. 1983.

[6] J.A. Cooper, Jr., F. Capasso, and K.K. Thornber, "Semiconductor structures for repeated velocity overshoot," *IEEE Elec. Dev. Lett.*, vol. EDL-3, no. 12, pp. 407-408, Dec. 1982.

[7] K.W. Böer, Survey of Semiconductor Physics Volume II: Barriers, Junctions, and Devices. New York: Van Nostrand Reinhold, 1992, pp. 680-681.

[8] J.Y-F. Tang and K. Hess, "Investigation of transient electronic transport in GaAs following high energy injection," *IEEE Trans. Elec. Dev.*, vol. ED-29, no. 12, pp. 1906-1911, Dec. 1982.

[9] R. Katoh, M. Kurata, and J. Yoshida, "Self-consistent particle simulation for (AlGa)As/GaAs HBT's with improved base-collector structures," *IEEE Trans. Elec. Dev.*, vol. 36, no. 5, pp. 846-853, May 1989.

[10] A. W. Smith, "Light confinement and hydrodynamic modelling of semiconductor structures by volumetric methods," Ph.D. Thesis, Georgia Institute of Technology, Atlanta, Ga., May 1992.

[11] K.F. Brennan, D.H. Park, K. Hess, and M.A. Littlejohn, "Theory of the velocity-field relation in AlGaAs," *J. Appl. Phys.*, vol. 63, pp. 5004-5008, May 15, 1988.

[12] T.C. Oppe, W.D. Joubert, and D.R. Kincaid, "An overview of NSPCG: a nonsymmetric preconditioned conjugate gradient package," *Comp. Phys. Comm.*, vol. 53, pp. 283-293, 1989.

[13] H.A. Van Der Vorst, "Bi-CGSTAB: a fast and smoothly converging variant of Bi-CG for the solution of nonsymmetric linear systems," *SIAM J. Sci. Stat. Comput.*, vol. 13, no. 2, pp. 631-644, Mar. 1992.

[14] H. Nakajima, M. Tomizawa, and T. Ishibashi, "Monte Carlo analysis of the space-charge effect in AlGaAs/GaAs ballistic collection transistors (BCT's) under high current injection," *IEEE Trans. Elec. Dev.*, vol. 39, no. 7, pp. 1558-1563, July 1992.

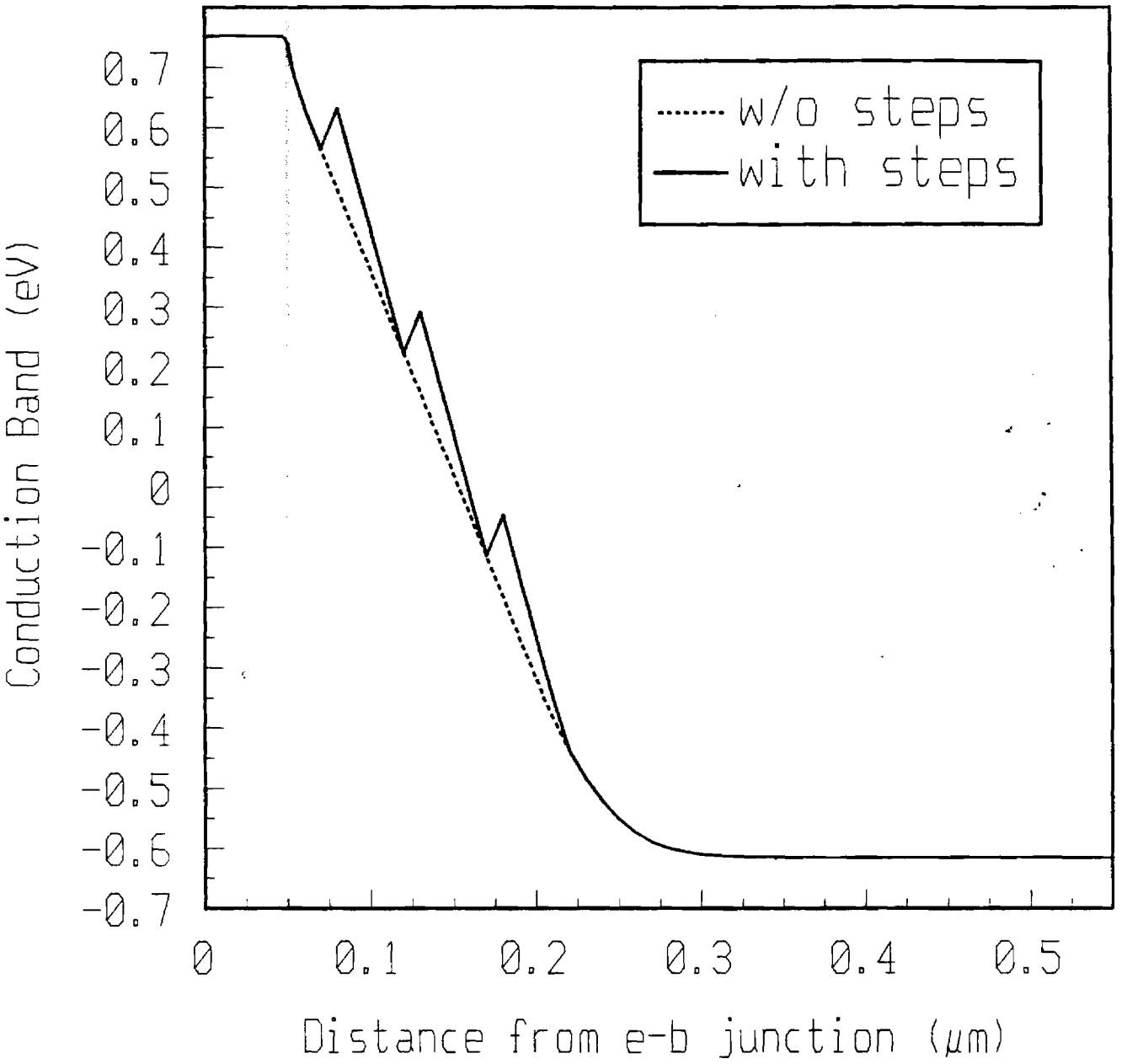

Fig. 1 Conduction band as a function of position in the base and collector regions of the device. The base-collector junction is shown at 500Å. The solid curve is the conduction band of the HBT structure with the ascending steps added. The steps start at 700Å. The dotted curve is the conduction band of the HBT structure without any steps.

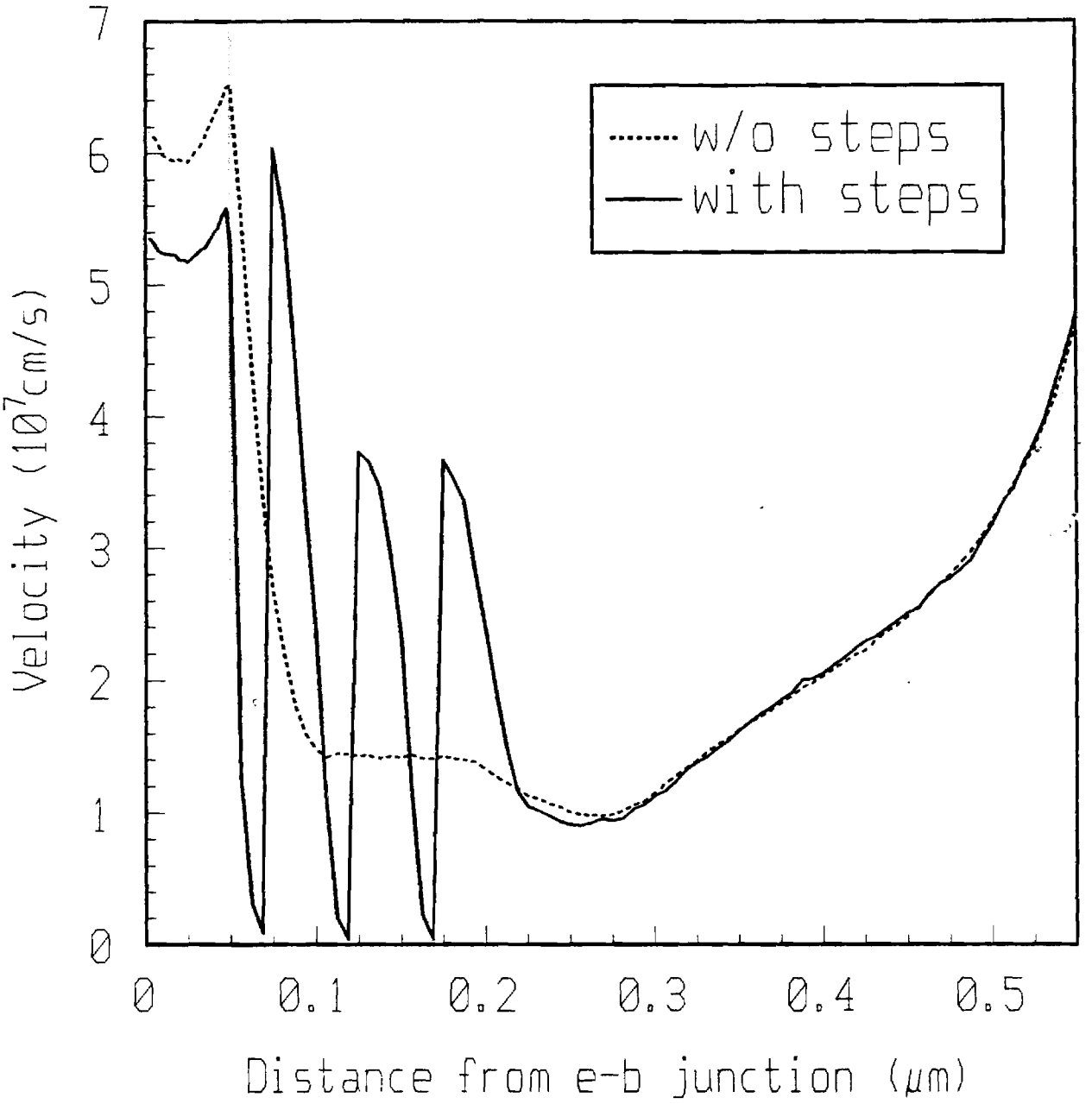

Fig. 2 Velocity as a function of position in the base and collector regions of the device. The base-collector junction is shown at 500Å. The solid curve is the velocity of the HBT structure with the ascending steps added. The steps start at 700Å. The dotted curve is the velocity of the HBT structure without any steps.

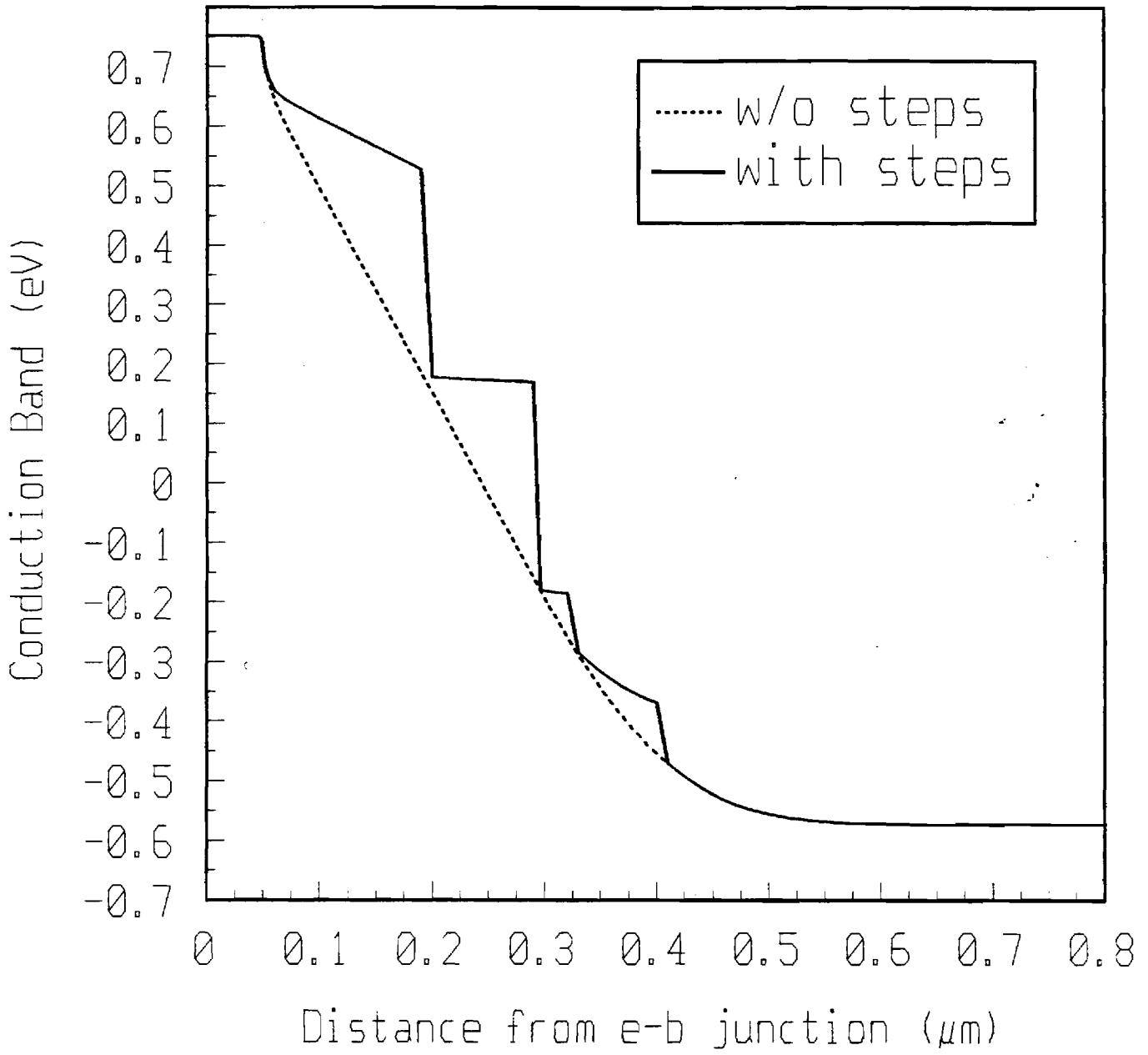

Fig. 3 Conduction band as a function of position in the base and collector regions of the device. The base-collector junction is shown at 500Å. The solid curve is the conduction band of the HBT structure with the descending steps added. The steps start at 530Å. The dotted curve is the conduction band of the HBT structure without any steps.

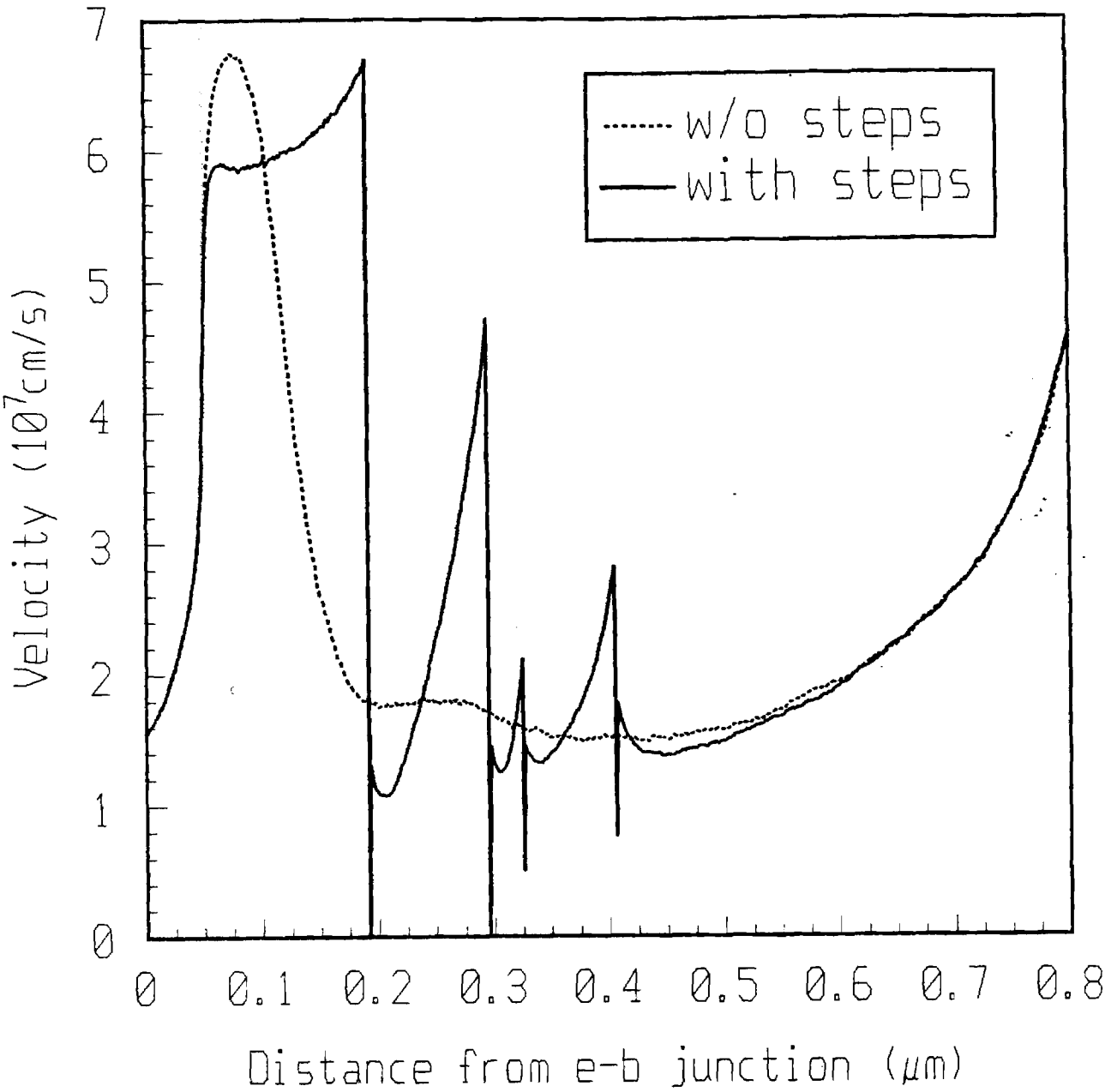

Fig. 4 Velocity as a function of position in the base and collector regions of the device. The base-collector junction is shown at 500Å. The solid curve is the velocity of the HBT structure with the descending steps added. The steps start at 530Å. The dotted curve is the velocity of the HBT structure without any steps.

Annual Report: Motorola Corp.

Contract #: E21-635

Deliverable #: 5

Title: Modeling of Three Terminal Devices

Authors: Steven H. Janzou and Kevin F. Brennan

Address: School of Electrical and Computer Engineering

Georgia Tech

Telephone: 894-6767

Abstract

In this report we present a summary of the advances made to a combined Monte Carlo- drift diffusion simulator for advanced heterostructure transistor simulation. During the past year several improvements to the simulator have been made. Among these are the inclusion of statistical enhancement in the regions of interest and improved treatment of the charge assignment and field interpolation. Current work is progressing towards studying current crowding in HBT structures and comparison of the workings of devices made from different materials.

Motorola Report

This report is a summary of the recent advances in our model development. Our heterojunction bipolar transistor (HBT) simulator consists of an ensemble Monte Carlo (EMC) model [1], and a drift diffusion model (Semiconductor transport energy balance simulation in two-dimensions STEBS2D) [2]. Electron and hole transport dynamics are described using the EMC model and the drift diffusion model, respectively. The Poisson equation is then updated at regular intervals to give an overall self-consistent simulation.

Our recent advances include:

1. Self-consistent updating of the Poisson equation.
2. Statistical enhancement in regions of interest.
3. Additional stability and enhancement to the underlying drift diffusion model.
4. Inclusion of the emitter region into the EMC portion of the simulation.
5. Higher order schemes for EMC electron assignment and field interpolation.

The remaining portion of this report discusses each of the above in detail with figures of some the results obtained to date.

First, the self-consistent updating of the Poisson equation has been recently achieved. The self-consistency allows for the examination of the interaction between the EMC electrons and the field. That is, long range electron-electron plasmon effects are naturally included. Also, charge assignment to the underlying EMC electrons is included for direct electron current calculations from the simulation. The effect of self-consistency can be seen in the velocity plots shown in Figs. 1-2. The simulated HBT structure is shown in Fig. 3. The orientation of Figs. 1-2 is such that the emitter contact is shown in the foreground and the collector contact is in the background. For

reference, the emitter contact is located vertically at 0μm and extends laterally from 0μm to 0.3μm, the base contact is located vertically at 0.2μm and extends laterally from 0.6μm to 0.9μm, and the collector contact is located vertically at 1.5μm and extends laterally across the entire device from 0μm to 0.9μm. Fig. 1 is for a self-consistent simulation in which the Poisson update frequency is 25fs; whereas, Fig. 2 shows the velocity profile when no Poisson equation update is performed (a non self-consistent simulation). The non self-consistent simulation results in an artificial increase in velocity throughout the collector bulk region (0.8μm to 1.5μm vertical distance in Fig. 2) due to the absorbing nature of the collector contact [3]. In the self-consistent solution, this velocity increase artifact is restricted to a much smaller region at the collector contact through the use of an appropriate EMC ohmic boundary conditions. The self-consistency allows for charge assignment of the EMC electrons which allows for local space charge neutrality to be enforced near the ohmic contacts. The region over which this EMC ohmic boundary condition is applied (1.4μm to 1.5μm vertical distance in Fig. 1) corresponds exactly to the region over which the rise in velocity occurs in the self-consistent simulation. Thus, the artificial rise in velocity due to the absorbing nature of the EMC collecting boundaries is minimized in a self-consistent simulation. In both the self-consistent and non self-consistent simulations, the HBT device is first simulated using the drift diffusion model. The drift diffusion results are then used by the EMC model to determine the initial number of physical electrons each EMC electron represents. In this manner, electron current calculations are made possible directly from the model. In the self-consistent simulations, the field profile dynamically changes based on the instantaneous positions of the EMC electrons, thereby describing electron transport more accurately than in the non self-consistent scheme in which the steady state drift diffusion field is used throughout.

Secondly, statistical enhancement [4] has been included in the model. The effect of statistical enhancement can be seen in Figs. 4-5. In Figs. 4-5, EMC electron count as a function of position is plotted. Figs. 4-5 are oriented such that the base contact is shown in the foreground and the collector contact is in the background. As in Fig.1-2, the emitter contact is located vertically at 0μm and extends laterally from 0μm to 0.3μm, the base contact is located vertically at 0.2μm and extends laterally from 0.6μm to 0.9μm, and the collector contact is located vertically at 1.5μm and extends laterally across the entire device from 0μm to 0.9μm. In Fig. 4, the simulation is run with 5000 EMC electrons for 25ps with no statistical enhancement. In Fig. 5, the simulation is run for 25 ps with 1000 initial EMC electrons with a statistical enhancement factor of 10 in the base and base-collector depletion regions (0.2μm to 0.8μm vertical distance in Fig. 5). Without any statistical enhancement, there are more EMC electrons in the emitter region than in the base and base-collector depletion regions as shown in Fig. 4. When statistical enhancement is employed as in Fig. 5, the number of EMC electrons in the emitter is significantly reduced and the number of EMC in the base and base-depletion region is increased. By use of statistical enhancement, the number of EMC electrons in areas of interest can be increased and the number of EMC electrons in unwanted regions of the structure can be decreased. Thus, more accurate physical quantities can be obtained in regions where non stationary transport is known to occur.

Thirdly, the drift-diffusion model has been significantly improved through the use of a different matrix storage mechanism and a new solution method. The matrix solution method used by the drift diffusion model is the NSPCG library [5]. By applying a different storage mechanism to the matrix, a significant (6.7 times) decrease in computational time is achieved. Also, the conjugate gradient squared method of solution results in a faster more stable solution profile than

the previously used generalized minimal residual method.

Fourthly, the emitter region shown in Fig. 3 is now included into the simulation model. Previously, the emitter region was not included in the simulation due to the electron retarding field present. Very few of the EMC electrons launched at the emitter contact would be able to surmount this retarding field. Thus, large statistical fluctuations in the values of the physical observables (energy, velocity, etc.) would be obtained throughout most of the simulated region (base and collector). As shown in Figs. 4-5, statistical enhancement can be used to increase the number of EMC electrons and, hence, the accuracy of the observables in the areas of interest in these structures. With the inclusion of the emitter region, emitter transit times are directly obtained from the simulation - eliminating the need for analytical approximations.

Finally, a higher order scheme is employed in EMC electron assignment and field interpolation. Since the simulation model uses discrete EMC electrons and then updates the continuous Poisson equation, an assignment scheme must be used to associate the EMC electrons to the underlying mesh used to solve the Poisson equation. The EMC electron assignment scheme used previously was a cloud in cell method (CIC) [6]. This method uses only the nearest four mesh points over which to spread the EMC electron. Thus, the CIC method is extremely sensitive to the mesh spacing. In HBT simulations, a highly non-uniform mesh is used to account for the locally large potential variations. Therefore, the CIC method leads to large variations in the electron distribution and has led to non convergence of the Poisson equation solution. To avoid these convergence problems, a higher order (second order accurate) triangular square cloud (TSC) EMC electron assignment scheme is employed. In the TSC scheme, an EMC electron is spread to the underlying grid over a constant radius. This leads to not only a numerically stable system but also a more physically realistic situation.

Future Directions

With the recent advancements in the model, an examination of the current crowding problem [7-9] is currently being assessed. Next, a study of different material systems will be performed. Finally, the use of a hydrodynamic model augmented with EMC parameters will be used to examine HBT structures. The EMC model will be used to obtain mobilities and diffusivities as a function of energy for use in the hydrodynamic model.

References

[1] K.F. Brennan, D.H. Park, K. Hess, and M.A. Littlejohn, "Theory of the velocity-field relation in AlGaAs," *J. Appl. Phys.*, vol. 63, pp. 5004-5008, May 15, 1988.

[2] A.W. Smith, "Light confinement and hydrodynamic modelling of semiconductor structures by volummetric methods," Ph.D. Thesis, Georgia Institute of Technology, Atlanta, GA, May 1992.

[3] P.I. Rockett, "Monte Carlo study of the influence of collector region velocity overshoot on the high-frequency performance of AlGaAs/GaAs heterojunction bipolar transistors," *IEEE Trans. Elec. Dev.*, vol. 35, no. 10, pp. 1573-1579, Oct. 1988.

[4] M.V. Fischetti and S.E. Laux, "Monte Carlo analysis of electron transport in small semiconductor devices including band-structure and space-charge effects," *Phys. Rev. B*, vol. 38, no. 14, pp. 9721-9744, Nov. 15, 1988.

[5] T.C. Oppe, W.D. Joubert, and D.R. Kincaid, "An overview of NSPCG: a nonsymmetric preconditioned conjugate gradient package," *Comp. Phys. Comm.*, vol. 53, pp. 283-293, 1989.

[6] R.W. Hockney and J.W. Eastwood, Computer Simulation Using Particles. Bristol and New York: Adam Hilger. 1989 (reprint).

[7] J.J. Liou, L.L. Liou, C.I. Huang, and B. Bayraktaroglu, "A physics-based, analytical heterojunction bipolar transistor model including thermal and high-current effects," *IEEE Trans. Elec. Dev.*, vol. 40, no. 9, pp. 1570-1577, Sep. 1993.

[8] L.L. Liou, J.L. Ebel, and C.I. Huang, "Thermal effects on the characteristics of AlGaAs/GaAs heterojunction bipolar transistors using two-dimensional numerical simulation," *IEEE Trans. Elec. Dev.*, vol. 40, no. 1, pp. 35-43, Jan. 1993.

[9] N. Jourdan, F. Alexandre, C. Dubon-Chevallier, J. Dangla, and Y. Gao, "Heavily doped GaAs(Be)/GaAlAs HBT's grown by MBE with high device performances and high thermal stability," *IEEE Trans. Elec. Dev.*, vol. 39, no. 4, pp. 767-770, Apr. 1992.

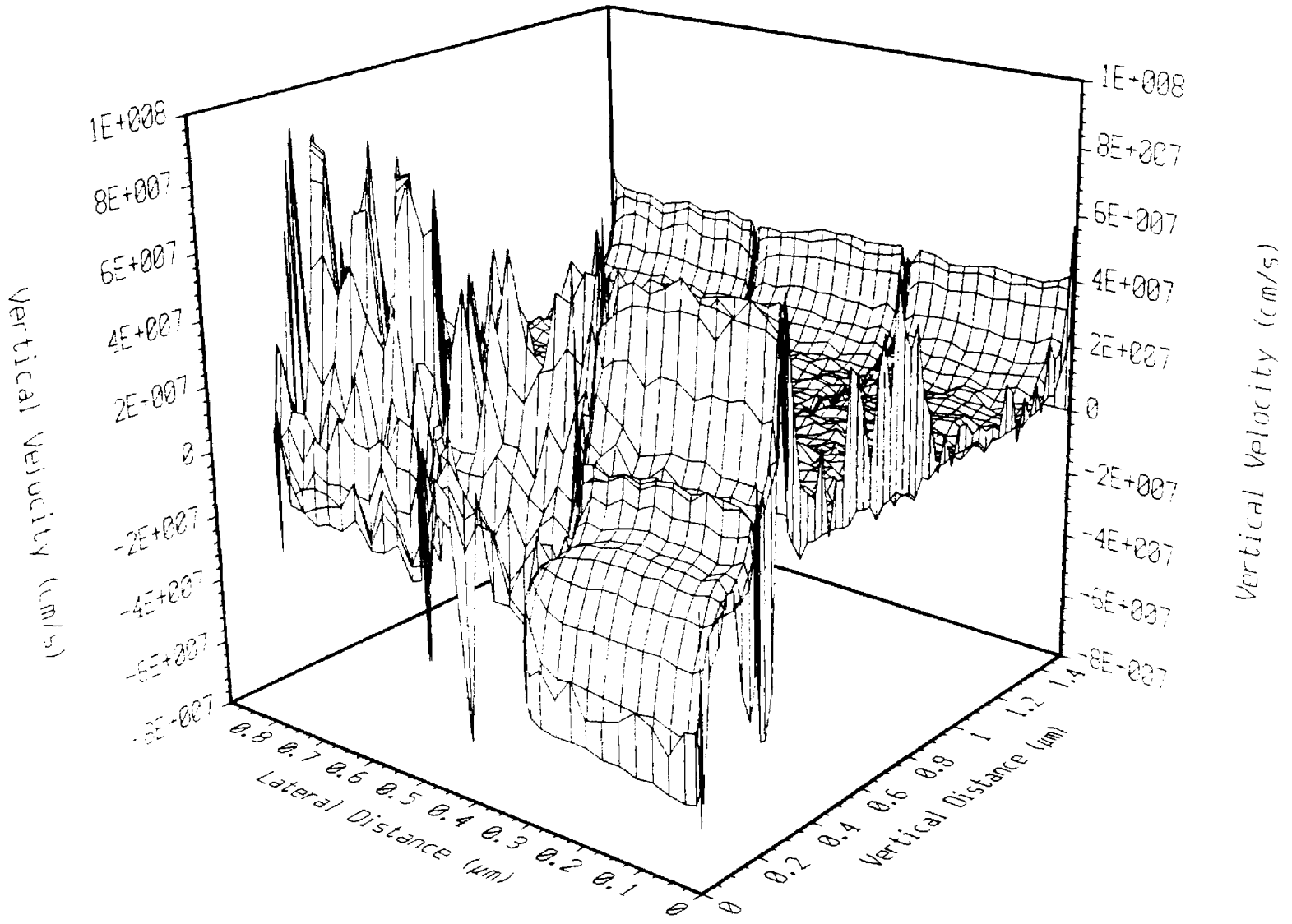

Fig. 1 Vertical velocity (velocity into the device) as a function of position for the self-consistent simulation. The emitter contact is located vertically at 0μm and extends laterally from 0μm to 0.3μm, the base contact is located vertically at 0.2μm and extends laterally from 0.6μm to 0.9μm, and the collector contact is located vertically at 1.5μm and extends laterally across the entire device from 0μm to 0.9μm.

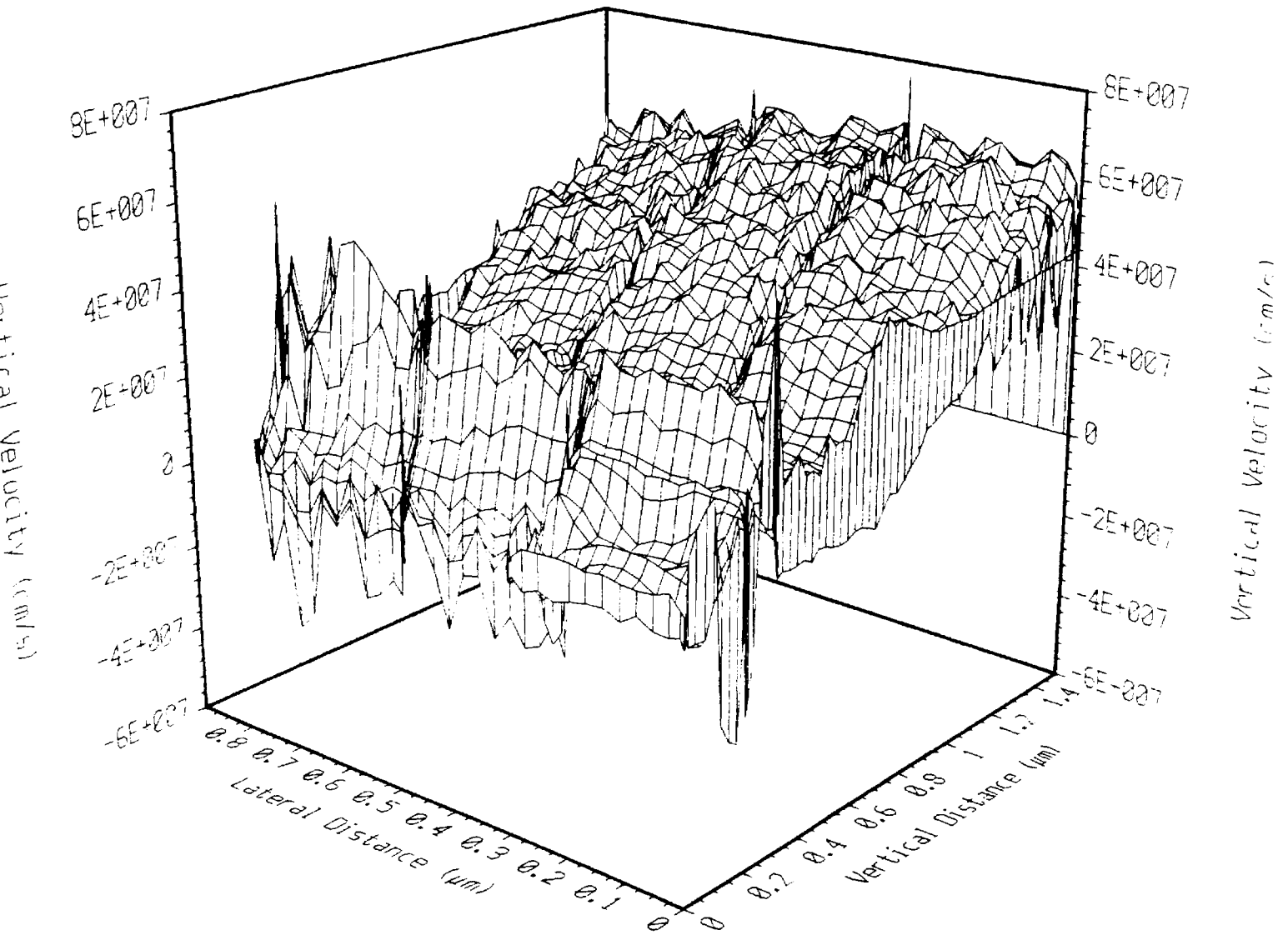

Fig. 2 Vertical velocity (velocity into the device) as a function of position for the non self-consistent simulation. The emitter contact is located vertically at 0μm and extends laterally from 0μm to 0.3μm, the base contact is located vertically at 0.2μm and extends laterally from 0.6μm to 0.9μm, and the collector contact is located vertically at 1.5μm and extends laterally across the entire device from 0μm to 0.9μm.

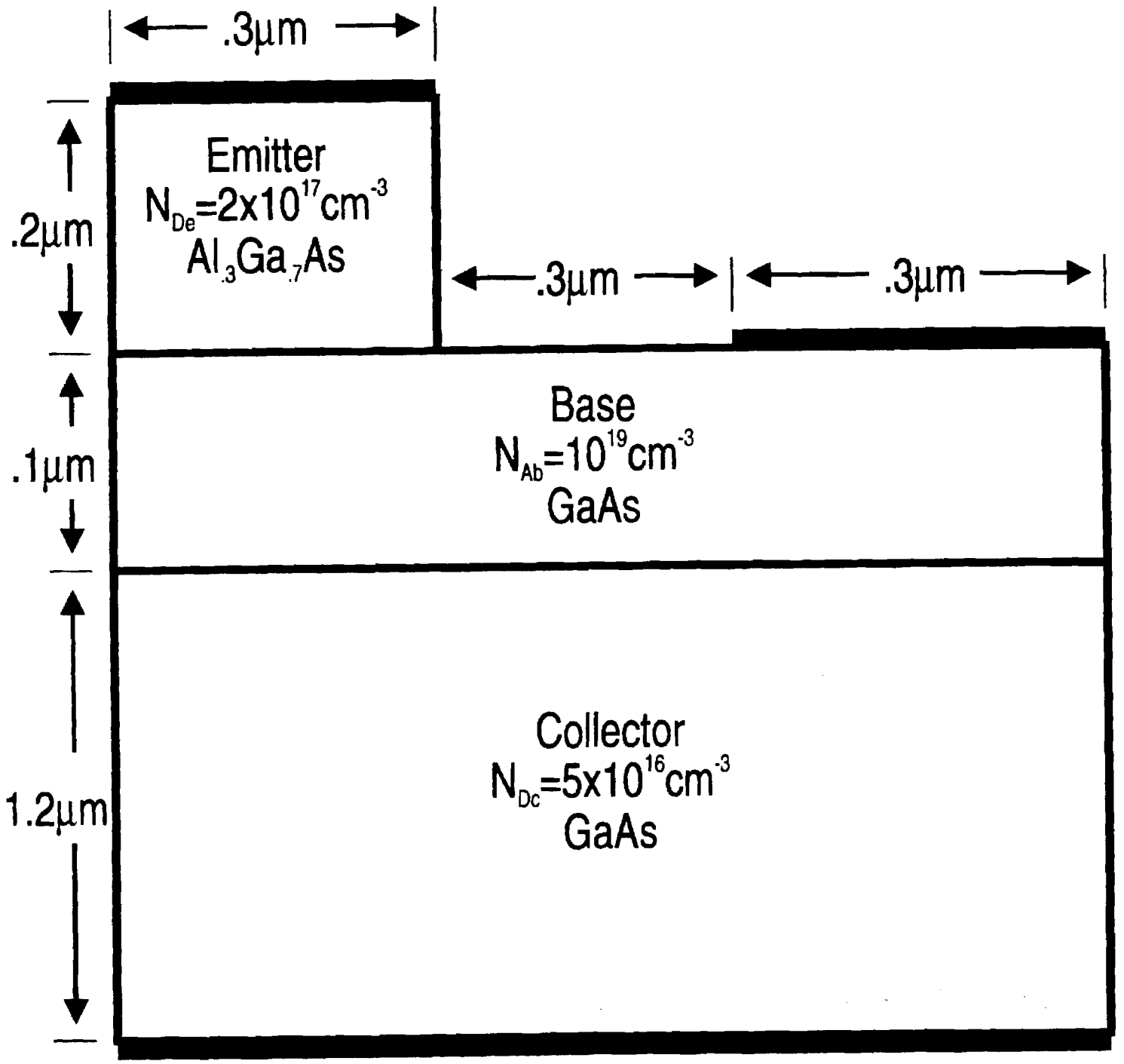

Fig. 3 Physical dimensions and material parameters used for the simulations performed.

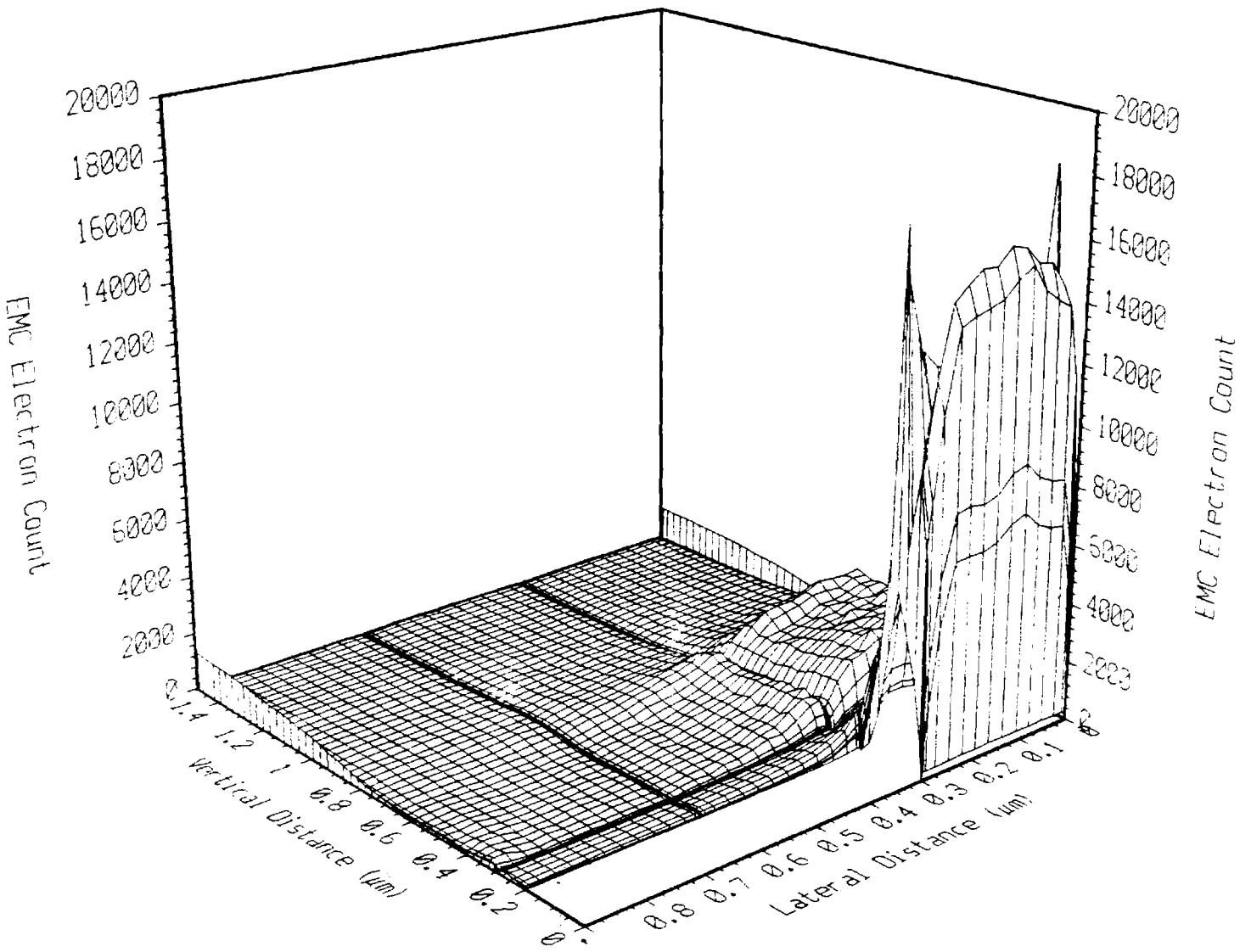

Fig. 4 Ensemble Monte Carlo electron count as a function of position when no statistical enhancement is used in the simulation. The emitter contact is located vertically at 0μm and extends laterally from 0μm to 0.3μm, the base contact is located vertically at 0.2μm and extends laterally from 0.6μm to 0.9μm, and the collector contact is located vertically at 1.5μm and extends laterally across the entire device from 0μm to 0.9μm.

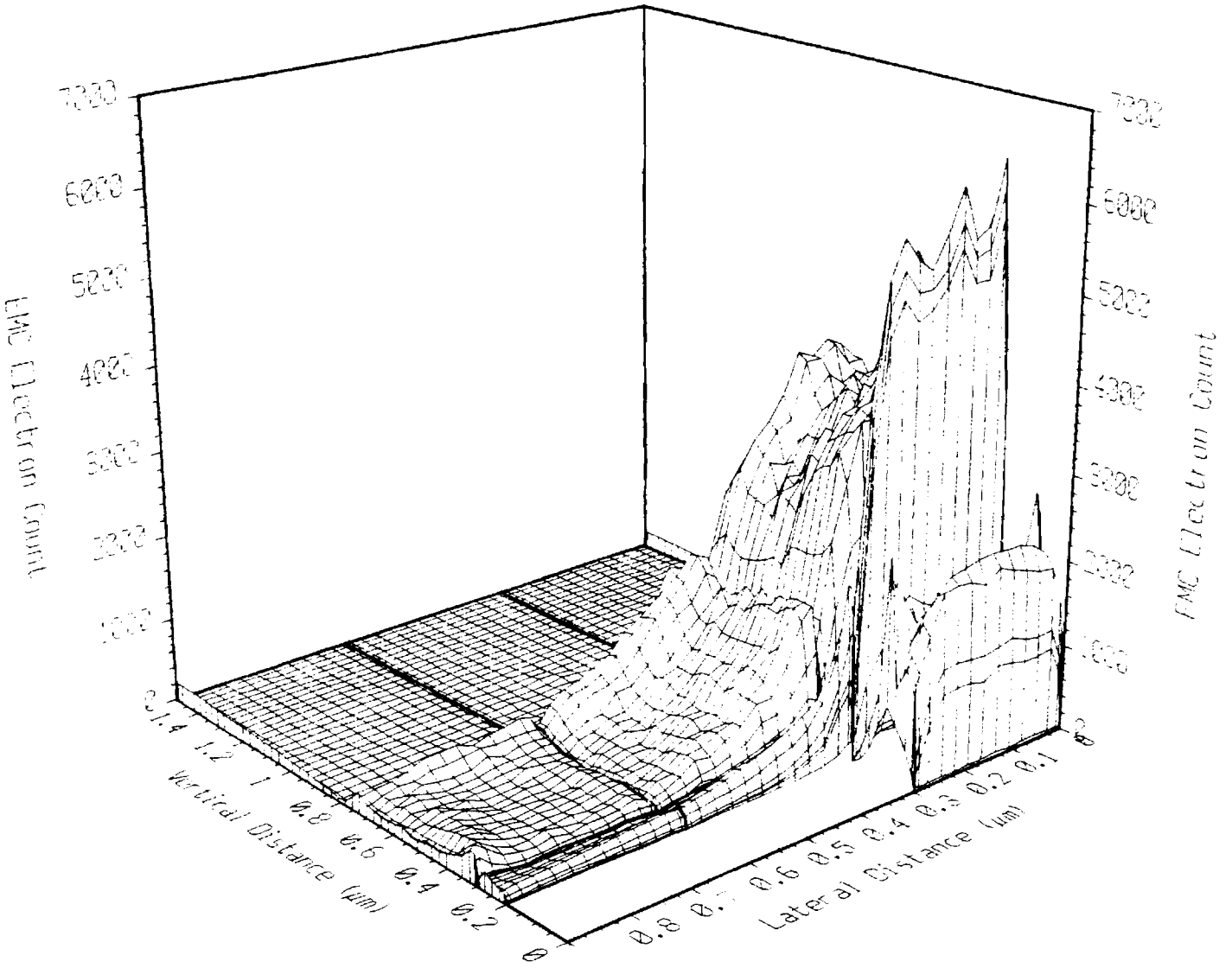

Fig. 5 Ensemble Monte Carlo electron count as a function of position when statistical enhancement in the base and base collector depletion region (vertically from 0.2μm to 0.8μm) is used in the simulation. The emitter contact is located vertically at 0μm and extends laterally from 0μm to 0.3μm, the base contact is located vertically at 0.2μm and extends laterally from 0.6μm to 0.9μm, and the collector contact is located vertically at 1.5μm and extends laterally across the entire device from 0μm to 0.9μm.

E-21-635
#7

Final Report: Motorola Corp.

Date: October, 1995

Title: Modeling of Heterostructure Bipolar Transistors

Investigator: Dr. Kevin F. Brennan

Organization: School of Electrical and Computer Engineering, Georgia Tech

Address: School of Electrical and Computer Engineering
Georgia Institute of Technology
Atlanta, Georgia 30332-0250

Telephone: (404) 894-6767

FAX: (404) 894-1256

Email: kbrennan@ee.gatech.edu

Abstract

In this final report, we review our progress in modeling heterostructure bipolar transistors. ***Though the project cannot be judged to be completely successful, we ultimately did develop a simulator which can handle HBTs.*** After meeting with little success in structuring the ensemble Monte Carlo simulator to model bipolar transistors, we abandoned that approach in favor of a hydrodynamic model. The hydrodynamic model is shown to be far better suited to the simulation of heterostructure transistors since it incorporates both carrier types and the Poisson equation simultaneously. In addition, the hydrodynamic model tracks the carrier energies enabling an accurate treatment of nonstationary transport phenomena such as what occurs near a heterostructure discontinuity. We present calculations of bipolar transistor operation as well as significant improvements to the hydrodynamic simulation technique which have been accepted for reviewed journal publication. We show the importance of including nonparabolicity of the energy bands in modeling electron transport in HBTs. ***In summary, our hydrodynamic model is shown to be a suitable technique for studying carrier transport and the operation of HBTs.***

I. Review of Device Modeling Approaches Examined

In this section, we review our attempt at modeling heterostructure bipolar transistors, HBTs, using an ensemble Monte Carlo, EMC, technique. The principal advantage of the Monte Carlo method is that it contains the full physics of the Boltzmann Equation, enabling an accurate solution to semiclassical transport problems. Our Monte Carlo codes have the additional feature that they contain the full physics of the band structure and carrier scattering mechanisms. The Monte Carlo simulator can also be made self-consistent through the solution of the Poisson equation though at further computational time expense. Our Monte Carlo code was tailored in the following manner to be used for bipolar transistor simulation:

1. Self-consistent updating of the Poisson equation
2. Statistical enhancement in regions of interest
3. Inclusion of the emitter region into the EMC portion of the simulation
4. Higher order schemes for EMC electron assignment to mesh for Poisson eq. calculation
5. Improved field interpolation

Though these additions make the EMC model more adaptable to bipolar transistor simulation, one key ingredient missing in this formulation is the hole transport dynamics. We have found that it is exceedingly difficult to couple the electrons and holes together in a Monte Carlo simulator without an impractically high computational time penalty. Basically, present machines are not capable of treating both electron and hole dynamics through a simultaneous self-consistent Monte Carlo solution. Alternatively, we tried coupling the hole dynamics through use of a drift-diffusion solution. In this approach, we calculate the electron motions using the Monte Carlo technique, but solve for the hole concentration, etc. using a drift-diffusion solver and input both the electron and hole positions into a Poisson solver to

make the solution self-consistent. In principle, this approach is physically viable since the hole motions are much slower than the electrons in a HBT, and the majority of the holes reside in the base where the electric field is very small. However, this approach also turned out to be unsuccessful since it was exceedingly difficult to balance the charge weightings between the Monte Carlo and the drift-diffusion models. The Monte Carlo model is a particle based model while the drift-diffusion is a macroscopic model. Since the particle concentration is necessarily small and variable within a unit cell in a Monte Carlo calculation, an accurate calculation of the electron concentration proved to be difficult. As such we were not successful in scaling the charge between the Monte Carlo and drift diffusion models .

Due to these problems with the Monte Carlo code and the hybrid Monte Carlo and drift-diffusion codes, we decided to abandon their implementation for this project. Instead, we chose to use a newly developed hydrodynamic simulator.

The hydrodynamic model we have developed includes two-three dimensions in real space, Fermi-Dirac statistics, the lattice temperature, multiple materials, heterojunctions, tunneling, thermionic emission, photogeneration, etc. [1,2]. All of the essential physical mechanisms necessary for modeling a semiclassical device are present in our simulator or can readily be added. The simulator can treat tunneling through thin layers, interface states, heterostructures, generation-recombination, high field effects, etc. For the simulations examined within this work, the lattice temperature effects were typically neglected, though included when necessary. The resulting partial differential equations describing the system and solved within the context of the hydrodynamic simulator are:

$$\nabla(\xi_r \nabla\psi) = \frac{q}{\xi_o}(p - n + N_d^+ - N_a^-) \quad (1)$$

$$\left(\frac{\partial n}{\partial t}\right) + \nabla\bullet(n\overline{v_n}) = -R + G \quad (2)$$

$$\left(\frac{\partial p}{\partial t}\right) + \nabla\bullet(p\overline{v_p}) = -R + G \quad (3)$$

$$n\overline{v_n} = \mu\left[-k_b T_e \Lambda_c \nabla n + n\nabla(\epsilon_c - \chi) + \frac{3}{2} n k_b T_e \Lambda_c \frac{\nabla m_e^*}{m_e^*}\right] \quad (4)$$

$$p\overline{v_p} = \mu_h\left[-k_b T_h \Lambda_v \nabla p - p\nabla(\epsilon_v - \chi - E_g) + \frac{3}{2} p k_b T_h \Lambda_v \frac{\nabla m_h^*}{m_h^*}\right] \quad (5)$$

Equation (1) is Poisson's equation for the potential. Equations (2) and (3) are the electron and hole current continuity equations. The electron and hole flux equations are given in equations (4) and (5). On the right hand side of equations (2) and (3), the generation/recombination terms (R and G) account for band to band, Auger, and Shockley-Read-Hall (SRH) recombination.In Eqs. 1-5 above n and p are the electron and hole concentrations, T_e and T_h are the electron and hole carrier temperatures, Λ_c and Λ_v are the ratio of the Fermi integrals involving the conduction and valence bands ($\Im_{1/2}(\eta_c)/\Im_{-1/2}(\eta_c)$), v_n and v_p are the electron and hole velocities respectively and χ is the affinity. The partial differential equations are discretized using the control volume method as described in [1]. All material parameters i.e. bandgap, mobility, density of states, recombination parameters are determined using the formulas stated in PC-1D [3]. In addition, a thermionic-field emission boundary condition [4] for the currents is implemented at each material discontinuity. Equations (1-5) along with the appropriate boundary conditions for the device domain are solved for the three fundamental variables ψ, n, and p.

The simulation domain is non-uniformly discretized using rectangular control volumes. The node placement is performed adaptively during the equilibrium portion of the simulation. The adaptive gridding depends upon the change in potential, changes in material types or boundary conditions, and fluctuations in the doping concentrations. Generally the adaptive gridding results in a mesh consisting of approximately 107 x 41 points. The system of equations is linearized using Newton's method. The resulting system is solved using an iterative approach known as the conjugate gradient squared and stabilized method [5]. The code for this accelerator was added to the NSPCG library for the solution of non-symmetric systems of equations [6].

We have developed a hierarchy of semiconductor device models. The input quantities for the hydrodynamic model are obtained using a fundamental physics based, microscopic Monte Carlo model [7]. The Monte Carlo model provides input parameters, such as mobility, diffusivity, carrier relaxation rates, etc. for the hydrodynamic model ensuring its accuracy and reliability. The hydrodynamic model yields macroscopic quantities, such as current-voltage, capacitance-voltage, frequency response, etc. which enables direct comparison to experiment.

The particular advantage of the hydrodynamic simulator is that it includes the energy balance equations for both the electrons and holes in addition to the usual electron and hole continuity equations used within the drift-diffusion solution. The energy balance equations enable the accurate calculation of nonstationary transport phenomena such as velocity overshoot which arises for electrons injected across a heterobarrier. In the next section, we review our results.

We have made extensive revisions to the standard hydrodynamic model by including

nonparabolicity effects. To date, most hydrodynamic codes are formulated using a simple parabolic E(k) energy band relation, contain only one valley, and assume either a Maxwellian or drifted Maxwellian shape for the distribution function. All of these assumptions are of questionable validity for high field, high energy transport. At high carrier energies within the conduction band, the energy bands become warped and strong deviations from parabolicity are observed. As such, simple parabolic formulations of the E(k) relation when incorporated into the transport equations within the hydrodynamic model do not accurately reflect the transport conditions leading to inaccuracies in the calculated macroscopic observables. Additionally, Monte Carlo investigations have shown that the distribution function departs from a simple Maxwellian and even from a drifted Maxwellian at high electric field strengths. During the past year we have been working towards addressing each of these concerns to more properly account for high energy transport using a hydrodynamic model.

The first step towards exploiting the hydrodynamic simulation tool in high energy, high electric field devices then, is to tailor the code to include nonparabolicity effects. We succeeded in extensively revising the hydrodynamic code to accurately simulate carrier transport at high energies and at high electric fields taking account of band nonparabolicity. We have applied the newly revised hydrodynamic simulator to the study of representative HBT semiconductor devices which will be discussed below.

The full details of the model and the material parameters used in the simulation have been disclosed in the copies of the accepted journal publications enclosed in the two previous reports. These papers have been accepted for publication in Solid State Electronics. Two different formulations of the energy dispersion relation were examined. The first was the simple Kane dispersion relation and the second was a power law formulation. For the devices

and materials systems examined during this past quarter, it is found that the use of the nonparabolic as opposed to the parabolic dispersion relation always leads to a lower calculated current in both the drift-diffusion and hydrodynamic simulations. The calculated carrier energy and velocity are similarly lower when the non-parabolic model is employed. These variables are lower because the non-parabolicity reduces the effective mobility and diffusivity of the material, thereby lowering the calculated current. In the next section, we discuss hydrodynamic calculations of HBT performance.

II. Calculated Results for HBTs Based on the Hydrodynamic Model

The hydrodynamic simulator described above has been used to simulate a standard HBT structure which is shown in Figure 1. The device examined is a GaAs/AlGaAs device with a very narrow base of 0.1 μm in width. In this section, we review calculations made on the carrier transport and current-voltage characteristic for this device using three variations of our hydrodynamic simulator. As mentioned above, the hydrodynamic simulator has been extended to include nonparabolicity effects in the band structure. Typical hydrodynamic models are formulated assuming that the energy bands are parabolic. As is well known, the energy bands deviate substantially from parabolicity at carrier energies only a few tenths of an eV above the band edge. Since these energies are common in HBTs due to the high energy injection of the heterostructure emitter, it is important in modeling HBTs to include nonparabolicity effects. As discussed in the previous section, we use two different formulations of the energy dispersion relation to account for band nonparabolicity, a Kane model [8], often referred to as the alpha formulation, and a power law model [9].

The drift-diffusion and hydrodynamic models' predictions of the currents in the emitter, base and collector are first examined. In Figures 2-4, the emitter, base and collector

currents are plotted as a function of the base-emitter voltage at fixed collector-base voltage of 5 V using both the drift diffusion, marked as ddm, and the hydrodynamic models, marked as hdm. The results presented in these figures are obtained by changing both the drift diffusion and the hydrodynamic models in each case. In the first instance, that shown in Figure 2, both models are formulated assuming parabolic energy bands. The results shown in Figures 3 and 4, are obtained assuming a Kane formulation and a power law formulation within the drift diffusion and hydrodynamic models respectively.

It is first interesting to note that when using the parabolic formulation of the energy band dispersion relation, there is no appreciable difference in the calculated emitter, collector or base currents independent of whether the drift diffusion or hydrodynamic models are used. However, inspection of Figures 3 and 4 shows that the usage of the Kane formulation (denoted as alpha formulation in the figure) predicts a lower emitter and collector current within the hydrodynamic model than the drift-diffusion result particularly at lower base-emitter voltages. Notice that the power law model, shown in Figure 4, does not have as great of a deviation as the alpha formulation but still shows a lower calculated current from the hydrodynamic model compared to the drift diffusion model. These results can be explained by noting that in the nonparabolic models, the carriers are essentially colder which leads to a lower mobility. As such, the current is lower.

The above results are summarized in Figure 5. In Figure 5, the calculated collector current as a function of base emitter voltage is plotted for the six different models; parabolic energy bands, drift diffusion and hydrodynamic, alpha formulation drift diffusion and hydrodynamic, and power law formulation drift diffusion and hydrodynamic. A clear difference is observed between the drift diffusion and the hydrodynamic models in the

diagram.

We also present calculations of the carrier energies in these devices. It is important to recognize that the hydrodynamic model provides a means of tracking the carrier energies much like the Monte Carlo method. The Monte Carlo method is generally a far more reliable means of calculating the energies since it includes the band structure and phonon scattering rates directly. However, by extending our hydrodynamic code to include nonparabolicity effects, the carrier energies can be calculated with greater precision approaching the reliability of the Monte Carlo analysis, particularly for the energies considered in HBTs. The electron and hole temperatures are presented in Figures 6 and 7 respectively for the device structure of Figure 1. In each case, the base-emitter voltage is chosen as -1.3 V and the base-collector voltage is 5 V. As can be seen from the figures the electrons are very much hotter than the holes. Additionally, the electron temperature is greatest in the base-collector depletion region due to the high reverse bias field present there. Also notice a spike in the electron temperature at the emitter-base junction due to the potential discontinuity present at the interface.

III. Conclusions

During the course of this work, we have developed a hydrodynamic simulator which is particularly well fashioned to study carrier transport in HBTs. The simulator contains band nonparabolicity effects which greatly extends its accuracy in treating high energy, high field transport. We have determined that the hydrodynamic simulator is much more readily adaptable to the study of bipolar devices than either a Monte Carlo simulator or a hybrid drift diffusion, Monte Carlo simulator. The particular advantage of the hydrodynamic simulator

over either the Monte Carlo or hybrid models is that it contains energy dependencies as well as tracks both carrier types. The hydrodynamic simulator was used to study the effect of different choices in the energy dispersion relation on the calculated currents in a representative HBT structure. ***It was determined that the commonly used parabolic formulation of the energy dispersion relation within a hydrodynamic model overestimates the currents at low emitter base voltages in HBTs.*** We have found that it is important to use a nonparabolic formulation of the energies to correctly determine the currents in HBT devices.

References

1. A. W. Smith and A. Rohatgi, "Non-isothermal extension of the Scharfetter-Gummel technique for hot carrier transport in heterostructure simulations," *IEEE Trans. Computer-Aided Design of Integrated Circuits and Systems,* vol. 12, pp. 1515-1523, Oct., 1993.

2. Smith, A. W., Kenney, J. S., Hunt, W. D., Brennan, K. F., Benz, R., and Summers, C. J., "Theoretical calculations of charge confinement in a pn-np heterojunction acoustic charge transport device," *IEEE Trans. Electron Dev.*, vol. 42, pp. 977-990, April, 1995.

3. P. A. Basore, "PC-1D installation manual and user's guide version 3.0," Sandia National Laboratories, Albuquerque, NM, 1991.

4. S. Selberherr, Analysis and Simulation of Semiconductor Devices, Springer-Verlag, Wien, New York, 1984.

5. P. Chin and P. A. Forsyth, "A comparison of GMRES and CGSTAB accelerations for incompressible Navier-Stokes problems," *J. Comp. and Appl. Math.*, vol. 46, pp. 415-26, 1993.

6. T. C. Oppe, W. D. Joubert, and D. R. Kincaid, "An overview of NSPCG: a nonsymmetric preconditioned conjugate gradient package," *Computer Physics Communications*, vol. 53, pp. 283-93, 1989.

7. Brennan, K.F., Mansour, N., and Wang, Y., "Simulation of Advanced Semiconductor Devices Using Supercomputers," *Computer Physics Communications*, Vol. 67, pp. 73-92, 1991.

8. E. O. Kane, "Band structure of indium antimonide," J. Phys. Chem. Solids, vol. 1, pp. 249-261, 1957.

9. D. Cassi and B. Ricco, "An analytical model of the energy distribution of hot electrons," IEEE Trans. Electron Dev., vol. 37, pp. 1514-1521, June, 1990.

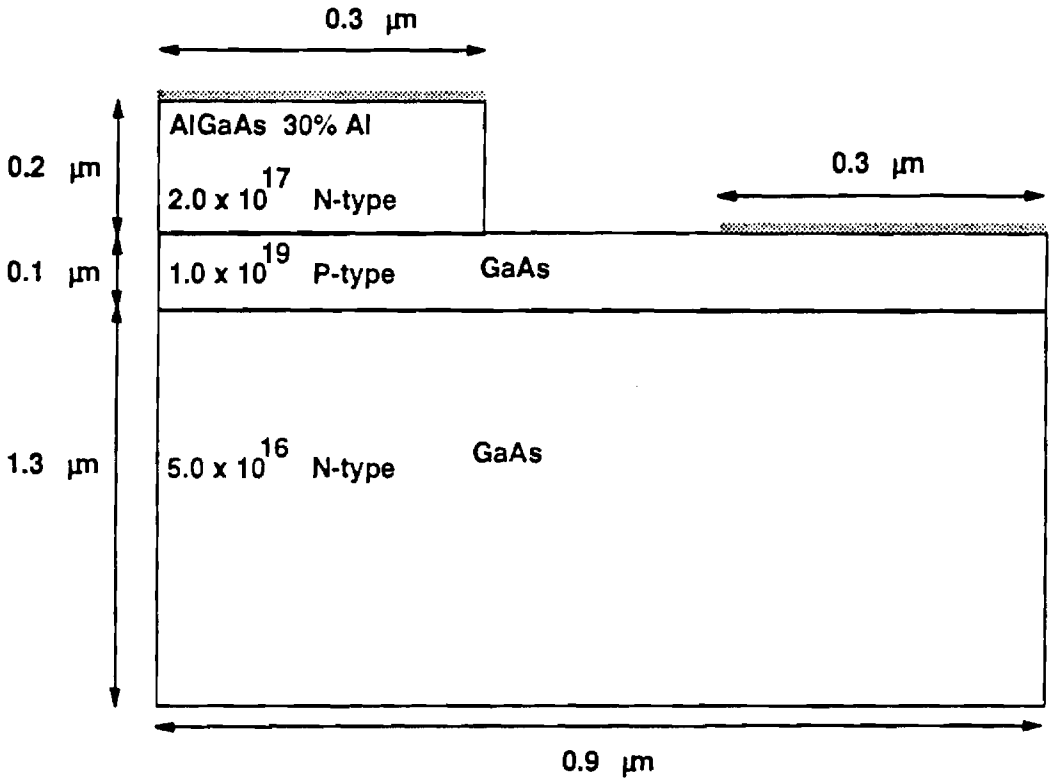

Figure 1: Heterostructure Bipolar Transistor structure and doping concentrations used in the calculations.

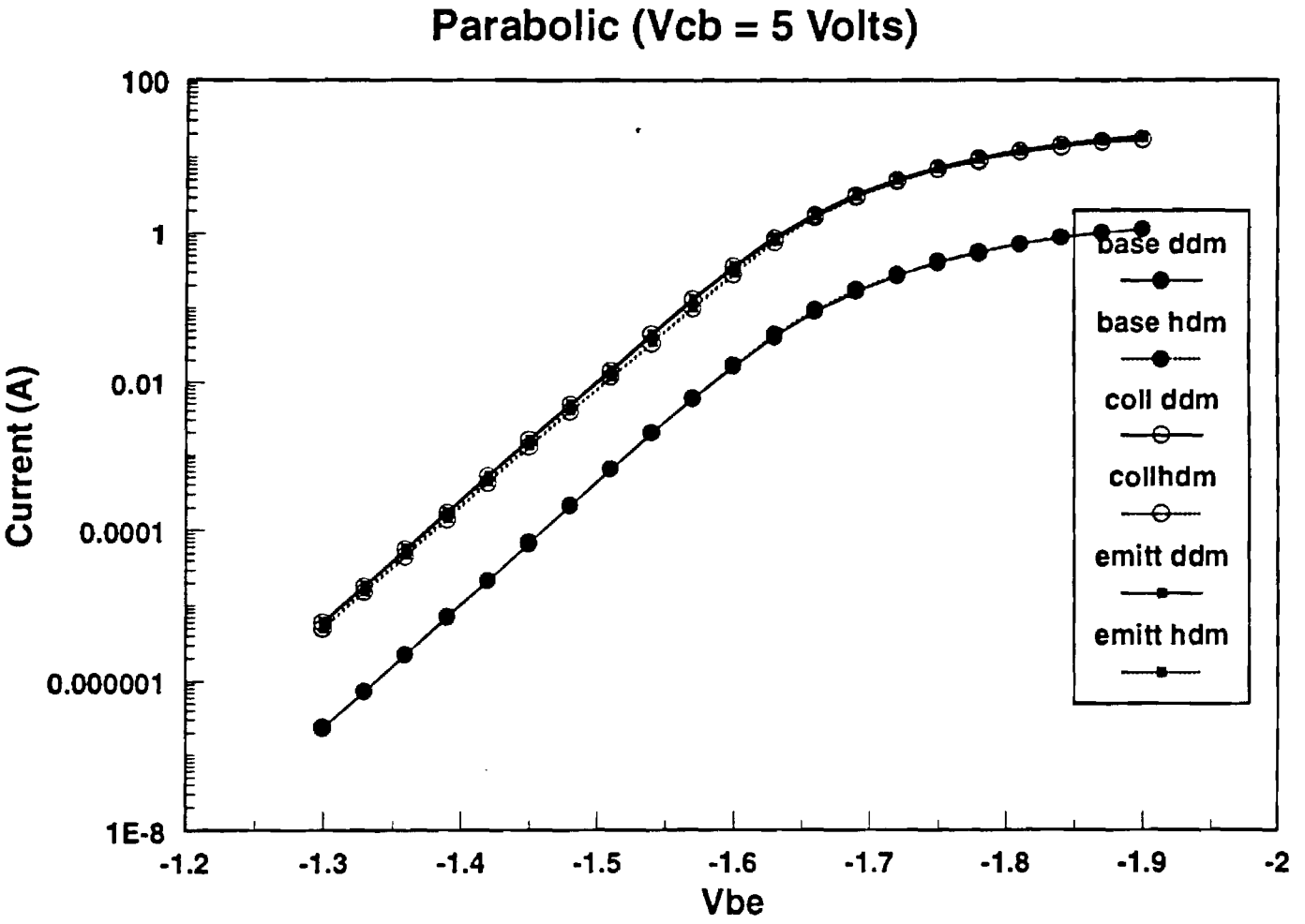

Figure 2: Calculated emitter, base, and collector currents for the device of Figure 1, using both the drift diffusion, ddm, and hydrodynamic, hdm, models assuming a parabolic energy dispersion relation.

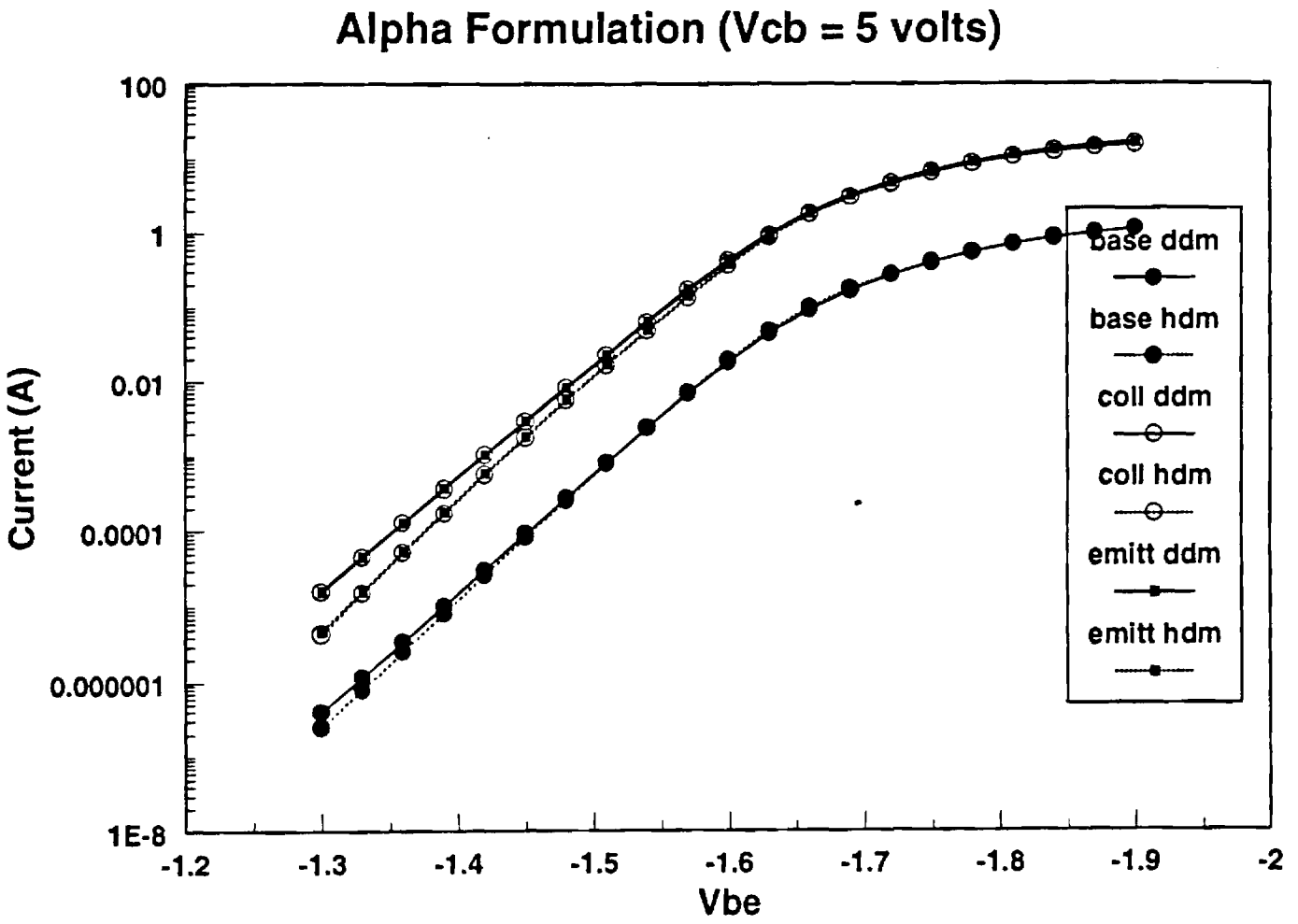

Figure 3: Calculated emitter, base, and collector currents for the device of Figure 1, using both the drift diffusion, ddm, and hydrodynamic, hdm, models assuming the nonparabolic energy dispersion relation given by Kane.

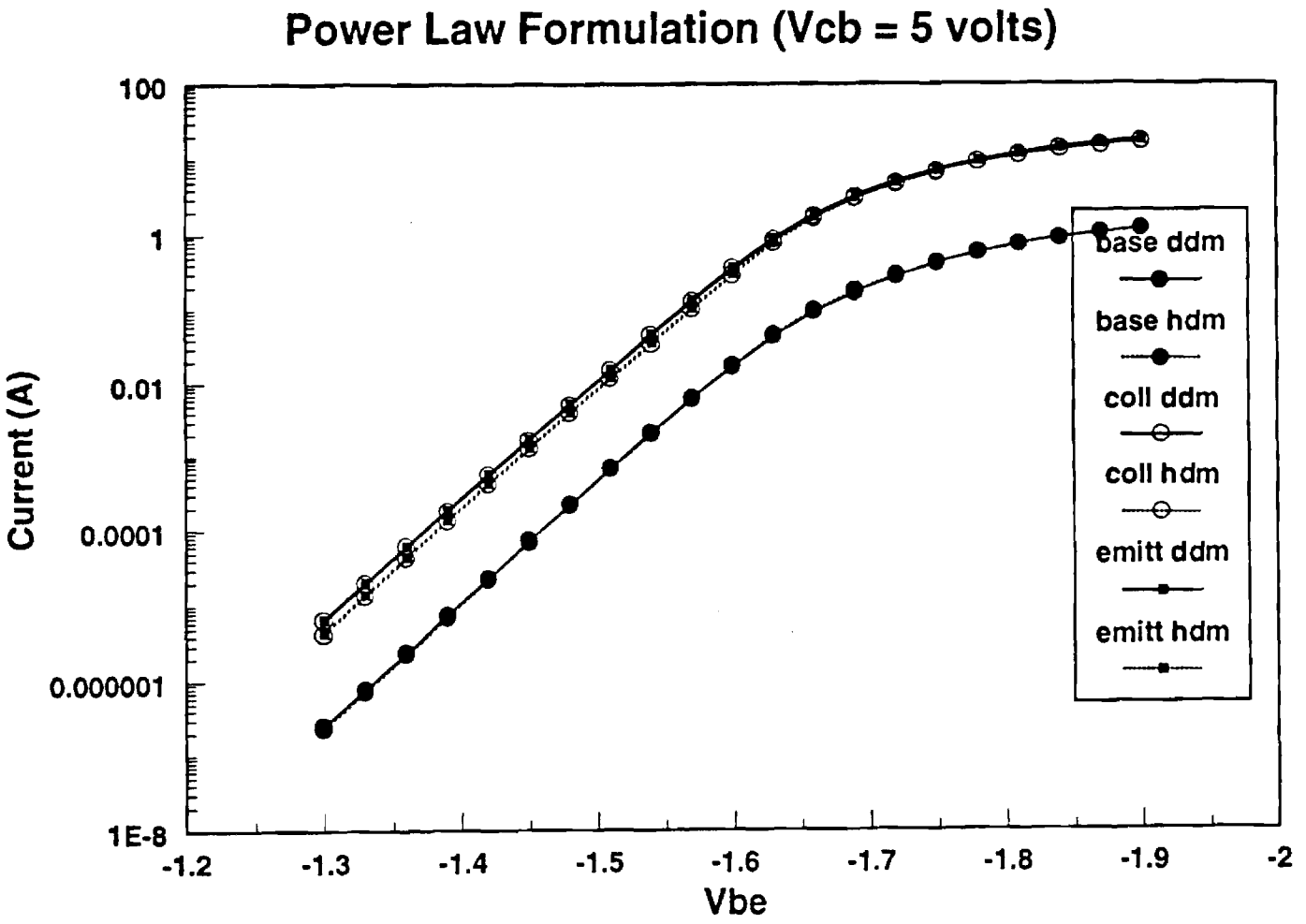

Figure 4: Calculated emitter, base, and collector currents for the device of Figure 1, using both the drift diffusion, ddm, and hydrodynamic, hdm, models assuming a power law energy dispersion relation.

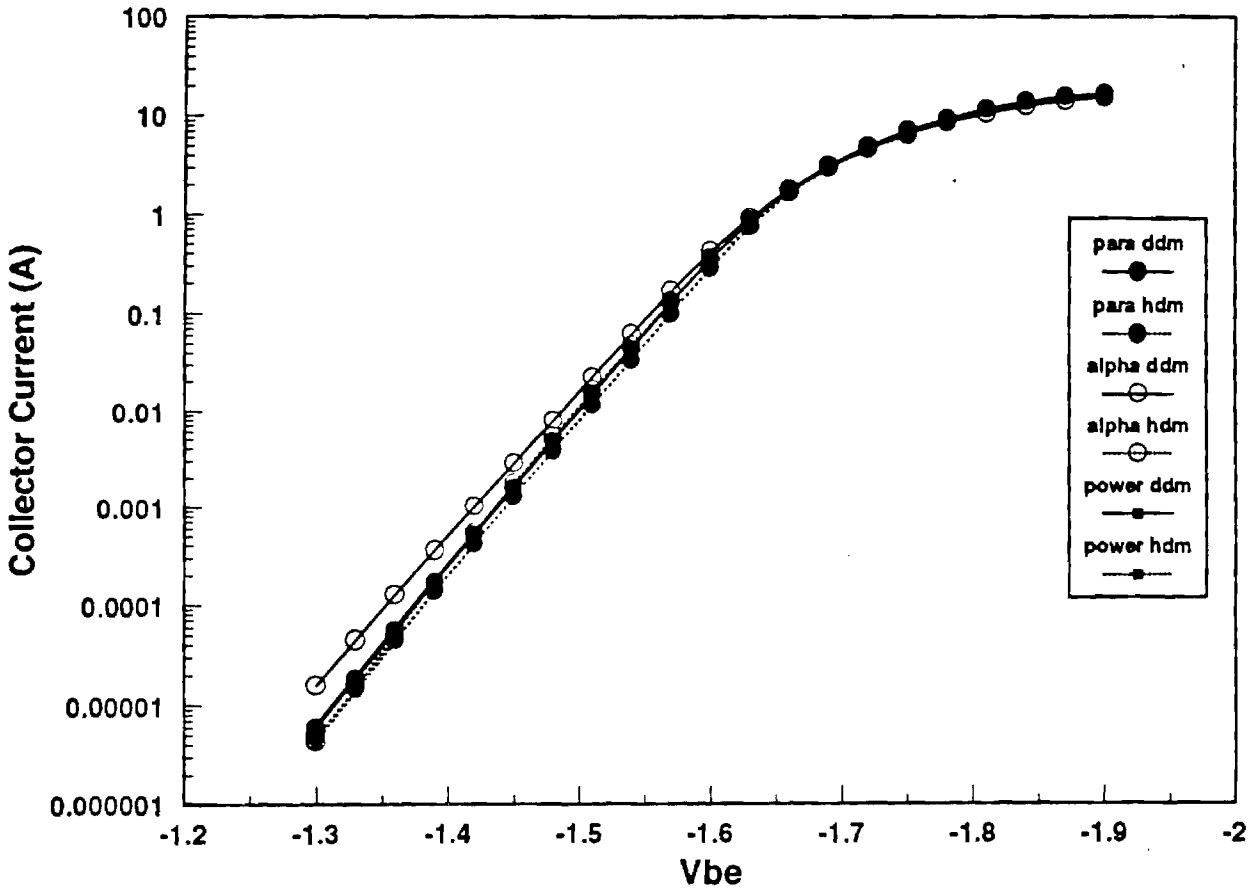

Figure 5: Calculated collector current as a function of base emitter voltage at fixed collector-base voltage of 5 V using the drift diffusion and hydrodynamic models with parabolic, alpha, and power law dispersion relations.

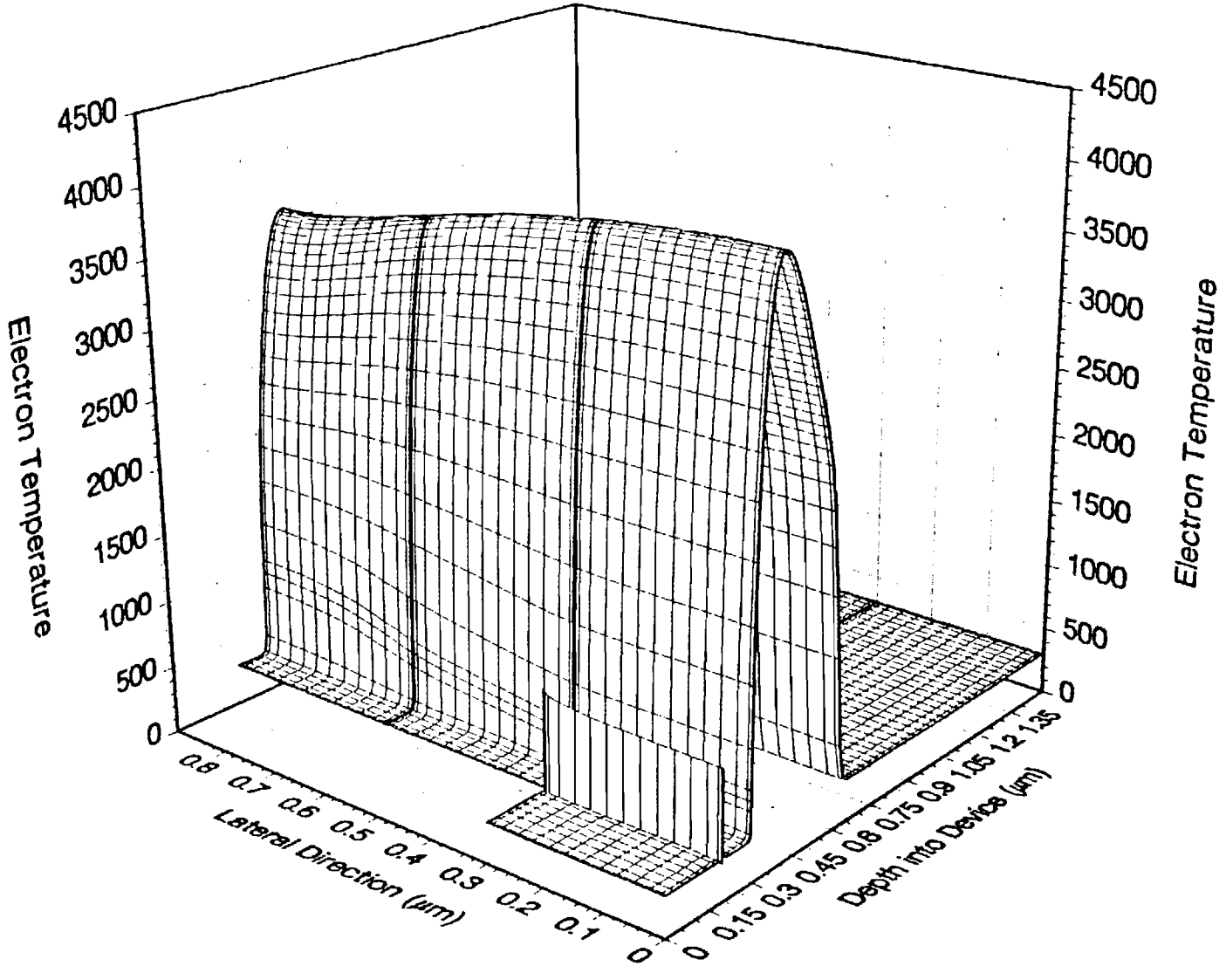

Figure 6: Calculated electron temperature for the device shown in Figure 1 at 5 V base-collector voltage and -1.3 V emitter-base voltage. Notice that the electron temperature greatly exceeds thermal equilibrium.

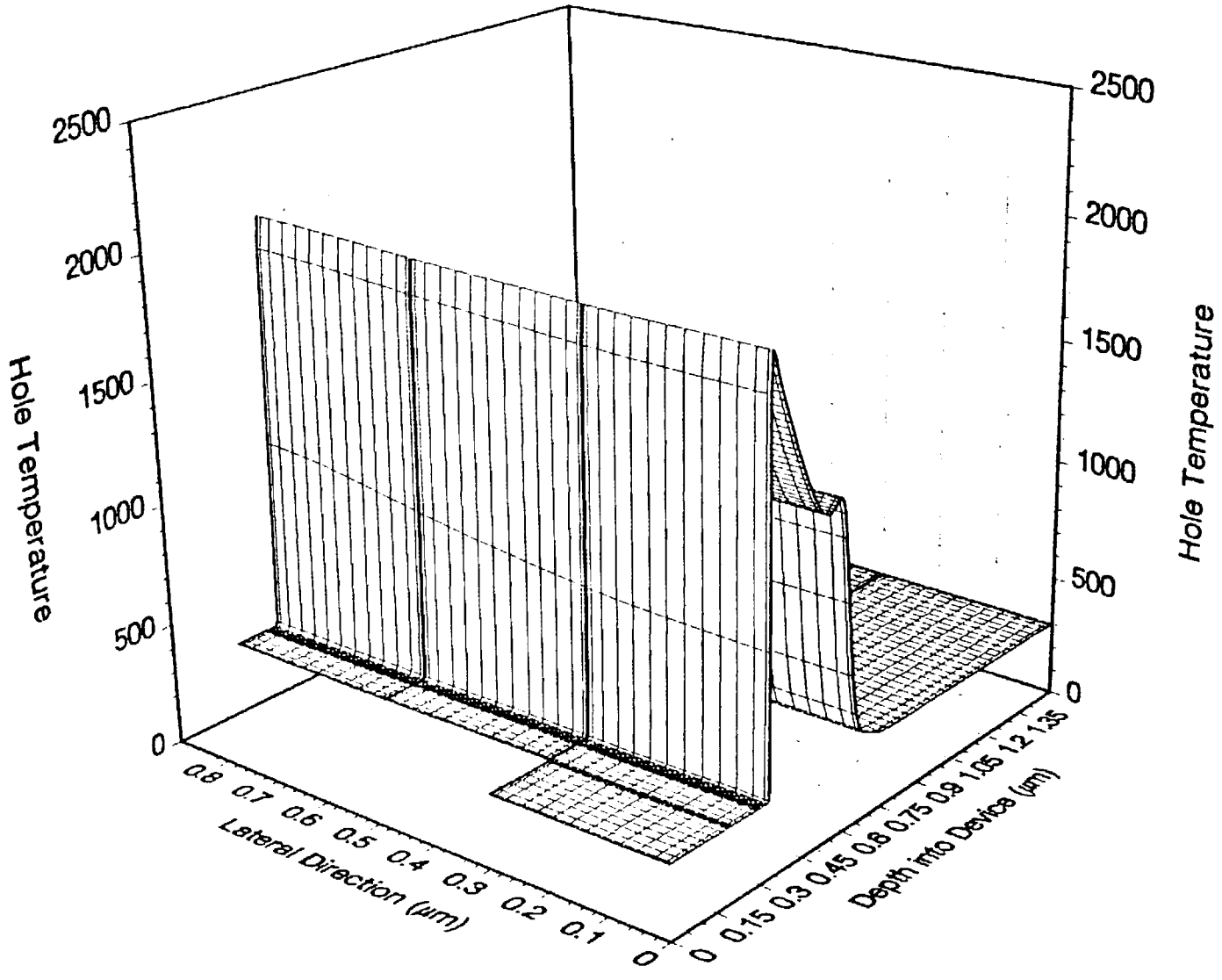

Figure 7: Calculated hole temperature for the device shown in Figure 1 at 5 V base- collector voltage and -1.3 V emitter-base voltage.

Comparison of Non-Parabolic Hydrodynamic Simulations for Semiconductor Devices

Arlynn W. Smith and Kevin F. Brennan
School of Electrical and Computer Engineering
and
Microelectronics Research Center
Georgia Institute of Technology
Atlanta, GA 30332-0250

ABSTRACT

Parabolic drift-diffusion simulators are common engineering level design tools for semiconductor devices. Hydrodynamic simulators, based on the parabolic band approximation, are becoming more prevalent as device dimensions shrink and energy transport effects begin to dominate device characteristics. However, band structure effects present in state of the art devices necessitates relaxing the parabolic band approximation. This paper presents simulations of ballistic diodes, a benchmark device, of Si and GaAs using two different non-parabolic hydrodynamic formulations. The first formulation uses the Kane dispersion relationship in the derivation of the conservation equations. The second model uses a power law dispersion relation $\{(\hbar k)^2/2m = xW^y\}$. Current-voltage relations show that for the ballistic diodes considered the non-parabolic formulations predict less current than the parabolic case. Explanations of this will be provided by examination of velocity and energy profiles. At low bias the simulations based on the Kane formulation predict greater current flow than the power law formulation. As the bias is increased this trend changes and the power law predicts greater current than the Kane formulation. It will be shown that the non-parabolicity and energy range of the hydrodynamic model based on the Kane dispersion relation is limited due to the binomial approximation which was utilized in the derivation.

NOMENCLATURE

$\hbar$	Planck's constant divided by 2π
$\mathbf{k}$	Reciprocal lattice vector
α	Non-parabolicity factor under the Kane dispersion relation
m	Carrier mass at the band edge, a constant
x,y	Adjustable parameters for the power law dispersion relation
W	Energy
T	Electron temperature
$\mathscr{F}_?$	Fermi integral of order ? divided by Gamma function (? + 1)
Γ	Gamma function
μ_o	Low field mobility value
μ	Mobility value
E	Electric Field
ϵ_c	Band edge parameters (potential, bandgap narrowing, affinity)
∇	Gradient operator in physical space
v	Electron velocity
S	Electron energy flux
τ	Relaxation times
p	Hole concentration
n	Electron Concentration
K	Boltzmann's constant

INTRODUCTION

Drift-diffusion simulators and more recently hydrodynamic simulators are commonly being used as design tools for semiconductor devices. The hydrodynamic simulators are required as device dimensions decrease and the energy transport effects begin to dominate device characteristics. These simulation tools are commonly based on the parabolic band approximation for the semiconductor materials. However, band structure effects present in state of the art devices necessitates relaxing the parabolic band approximation. Several non-parabolic hydrodynamic models have been reported for homogeneous materials systems [1-5] using the Kane dispersion relationship [6]. Very limited device simulations based on these models have been presented [2,5], and fewer still have been compared to drift-diffusion simulations or parabolic hydrodynamic simulations of the same device [3]. The lack of simulation results may be due to the limited energy and non-parabolicity range over which the binomial Kane formulation is valid.

In a previous paper [7] we have presented two different non-parabolic hydrodynamic formulations suitable for device simulation; the parabolic form was also presented for reference. These forms resulted from the use of two different non-parabolic formulations for the dispersion relationship of the semiconductor in the derivation of the conservation equations. The first uses the classical non-parabolic Kane dispersion relationship, $\{(\hbar k)^2/2m = W(1 + \alpha W)\}$ [6], hereafter also called the α formulation. The second uses a power law dispersion relation $\{(\hbar k)^2/2m = xW^\gamma\}$ [8]. The purpose of this paper is to present device simulations based on the non-parabolic hydrodynamic equations presented in reference [7]. These simulations are compared to the parabolic hydrodynamic case for the same device, as

well as the drift-diffusion simulations. Ballistic diodes, the benchmark device for hydrodynamic simulations, of silicon and gallium arsenide are simulated under a variety of bias conditions. Current-voltage characteristics of the three dispersion relations are compared utilizing the drift-diffusion approximation and the full hydrodynamic formulations.

This paper will proceed as follows: First, the ballistic diode structure is introduced, the doping and structure are the same for both material systems considered. The numerical aspects and physical models of the simulation code will then be presented. The material properties, including the non-parabolicity factors used, are presented for both Si and GaAs. Current-voltage characteristics for the silicon diode are discussed and explained using velocity and energy profiles. The discussion covers both drift-diffusion simulations and hydrodynamic simulations under the same conditions. Current-voltage characteristics for the GaAs diode are then presented. As in the case of the silicon simulations velocity and energy profiles will be used to explain the results. In addition, mobility profiles will also be presented and explained in terms of the electric field and energy profiles. Energy profiles at high bias will be used to explain the breakdown in the α formulation.

BALLISTIC DIODE STRUCTURE

The ballistic diode structure examined is comprised of source and drain regions 0.2 μm in length doped at 5.0×10^{17} cm^{-3} on both ends of a 0.4 μm thick 2.0×10^{15} cm^{-3} n-type layer. This device structure is the benchmark for hydrodynamic (energy balance) simulations [9]. It was one of the first devices simulated using a full hydrodynamic simulator [10]. Although the device structure does not reflect all of the advanced physics included in the

equations of reference [7] {Fermi-Dirac statistics, inhomogeneous materials}, enough are present to highlight the applicability of the models. The bias is applied on the drain side, right hand side, of the device. The electrons enter the source and are swept out of the drain. The doping profiles and boundary conditions are assumed the same regardless of the material system being simulated, silicon or GaAs.

NUMERICAL MODELS

The particle and energy continuity equations are presented as equations (22) and (23) in reference [7] and are the same as those derived by Woolard et. al. [11]. The flux equations presented in this paper will be a subset of those presented in reference [7] in that all of the inhomogeneous material terms will be neglected. The particle flux equation (the derivation for all three cases is given in reference [7]) for the parabolic band case is

$$-n\bar{v} = \mu KT\left[\frac{\mathcal{F}_{\frac{1}{2}}}{\mathcal{F}_{-\frac{1}{2}}}\right]\nabla n + \mu n\nabla\epsilon_c + \frac{5}{2}\mu nKT\frac{\mathcal{F}_{\frac{3}{2}}}{\mathcal{F}_{\frac{1}{2}}}\left[1-\frac{3}{5}\frac{\mathcal{F}^2_{\frac{1}{2}}}{\mathcal{F}_{-\frac{1}{2}}\mathcal{F}_{\frac{3}{2}}}\right]\frac{\nabla T}{T} \tag{1}$$

The flux equation for the binomial α formulation is

$$-n\bar{v} = \mu KT\left[\frac{\mathcal{F}^2_{\frac{1}{2}}+\frac{10}{4}\alpha KT\mathcal{F}_{\frac{3}{2}}\mathcal{F}_{\frac{1}{2}}}{\mathcal{F}_{\frac{1}{2}}\mathcal{F}_{-\frac{1}{2}}+\frac{15}{4}\alpha KT\left(\mathcal{F}^2_{\frac{1}{2}}+\frac{\mathcal{F}_{-\frac{1}{2}}\mathcal{F}_{\frac{3}{2}}}{2}\right)}\right]\nabla n + \mu\left[\frac{\mathcal{F}_{\frac{1}{2}}-\frac{21}{4}\alpha KT\mathcal{F}_{\frac{3}{2}}}{\mathcal{F}_{\frac{1}{2}}+\frac{15}{4}\alpha KT\mathcal{F}_{\frac{3}{2}}}\right]n\nabla\epsilon_c$$
$$+\frac{\mu nKT}{\left(\mathcal{F}_{\frac{1}{2}}+\frac{15}{4}\alpha KT\mathcal{F}_{\frac{3}{2}}\right)\left(\mathcal{F}_{-\frac{1}{2}}+\frac{15}{4}\alpha KT\mathcal{F}_{\frac{1}{2}}\right)}\left[\frac{5}{2}\mathcal{F}_{-\frac{1}{2}}\mathcal{F}_{\frac{3}{2}}-\mathcal{F}^2_{\frac{1}{2}}-\frac{\mathcal{F}^2_{\frac{1}{2}}}{2\left(\mathcal{F}_{\frac{1}{2}}+\frac{15}{4}\alpha KT\mathcal{F}_{\frac{3}{2}}\right)}\right]\frac{\nabla T}{T} \tag{2}$$

The flux equation for the power law formulation is

$$-n\bar{v} = \frac{2\mu}{3xy^2}(KT)^{2-y}\frac{\left(\frac{y}{2}+1\right)\Gamma\left(\frac{y}{2}+1\right)\mathcal{F}_{\frac{y}{2}}}{\left(\frac{3}{2}y-1\right)\Gamma\left(\frac{3}{2}y-1\right)\mathcal{F}_{\frac{3}{2}y-2}}\nabla n + \frac{(2-y)\mu}{xy^2}(KT)^{1-y}\frac{\Gamma\left(\frac{y}{2}+1\right)\mathcal{F}_{\frac{y}{2}}}{\Gamma\left(\frac{3}{2}y\right)\mathcal{F}_{\frac{3}{2}y-1}}n\nabla\epsilon_c$$

$$+\frac{\mu n}{xy^2}(KT)^{2-y}\left[\frac{-y\left(\frac{y}{2}+1\right)\Gamma\left(\frac{y}{2}+1\right)\mathcal{F}_{\frac{y}{2}}}{\left(\frac{3}{2}y-1\right)\Gamma\left(\frac{3}{2}y-1\right)\mathcal{F}_{\frac{3}{2}y-2}} - \frac{(4+y)\Gamma\left(\frac{y}{2}+2\right)\mathcal{F}_{\frac{y}{2}+1}}{3\Gamma\left(\frac{3}{2}y\right)\mathcal{F}_{\frac{3}{2}y-1}}\right]\frac{\nabla T}{T} \qquad (3)$$

The complete inhomogeneous energy flux equations for the three dispersion relations are listed as equations (45 - 47) in reference [7]. The homogeneous material equations, which apply to the device structures of interest here, simplify to

$$-\bar{S} = \frac{5}{2}\mu nKT\left[KT\left[\frac{\mathcal{F}_{\frac{3}{2}}}{\mathcal{F}_{-\frac{1}{2}}}\right]\frac{\nabla n}{n} + \left[\frac{\mathcal{F}_{\frac{3}{2}}}{\mathcal{F}_{\frac{1}{2}}}\right]\nabla\epsilon_c + \frac{7}{2}KT\frac{\mathcal{F}_{\frac{5}{2}}}{\mathcal{F}_{\frac{1}{2}}}\left[1-\frac{3}{7}\frac{\mathcal{F}_{\frac{1}{2}}\mathcal{F}_{\frac{3}{2}}}{\mathcal{F}_{-\frac{1}{2}}\mathcal{F}_{\frac{5}{2}}}\right]\frac{\nabla T}{T}\right] \qquad (4)$$

$$-\bar{S} = \frac{5\mu(KT)^2}{2}\left[\frac{\mathcal{F}_{\frac{3}{2}}\left(\mathcal{F}_{\frac{1}{2}}+\frac{15}{4}\alpha KT\mathcal{F}_{\frac{3}{2}}\right)-\frac{7}{4}\alpha KT\mathcal{F}_{\frac{1}{2}}\mathcal{F}_{\frac{3}{2}}}{\left(\mathcal{F}_{\frac{1}{2}}+\frac{15}{4}\alpha KT\mathcal{F}_{\frac{3}{2}}\right)\left(\mathcal{F}_{-\frac{1}{2}}+\frac{15}{4}\alpha KT\mathcal{F}_{\frac{1}{2}}\right)}\right]\nabla n + \frac{5\mu nKT}{2}\left[\frac{\mathcal{F}_{\frac{3}{2}}-\frac{23}{4}\alpha KT\mathcal{F}_{\frac{5}{2}}}{\left(\mathcal{F}_{\frac{1}{2}}+\frac{15}{4}\alpha KT\mathcal{F}_{\frac{3}{2}}\right)}\right]\nabla\epsilon_c$$

$$+\frac{5\mu n(KT)^2}{2\left(\mathcal{F}_{\frac{1}{2}}+\frac{15}{4}\alpha KT\mathcal{F}_{\frac{3}{2}}\right)}\left[\frac{5}{2}\mathcal{F}_{\frac{5}{2}}-\frac{21}{8}\alpha KT\mathcal{F}_{\frac{7}{2}}+\frac{\mathcal{F}_{\frac{1}{2}}\mathcal{F}_{\frac{5}{2}}-\frac{3}{20}\alpha KT\mathcal{F}_{\frac{1}{2}}\mathcal{F}_{\frac{3}{2}}}{\left(\mathcal{F}_{\frac{1}{2}}+\frac{15}{4}\alpha KT\mathcal{F}_{\frac{3}{2}}\right)}\right. \qquad (5)$$

$$\left.-\frac{3\mathcal{F}_{\frac{3}{2}}\left(\mathcal{F}_{\frac{1}{2}}+\frac{25}{4}\alpha KT\mathcal{F}_{\frac{3}{2}}\right)-\frac{101}{8}\alpha KT\mathcal{F}_{\frac{1}{2}}\mathcal{F}_{\frac{3}{2}}}{2\left(\mathcal{F}_{-\frac{1}{2}}+\frac{15}{4}\alpha KT\mathcal{F}_{\frac{1}{2}}\right)}\right]\frac{\nabla T}{T}$$

$$-S = \frac{2\mu}{3xy^2}(KT_e)^{3-\gamma}\frac{\left(\frac{\gamma}{2}+2\right)\Gamma\left(\frac{\gamma}{2}+2\right)\mathcal{F}_{\frac{\gamma}{2}+1}}{\left(\frac{3}{2}\gamma-1\right)\Gamma\left(\frac{3}{2}\gamma-1\right)\mathcal{F}_{\frac{3}{2}\gamma-2}}\nabla n + \frac{(8-3\gamma)\mu n}{3xy^2}(KT_e)^{3-\gamma}\frac{\Gamma\left(\frac{\gamma}{2}+2\right)\mathcal{F}_{\frac{\gamma}{2}+1}}{\Gamma\left(\frac{3}{2}\gamma\right)\mathcal{F}_{\frac{3}{2}\gamma-1}}\nabla\epsilon_c$$

$$+\frac{\mu n}{xy^2}(KT_e)^{3-\gamma}\left[\frac{-\gamma\left(\frac{\gamma}{2}+2\right)\Gamma\left(\frac{\gamma}{2}+2\right)\mathcal{F}_{\frac{\gamma}{2}+1}}{\left(\frac{3}{2}\gamma-1\right)\Gamma\left(\frac{3}{2}\gamma-1\right)\mathcal{F}_{\frac{3}{2}\gamma-2}}+\frac{(6+\gamma)\Gamma\left(\frac{\gamma}{2}+3\right)\mathcal{F}_{\frac{\gamma}{2}+2}}{3\Gamma\left(\frac{3}{2}\gamma\right)\mathcal{F}_{\frac{3}{2}\gamma-1}}\right]\frac{\nabla T_e}{T_e} \qquad (6)$$

Equation (4) is the parabolic energy flux, while equation (5) is for the alpha formulation and equation (6) is for the power law formulation. The non-parabolic formulations have now been included in the two dimensional device simulator STEBS-2D [12], which was originally a parabolic band hydrodynamic device simulator. The equations were discretized using the techniques in references [12] and [13]. For the exponential terms in the discretization equation with factors composed of powers of the temperature we have made the assumption that the position dependent temperature can be replaced by the average nodal temperature.

It has been shown by several researchers that the choice of the mobility model used in the hydrodynamic simulation can effect the shape of the velocity field relation [14] and the electronic thermal conductivity [15]. However, to provide a fair comparison to drift-diffusion simulations, which by their nature can not use an energy dependent mobility, we have chosen to use a field dependent mobility model for all of the hydrodynamic and drift-diffusion calculations presented here. The standard field dependent models for Si [16] and GaAs [16] are used. The form used for GaAs captures the overshoot in the velocity-field relation. The value of the low field mobility, μ_o, depends upon the doping density and temperature of the device and is given in the next section. The equation used for μ_o is given in reference [17] and will not be repeated here.

Another important physical model which is included in the simulation is a non-infinite heat sink for the lattice. This effect is included by using the energy exchange terms of Szeto [18] which are included as source\sink terms in the energy continuity equations (power density terms). The values used for the relaxation times (τ's) used in these expressions are listed in the next section.

The final numerical aspect of the model which must be addressed are the choices for the boundary conditions, both electrical and thermal in nature. Along both lateral sides of the ballistic diode symmetry boundary conditions are assumed for all of the variables. At the source and drain contacts true ohmic conditions are used for the electrical contacts [16]. In the cases of the energy equations the temperatures (lattice and carriers) were set to 300 K at both ends of the device, implying full thermalization of the carriers.

MATERIAL PARAMETERS

The material parameters which are important for the successful simulation of the devices are the non-parabolicity factors and the energy relaxation times. For silicon using a bandgap of 1.124 eV and an effective mass of 0.326 [19], the non-parabolicity factor can be estimated, from equation (6) of reference [7], to be 0.4039 eV^{-1}. Fitting the band to the energy range ($0 \leq W \leq 0.2$) eV results in band parameters of $x = 1.15512$ and $y = 1.0439$ for the power law dispersion relation. The low field mobility values for Si are 1,332.2 and 380.6 ($cm^2/V/sec$) for doping densities of 2.0×10^{15} cm^{-3} and 5.0×10^{17} cm^{-3}, respectively. The energy relaxation time in silicon is set to 0.2 ps for the electrons and 20 fs for the holes. Using

GaAs with a bandgap of 1.424 eV and an effective mass of 0.070 the non-parabolicity factor is estimated to be 0.60736 eV^{-1}. Fitting the bands to the same range as in silicon, the power law non-parabolicity parameters for GaAs are x = 1.2375 and y = 1.06489. The low field electron and hole mobility values used for GaAs were 7,940.9 and 2,972 ($cm^2/V/sec$) respectively for the doping densities of the ballistic diode. The energy relaxation time in GaAs is set to 0.1 ps for both electrons and holes.

SILICON BALLISTIC DIODE

Figure 1 displays the calculated current-voltage characteristics of the silicon ballistic diode for six different cases considered: Three drift-diffusion simulations with different dispersion relations (parabolic, α formulation, and power law) and three hydrodynamic simulations. The first observation is that the current calculated using the parabolic case is always greater than that determined using the non-parabolic models. This is true regardless of the use of the full hydrodynamic formulation or just the drift-diffusion formulation. A cursory examination of equations (1) - (3) shows that the non-parabolicity tends to reduce the effective mobility and diffusivity of the material system. The second observation is that the α formulation predicts greater current than the power law formulation at the same bias when using the drift-diffusion approximation. However, when the full hydrodynamic formulation is used the power law predicts greater current than the α formulation, at least at the higher values of applied bias. Figure 2 shows the calculated velocity profiles through the device for the six cases considered. The figure confirms the current-voltage characteristics in Figure 1, the non-parabolic velocities are all less than the parabolic case. Also, the velocity of the

power law formulation under the drift-diffusion approximation is less than the α formulation. However, when the full hydrodynamic simulation is performed the velocity of the power law form exceeds that obtained using the α formulation. Figure 3 displays the energy profile through the device, calculated using the temperature and the velocity from the current density. The small difference in the drift-diffusion energies is due to the differences in the velocities. These energy profiles are typical of those obtained for the ballistic diode [9,10]. However, notice that the non-parabolic formulations predict lower energy peaks than the parabolic formulation. This is contrary to that obtained in reference [3] for a similar structure. The cause of this discrepancy is currently unknown. However, since the non-parabolicity factors tend to decrease the mobility and diffusivity the energy trends displayed in Figure 3 are consistent with all of the results presented here. These same trends in current, velocity, and energy have also been observed when a self-consistent energy dependent mobility model [20] was used in the hydrodynamic simulations.

GALLIUM ARSENIDE BALLISTIC DIODE

Figure 4 displays the current-voltage characteristics simulated for the GaAs ballistic diode. Figure 4 shows the same trends as observed in Figure 1 for silicon: The non-parabolic formulations predict less current than the parabolic formulation using drift-diffusion or the full hydrodynamic form; the α formulation predicts more current than the power law form using the drift-diffusion approximation, but less current when the full hydrodynamic equations are simulated. However, at 0.2 volts applied bias the power law does predict slightly less current. To resolve this the structure was simulated at finer voltage steps under

low bias. The current-voltage characteristics from 0.0 to 0.4 volts for the two non-parabolic hydrodynamic formulations are shown as an insert to Figure 4. The power law predicts smaller current values than the α formulation until the applied bias exceeds 0.32 volts, after which the power law predicts greater current. Another feature which is different than the case of silicon is that at higher biases the α formulation predicts lower current than at lower bias. It will be shown that this can be attributed to the breakdown of the binomial approximation used in the derivation.

The velocity and energy profiles for the GaAs structure under 1 volt bias are plotted in Figures 5 and 6. As for the case of the current, the same trend occurs as in silicon, the velocity predicted by the non-parabolic formulations is less than the parabolic case. The energy profile is different than that obtained for silicon, Figure 3. First, near the source end of the device the non-parabolic forms predict greater energy than the parabolic case. At the drain end of the device the energy of the parabolic case does exceed the non-parabolic cases. However, the peak energy predicted by the power law is quite close to the parabolic case, whereas the α form has a peak energy which is much lower.

Since the device is dominated by drift effects it is beneficial to examine in detail the quantities which effect the drift component of the current. This includes the 'effective' mobility and the field itself. Figure 7 is the 'effective' mobility of the field term. This is the prefactor in front of the electric field term, $n\nabla\varepsilon_n$, in equations (1) - (3). In the drift-diffusion simulations these factors are a constant, unless the field or doping changes the mobility. The field profiles for the hydrodynamic formulations differ only slightly from each other and the drift-diffusion cases. This is due to slight changes in carrier profiles caused by changes in the

density of states and other parameters. The small differences in the field profile do not explain the large variations in 'effective' mobility observed in Figure 7. The doping profile does play a role in changing the mobility as displayed in Figure 7 for the drift-diffusion cases where there is an abrupt change in mobility when the doping changes. Notice that the 'effective' mobility of the power law form is lower than the α form in the drift-diffusion model as shown in Figure 7. This leads to the lower current values under the drift-diffusion approximation for the power law. In contrast, under the full hydrodynamic simulation the α formulation's 'effective' mobility is lower leading to smaller current values. The current-voltage trend observed in the insert of Figure 4 can be now explained using Figure 7. At low bias the energy of the carriers has not risen significantly above the drift-diffusion case, the 'effective' mobility of the α formulation is greater than the power law formulation and for the same field this leads to higher current using the α formulation. As the bias is increased substantial heating of the carriers occurs, the 'effective' mobility under the α formulation decreases more than the power law form leading to lower current values.

As previously stated, the current simulated under the hydrodynamic α formulation decreases as the bias is increased. This can be attributed to the breakdown in the binomial expansion used in the derivation of the closed form coefficients. Azoff [21] predicted that the binomial expansion on the diffusion term becomes inaccurate when the condition $2\alpha W < 1$ no longer holds. In Azoff's work [21] non-parabolicity effects on the field were not taken into account. For Azoff's value of $\alpha = 0.5823$ this condition implies a hot carrier energy limit of 0.859 eV, i.e. the average energy of the carriers should not exceed 0.859 eV. In this paper, we have used an $\alpha = 0.60736$ which implies a hot carrier limit of 0.823 eV for the diffusion

term. However, in the derivation of the field dependent term within the present work, where non-parabolicity is included {reference [7] equation (34)}, the use of the binomial expansion in simplifying the denominator leads to an extra factor of two. In this case, the binomial expansion becomes inaccurate yielding unreliable results when the condition $4\alpha W < 1$ is invalid. For the choice of $\alpha = 0.60736$, this restriction implies a hot carrier energy limit of 0.4115 eV. The peak average energy in Figure 6 is less than 0.4115 eV for all three cases of the dispersion relation and the difference in peak energies for all three formulations is not large. However, at a two volt bias the average energy of the parabolic and power law formulations exceeds the limiting value reaching values of approximately 0.7 eV, as shown in Figure 8. On the other hand the peak average energy of the α formulation fails to track the increase in the energy predicted by the parabolic and power law models. As can be seen from Figure 8, the α formulation predicts a much lower peak average energy of 0.5 eV, still above the range of energies for which this model is suspect. It is clear then, that at higher applied voltages and consequently high average energies, use of the α formulation containing a binomial expansion leads to inaccurate predictions of the key macroscopic observables, i.e. average energy and current.

CONCLUSIONS

In this paper, ballistic diode simulations using two different non-parabolic formulations of the energy dispersion relation within a hydrodynamic model have been performed. These calculations have been compared to those made with non-parabolic drift-diffusion models and a parabolic hydrodynamic model. The first non-parabolic formulation of the energy utilizes

the Kane dispersion relation. In order to produce closed form coefficients in the transport equations, thereby making the calculation numerically tractable, it is essential that the terms be simplified using a binomial expansion. Unfortunately, the resulting binomial expansion is only valid for a narrow, low energy range at modest values of non-parabolicity. As a result, the non-parabolic formulation based on the Kane dispersion relation is only suitable for calculation within a narrow energy range.

In contrast, the power law formulation for the energy dispersion relation has a much greater range of energy over which it provides a valid description of the transport coefficients. This can be attributed to the observation that the transport coefficients at high energy become non-physical when the binomial expansion , Kane dispersion relation, α formulation is employed, while in the power law formulation no non-physical effects are observed.

For devices and material systems considered here, it is found that the use of the non-parabolic as opposed to the parabolic dispersion relation always leads to a lower calculated current in both the drift-diffusion and hydrodynamic simulations. The calculated carrier energy and velocity are similarly lower when the non-parabolic model is employed. These variables are lower because the non-parabolicity reduces the effective mobility and diffusivity of the material, thereby lowering the calculated current.

The relationship between the two non-parabolic models, the power law and the α formulation, is somewhat more complicated. The power law formulation predicts smaller current values than the α formulation under the drift-diffusion approximation in both silicon and GaAs. However, when the full hydrodynamic formulation is used, the power law predicts greater current than the α formulation, at least at high bias. At low bias, the power law

predicts a slightly lower current than the α formulation. These results can be attributed to the behavior of the 'effective' mobility since in the ballistic diodes considered here, the current is dominated by drift effects. When the drift-diffusion model is employed, the 'effective' mobility (defined as the prefactor in front of the electric field term) of the power law form is lower than that of the α form leading to a lower calculated current. In contrast, when the full hydrodynamic model is employed, the 'effective' mobility of the power law form is greater than that of the α form resulting in a larger calculated current. The observation of the power law initially yielding a lower current at low bias but yielding a higher current at high bias as compared to the α form, can be explained then as follows. At low bias, the devices are close to equilibrium and the carriers are relatively cold. Consequently, the system responds as in the drift-diffusion case resulting in a greater current for the α case than the power law case. At higher biases, the effects of carrier heating are more important, and the situation reverses, since the full hydrodynamic results dominate the 'effective' mobility.

ACKNOWLEDGEMENTS

This work was sponsored in part by ARPA through contract to NASA, NAGW-2753, the National Science Foundation through grant ECS-9313635, and by ARPA through the Phosphor Technology Center of Excellence, Contract MDA972-93-1-0030.

REFERENCES

1. R. A. Stewart and J. N. Churchill, Solid State Electronics, Vol 33, #7, pp. 819, (1990).

2. R. Thoma, A. Edmunds, B. Meinerzhagen, H.-J. Peifer, and W. L. Engl, IEEE Trans Elec. Dev., Vol. 38, #6, pp. 1343, (1991).

3. T. J. Bordelon, X.-L. Wang, C. M. Maziar, and A. F. Tasch, Proceedings of the IEDM, pp. 353, (1990).

4. T. J. Bordelon, X.-L. Wang, C. M. Maziar, and A. F. Tasch, Solid State Elec., Vol. 35, #2, pp. 131, (1992).

5. D. Chen, E. C. Kan, U. Ravaioli, C.-W. Shu, and R. W. Dutton, IEEE Elec. Dev. Letts., Vol. 13, #1, pp. 26, (1992).

6. E. O. Kane, J. Phys. Chem. Solids, Vol. 1, pp. 249, (1957).

7. A. W. Smith and K. F. Brennan, "Non-Parabolic Hydrodynamic Formulations for the Simulation of Inhomogeneous Semiconductor Devices", submitted to Solid State Electronics.

8. D. Cassi and B. Riccò, IEEE Trans Elec. Dev., Vol. 37, #6, pp. 1514, (1990).

9. S. Ramaswamy and T.-W. Tang, IEEE Trans Elec. Dev., Vol. 41, #1, pp. 76, (1994).

10. R. K. Cook and J. Ferry, IEEE Trans Elec. Dev., Vol. 28, #8, pp. 951, (1981).

11. D. L. Woolard, H. Tain, R. J. Trew, M. A. Littlejohn, and K. W. Kim, Phys. Rev. B, Vol. 44, #20, pp. 11119, (1991).

12. A. W. Smith, Ph. D. Dissertation, Georgia Institute of Technology, May (1992).

13. A. W. Smith and A. Rohatgi, IEEE Trans. Computer Aided Design and Integrated Circuits, Vol. 12, #10, pp. 1515, (1993).

14. A. D. Sandovnikov and D. J. Roulston, COMPEL, Vol. 12, #4, pp. 245, (1993).

15. K. Souissi, F. Odeh, H. H. K. Tang, and A. Gnudi, COMPEL, Vol. 13, #2, pp. 439, (1994).

16. S. Selberherr, Analysis and Simulation of Semiconductor Devices, Springer-Verlag, NY, NY, (1984).

17. P. A. Basore, "PC-1D installation manual and user's guide version 3.0," Sandia National Laboratories, Albuquerque, NM, (1991).

18. S. Szeto and R. Reif, Solid State Elec., Vol. 32, #4, pp. 307, (1989).

19. M. A. Green, J. Appl. Phys., Vol. 67, #6, pp. 2944, (1990).

20. B. Pejčinović, T.-W. Tang, S.-C. Lee, and D. H. Navon, IEEE Trans Elec. Dev., Vol. 39, #9, pp. 2021, (1992).

21. E. M. Azoff, J. Appl. Phys., Vol. 64, #5, pp. 2439, (1988).

Figure Captions

Figure 1. Current-voltage relation of a silicon ballistic diode using the drift-diffusion approximation with three different energy dispersion relations and the full hydrodynamic formulation using the same three energy dispersion relations. (ddm is drift-diffusion model, hdm is full hydrodynamic model)

Figure 2. Velocity profile of the silicon ballistic diode biased to 1 volt for the three energy dispersion relations under drift-diffusion conditions and hydrodynamic conditions.

Figure 3. Energy profile of the silicon ballistic diode biased to 1 volt for the three energy dispersion relations under drift-diffusion conditions and hydrodynamic conditions.

Figure 4. Current-voltage relation of a GaAs ballistic diode using the drift-diffusion approximation with three different dispersion relations and the full hydrodynamic formulation using the same three dispersion relations. Insert shows current values of the full hydrodynamic formulation and the two non-parabolic dispersion relations at low bias.

Figure 5. Velocity profile of the GaAs ballistic diode biased to 1 volt for the three cases of dispersion relations under drift-diffusion conditions and hydrodynamic conditions.

Figure 6. Energy profile of the GaAs ballistic diode biased to 1 volt for the three cases of dispersion relations under drift-diffusion conditions and hydrodynamic conditions.

Figure 7. 'Effective' mobility on the field term in the flux equations. Under drift-diffusion conditions the mobility only changes due to doping and field effects. Under non-parabolic hydrodynamic conditions at high energy the 'effective' mobility decreases.

Figure 8. Energy profile of the GaAs ballistic diode biased to 2 volts for the three cases of dispersion relations under drift-diffusion conditions and hydrodynamic conditions. The validity conditions of the binomial expansion in the α formulation have been exceeded.

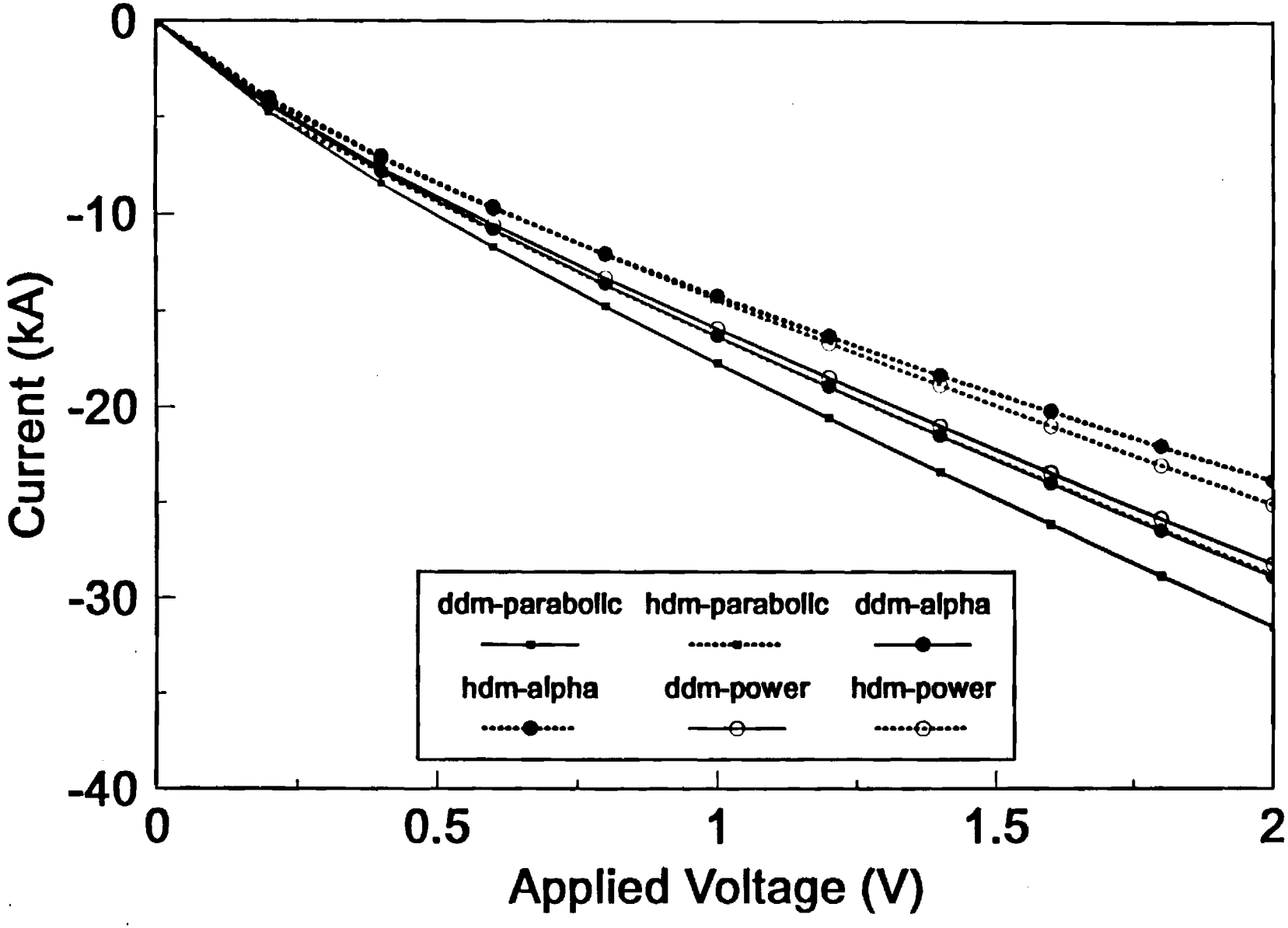

Smith, Brennan "Comparison.... " Fig 1

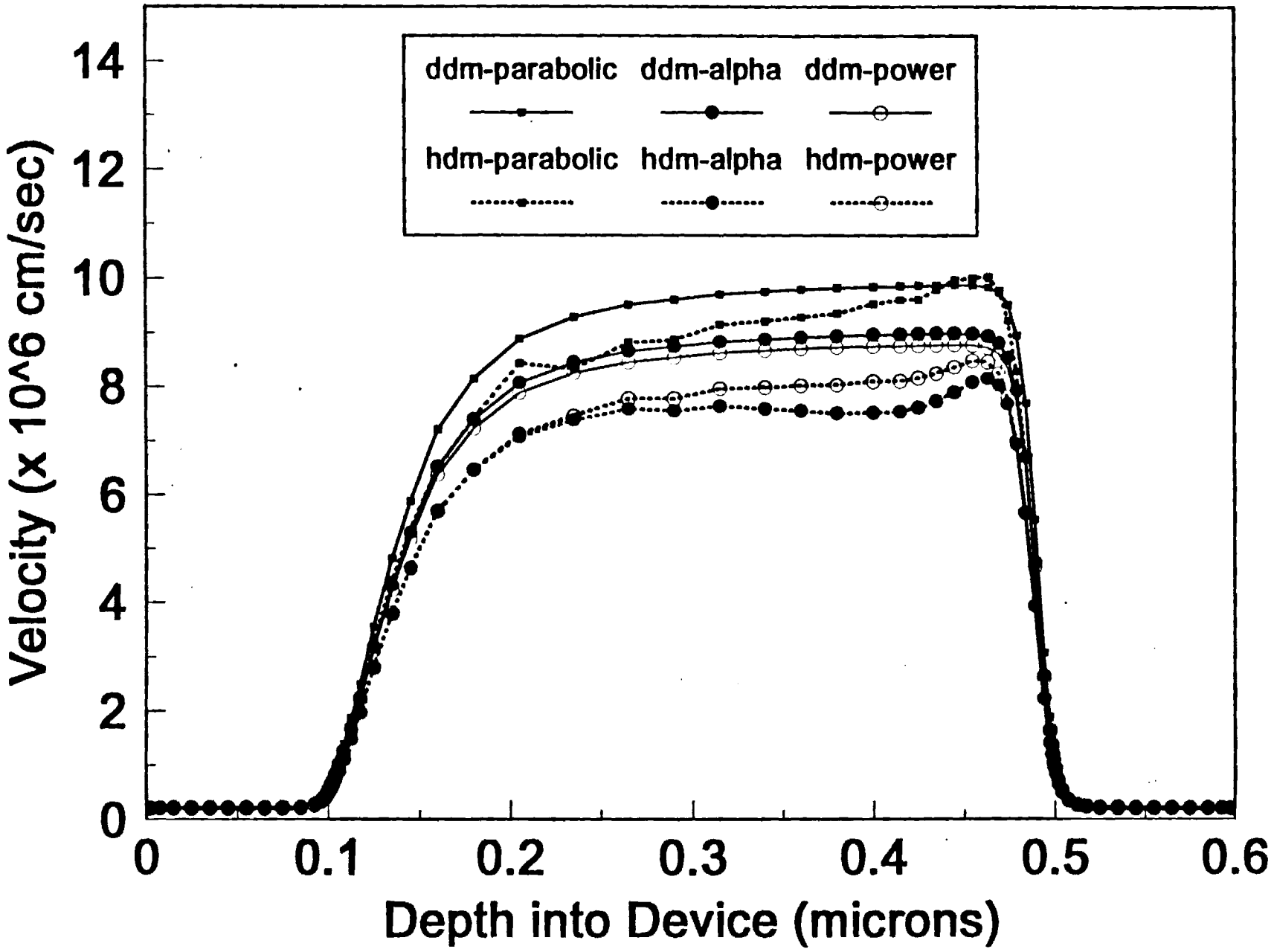
ddm-parabolic
ddm-alpha
ddm-power
hdm-parabolic
hdm-alpha
hdm-power
Velocity (x 10^6 cm/sec)
0
2
4
6
8
10
12
14
0
0.1
0.2
0.3
0.4
0.5
0.6
Depth into Device (microns)

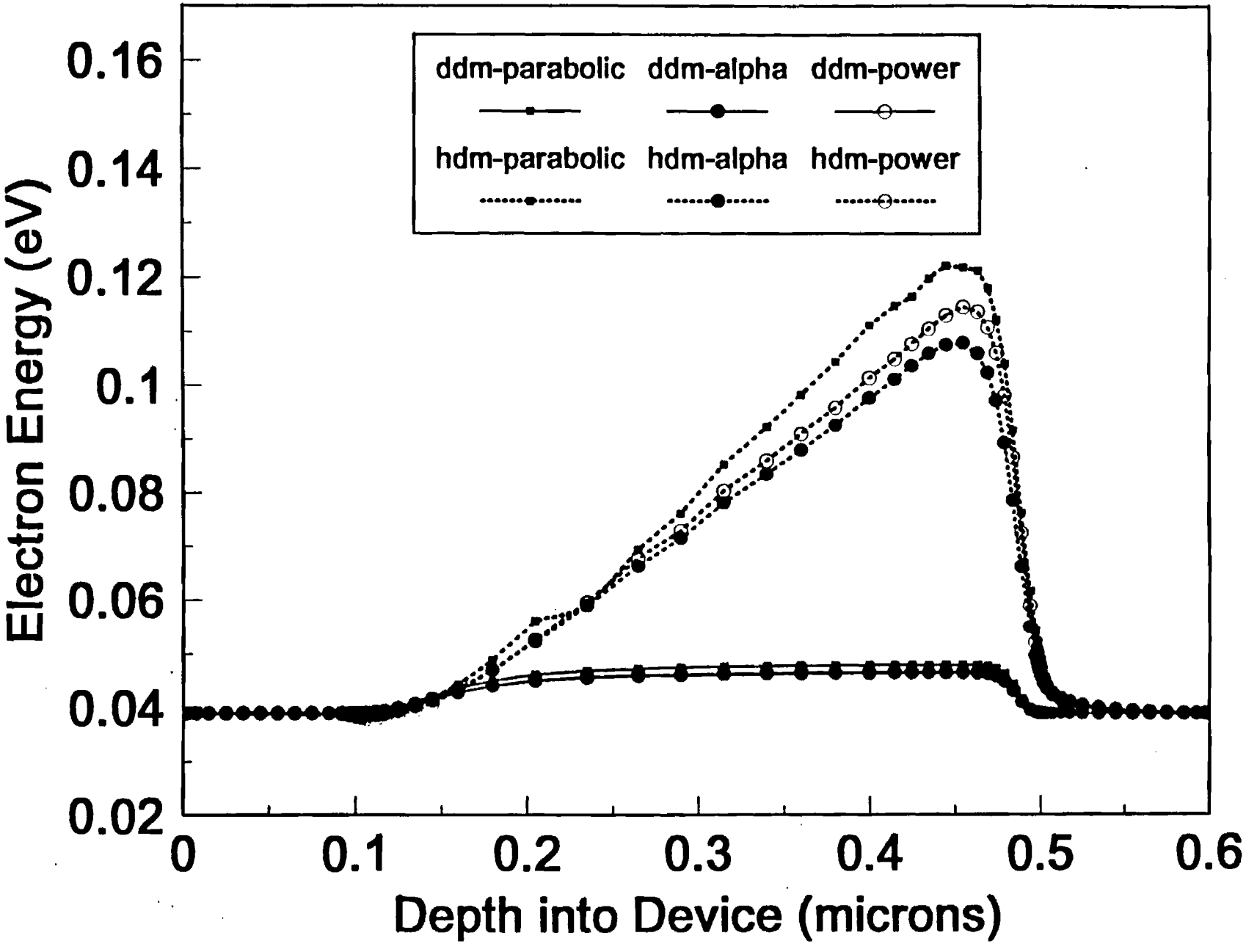

Smith, Brennan "Comparison.... " Fig 3

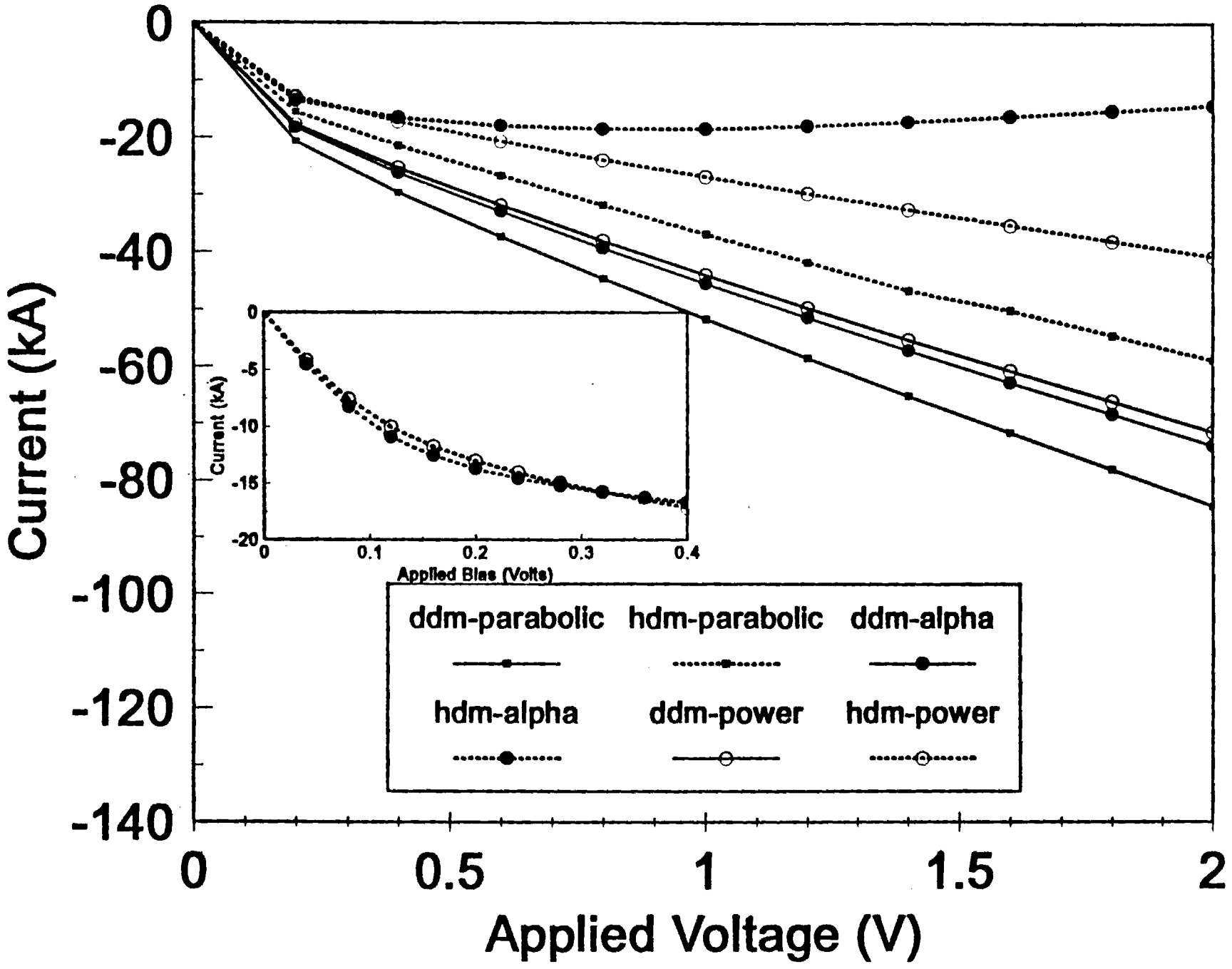

Smith, Freeman, "Comparison ... " Fig 4

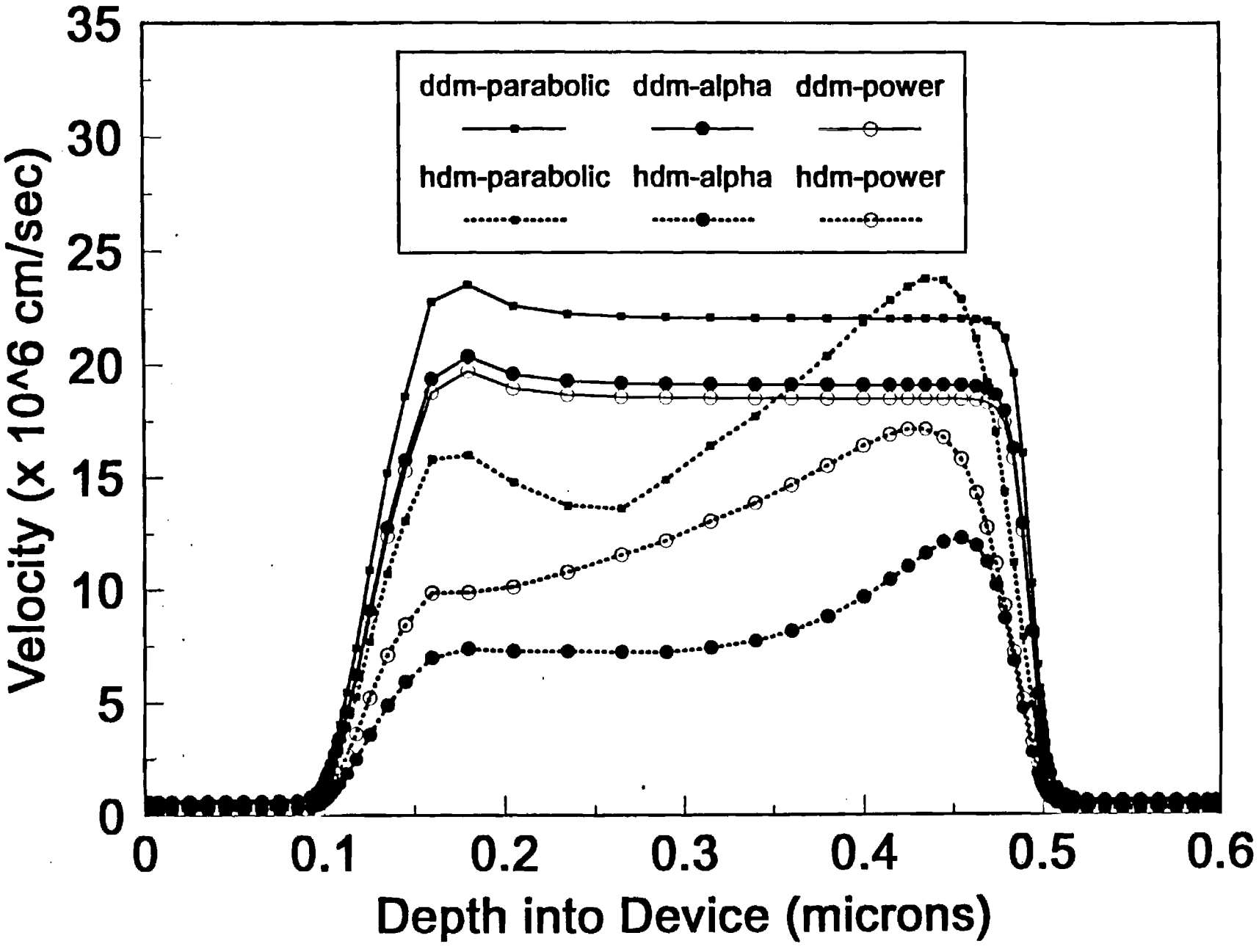

Smith, Brennan "Comparison.... " Fig 5

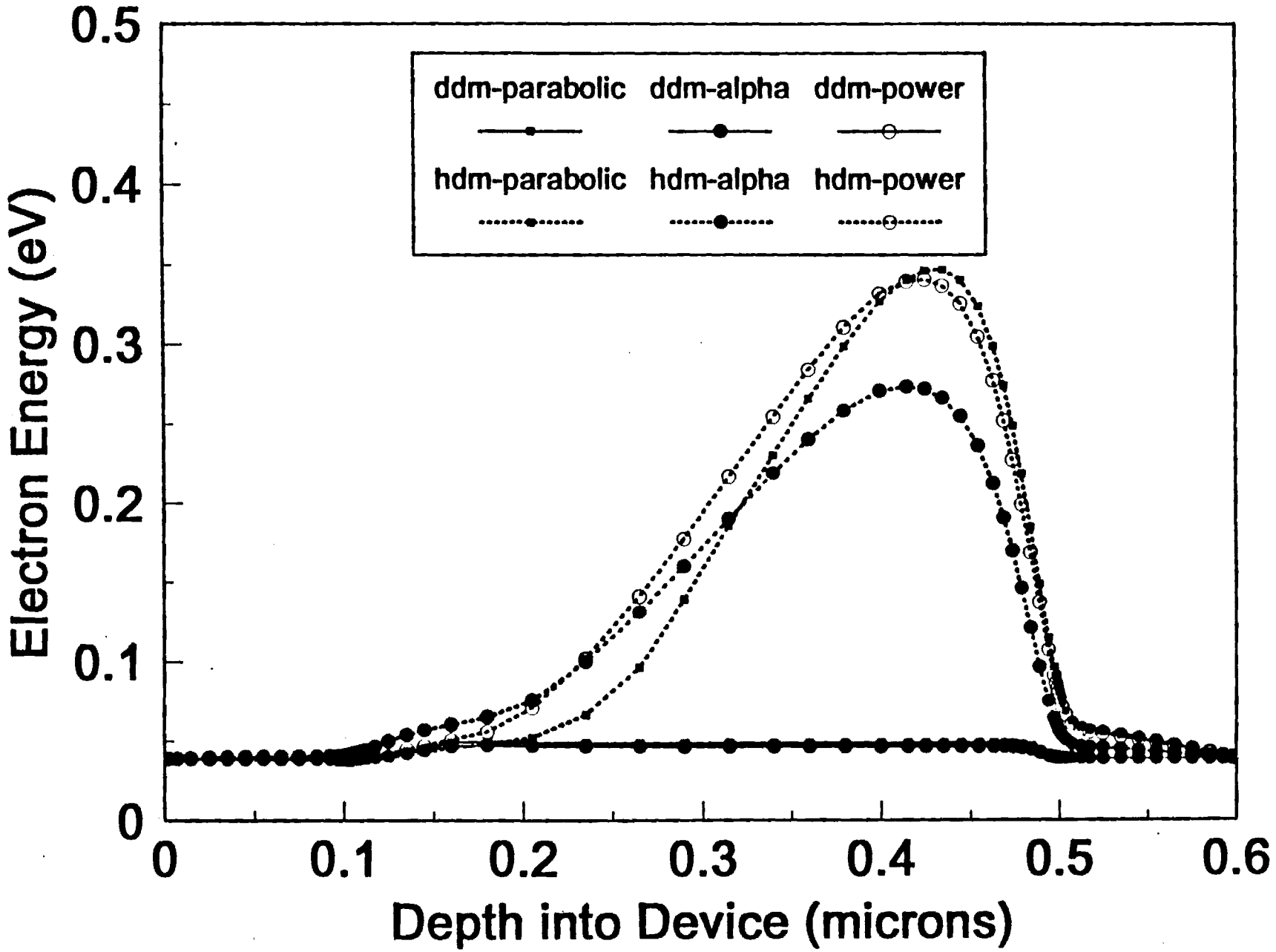

Smith, Brennan "Comparison...." Fig 6

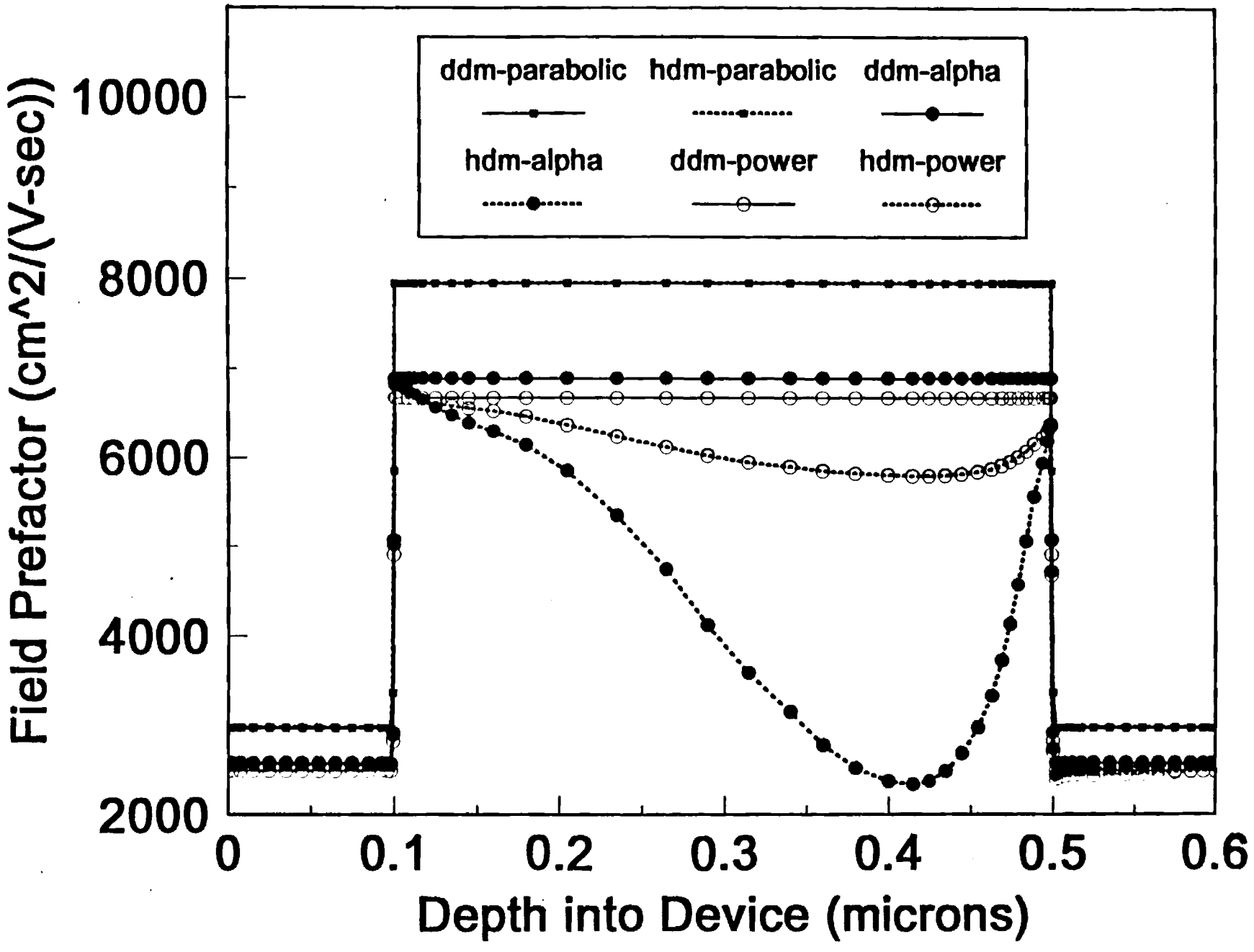

Smith, Brennan "Comparison...." Fig 7

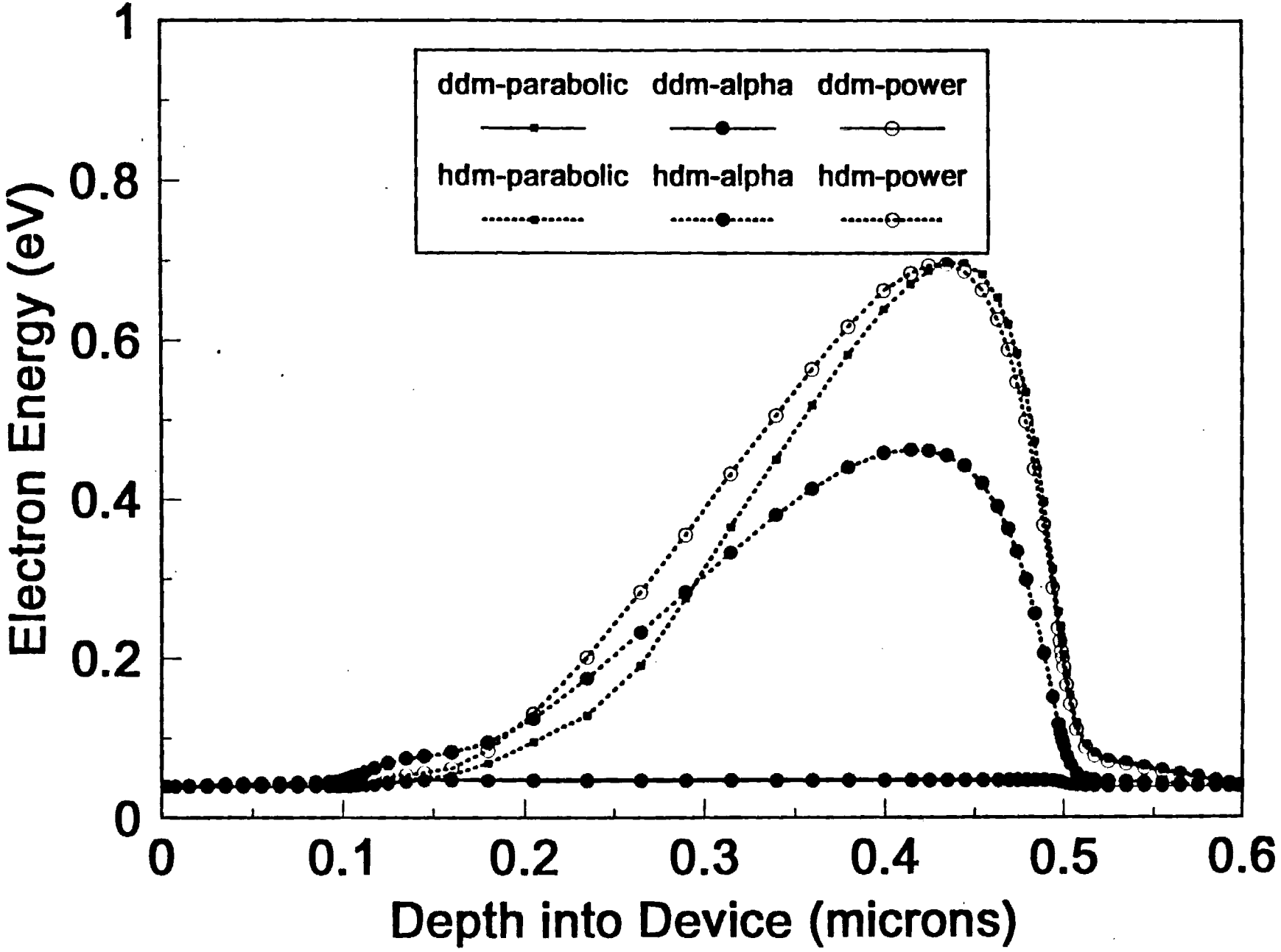
ddm-parabolic
ddm-alpha
ddm-power
hdm-parabolic
hdm-alpha
hdm-power
Electron Energy (eV)
0
0.2
0.4
0.6
0.8
1
0
0.1
0.2
0.3
0.4
0.5
0.6
Depth into Device (microns)

Revised Oct '15

Non-Parabolic Hydrodynamic Formulations for the Simulation of Inhomogeneous Semiconductor Devices

Arlynn W. Smith and Kevin F. Brennan
School of Electrical and Computer Engineering
and
Microelectronics Research Center
Georgia Institute of Technology
Atlanta, GA 30332-0250

ABSTRACT

Hydrodynamic models are becoming prevalent design tools for small scale devices and other devices in which high energy effects can dominate transport. Most current hydrodynamic models use a parabolic band approximation to obtain fairly simple conservation equations. Interest in accounting for band structure effects in hydrodynamic device simulation has begun to grow since parabolic models can not fully describe the transport in state of the art devices due to the distribution populating non-parabolic states within the band. This paper presents two different non-parabolic formulations of the hydrodynamic model suitable for the simulation of inhomogeneous semiconductor devices. The first formulation uses the Kane dispersion relationship $(\hbar k)^2/2m = W(1 + \alpha W)$. The second formulation makes use of a power law $\{(\hbar k)^2/2m = xW^y\}$ for the dispersion relation. Hydrodynamic models which use the first formulation rely on the binomial expansion to obtain moment equations with closed form coefficients. This limits the energy range over which the model is valid. The power law formulation readily produces closed form coefficients similar to those obtained using the parabolic band approximation. However, the fitting parameters (x,y) are only valid over a limited energy range. The physical significance of the band non-parabolicity is discussed as well as the advantages\disadvantages and approximations of the two non-parabolic models. A companion paper describes device simulations based on the three dispersion relationships; parabolic, Kane dispersion, and power law dispersion.

NOMENCLATURE

W	Carrier Energy
$\hbar$	Planck's constant divided by 2π
k	Reciprocal lattice vector
α	Non-parabolicity factor under the Kane dispersion relation, positional dependent
m	Carrier mass at the band edge, a constant but positional dependent
x,y	Adjustable parameters for the power law dispersion relation, both positional dependent
$g(k)$	Density of states in momentum space
W_c	Conduction band edge
E_f	Electron quasi-fermi level
K_b	Boltzmann's constant
T_e	Electron temperature
F_γ	Fermi integral of various order
$\mathcal{F}_\gamma$	Fermi integral divided by Gamma function
Γ	Gamma function
N_c	Effective density of states
η	Reduced energy $\{(E_{fn}-E_c)/(KT_e)\}$
E_g	Semiconductor band gap
∇, ∇_r	Gradient operator in physical space
∇_k	Gradient operator in k space
v_g	Group velocity
f	Distribution function
f_o	Equilibrium distribution function
τ	Relaxation time
ε_c	Conduction band potentials (electrostatic, affinity, and band gap narrowing)
n	Electron concentration
I	Identity matrix

$$g = \frac{1}{2\pi^2}\left(\frac{2m_e}{\hbar^2}\right)^{\frac{3}{2}} \qquad \Psi = 1+2\alpha W \qquad \Upsilon = 1+\alpha W$$

$$\Omega = \left(\mathcal{F}_{\frac{1}{2}} + \frac{15}{4}\alpha K T_e \mathcal{F}_{\frac{3}{2}}\right) \qquad \Lambda = \left(\mathcal{F}_{-\frac{1}{2}} + \frac{15}{4}\alpha K T_e \mathcal{F}_{\frac{1}{2}}\right)$$

INTRODUCTION

The use of hydrodynamic models for device simulation are becoming common as characteristic device dimensions continue to decrease. Hot electron effects can play a dominant role in carrier transport for high mobility semiconductors. Current hydrodynamic models consist of a set of conservation equations derived by taking moments of the Boltzmann transport equation (BTE). During the derivation of the conservation equations the parabolic band approximation is used to obtain rather simple coefficients on the forcing terms in the flux equations. By relying on the parabolic band approximation higher order energy transport effects due to variation in the band structure are neglected. Interest in accounting for band structure effects in hydrodynamic device simulation has begun to grow because parabolic models can not adequately account for high energy effects in semiconductors with non-parabolic band structures. Non-parabolic band formulations have a history dating back to the 1950's [1-3]. However drift-diffusion models and more specifically hydrodynamic simulators with non-parabolic band formulations are a very recent topic of research.

Several non-parabolic hydrodynamic models have been reported for homogeneous material systems [4-7] using the Kane dispersion relationship [3]. The general functional form obtained is similar to parabolic hydrodynamic models with first order corrections on the diffusion term. Azoff [8] derived a hydrodynamic model suitable for degenerate heterostructure semiconductors though the final form of the equations was not directly amenable to current device simulation codes. However, Azoff clearly showed that a forcing term due to a gradient in the non-parabolicity factor exists. Woolard et. al. [9] presented a non-parabolic hydrodynamic model based on moments of the velocity and energy (u, $W(k)$) instead of the momentum and momentum squared ($\hbar k$, $\hbar^2 k^2$). This leads to a simpler energy conservation equation. However, the non-parabolic coefficient in the field term and the forcing terms due to non-uniform band structure were neglected in the other moment equations. Cassi and Riccò [10] introduced an alternative to the Kane relation in the form of a power law for the dispersion

relationship. Instead of using the classical Kane dispersion law relating the energy and momentum, the band was fit over a specified energy range using two adjustable parameters. The approximations and assumptions implied by assuming the power law formulation were absent. It will be shown below that the power law formulation of the dispersion relation leads to a more simplistic and compact formulation than the classical Kane expression.

The purpose of this paper is to introduce two non-parabolic hydrodynamic formulations suitable for the simulation of devices with inhomogeneous material layers. The final form of the conservation equations will be in a form which will allow incorporation into existing device simulation codes, similar to the parabolic formulation. These different formulations are based on different choices for the dispersion relationship, one uses the standard Kane dispersion for non-parabolic bands and the second uses a power law relationship [10]. For comparison the parabolic hydrodynamic formulation will also be presented. The form of the conservation equations are strongly affected by the non-parabolicity factor of the bands, the choice of the dispersion relationship, and the assumptions made to simplify the coefficients. As in the case of the parabolic formulation, both non-parabolic formulations require estimates of higher order moments to provide mathematical closure of the relationships. It will be shown that more physical insight can be obtained by examining the terms from the power law formulation due to their similarity to the parabolic formulation. The power law is advantageous in that the terms of the conservation equations are the same as in the parabolic formulation, except for a simple multiplicative constant when Boltzmann statistics are employed.

Dispersion Relations and Carrier Concentration

The two non-parabolic dispersion relations relating the energy to the momentum are

$$W(1 + \alpha W) = \frac{(\hbar k)^2}{2m} \qquad\qquad \gamma W^{\gamma} = \frac{(\hbar k)^2}{2m} \tag{1}$$

Where α is the non-parabolicity factor in the Kane dispersion relation. This parameter is usually calculated from a k•P perturbation approach to the band structure. The α factor can also be estimated in terms of known parameters of the semiconductor [10]. The second non-parabolic dispersion relation is the power law formulation of Cassi and Riccò [10] which is not a first order approach to the band structure as compared to the Kane dispersion relation. Instead, the parameters x and y are obtained by a best fit to equation (1a) over a specified energy range. In reference [10] this energy range was (1.5 eV, 3.0 eV) and the authors produced a very good fit for $\alpha = 0.4789$, determined by inference from x and y and is reproduced in Figure 1. The formulae for the carrier concentration using these two dispersion relations and assuming Fermi-Dirac statistics are (the binomial expansion has been employed for equation (2a))

$$n = N_c(T_e)\left[\mathcal{F}_{\frac{1}{2}}(\eta) + \frac{15}{4}\alpha K_B T_e \mathcal{F}_{\frac{3}{2}}(\eta)\right] \qquad n = N_c(T_e)x^{\frac{3}{2}}y(K_B T_e)^{\frac{3}{2}(y-1)}\left[\frac{\Gamma(\frac{3}{2}y)}{\Gamma(\frac{3}{2})}\mathcal{F}_{\frac{3}{2}y-1}(\eta)\right] \quad (2)$$

In the case of the Kane dispersion the non-parabolicity is a perturbation to the parabolic model regardless of the fact that Fermi-Dirac statistics were used in the derivation instead of Boltzmann statistics. In the power law case, unlike the α formulation, the carrier concentration will only differ from the parabolic by a multiplicative constant if Boltzmann statistics are assumed.

Within the hydrodynamic simulation of a device the carrier concentration is calculated by directly solving the continuity equations. Inspection of equations (2a) and (2b) shows that the concentration in both cases is a function of the reduced energy, η. The determination of η at each position is crucial to the successful simulation of a device since most of the factors within the transport equations i.e. number of ionized dopants, Shockley-Read-Hall recombination etc., are functions of η as well. Therefore, from the knowledge of the carrier concentration at any specific position the reduced energy, η, is calculated by suitably inverting equations (2a) and (2b). With these facts in mind it is illustrative to compare the non-parabolic formulations for the carrier concentration

to the parabolic formulation at various reduced energy values. Figure 2 displays the deviation from the parabolic formulation for $\alpha = 0.4789$, $x = 1.365$, and $y = 1.52$ [10]. The case of the full Kane dispersion relation before binomial expansion is also given in Figure 2 and shows that the binomial expansion is justified for this case of the non-parabolicity parameter; the two curves are almost identical throughout the entire reduced energy range. Notice also that the deviation of the alpha nonparabolicity formulations is at most 5% from the parabolic case until the reduced energy exceeds zero, when the difference in the orders of the Fermi integral is larger. However, in the case of the power law fit at high energy, the deviation from the parabolic case is more than 82% and more than 87% from the α formulation. To explain this large difference the plots of the dispersion relations must be re-examined, Figure 1. At the high energy part of the curve the power law and α formulations have nearly identical dispersion relations. The insert in Figure 1 shows the low energy range and shows the maximum deviation of the two curves. Though there is a greater deviation between the two curves at lower energy than at high energy, the maximum difference between the two curves is insufficient by itself to fully account for the large difference in the carrier concentrations. However, carrier concentration depends upon both the density of states and the distribution function. Since the distribution function weights more heavily to lower energy states, a mismatch at low energy is strongly reflected in the product of the distribution function times the density of states and subsequently the carrier concentration. Therefore, in order to obtain a matched value of the carrier concentration, it is critical to have a closer fit to the low energy range of the band. For comparison, a low energy fit was made using a different set of for x and y, $x = 1.185$ and $y = 1.052$. These values of x and y were determined by fitting the power law dispersion relation over the low energy range ($0.0\ eV \leq W \leq 0.2\ eV$). As can be seen from the inset of Figure 1, the dispersion relations match very closely at low energy but deviate significantly at higher energy. Figure 2 also shows the calculated carrier concentrations for various reduced energy values using the low energy power law fit

factors. Compared to the power law fit to the high energy range, using the power law fit to the low energy range of the band produces concentration values which closely match those obtained using the α formulation.

Particle Flux Equations

The general flux ($\Theta = v_g$) conservation equation is determined by taking moments of the BTE as

$$\frac{\partial}{\partial t}\left(\overline{v_g f}\right) + \nabla_r \cdot \left(\overline{f v_g v_g}\right) - f\frac{\hbar^2(kk)}{m(k)} \cdot \nabla_r\left(\frac{1}{m(W)}\right)$$
$$- \overline{fF} \cdot \frac{1}{m(k)}\mathbf{I} + \overline{fF} \cdot \frac{3(k\nabla_k m(k))}{m(k)^2} = \overline{v_g}\frac{-(f-f_o)}{\tau} \tag{3}$$

Notice that the third, fourth and fifth terms on the left hand side are tensor products. The factor of 3 in the fifth term is due to the order of parenthesis in the original moment equation. This moment equation can not be processed further until some functional form of the effective mass is assumed, which depends on the choice of the dispersion relation. Using the parabolic dispersion and the two dispersion relations in equation (1), the resulting flux equations are (positional subscript on the gradient operators has been removed)

$$\frac{\partial}{\partial t}\left(\overline{v_g f}\right) + \frac{2}{3m_e}\nabla(fW) + \nabla\epsilon_e\frac{f}{m_e} - \frac{\nabla m_e}{m_e^2}fW = \overline{v_g}\frac{-(f-f_o)}{\tau} \tag{4}$$

$$\frac{\partial}{\partial t}\left(\overline{v_g f}\right) + \frac{2}{3m_e}\nabla\left(f\frac{W\Upsilon}{\Psi^2}\right) - \left(f\left[1+\frac{4}{3}\alpha W\Upsilon\right]\frac{W\Upsilon}{\Psi^4}\right)\frac{\nabla m_e}{m_e^2} + \left(f\frac{W^2\left(-1+\frac{4}{3}\Upsilon^2\right)}{m_e\Psi^4}\right)\nabla\alpha + \left(\frac{f}{m_e\Psi^3}\right)\nabla\epsilon_e = \overline{v_g}\frac{-(f-f_o)}{\tau} \tag{5}$$

$$\frac{\partial}{\partial t}(\overline{v_g}f)+\frac{2}{3m_e xy^2}\nabla(fW^{2-\gamma})+\left[\frac{\nabla m_e}{m_e}+\frac{\nabla x}{x}\right]\frac{fW^{2-\gamma}(y-4)}{3m_e xy^3}+\left(\frac{fW^{1-\gamma}}{m_e xy}\right)\left(\frac{2}{y}-1\right)\nabla\epsilon_c$$
$$+\left(\frac{fW^{2-\gamma}}{m_e xy^3}\right)\left(-\frac{2}{3}(1+2\ln(W))+y\ln(W)\right)\nabla y=\overline{v_g}\frac{-(f-f_o)}{\tau} \qquad (6)$$

Each of these equations must be integrated over all k space or equivalently over energy using the density of states [15]. Before the integration is performed one more assumption must be made, that the relaxation time is independent of k or W. If the constant relaxation time assumption is not made then the energy dependence of the relaxation time must be moved through the gradient operator on the second term in each of equations (4-6) and a term accounting for the gradient of the relaxation time must be re-created. Changing the integration from k space to energy space, substituting for the mobility, ($\mu=\tau/m$), and making $v_g f_o$ equal to zero gives the following integral equations

$$\tau\frac{\partial(nv)}{\partial t}+\frac{2\mu}{3}\nabla g\int fW^{\frac{3}{2}}dW-\mu\frac{\nabla m_e}{m_e}g\int fW^{\frac{3}{2}}dW+\mu\nabla\epsilon_c g\int fW^{\frac{1}{2}}dW=-nv \qquad (7)$$

$$\tau\frac{\partial(nv)}{\partial t}+\frac{2\mu}{3}\nabla\left[g\int f\frac{(W\Upsilon)^{\frac{3}{2}}}{\Psi}dW\right]-\mu\frac{\nabla m_e}{m_e}g\int f\frac{(W\Upsilon)^{\frac{3}{2}}\left(1+\frac{4}{3}\alpha W\Upsilon\right)}{\Psi^3}dW$$
$$+\mu\nabla\alpha g\int f\frac{W^2\left(-1+\frac{4}{3}\Upsilon^2\right)(W\Upsilon)^{\frac{1}{2}}}{\Psi^3}dW+\mu\nabla\epsilon_c g\int f\frac{(W\Upsilon)^{\frac{1}{2}}}{\Psi^2}dW=-nv \qquad (8)$$

$$\tau\frac{\partial(nv)}{\partial t}+\frac{2\mu\sqrt{x}}{3y}\nabla g\int fW^{\frac{\gamma}{2}+1}dW+\frac{\mu\sqrt{x}\nabla m_e}{3y^2m_e}[y-4]g\int fW^{\frac{\gamma}{2}+1}dW+\frac{\mu\sqrt{x}\nabla x}{3xy^2}[y-4]g\int fW^{\frac{\gamma}{2}+1}dW$$
$$+\frac{\mu\sqrt{x}\nabla y}{y^3}g\int fW^{\frac{\gamma}{2}+1}[-2-4\ln(W)+3y\ln(W)]dW+\mu\sqrt{x}\nabla\epsilon_c\left(\frac{2}{y}-1\right)g\int fW^{\frac{\gamma}{2}}dW=-nv \qquad (9)$$

To produce closed form solutions for the integrals in equation (8) the binomial expansion is used

repeatedly and all terms of order α^2 or higher are set to zero, to finally become

$$\tau\frac{\partial(nv)}{\partial t} + \frac{2\mu}{3}\nabla\left[g\int f W^{\frac{3}{2}}\left(1-\frac{\alpha W}{2}\right)dW\right] - \mu\frac{\nabla m_e}{m_e}g\int f W^{\frac{3}{2}}\left(1-\frac{19\alpha W}{6}\right)dW$$
$$+ \mu\nabla\alpha g\int f W^{\frac{5}{2}}\left(\frac{1}{3}+\frac{5\alpha W}{6}\right)dW + \mu\nabla\epsilon_c g\int f W^{\frac{1}{2}}\left(1-\frac{7\alpha W}{2}\right)dW = -nv \tag{10}$$

The only term in the power law flux equation (equation (9)) which will require an expansion is the ∇y term due to the ln(W) factor in the integrand. The expansion may only be required for certain choices of the distribution, but to maintain generality it is applied for all distributions. A parabolic interpolation, using the points 0, 0.5, and 1, to the part of the equation containing the log term is

$$\int f W^{\frac{\gamma}{2}+1}\ln(W)dW \approx 4(0.5)^{\frac{\gamma}{2}+1}\ln(0.5)\int f(W^2-W)dW \tag{11}$$

With the above substitution the power law flux equation can be written as

$$\tau\frac{\partial(nv)}{\partial t} + \frac{2\mu\sqrt{x}}{3y}\nabla g\int f W^{\frac{\gamma}{2}+1}dW + \frac{\mu\sqrt{x}\nabla m_e}{3y^2 m_e}[y-4]g\int f W^{\frac{\gamma}{2}+1}dW + \frac{\mu\sqrt{x}\nabla x}{3xy^2}[y-4]g\int f W^{\frac{\gamma}{2}+1}dW$$
$$- \frac{2\mu\sqrt{x}\nabla y}{y^3}g\int f W^{\frac{\gamma}{2}+1}dW + \frac{\mu\sqrt{x}\nabla y}{y^3}g[-4+3y]4\ln(0.5)(0.5)^{\frac{\gamma}{2}+1}\int f(W^2-W)dW \tag{12}$$
$$+ \mu\sqrt{x}\nabla\epsilon_c\left(\frac{2}{y}-1\right)g\int f W^{\frac{\gamma}{2}}dW = -nv$$

The approximation int equation (11) tends to degrade as y increases. However, this forcing term will not appear in simulations of homogeneous materials. In the case of inhomogeneous materials systems this term may be quite small as y has only a limited range, ($1 \le y \le 2$).

One of the goals of this paper is to derive a hydrodynamic model suitable for fast efficient simulation of state of the art devices. As previously stated the parabolic model is inadequate for

certain material systems due to the fact that their band structures deviate dramatically from a parabolic shape at high energies. In these situations, a non-parabolic band structure provides a more accurate description. As discussed above, the full α formulation captures the desired physics, but is unattractive because the coefficients within the transport equations need to be numerically evaluated. In contrast, the binomial α formulation and the power law formulation provide closed form expressions for the transport coefficients. However, the question remains as to their ability to display the proper trends; how closely do the coefficients match the full α formulation? We will show that the binomial α formulation has a limited energy and non-parabolicity range due to the binomial approximation. Non-physical results will be obtained if the formulation is extended into regions outside the binomial limit. The power law does not produce non-physical results but more closely matches the parabolic formulation when fit to the low energy part of the band.

The coefficients on similar forcing terms in the various formulations can now be compared to examine the impact of the non-parabolicity factor and approximations made during the derivation. The comparison is done at this time to avoid any confusion from assuming a distribution function. Table I lists the forcing terms which are compared and the terms within the integrands involved. Table II contains the values of the non-parabolicity factors at which these factors are compared, this includes values of α from 0.04 to 4.0 and appropriate (x,y) values fit to these α values over two different energy ranges (0.0, 0.2) and (1.5, 3.0). Figure 3 shows the prefactor for the diffusion term from all the flux equations; Figure 3a is for slightly non-parabolic bands (α = 0.04); 3b is for the non-parabolicity in reference [10] (α = 0.4789), and 3c is for a highly non-parabolic band (α = 4.0). Figures 4 a-c and 5 a-c display the prefactors on the forcing terms from changes in the effective mass and the field for the three degrees of non-parabolicity. For all three forcing terms at the lowest values of non-parabolicity (Figures 3a, 4a, 5a) the prefactors compare favorably with the parabolic formulation. For the diffusion term (Figures 3a-c) as the non-parabolicity factor increases the two

cases of the power law formulation match very closely to the full α formulation. On the other hand the α formulation that utilizes the binomial expansion is very different, especially at the highest value of non-parabolicity considered. From Figure 3c it is clear that the binomial α formulation is clearly incorrect if the energy exceeds 0.5 eV. Even before this point the diffusion will be underestimated. In the case of the mass term, Figure 4, the power law formulation which is fit over the low energy range is much closer to the parabolic case, as expected due to the small change in the fitting parameters from their parabolic values. However, the power law with the parameters fit over a larger energy range more closely matches the full α formulation. As in the case of the diffusion term, the binomial α formulation severely underestimates the effect of this forcing term especially as the non-parabolicity is increased, and is limited to energies less than 0.1 eV for $\alpha = 4.0$. The coefficients for the field term, Figure 5, follow the same conclusions as for the mass term. From these figures it is clear that the binomial α formulation has a very limited energy range of validity as the non-parabolicity factor is increased. Using this formulation at higher energies or high non-parabolicity factors can give un-physical results due to the prefactors changing sign. On the other hand, the power law formulation with parameters fit over a small energy range will tend to produce results which more closely match the parabolic band model. It will not produce un-physical trends and does appear to have a larger range of validity for both energy and non-parabolicity factors. The case of the power law with parameters fit over a large energy range more closely matches the full α formulation in terms of the forcing coefficients. However, due to the problems previously described for the calculation of the carrier concentration this advantage may be immaterial.

Table I can also be used to gain some physical insights into transport in the non-parabolic band structures, especially using the power law formulation. First notice that as the non-parabolicity factor is decreased ($\alpha \rightarrow 0$, $x \rightarrow 1$, $y \rightarrow 1$) all the coefficients reduce to the parabolic case indicating that all three formulations are equivalent in this respect. As the non-parabolicity factor and energy

increases the binomial α formulation can actually predict a change in the sign of a forcing term. In the full α formulation the sign on the forcing terms does not change but it is unclear as to how the term decreases. In the case of the power law, when the parameter y equals 2 it is obvious that the field term will become identically zero. The only terms which will be non-zero in the flux equation will be the diffusion, gradient in mass, and gradient in the non-parabolicity terms. This can be explained with the use of the power law energy equation {equation (1b)} and the group velocity equation. When y equals 2 there is a linear relationship between the momentum and energy, the bands are V shaped. The group velocity is proportional to the gradient of the energy with respect to k, which for the case of y equals 2 means that the group velocity is a constant. Therefore, no matter how much force is applied to the electron by external forces the velocity is not increased. The only factors which can produce current are gradients which can change this fixed velocity; i.e. changes in mass or non-parabolicity factor, or changes in the number of carriers moving at this fixed velocity, diffusion. Therefore, non-parabolic formulations which do not include coefficients to diminish the field term as the non-parabolicity increases overestimate the flux.

At this point in the derivation a recursion relation must be formulated, a distribution function assumed, or some other mathematical method {Minimum-Maximum theorem} must be used to provide mathematical closure for equations (7), (10), and (12). Since, a goal of this paper is the formulation of models suitable for the numerical simulation of devices the first two options are explored [16]. A recursion relation would allow moments of higher order to be approximated by lower order moments, the lower orders are calculated from the conservation equations. This option does not require that a specific form of the distribution function be used, unless the recursion relations are based on a specific distribution. However, in the case of non-parabolic bands the standard recursion relations may no longer be applicable [9]. Therefore, this option was not pursued. The other option, and the one chosen for this work, is to assume a specific form for the distribution function, higher moments can

then be calculated based on the known distribution function. Some of the choices for the distribution function include heated Maxwellian, shifted and heated Maxwellian, heated Fermi-Dirac, or shifted and heated Fermi-Dirac. Since the Maxwellian distributions can be recovered by relaxing the degeneracy, the Fermi-Dirac distributions were the only ones considered for this work.

In the non-parabolic formulation a simple relation between energy and velocity will not exist due to the change in the density of states. Also higher order powers of the energy are required to close the relationships in the α formulation, this will require cross product terms involving the temperature and the velocity. In addition, the power law formulation has non-integer powers of the energy which will be very difficult to evaluate for the shifted and heated distributions. Due to these conditions and the fact that all the formulations break down as the energy rises, the heated Fermi-Dirac distribution was used to close the relationships. The flux equation in the binomial α formulation is

$$
\begin{aligned}
-n\bar{v} = {} & \mu K T_e \left[\frac{\mathcal{F}_{\frac{1}{2}}^2 + \frac{10}{4}\alpha K T_e \mathcal{F}_{\frac{3}{2}} \mathcal{F}_{\frac{1}{2}}}{\mathcal{F}_{\frac{1}{2}} \mathcal{F}_{-\frac{1}{2}} + \frac{15}{4}\alpha K T_e \left(\mathcal{F}_{\frac{1}{2}}^2 + \frac{\mathcal{F}_{-\frac{1}{2}} \mathcal{F}_{\frac{3}{2}}}{2} \right)} \right] \nabla n + \mu n \left[\frac{\mathcal{F}_{\frac{1}{2}} - \frac{21}{4}\alpha K T_e \mathcal{F}_{\frac{3}{2}}}{\Omega} \right] \nabla \epsilon_c \\
& - \frac{\mu n K T_e}{A} \left[\mathcal{F}_{\frac{1}{2}} + \frac{\mathcal{F}_{\frac{1}{2}}^2 + 20\alpha K T_e \mathcal{F}_{\frac{3}{2}} \mathcal{F}_{-\frac{1}{2}}}{2\Omega} \right] \frac{\nabla m}{m} + \frac{\mu n K T_e}{A\Omega} \left[\frac{5}{2} \mathcal{F}_{-\frac{1}{2}} \mathcal{F}_{\frac{3}{2}} - \mathcal{F}_{\frac{1}{2}}^2 - \frac{\mathcal{F}_{\frac{1}{2}}^3}{2\Omega} \right] \frac{\nabla T_e}{T_e} \\
& - \frac{4\mu n (K T_e)^2}{\Omega} \left[\frac{10 \mathcal{F}_{\frac{1}{2}} \mathcal{F}_{\frac{3}{2}}}{A} - \frac{175}{4}\alpha K T_e \mathcal{F}_{\frac{7}{2}} + \frac{\mathcal{F}_{\frac{1}{2}}^2 \mathcal{F}_{\frac{3}{2}}}{A\Omega} \right] \nabla \alpha
\end{aligned}
\tag{13}
$$

The flux equation in the power law formulation becomes

$$
\begin{aligned}
-n\overline{v} = {} & \frac{2\mu}{3xy^2}(KT_e)^{2-\gamma}\frac{\left(\frac{\gamma}{2}+1\right)\Gamma\left(\frac{\gamma}{2}+1\right)\mathcal{F}_{\frac{\gamma}{2}}}{\left(\frac{3}{2}y-1\right)\Gamma\left(\frac{3}{2}y-1\right)\mathcal{F}_{\frac{3}{2}y-2}}\nabla n + \frac{(2-y)\mu n}{xy^2}(KT_e)^{1-\gamma}\frac{\Gamma\left(\frac{\gamma}{2}+1\right)\mathcal{F}_{\frac{\gamma}{2}}}{\Gamma\left(\frac{3}{2}y\right)\mathcal{F}_{\frac{3}{2}y-1}}\nabla\epsilon_c \\
& + \frac{\mu n}{xy^2}(KT_e)^{2-\gamma}\left[\frac{-y\left(\frac{\gamma}{2}+1\right)\Gamma\left(\frac{\gamma}{2}+1\right)\mathcal{F}_{\frac{\gamma}{2}}}{\left(\frac{3}{2}y-1\right)\Gamma\left(\frac{3}{2}y-1\right)\mathcal{F}_{\frac{3}{2}y-2}} + \frac{(4+y)\Gamma\left(\frac{\gamma}{2}+2\right)\mathcal{F}_{\frac{\gamma}{2}+1}}{3\Gamma\left(\frac{3}{2}y\right)\mathcal{F}_{\frac{3}{2}y-1}}\right]\frac{\nabla T_e}{T_e} \\
& - \frac{\mu n}{xy^2}(KT_e)^{2-\gamma}\left[\frac{\left(\frac{\gamma}{2}+1\right)\Gamma\left(\frac{\gamma}{2}+1\right)\mathcal{F}_{\frac{\gamma}{2}}}{\left(\frac{3}{2}y-1\right)\Gamma\left(\frac{3}{2}y-1\right)\mathcal{F}_{\frac{3}{2}y-2}} - \frac{4\Gamma\left(\frac{\gamma}{2}+2\right)\mathcal{F}_{\frac{\gamma}{2}+1}}{3\Gamma\left(\frac{3}{2}y\right)\mathcal{F}_{\frac{3}{2}y-1}}\left(1-\frac{1}{y}\right)\right]\left(\frac{\nabla m}{m}+\frac{\nabla x}{x}\right) \\
& + \frac{\mu n}{xy^3}(KT_e)^{2-\gamma}\left[\frac{-2\left(\frac{\gamma}{2}+1\right)\Gamma\left(\frac{\gamma}{2}+1\right)\mathcal{F}_{\frac{\gamma}{2}}}{3\left(\frac{3}{2}y-1\right)\Gamma\left(\frac{3}{2}y-1\right)\mathcal{F}_{\frac{3}{2}y-2}}\left(1+\frac{3}{2}y\ln(KT_e)\right) + \frac{\Gamma\left(\frac{\gamma}{2}+2\right)\mathcal{F}_{\frac{\gamma}{2}+1}}{3\Gamma\left(\frac{3}{2}y\right)\mathcal{F}_{\frac{3}{2}y-1}}\left(-4+y\ln(KT_e)\right)\right. \\
& \left. + (3y-4)4\ln(0.5)(0.5)^{\frac{\gamma}{2}+1}(KT_e)^{-\frac{\gamma}{2}}\left(\frac{KT_e\Gamma(3)\mathcal{F}_2-\Gamma(2)\mathcal{F}_1}{\Gamma\left(\frac{3}{2}y\right)\mathcal{F}_{\frac{3}{2}y-1}}\right)\right]\nabla y
\end{aligned}
\tag{14}
$$

The reader can verify that as the non-parabolicity factors are diminished, ($\alpha\rightarrow 0$, $x,y\rightarrow 1$), the two non-parabolic formulations reduce to the standard parabolic case. The equations also reduce to simpler forms when the degeneracy effects are ignored (all orders of Fermi integral reduce to exponentials). The flux equations can be discretized using normal techniques to produce comparable simulation codes under various assumptions [17].

Energy Flux Equations

For the energy flux equation ($\Theta = Wv_g$) the general conservation equation is

$$
\begin{aligned}
& \frac{\partial}{\partial t}\left(W\overline{v_g f}\right) + \nabla\cdot\left(fW\overline{v_g v_g}\right) - f\overline{v_g v_g}\cdot\nabla W - fW\frac{\hbar^2(k\,k)}{m(k)}\cdot\nabla\left(\frac{1}{m(W)}\right) \\
& - f\overline{F}\cdot\overline{v_g v_g} - f\overline{F}\cdot\frac{W}{m(k)}\mathbf{I} + f\overline{F}\cdot\frac{3W(k\nabla_k m(k))}{m(k)^2} = W\overline{v_g}\frac{-(f-f_o)}{\tau}
\end{aligned}
\tag{15}
$$

Notice that the fourth through seventh terms on the left hand side are tensor products. As in the case of the particle flux moment the energy flux moment equation can not be processed further until some functional form of the effective mass is assumed. By making similar assumptions, substitutions, and approximations {binomial expansion, Fermi-Dirac statistics, equipartition of energy ...} the energy flux equations for the three dispersion relationships become

$$-\bar{S} = \frac{5}{2}\mu n K T_e \left[K T_e \left[\frac{\mathcal{F}_{\frac{3}{2}}}{\mathcal{F}_{-\frac{1}{2}}} \right] \frac{\nabla n}{n} + \left[\frac{\mathcal{F}_{\frac{3}{2}}}{\mathcal{F}_{\frac{1}{2}}} \right] \nabla \epsilon_c - \frac{3KT_e}{2} \left[\frac{\mathcal{F}_{\frac{3}{2}}}{\mathcal{F}_{-\frac{1}{2}}} \right] \frac{\nabla m}{m} + \frac{7}{2} K T_e \frac{\mathcal{F}_{\frac{5}{2}}}{\mathcal{F}_{\frac{3}{2}}} \left[1 - \frac{3}{7} \frac{\mathcal{F}_{\frac{1}{2}} \mathcal{F}_{\frac{3}{2}}}{\mathcal{F}_{-\frac{1}{2}} \mathcal{F}_{\frac{5}{2}}} \right] \frac{\nabla T_e}{T_e} \right] \tag{16}$$

$$\begin{aligned} -\bar{S} = {} & \frac{5\mu (KT_e)^2}{2} \left[\frac{\mathcal{F}_{\frac{3}{2}} \Omega - \frac{7}{4} \alpha K T_e \mathcal{F}_{\frac{1}{2}} \mathcal{F}_{\frac{5}{2}}}{\Lambda \Omega} \right] \nabla n + \frac{5\mu n K T_e}{2} \left[\frac{\mathcal{F}_{\frac{3}{2}} - \frac{23}{4} \alpha K T_e \mathcal{F}_{\frac{5}{2}}}{\Omega} \right] \nabla \epsilon_c \\ & - \frac{5\mu n (KT_e)^2}{2} \left[\frac{3\mathcal{F}_{\frac{3}{2}}}{2\Lambda} - \frac{14 \alpha K T_e \mathcal{F}_{\frac{7}{2}}}{\Omega} - \frac{21 \alpha K T_e \mathcal{F}_{\frac{5}{2}} \mathcal{F}_{\frac{1}{2}}}{8 \Lambda \Omega} \right] \frac{\nabla m}{m} \\ & + \frac{5\mu n (KT_e)^2}{2\Omega} \left[\frac{5}{2} \mathcal{F}_{\frac{5}{2}} - \frac{21}{8} \alpha K T_e \mathcal{F}_{\frac{7}{2}} + \frac{\mathcal{F}_{\frac{1}{2}} \mathcal{F}_{\frac{5}{2}} - \frac{3}{20} \alpha K T_e \mathcal{F}_{\frac{1}{2}} \mathcal{F}_{\frac{3}{2}}}{\Omega} - \frac{3\mathcal{F}_{\frac{3}{2}} \Omega - \frac{101}{8} \alpha K T_e \mathcal{F}_{\frac{1}{2}} \mathcal{F}_{\frac{5}{2}}}{2\Lambda} \right] \frac{\nabla T_e}{T_e} \\ & - \frac{5\mu n (KT_e)^3}{2\Omega} \left[\frac{3\mathcal{F}_{\frac{3}{2}}^2}{2\Lambda} - \frac{315}{16} \alpha K T_e \mathcal{F}_{\frac{9}{2}} + \frac{105 \alpha K T_e \mathcal{F}_{\frac{1}{2}} \mathcal{F}_{\frac{3}{2}} \mathcal{F}_{\frac{5}{2}}}{16 \Lambda \Omega} \right] \nabla \alpha \end{aligned} \tag{17}$$

$$
\begin{aligned}
-\bar{S} = {} & \frac{2\mu}{3xy^2}(KT_e)^{3-\gamma}\frac{\left(\frac{\gamma}{2}+2\right)\Gamma\left(\frac{\gamma}{2}+2\right)\mathcal{F}_{\frac{\gamma}{2}+1}}{\left(\frac{3}{2}y-1\right)\Gamma\left(\frac{3}{2}y-1\right)\mathcal{F}_{\frac{3}{2}y-2}}\nabla n + \frac{(8-3y)\mu n}{3xy^2}(KT_e)^{3-\gamma}\frac{\Gamma\left(\frac{\gamma}{2}+2\right)\mathcal{F}_{\frac{\gamma}{2}+1}}{\Gamma\left(\frac{3}{2}y\right)\mathcal{F}_{\frac{3}{2}y-1}}\nabla\epsilon_c \\
& + \frac{\mu n}{xy^2}(KT_e)^{3-\gamma}\left[\frac{-y\left(\frac{\gamma}{2}+2\right)\Gamma\left(\frac{\gamma}{2}+2\right)\mathcal{F}_{\frac{\gamma}{2}+1}}{\left(\frac{3}{2}y-1\right)\Gamma\left(\frac{3}{2}y-1\right)\mathcal{F}_{\frac{3}{2}y-2}} + \frac{(6+y)\Gamma\left(\frac{\gamma}{2}+3\right)\mathcal{F}_{\frac{\gamma}{2}+2}}{3\Gamma\left(\frac{3}{2}y\right)\mathcal{F}_{\frac{3}{2}y-1}}\right]\frac{\nabla T_e}{T_e} \\
& - \frac{\mu n}{xy^2}(KT_e)^{3-\gamma}\left[\frac{\left(\frac{\gamma}{2}+2\right)\Gamma\left(\frac{\gamma}{2}+2\right)\mathcal{F}_{\frac{\gamma}{2}+1}}{\left(\frac{3}{2}y-1\right)\Gamma\left(\frac{3}{2}y-1\right)\mathcal{F}_{\frac{3}{2}y-2}} - \frac{4\Gamma\left(\frac{\gamma}{2}+3\right)\mathcal{F}_{\frac{\gamma}{2}+2}}{3\Gamma\left(\frac{3}{2}y\right)\mathcal{F}_{\frac{3}{2}y-1}}\left(1-\frac{1}{y}\right)\right]\left(\frac{\nabla m}{m}+\frac{\nabla x}{x}\right) \qquad (18) \\
& + \frac{\mu n}{xy^3}(KT_e)^{3-\gamma}\left[\frac{-2\left(\frac{\gamma}{2}+2\right)\Gamma\left(\frac{\gamma}{2}+2\right)\mathcal{F}_{\frac{\gamma}{2}+1}}{3\left(\frac{3}{2}y-1\right)\Gamma\left(\frac{3}{2}y-1\right)\mathcal{F}_{\frac{3}{2}y-2}}\left(1+\frac{3}{2}y\ln(KT_e)\right) + \frac{\Gamma\left(\frac{\gamma}{2}+3\right)\mathcal{F}_{\frac{\gamma}{2}+2}}{3\Gamma\left(\frac{3}{2}y\right)\mathcal{F}_{\frac{3}{2}y-1}}\left(-4+y\ln(KT_e)\right)\right. \\
& \left. + (3y-4)4\ln(0.5)(0.5)^{\frac{\gamma}{2}+2}(KT_e)^{-\frac{\gamma}{2}+1}\left(\frac{KT_e\Gamma(3)\mathcal{F}_2-\Gamma(2)\mathcal{F}_1}{\Gamma\left(\frac{3}{2}y\right)\mathcal{F}_{\frac{3}{2}y-1}}\right)\right]\nabla y
\end{aligned}
$$

First, equation (16) corrects a sign error on the order of a Fermi integral which occurred in an earlier publication [17]. Again, the reader can verify that the non-parabolic formulations reduce to the parabolic case as the non-parabolicity factors are decreased. As in the case of the particle flux equations the energy flux equations can be discretized using normal techniques [17].

CONCLUSIONS

Two formulations of the hydrodynamic model have been presented for the simulation of non-parabolic inhomogeneous material systems, the standard Kane formulation and the power law formulation of Cassi and Riccò. Both forms reduce to the parabolic hydrodynamic model as the non-parabolicity factors are diminished. The forcing terms in the particle and energy flux equations due to

variations in the non-parabolicity factors of the bands as suggested by Azoff have been re-created in both non-parabolic formulations. It was shown that the binomial α formulation is suitable for the calculation of the carrier concentration but has a limited energy and non-parabolicity range when applied to the coefficients of the flux equations. Extending the binomial α formulation past these limits leads to non-physical terms in both the particle and energy flux equations. In the case of the power law formulation it was shown that when the adjustable parameters were fit to the high energy range the deviation in the carrier concentration from both the parabolic and α cases was extreme. When fit to the lower energy range the power law produced carrier concentrations comparable to the α formulations. The energy and non-parabolicity range of the power law formulation for the particle and energy flux equations is larger than the binomial α formulation, but it is still limited by the adjustable parameters. However, unlike the binomial α formulation the power law will not lead to physically unrealistic results, but will tend to more closely match the parabolic formulation when the adjustable parameters are fit over the low energy portion of the band. It is shown and argued using the power law formulation and a high non-parabolicity factor ($y = 2$) that a dampening factor must exist on the field term in the particle flux equation to account for the non-parabolicity of the bands in both non-parabolic formulations. Particle flux and energy flux equations using a heated Fermi-Dirac distribution function are also presented, to allow for incorporation into existing device simulators.

ACKNOWLEDGEMENTS

This work was sponsored in part by ARPA through contract to NASA, NAGW-2753, the National Science Foundation through grant ECS-9313635, and by ARPA through the Phosphor Technology Center of Excellence, Contract MDA972-93-1-0030.

REFERENCES

1. G. Dresselhaus, Phys. Rev., Vol. 100, pp. 580, (1955).

2. R. H. Parmenter, Phys. Rev., Vol. 100, pp. 573, (1955).

3. E. O. Kane, J. Phys. Chem. Solids, Vol. 1, pp. 249, (1957).

4. R. A. Stewart and J. N. Churchill, Solid State Electronics, Vol 33, #7, pp. 819, (1990).

5. R. Thoma, A. Emunds, B. Meinerzhagen, H.-J. Peifer, and W. L. Engl, IEEE Trans Elec. Dev., Vol. 38, #6, pp. 1343, (1991).

6. T. J. Bordelon, X.-L. Wang, C. M. Maziar, and A. F. Tasch, Solid State Elec., Vol. 35, #2, pp. 131, (1992).

7. D. Chen, E. C. Kan, U. Ravaioli, C.-W. Shu, and R. W. Dutton, IEEE Elec. Dev. Letts., Vol. 13, #1, pp. 26, (1992).

8. E. M. Azoff, J. Appl. Phys., Vol. 64, #5, pp. 2439, (1988).

9. D. L. Woolard, H. Tain, R. J. Trew, M. A. Littlejohn, and K. W. Kim, Phys. Rev. B, Vol. 44, #20, pp. 11119, (1991).

10. D. Cassi and B. Riccò, IEEE Trans Elec. Dev., Vol. 37, #6, pp. 1514, (1990).

11. H. B. Bebb and C. R. Ratliff, J. Appl. Phys., Vol. 42, #8, pp. 3189, (1971).

12. E. M. Azoff, COMPEL, Vol. 6, #1, pp. 25, (1987).

13. C. C. McAndrew, E. L. Heasell, and K. Singhal, Semicond. Sci. Technol., Vol. 2, pp. 643, (1987).

14. R. Kishore, Physica A, Vol. 196, pp. 133, (1993).

15. N. W. Ashcroft and N. D. Merman, Solid State Physics, Holt, Rinehart and Winston, N. Y., N. Y., (1976).

16. J. Higman and K. Hess, Solid State Elec., Vol. 29, #9, pp. 915, (1986).

17. A. W. Smith and A. Rohatgi, IEEE Trans. Computer Aided Design and Integated Circuits, Vol. 12, #10, pp. 1515, (1993).

Table I. Terms (prefactors) within the integrands of the forcing coefficients which are graphically compared.

Formulation	Equation Number	Diffusion Term	Mass Term ∇m	Field Term $\nabla \varepsilon_0$
parabolic	(7)	$W^{\frac{3}{2}}$	$W^{\frac{3}{2}}$	$W^{\frac{1}{2}}$
α formulation	(8)	$\frac{(W(1+\alpha W))^{\frac{3}{2}}}{(1+2\alpha W)}$	$\frac{(W(1+\alpha W))^{\frac{3}{2}}(1+4\alpha W)}{(1+2\alpha W)^3}$	$\frac{W^{\frac{1}{2}}(1+\alpha W)^{\frac{1}{2}}}{(1+2\alpha W)^2}$
α with binomial expansion used	(10)	$W^{\frac{3}{2}}\left(1-\frac{\alpha W}{2}\right)$	$W^{\frac{3}{2}}\left(1-\frac{19\alpha W}{6}\right)$	$W^{\frac{1}{2}}\left(1-\frac{7\alpha W}{2}\right)$
power law	(12)	$\frac{x^{\frac{1}{2}}}{y}W^{1+\frac{y}{2}}$	$\frac{x^{\frac{1}{2}}}{3y^2}[4-y]W^{1+\frac{y}{2}}$	$x^{\frac{1}{2}}\frac{(2-y)}{y}W^{\frac{y}{2}}$

Table II. Values of the non-parabolicity factors which are compared. This includes α values from 0.04 to 4.0 and (x,y) values fit to these α values over two different energy ranges (0.0, 0.2) and (1.5, 3.0).

Case	α	x, y {0.0, 0.2}	x, y {1.5, 3.0}
a	0.04	1.0148, 1.0045	1.0207, 1.0827
b	0.4789	1.185,1.052	1.365, 1.52
c	4.0	2.975,1.322	4.8233, 1.901

Figure Captions

Figure 1. Dispersion relations for the Kane model (solid line, $\alpha = 0.4789$), the power law formulation (dashed line, x=1.365, y = 1.52 fit over high energy, $1.5 \leq W \leq 3.0$ eV) and the power law formulation (dotted line, x=1.185, y = 1.052 fit over low energy, $0.0 \leq W \leq 0.2$ eV). The insert shows the detail of the low energy range.

Figure 2. Deviation, from the parabolic case, of the carrier concentration as a function of the reduced energy for the full α formulation (solid line, $\alpha = 0.4789$), binomial α (dotted), power law fit at high energy (dashed, x=1.365, y=1.52), and power law fit at low energy (dashed, x=1.185, y=1.052) dispersion relations as a function of the reduced energy (η) at T_o=300 K.

Figure 3. Comparison of the integrand coefficients (prefactors) occurring on the diffusion term of the particle flux formulations. See Table I and II for the exact form of the equations and degrees of non-parabolicity considered.

Figure 4. Comparison of the integrand coefficients (prefactors) occurring on the gradient of the effective mass term of the particle flux formulations. See Table I and II for the exact form of the equations and degrees of non-parabolicity considered.

Figure 5. Comparison of the integrand coefficients (prefactors) occurring on the gradient of the potential term occurring in the particle flux formulations. See Table I and II for the exact form of the equations and degrees of non-parabolicity considered.

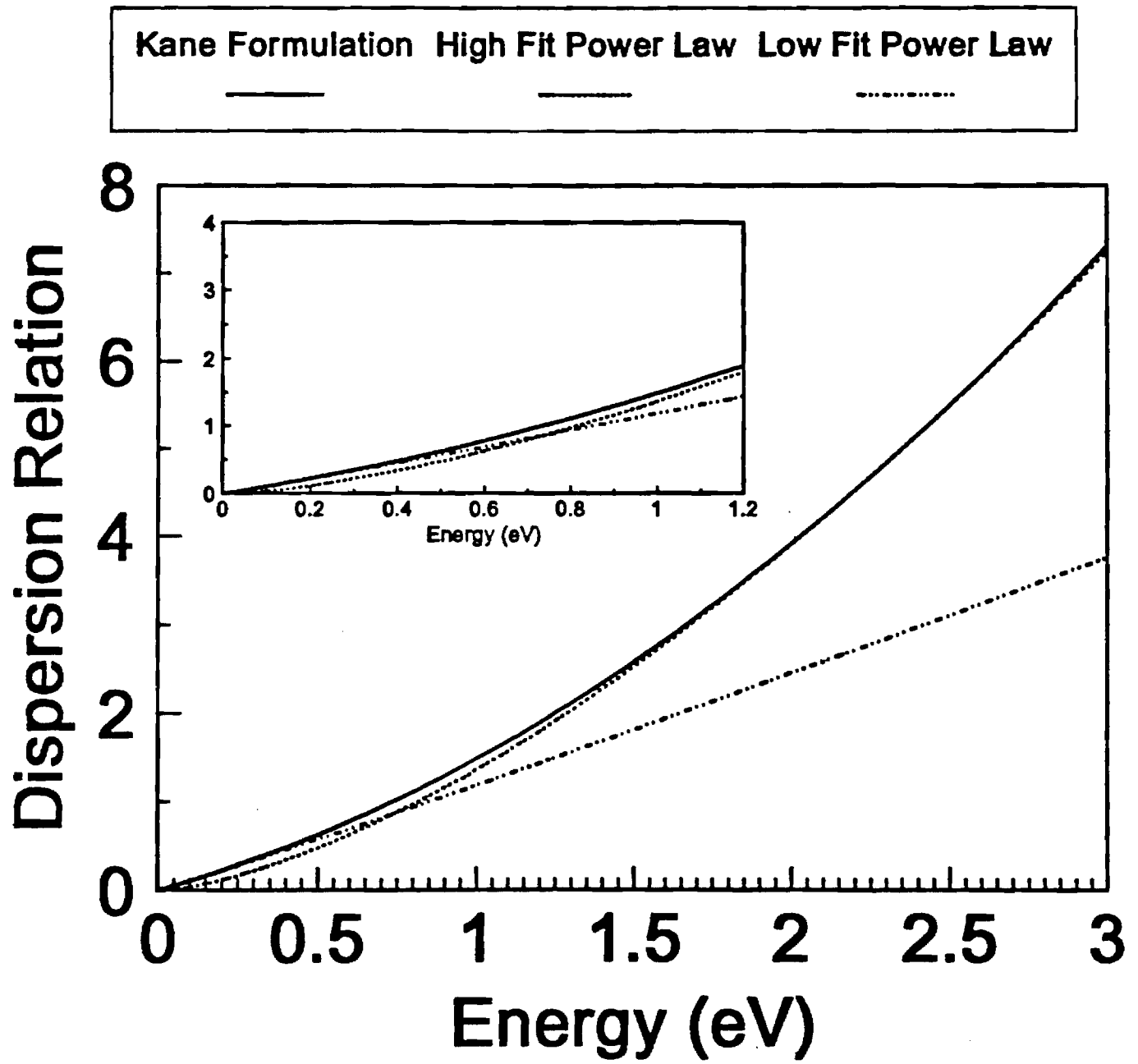

Smith, Brennan "Non-Parabolic...." Fig. 1

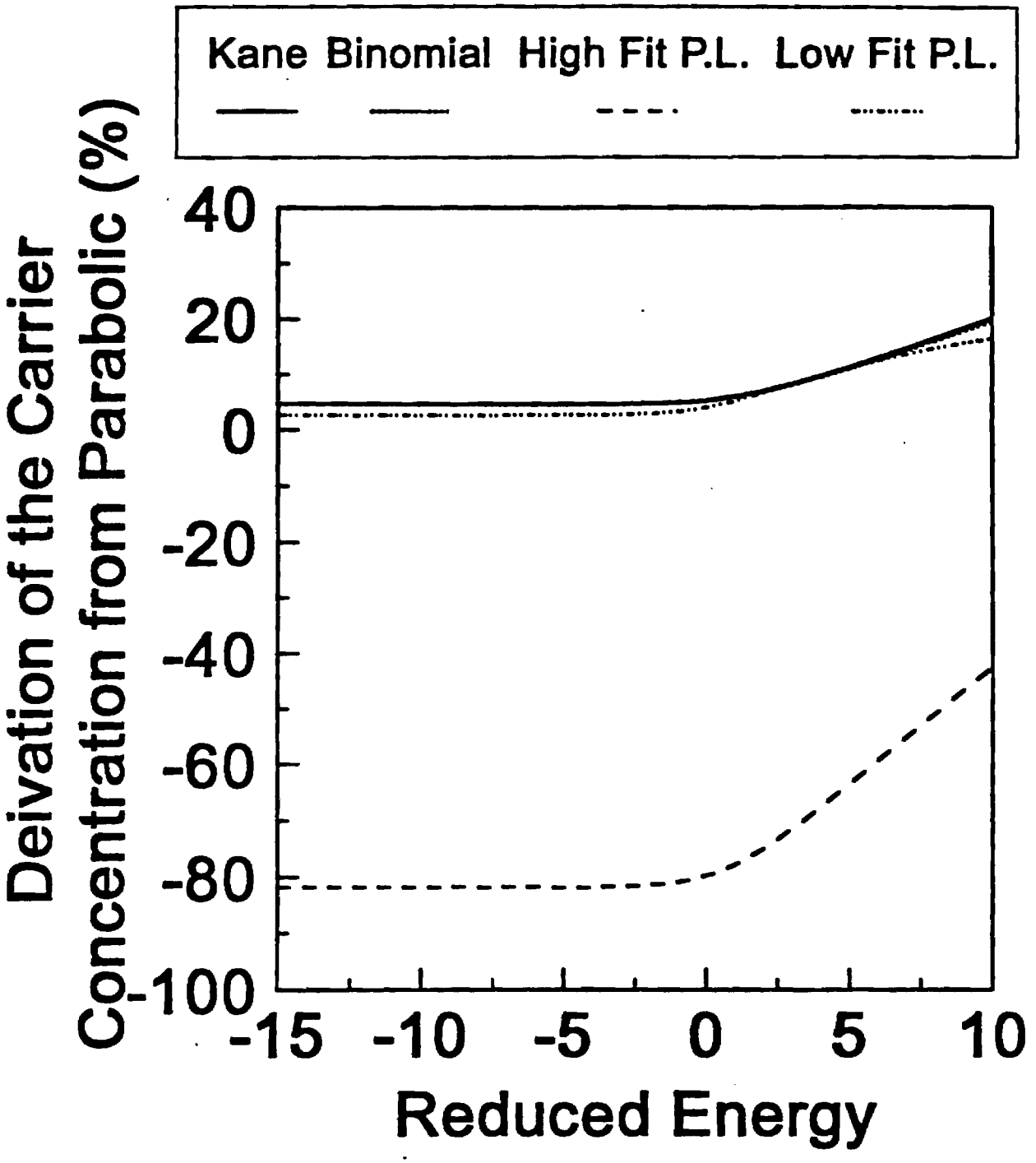

Smith, Brennan "Non-Parabolic...." Fig. 2

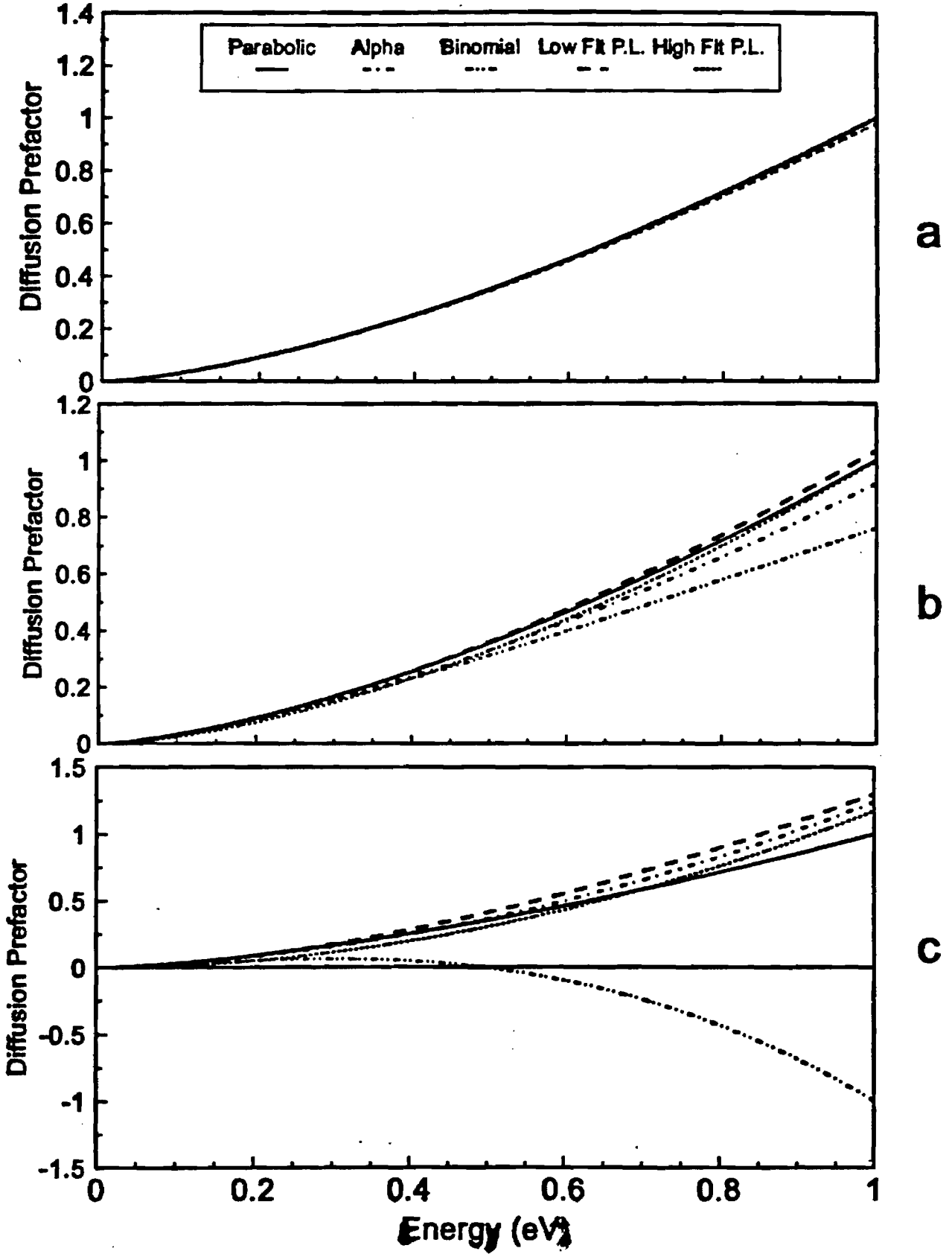

Smith, Brennan "Non-Parabolic...." Fig. 3

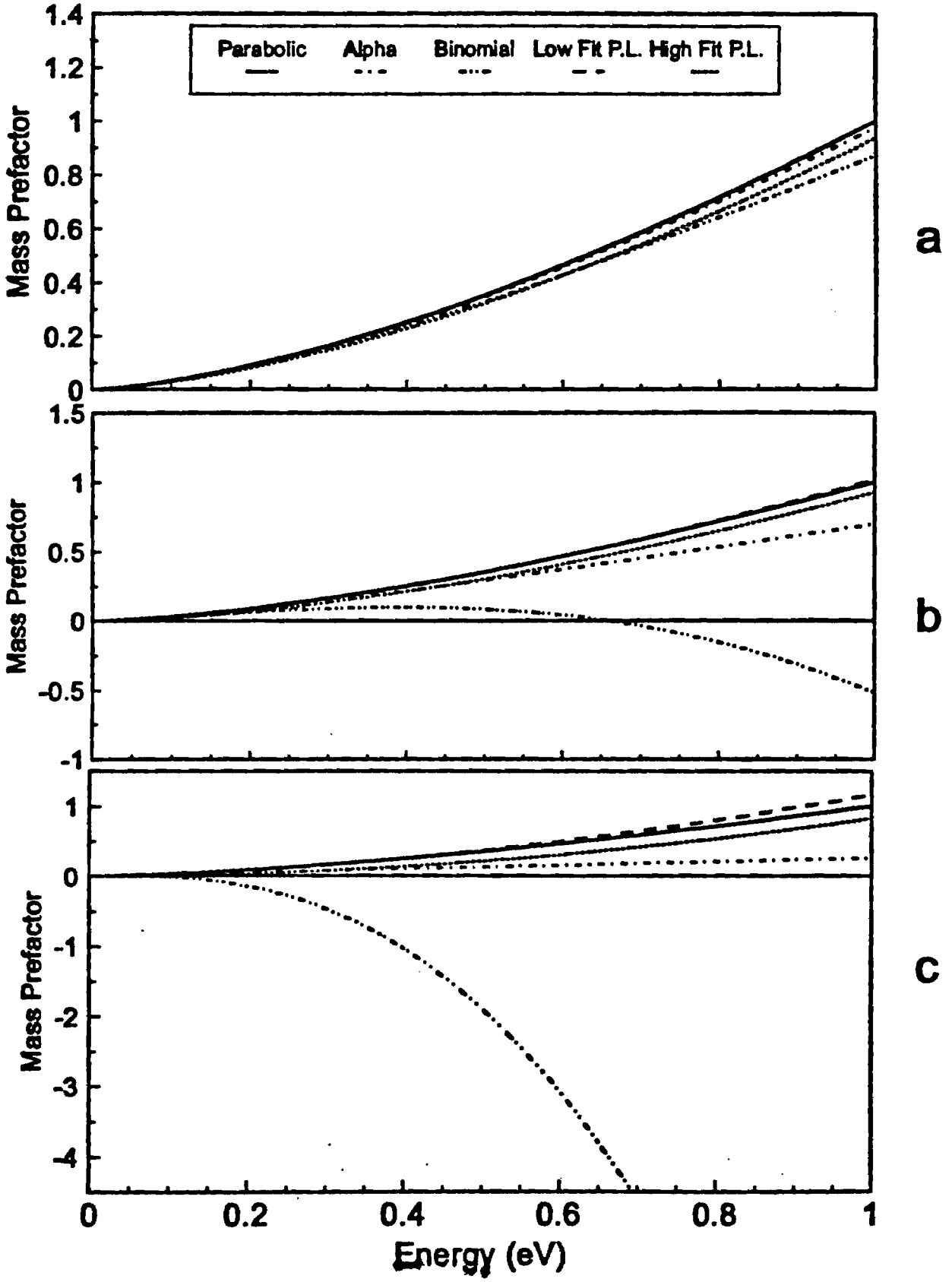

Smith, Brennan "Non-Parabolic...." Fig. 4

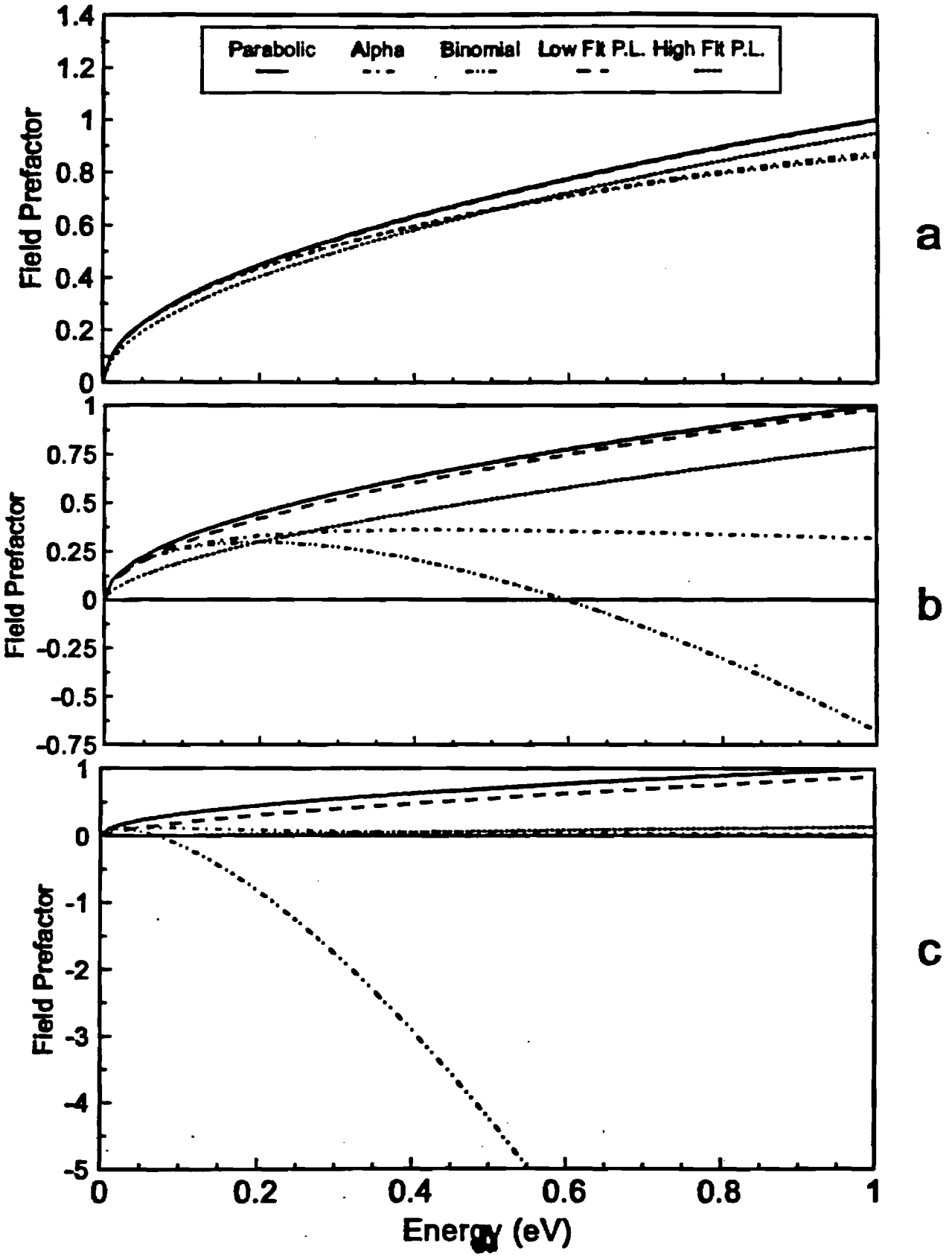

Smith, Brennan "Non-Parabolic...." Fig. 5